

## **Resubmission Summary**

As per communications with examiners, the following required corrections have been made:

1. "Remove comments/references in the literature review that were misleading or overly simplistic, as identified during the examination, e.g. to PLA, where uncertain quality assurance was not a sound reason to exclude them from further research."
  - ✓ Comments and references removed.
  
2. "Add a short section or "summary" set of requirements for your proposed alginate biomaterials solution including relevant wider comments (e.g. on the need for fixation/integration solution). Some of this information is found in elements of the literature review – albeit in places relatively superficial - but you are required to "draw this together" at the end of the literature review prior to moving to Aims & Objectives."
  - ✓ Short summary requirements section has been added at the end of literature review to properly outline proposed solution.
  
3. "Also therefore "tone down" narrative around alginates e.g. from "stand out" to "could be considered a platform". You should also mention, as discussed in the examination, that alginates alone once characterised will require further modification to deliver the properties in your summary statement referred to above under (2)."
  - ✓ Thesis has been edited to tone down the narrative and highlight knowledge gaps within the body of work that need to be further addressed. Specifically, further modification has been identified in the future work in detail.
  
4. "Likewise, do not overstate or overinterpret data where there are clear limitations, for example the nmr data demonstrates that you have alginates (where characterisation of starting materials is good practice), but you cannot extrapolate from n=1 that these are different materials in terms of composition/chemistry. Ensure that these corrections are applied to discussion and conclusions too."
  - ✓ Three repeats of each NMR sample (A-C) have now been included in the thesis so that n=3 and previous comments are sound. All data has been updated and relevant changes made to results, conclusion + discussion.



The  
University  
Of  
Sheffield.

# 3D Printing Biomaterials for Cleft Palate Repair

Alexander Patrick Bolger

May 28<sup>th</sup> 2023

The University of Sheffield  
Faculty of Medicine Dentistry & Health  
School of Clinical Dentistry

Thesis submitted for the degree of Master of Philosophy

# Acknowledgements

Thanks to my supervisors Prof Cheryl Miller, Dr Ilida Ortega and Dr Robert Moorehead for putting up with me as long as they have. I can safely say without their support and professionalism I would have quit this project many years ago. This thesis is a testament to their abilities as supervisors as, from hearing surprisingly common horror stories over the years of other supervisors, it is clear I was very lucky with mine. I doubt any of us thought this was going to get as spicy as it did but 'c'est la vie' and we move on.

Shout out to my dad, Paul Bolger, who has been a never-ending pillar of support in some very trying times; I also would not have made it to the point of submission without his help.

It is impossible for me to remember all of the help around the lab I have received over the years so I will just say a big thank you to all members of the School of Clinical Dentistry.

To George, Johnny and the rest of the climbing gang, a big thanks also goes out to you for the advice and good times over the years.

Finally, to Mahmoud, Toby and Chris – It was an absolute pleasure to be around such upstanding gentlemen over the past year and a half, I only wish we had met earlier.

# Abstract

Cleft palate is a component of the second most common birth defect found in humans, cleft lip and palate. The gold-standard for treating the defect for decades has been traditional flap surgeries however these have seen little modernisation and present several limitations. Recent advances in 3-dimensional (3D) printing have enabled the 3D printing of biomaterials which could be used to produce bespoke implants for patients as part of a novel, regenerative method for treating cleft palate. Sodium alginate is a biocompatible, natural polysaccharide which has previously been used in drug delivery and as part of cell scaffolds. In the presence of water, it readily forms hydrogels which can be crosslinked to further increase their strength, making it an ideal candidate for 3D printing.

This project aimed to develop alginate-based biomaterials for 3D printing that could be used as part of an alternative method for treating cleft palate. Proton nuclear magnetic resonance was used to identify an ideal candidate strain for the project. Then, the relationship between sodium alginate and calcium chloride ( $\text{CaCl}_2$ ), a popular crosslinking agent, was studied to optimise initial hydrogel compositions and consider their suitability for 3D printing. Rheological characterisation was then conducted to further investigate the complex viscoelastic properties these hydrogels exhibited before a 3D printing assessment was performed. Secondary and tertiary crosslinking was used to increase the strength of printed samples then assessed as potential implants mechanically and biologically.

Heterogenous hydrogels were successfully produced that exhibited a wide range of viscoelastic properties allowing relationships between material properties and hydrogel compositions to be established. Hydrogels that exhibited elastic-dominated properties were most applicable to 3D printing. Hydrogel compositions were shown to 3D print at high fidelity and through secondary-crosslinking were shown to be biomimetic to typical soft tissue. This project indicates that 3D printed alginate hydrogels could be accurately 3D printed in the



shapes and dimensions required to plug a cleft palate void as an alternative to traditional flap surgery. Secondary crosslinking of 3D printed structures produces appropriate biomimetic mechanical properties to soft tissue the obturator could be used to replace.

# Glossary of Acronyms

$^1\text{H}$ NMR	Proton nuclear magnetic resonance
2D	2-dimensional
3D	3-dimensional
3DP <sup>TM</sup>	3D Printing
3ITT	3-interval thixotropy test
ABS	Acrylonitrile butadiene styrene
ADM	Acellular dermal matrix
AM	Additive manufacturing
ANOVA	Analysis of variance
ASTM	American Society for Testing and Materials
CaCl <sub>2</sub>	Calcium chloride
CAD	Computer aided design
CL or CLO	Cleft lip only
CL/P or CP $\pm$ L	Cleft lip with or without palate
CLA	Cleft lip and alveolar process
CLP	Cleft lip and palate only
COME	Chronic otitis media with effusion
CoV	Coefficient of variance
CP or CPO	Cleft palate only
CP	Cone-plate
CT	Computed tomography
D <sub>2</sub> O	Deuterium Oxide
DIN	Deutsches Institute for Normung
ECM	Extracellular matrix

FDA	Food and Drug Administration
FDM™	Fused deposition modelling
FFF	Fused filament fabrication
G	Guluronic acid or guluronate
G'	Storage modulus
G''	Loss modulus
HA	Hyaluronic acid
HCl	Hydrochloric acid
HPDC	High pressure die casting
ISO	International Organisation for Standardisation
IVV	Intra-velar veloplasty
LVER	Linear viscoelastic region
M	Mannuronic acid or mannuronate
NaOH	Sodium Hydroxide
N <sub>G</sub>	Average guluronic acid section length
N <sub>G &gt; 1</sub>	Average guluronic acid section length (excluding single blocks)
N <sub>M</sub>	Average mannuronic acid section length
OFC	Orofacial clefts
ONF	Oronasal fistula
PC	Primary-crosslinked
PCL	Polycaprolactone
PEEK	Polyetheretherketone
PGA	Polyglycolic acid
PLA	Polylactic acid
PLGA	Polylactic-co-glycolic acid
PP	Plate-plate

SLA	Stereolithography apparatus
SLS	Selective laser sintering
SMCP	Submucosal cleft palate
SNR	Signal to noise ratio
STL	Stereolithography
TTHA	Triethylenetetramine-hexaacetic acid
UC	Uncrosslinked
UK	United Kingdom
US	United States
VPI	Velopharyngeal insufficiency or incompetence
VWK	Veau-Wardill-Kilner

# Table of Contents

1.	Introduction .....	12
2.	Literature Review .....	16
2.1.	Cleft Palate.....	16
2.1.1.	Anatomy & Classification.....	16
2.1.2.	Epidemiology .....	21
2.1.3.	Embryology and Aetiology.....	25
2.1.4.	Effects of Cleft Palate .....	29
2.2.	Cleft Palate Treatment.....	34
2.2.1.	Surgical Treatment.....	34
2.2.2.	Alternative Treatments .....	40
2.3.	Biomaterials .....	43
2.3.1.	Biomaterial Classification .....	43
2.3.2.	Biomaterial Requirements.....	50
2.3.3.	Alginate.....	52
2.4.	3D Printing .....	56
2.4.1.	Introduction to 3D Printing.....	56
2.4.2.	3D Printing vs Traditional Manufacturing.....	58
2.4.3.	3D Printing in Medicine .....	62
2.5.	Requirements for Proposed Biomaterials Approach to Treating Cleft Palate.....	67
3.	Aims and Objectives .....	70
4.	Materials & Methods.....	72
4.1.	Materials.....	73
4.2.	Hydrogel Preparation .....	75
4.2.1.	Aqueous Sodium Alginate.....	76
4.2.2.	Primary Crosslinking of Alginate Hydrogels .....	77
4.3.	Proton Nuclear Magnetic Resonance Spectroscopy of Alginate.....	79
4.4.	Hydrogel Composition Optimisation .....	84
4.4.1.	Experimental Design .....	84
4.4.2.	Visual Assessment.....	86
4.4.3.	Extrudability.....	86
4.4.4.	Extrusion Form .....	87
4.4.5.	3D Printed Stress Test .....	88
4.5.	Rheology.....	93
4.5.1.	Introduction .....	93
4.5.2.	Setup .....	96
4.5.3.	Constant Shear .....	98
4.5.4.	Amplitude Sweep .....	99
4.5.5.	Frequency Sweep .....	101
4.5.6.	Temperature Sweep.....	101
4.5.7.	3-Interval Thixotropy Test .....	102
4.5.8.	Post-Mix Time Sweep.....	102
4.5.9.	Data Presentation .....	103
4.6.	Evaluation of 3D Printed Hydrogels.....	103
4.6.1.	Advanced G-code Generation.....	104
4.6.2.	Line Width .....	105
4.6.3.	Single Layer Infill .....	106
4.6.4.	Multi-Layer Geometries .....	107

4.7.	Mechanical Testing of 3D Printed Hydrogels.....	109
4.7.1.	Secondary Crosslinking.....	109
4.7.2.	Compressive Testing .....	110
5.	Results.....	115
5.1.	Proton Nuclear Magnetic Resonance Spectroscopy of Alginate.....	115
5.2.	Hydrogel Composition Optimisation .....	120
5.2.1.	Visual Assessment.....	120
5.2.2.	Extrudability.....	122
5.2.3.	Extrusion Form .....	123
5.2.4.	Extrusion Pressure.....	125
5.2.5.	Layer Formation and Retention .....	128
5.2.6.	Viscosity.....	131
5.3.	Rheology.....	133
5.3.1.	Constant Shear .....	133
5.3.2.	Amplitude Sweep .....	136
5.3.3.	Frequency Sweep .....	142
5.3.4.	Temperature Sweep.....	147
5.3.5.	3-Interval Thixotropy Test .....	152
5.3.6.	Post-mix Time Sweep .....	160
5.4.	3D Printing .....	166
5.4.1.	Line Width .....	166
5.4.2.	Single Layer Infill .....	170
5.4.3.	Multi-Layer Geometries .....	178
5.5.	Mechanical Testing of 3D Printed Hydrogels.....	192
5.5.1.	Elastic modulus .....	192
5.5.2.	60 % Strain Toughness .....	193
6.	Discussion.....	196
6.1.	Proton Nuclear Magnetic Resonance Spectroscopy.....	196
6.2.	Hydrogel Composition Optimisation .....	199
6.2.1.	Visual Assessment.....	199
6.2.2.	Extrudability.....	199
6.2.3.	Extrusion Form .....	200
6.2.4.	Extrusion Pressure.....	201
6.2.5.	Layer Formation and Retention .....	202
6.2.6.	Viscosity.....	203
6.3.	Rheology.....	204
6.3.1.	Constant Shear .....	204
6.3.2.	Amplitude sweep .....	205
6.3.3.	Frequency Sweep .....	206
6.3.4.	Temperature Sweep.....	207
6.3.5.	3-Interval Thixotropy Test .....	208
6.3.6.	Post-mix Time Sweep .....	209
6.4.	3D Printing .....	210
6.4.1.	Line width .....	210
6.4.2.	Single layer infill .....	212
6.4.3.	Multi-Layer Geometries .....	216
6.5.	Mechanical testing .....	219
7.	Conclusions .....	222
8.	Future Work .....	226

9. References..... 228  
10. Appendix ..... 245

# 1. Introduction

Cleft lip with or without (CL/P) is one of the most common birth defects in humans with an incidence of 1.42 and 0.924 per 1,000 live births within the United Kingdom (UK) and worldwide respectively (Goodacre and Swan, 2008; Mossey and Modell, 2012). CL/P is a broad term which encompasses the several different variations of cleft lip without or without palate however this thesis focuses on treatment of cleft palate alone (CP). CP accounts for approximately 25 % of cases, cleft lip alone (CL) is a further 25 % and cleft lip and palate together (CLP) is the final 50 % of cases (Conway *et al.*, 2015; Burg *et al.*, 2016). CP is a congenital disorder that is defined by an abnormal cleft in the roof of the mouth, the palate, which incorrectly joins the oral and nasal cavities. Typically, in high- income countries, CP is not considered a life-threatening condition however it still has significant effects on the quality of life of patients. This is due to a variety of complications from feeding, hearing, dental and speech issues to known psychosocial complications.

The widely accepted standard when treating CP is surgical intervention which is typically scheduled for when the patient is 9-12 months old. Surgical methodologies and results are case dependent but all are based on the raising and suturing of mucosal flaps from adjacent tissue to achieve oral and nasal separation. Mucosal flaps are raised from adjacent tissue and sutured together to achieve oral and nasal cavity separation, a process which remains largely unchanged since its inception in the early 19<sup>th</sup> century (Katzel *et al.*, 2009).

This generally provides good clinical outcomes however in a small but significant number of patients between 14-27 % (Cohen *et al.*, 1991; Sadhu, 2009; Landheer, Breugem and van Mink Der Molen, 2010) complications such as wound dehiscence arise which lead to the need for revision surgery. Additionally, as surgery is a very invasive technique, it causes significant amounts of scar tissue to form in the maxillofacial region which commonly grow at a reduced rate, leading to abnormal mid-facial appearance following surgery. In countries



where healthcare is not free at the point of use, the economic costs of CP are a huge burden, with an overall lifetime cost estimated to be \$100,000-200,000 (Boulet *et al.*, 2009). It is therefore no surprise to find that in low-income countries with less established medical systems, cases of untreated CP in adults is not uncommon (Murthy, 2009). These limitations are fundamentally linked to the use of mucosal flaps within surgical approaches when treating CP which is why since these techniques were introduced decades ago, problems persist. This has led to research into alternative treatments.

One such example is the use of electrospun multi-layered membranes as cell scaffolds (Puwanun *et al.*, 2016). These scaffolds, however, are less suitable in filling the void of a cleft palate because they are produced in  $\mu\text{m}$ -scale whereas the soft palate is typically between 3-4 mm thick (Hormdee, Yamsuk and Sutthipraporn, 2020). An ideal solution would be to use methods such as 3D printing that can accurately produce larger scaffolds in comparison whilst maintaining accuracy.

3D printing has been around since the early 1980s but recently it has rapidly grown into a multi-billion-pound industry with many biomedical applications (Campbell *et al.*, 2012). Conventional fused filament fabrication (FFF) involves heating thermoplastic materials such as polylactic acid (PLA) or acrylonitrile butadiene styrene (ABS) to a molten state and extruding them onto a platform where they re-solidify as they cool. One particularly exciting prospect in medical 3D printing is the production of customised implants that are designed using patient imaging data to obtain a unique geometry for that individual (Rotaru *et al.*, 2012). This has previously been used to produce devices for craniofacial defects and total hip replacements however these methods could also be used in designing bespoke constructs for CP patients. Traditional polymers such as ABS are often unsuitable for many applications in medical 3D printing as they have poor biocompatibility. PLA has improved biocompatibility but, in some cases, its true composition is not known which severely limits its use in biomedical applications (Ravi, Shiakolas and Welch, 2017).

Different printing materials should therefore be considered for use in biomedical applications that retain the high printing accuracy of traditional polymers whilst improving upon their generally poor biological qualities.

Natural polysaccharides and extracellular matrix (ECM) components such as chitosan, alginate, agarose, collagen and gelatin have been studied as printing materials that are commonly referred to as bioinks. These are naturally-occurring materials which can be sourced from plants, animals or even from human donors. Their established use within biomedical applications is testament to their ability to pass rigorous biocompatibility and cytotoxicity standards. In addition, not only are they not harmful to the body but they actively improve cell proliferation and could be used to regenerate tissues (Tamay *et al.*, 2019). This is due to their ability to act as artificial extracellular matrices which can incorporate cells and allow diffusion of nutrients and waste materials, demonstrating many potential benefits in regenerative medicine (Malda *et al.*, 2013).

Alginate is a hydrogel derived from species of brown algae which has a well-established performance in areas of biodegradability and supporting cell viability but also has mechanical properties that can be tailored through a variety of crosslinking methods to suit many applications (Catherine K. Kuo and Ma, 2001). It forms high water-content hydrogels that can rapidly gel in the presence of calcium ions and be used to produce 3D structures. This is useful as one of the main limitations of using hydrogels as bioinks is the poor physical characteristics in printed structures due to their low viscosity and mechanical strength (Billiet *et al.*, 2012).

With this in mind, this research will focus on employing recent advancements within 3D printing to produce alginate-based materials that could be used as potential palatal obturators. In order to do this effectively, chemical characterisation of alginate will be undertaken as well as an investigation into which hydrogel compositions are most suitable for 3D printing. Rheological analysis will be used to better understand viscoelastic nature of

hydrogels and then their 3D printing fidelity will be assessed. Finally, mechanical properties of 3D printed objects will be assessed to see if they could function as a potential palatal obturator. The following section will conduct a thorough literature review of all relevant aspects for this project work.

## 2. Literature Review

The following literature review explains all the relevant aspects of the project in detail. Accurate at the time of submission, this literature review describes the state of the art following a comprehensive search through the available literature. The literature will critically review and evaluate available information on topics including CP, biomaterials and 3D printing.

### 2.1. Cleft Palate

#### 2.1.1. Anatomy & Classification

The oral and nasal cavities are located within the maxillofacial region that, along with surrounding tissues and structures, contribute to essential bodily functions including respiration, mastication, swallowing, speech and smell (Mitchell and Wood, 2000). The palate is situated between the oral cavity, nasal cavity and the pharynx which can be further divided into the nasopharynx, oropharynx and laryngopharynx (superior to inferior). The palate is comprised of the tissues that form the roof of the mouth and floor of the nasal cavity (Figure 2.1) which acts as a physical barrier between them. It can be separated into two distinct regions where the anterior and posterior are known as the hard palate (bone) and soft palate (muscle and connective tissue) respectively, both of which are sheathed in a mucosal membrane. The uvula is a teardrop shaped free-hanging extension located at the centre of the posterior edge of the soft palate. In healthy adults the soft palate is approximately half the size of the hard palate, 35 – 40 mm long and 9 – 10 mm thick although these have several distinct morphologies (Barrera *et al.*, 2017).

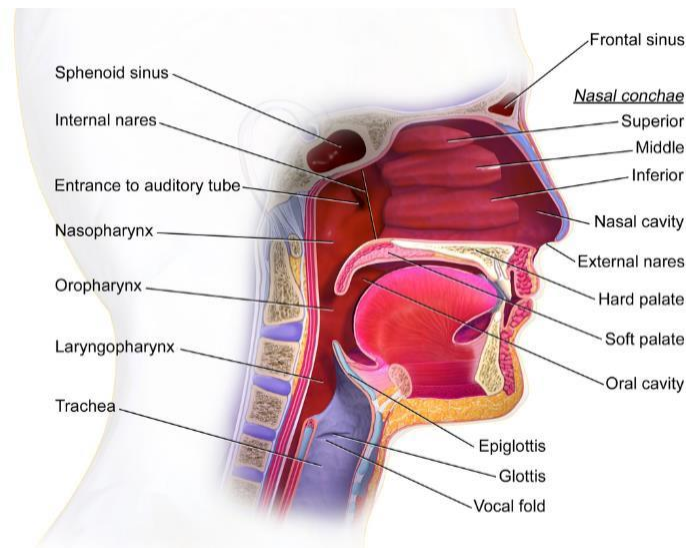


Figure 2.1: *The Upper Respiratory System* (Blausen.com staff, 2014).

Figure 2.1 shows the relaxed position of the soft palate, also known as the velum or muscular palate, where it freely hangs downwards and maintains openings at both the nasopharynx and oropharynx. The soft palate adopts a superior tensed position to form a seal with the posterior pharyngeal wall during oral functions such as swallowing to prevent food and liquid entering the nasal cavity. This is aided by laryngeal elevation, where the epiglottis moves downwards during swallowing and forms a lid that seals the glottis and aids direction of ingested products towards the oesophagus. These two movements prevent both choking and the misdirection of food into the nasal cavities or lungs where subsequent infections may occur.

Another position it can adopt is the inferior tensed position which seals off the oropharynx in activities like pronunciation of the nasal English language phonemes /m/, /n/ and /ng/ which all require exhaled air to be diverted through the nasal cavity alone (Kummer, 2011). The soft palate also performs a function at the resting position where it diverts a proportion of air away from the nose and through the mouth to protect the nasal cavity from damage. The five muscles that coordinate to allow for this movement and tensing of the soft palate are the tensor veli palatini, the levator veli palatini, the palatoglossus, the palatopharyngeus and the musculus uvulae.

CP is a condition where, during embryogenesis, part of the palate has failed to form correctly and has left a gap between the nasal and oral cavities. It can be present in a variety of different morphologies and in combination with other defects such as CL. CL occurs at varying degrees of seriousness, from only a minor indent in the upper lip to a larger defect which presents a complete gap, connecting the nostril(s) to the mouth and the CP if present. When a single nostril is involved this is referred to as unilateral CL, accounting for 80 % of cases, however when both nostrils are involved it is bilateral CL (Baxter and Shroff, 2011). Both CL and CP can also be described as ‘complete’ and ‘incomplete’. A complete CL or CP presents full-depth missing tissue throughout the upper lip or palate which spans the entire sections of either the upper lip or the palate respectively. In contrast, an incomplete version is where CL or CP are present but do not stretch the entire length of the upper lip or palate.

The terms ‘primary’ or ‘secondary’ palate refer to locations depending on their developmental origins in palatogenesis, not to be confused as interchangeable terms with hard and soft palates. As seen in Figure 2.2, the primary palate is a rough triangle-shape section between the lip philtrum and incisive foramen, hosting the upper 4 incisor teeth in adults, whereas the secondary palate is comprised of the soft palate primordia and the remaining hard palate majority.

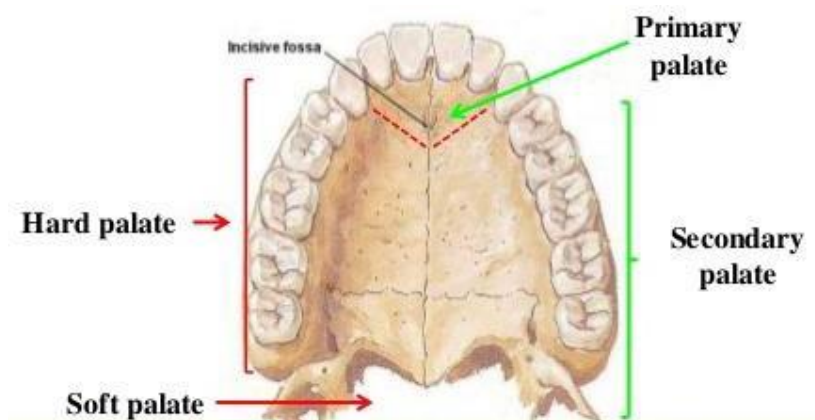


Figure 2.2: Palatal Anatomy (Chetan, 2015).

Orofacial clefts (OFCs) are commonly divided depending on the affected areas, such as the previously mentioned CL/P, CL, CP and CLP. For clarity, the following definitions will be used for this thesis:

- CL/P – Cleft lip with or without palate
- CL – Cleft lip only
- CP – Cleft palate only
- CLP – Cleft lip and cleft palate

Interestingly, CL and CLP have different developmental origins to CP which is why they are often grouped as cleft lip with/without palate (CL/P) (Burg *et al.*, 2016). Although these various forms of OFCs are often obvious upon visual examination, a submucosal cleft palate (SMCP) is a subtler type of CP where the bone is not intact but the mucosal layer of the palate is, leading to a ‘translucent look’. SMCP is also accompanied by a triad of classic symptoms: soft palatal muscle diastasis, a bifid uvula and a midline notch at the posterior of the bony palate (Levi *et al.*, 2011). If these are not present, it is known as an ‘occult’ SMCP.

It is important to appreciate there is a lack of standardisation or consistency regarding classification of OFCs and that studies use different terminologies and corresponding groupings depending on whether they are organising through morphology or embryology. These include CLO for cleft lip only, CPO for cleft palate only, CP±L for cleft palate with or without lip, CLA for cleft lip and alveolar process, etc. (Hagberg, Larson and Milerad, 1998; Zheng *et al.*, 2008). As well as multiple acronyms that may be confused, some of the definitions themselves are contradictory between different studies. One example is the term ‘isolated’ which, when used properly, describes clefts not present as part of a syndrome but is incorrectly used when describing CL or CP without the other present (Hagberg, Larson and Milerad, 1998; Ngai *et al.*, 2005; Goodacre and Swan, 2008; Sekhon *et al.*, 2011). This is problematic when making cross-comparisons amongst articles as inaccurate or diluted conclusions could be drawn from mislabelled or inappropriately assigned results.

Furthermore, when collating data into reviews or meta-analyses any mislabelling of groups may present false-negatives or false-positives over a broader spectrum.

Classification systems were devised to reliably collect data on OFCs which should ideally be simple to understand and function independent of written explanations due to errors in translating. The first widely accepted classification was the 1971 Kernahan and Stark striped-Y symbolic model (Figure 2.3) that allowed differentiation between a multitude of clefts where a medical professional simply highlighted the areas included in the cleft (Kernahan and Stark, 1971).

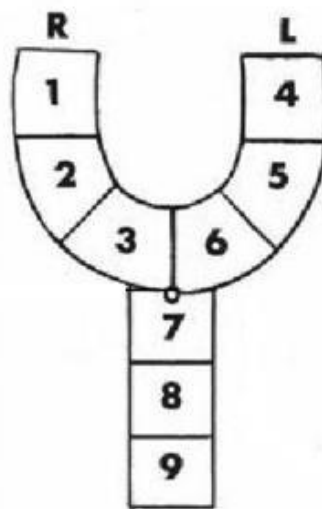


Figure 2.3: Kernahan-Clark striped-Y model where R = right, L = left, 1&4 = lip, 2&5 = alveolus, 3&6 = primary palate before incisive foramen (represented by small central circle), 7 = anterior hard palate, 8 = posterior hard palate and 9 = soft palate (Zreaqat, Hassan and Hanoun, 2017).

Since then, there have been numerous suggested modifications to this model by a multiplicity of authors to account for potential shortfalls including difficulties in recording rare OFCs types which has led to a lack of standardisation today. Moreover, these models do not pertain to the benefits and risks involved with treatment options, something that should be emphasised, which would allow for more informed decisions to be made by patients, their family and medical professionals (Richardson and Agni, 2014). The Veau classification system (Figure 2.4) is another popular tool which has four simple groups. Although the lack



of complexity limits the detail that can be provided, the simplicity removes any potential misclassification by users.

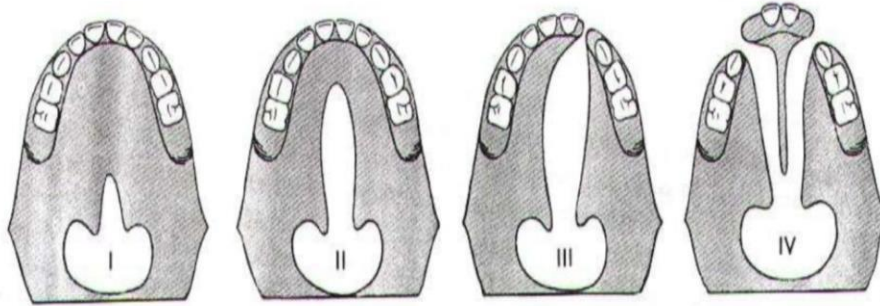


Figure 2.4: Veau Classification System groups I-IV: (I) isolated soft palate cleft, (II) isolated soft and hard palate cleft, (III) unilateral CLP and (IV) bilateral CLP (Zangana, 2011).

## 2.1.2. Epidemiology

Approximately 7.9 million, or 3-6 %, of live births annually are accompanied by the presence of major birth defects, also known as congenital disorders, which are broadly defined as a major structural anomaly present at birth (Christianson, Howson and Modell, 2006; Carmichael, 2014). Of these, 10-20 % are part of a wider syndrome where multiple major structural defects occur across different systems of the body forming a pattern that is repeated in non-family members of the wider population (Wehby and Murray, 2011; Carmichael, 2014). There are over 400 syndromes associated with CP, the most common of which is Van der Woude's syndrome (2 % of all CL/P cases) with DiGeorge syndrome and Pierre Robin Syndrome as other notable mentions (Burg *et al.*, 2016). Defects that occur outside of syndromes are termed isolated birth defects or non-chromosomal defects although some authors incorrectly use the term 'isolated' as previously discussed in Section 2.1.1. In the United States (US), congenital disorders are the single leading cause of infant mortality (< 5 years of age) which equates to 3.3 million deaths per year when including the rest of the world and a further 3.2 million infants that could be permanently disabled (Christianson, Howson and Modell, 2006; Mathews and MacDorman, 2013).

Some of the most severe of these defects are those of the craniofacial region due to its sole hosting of four of the five traditional senses (sight, smell, hearing and taste) and the key role it plays in aesthetics, which are all key factors when assessing a person's quality of life. OFCs are the most common of these which occur in 1.42 of every 1,000 live births in the UK which equates to 1,000 new cases per annum (Goodacre and Swan, 2008). Cleft cases generally follow a rule of 25 % CL, 50 % with both CL and CP and finally 25 % CP (Conway *et al.*, 2015).

Globally, CP and CL/P have largely varying incidence rates of 0.34 – 2.29 and 0.13–2.53 per 1,000 births respectively which are greatly influenced by ethnic and geographical factors (Mossey *et al.*, 2009; Mossey and Modell, 2012). For instance, parts of Latin America, Australasia and North America have the highest prevalence of non-syndromic OFCs whereas Sub-Saharan Africa, North Africa and the Caribbean have the lowest (Table 2.1). These regions also show no obvious pattern between CP incidence proportional to overall OFC incidence as the respective ratios within areas also vary greatly. Interestingly, typically low-income countries within Sub-Saharan African, which are typically highlighted for worse health than their high-income counterparts, have a reduced incidence of OFCs. High income areas like North America and Asia Pacific in contrast, have significantly higher incidence rates.

Table 2.1: Estimated birth prevalence of OFCs by GBD region (Mossey and Modell, 2012).

Global Burden of Disease Region	OFCs per 1,000 births	CP per 1,000 births	CL/P per 1,000 births	CP % of total
Latin America, Southern	2.39	0.72	1.67	30
Latin America, Tropical	2.39	0.72	1.67	30
Australasia	2.01	1.02	0.98	51
North America, High Income	2.00	0.83	1.17	41
Oceania	1.85	1.13	0.72	61
Europe, Western	1.66	0.59	1.07	35
Asia Pacific, High Income	1.65	0.64	1.00	39
Asia, South	1.60	0.30	1.30	19
Latin America, Central	1.54	0.39	1.15	25
Europe, Central	1.45	0.67	0.77	47
Asia Southeast	1.36	0.28	1.08	20
Latin America, Andean	1.29	0.17	1.12	13
Asia, East	1.28	0.27	1.01	21
Europe, Eastern	1.22	0.59	0.63	49
Asia, Central	1.19	0.62	0.57	52
Middle East	1.02	0.30	0.72	29
Caribbean	0.93	0.31	0.62	34
Sub-Saharan Africa, Central	0.54	0.04	0.51	7
Sub-Saharan Africa, West	0.54	0.08	0.46	15
Sub-Saharan Africa, Southern	0.45	0.15	0.30	33
North Africa	0.44	0.15	0.29	35
Sub-Saharan Africa, East	0.38	0.12	0.27	31
World	1.25	0.31	0.94	25

Even within these economically similar regions such as Western Europe there can still be a large amount of variation though, such as in Western Europe where Germany has more than triple the incidence of non-syndromic OFCs compared to Portugal (Figure 2.5).

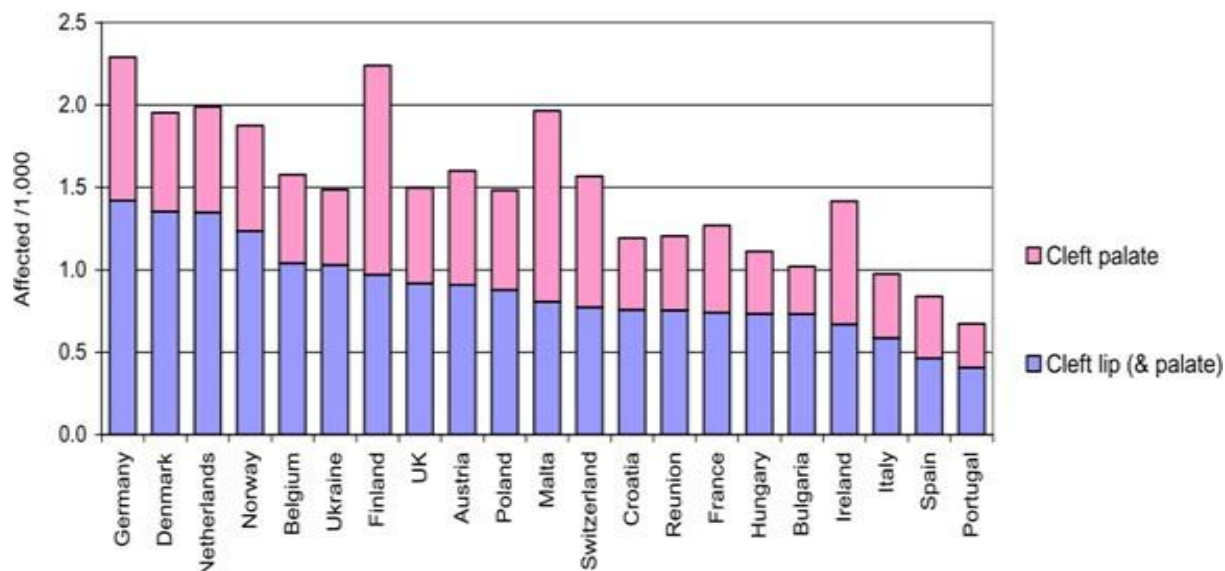


Figure 2.5: Prevalence of non-syndromic OFCs in Europe (Mossey and Modell, 2012).

CL/P is not considered a life-threatening condition in the western world although there is a documented increase in perinatal mortality, particularly amongst syndromic cases, when compared to the general population (Christensen *et al.*, 2004). The perinatal mortality rate for 202,308 births in the West Midlands between 1995-1997 was 10.0 per 1,000 live births whereas isolated CL/P was 31.8 and syndromic cases was 228.3 (Ngai *et al.*, 2005). Terminations of pregnancy were excluded from data sets which may have skewed the data, particularly the syndromic cases figure where the termination rate was significantly higher (27.8 % compared to < 0.1 % for isolated) (Ngai *et al.*, 2005). Ultrasound screening and face visualization was being used for diagnosis so hypothetically foetuses with the more severe deformities may have been terminated at a greater rate, so the would-be perinatal mortality rate could have been higher if not terminated. Unfortunately, due to this being a retrospective study this detailed information was not available.

Interestingly, higher mortality rates have also been reported for OFC patients of all ages due to cancer, cardiovascular disease and suicide (Christensen *et al.*, 2004). Unfortunately, OFCs are a clear example of the severe health inequalities in the modern world. Where, in low-income countries, anything more than a mild deformation may result in excessive infant mortality due to a lack of education and medical services. Maharashtra, India, is one such

example where evidence suggests that in rural communities many children with cleft deformities died within days of birth from starvation due to the inability to suckle correctly and hence feed (Mossey and Modell, 2012). Section 2.1.4.1 discusses this in more detail.

### 2.1.3. Embryology and Aetiology

Facial development begins in the fourth week of gestation from 5 primordia: 2 maxillary processes, 2 mandibular arches and a frontonasal process as seen in Figure 2.6A. Over the course of the next few weeks these primordia grow, spread and begin to fuse with each other. The nostrils are formed by pairs of nasomedial and nasolateral processes seen in Figure 2.6B. It is during week seven when these fuse with each other and the maxillary processes that developmental failures form CL. Otherwise, by week seven, formation of the triangular primary palate and upper lip is complete (Levi *et al.*, 2011).

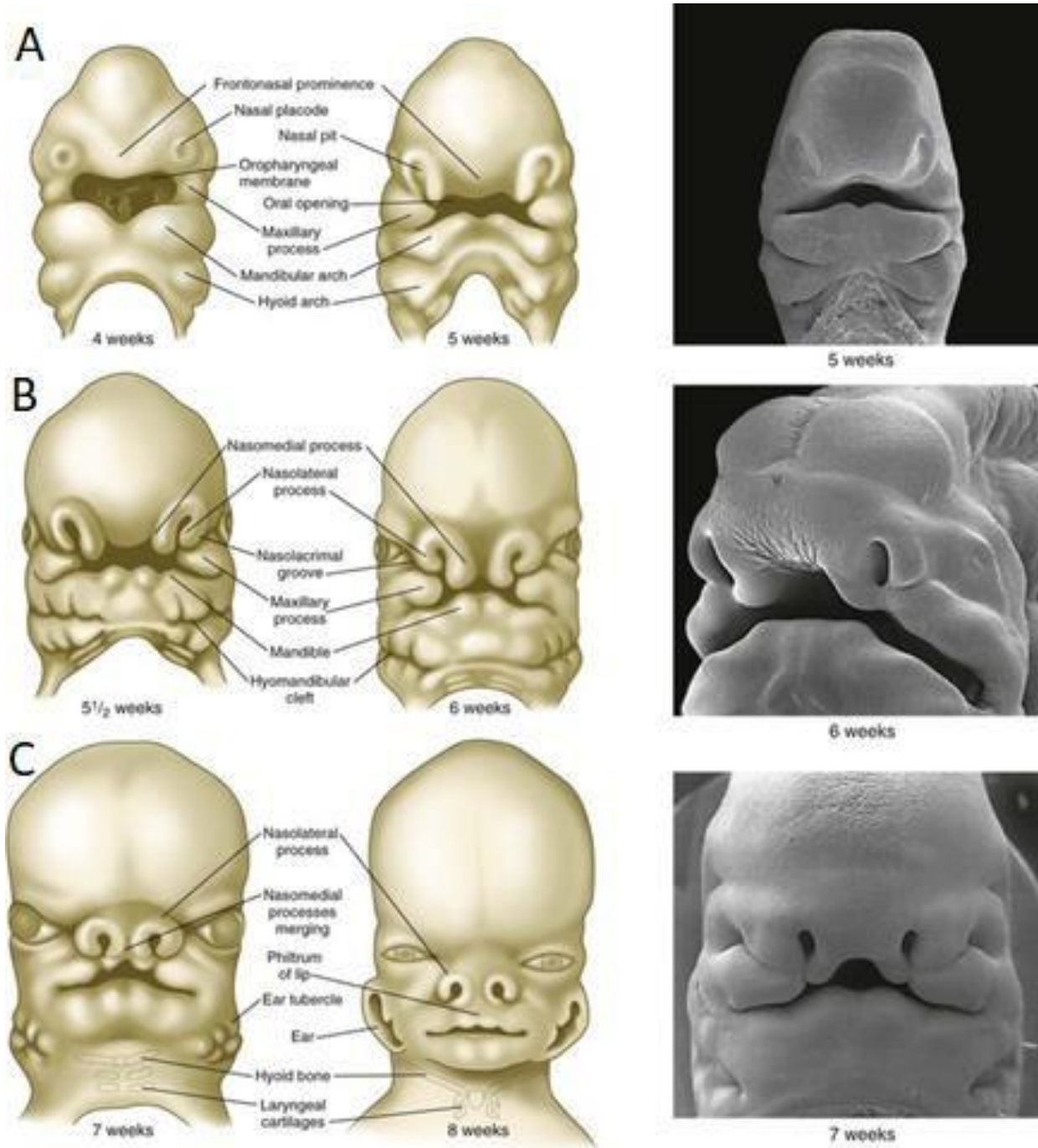


Figure 2.6: Facial development in gestation weeks 4-8: (A) The 5 primordia grow and spread (B) Primordia begin to fuse and (C) Complete formation of the upper lip and primary palate (Oostra, Steding and Virágh, 2007).

The lateral palatine shelves appear on the medial surfaces of the maxillary processes in week 6 which form the secondary palate. They initially grow obliquely inferior but as the jaw develops and the tongue lowers during week seven, they dramatically reposition to a horizontal position as seen in Figure 2.7. The primary palate and nasal septum continue to grow until week nine when the shelves begin to fuse, starting anteriorly, which is completed by week twelve (Pansky, 1982; Sadler, 2014). Ossification of the palate begins

at the lateral edges of the palatine shelves by week eight and then the primary palate by week ten. The posterior edges of the secondary palate become the soft palate and hence do not ossify.

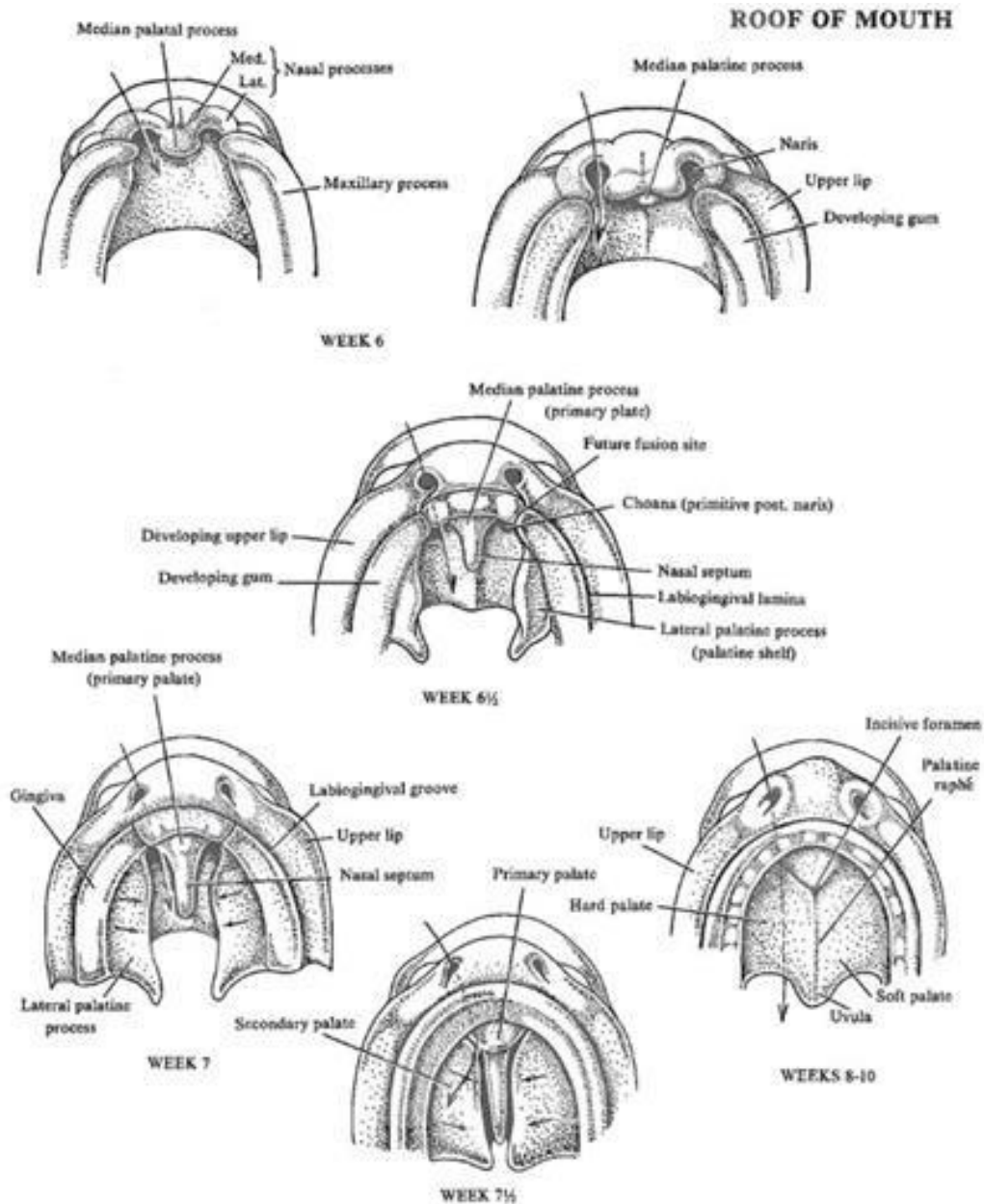


Figure 2.7: Palatal development between week 6-10 (Pansky, 1982).

Five mechanisms have been identified which cause CP: insufficient growth of shelves, shelf elevation failure, shelf midline fusion failure, post fusion rupturing and a failure of the apoptotic activity of the overlying mucosa (Singh, 2015). A SMCP, however, is caused by a lack of complete fusion of the palatine shelves, where the mesoderm does not penetrate the



mucosal covering. Because CL occurs between weeks four to eight and OFCs of the secondary palate occur between 6-12 weeks, a multifactorial aetiology is hypothesised for CL/P and CP. Genetic influence is significant and is easy to identify from high levels of familial aggregation, recurrence risk and specific examples of CL/P concordance in monozygotic and dizygotic twins (40-60 % and 5 % respectively) (Murray, 2002). Interestingly, concordance is not 100 % for monozygotic twins (who are genetically identical) which indicates that *in utero* (IU) environmental factors definitely play a part in developing CL/P.

Animal model research using direct candidate gene analysis, association studies and genome-wide scans using large CL/P families has led to identification of a plethora of genes and loci that are associated with OFCs (Stanier and Moore, 2004). These are generally grouped into isolated and syndromic cases although there is little separation within studies to individually evaluate the separate genetics of CL/P and CP. This is crucial considering authors have recently reported CL to have its own distinct aetiological features which contrasts to the conventional grouping of CL/P (Dixon *et al.*, 2011). Despite the large number of genes/loci researched there is a considerable lack of definitive evidence associated with the majority because of large inconsistencies found between studies (Murray, 2002). This could be because the data was collected from the multiple countries which are known to have inherent ethnic and geographical variation which have been previously discussed in Section 2.1.2.

Strong evidence has been put forward for the increased maternal risk of OFCs due to risk factors such as tobacco, alcohol and anticonvulsant drugs (Yu *et al.*, 2009). Dietary fortification of folic acid, a B vitamin, of around 400 µg daily is highly recommended for any women of childbearing age to the extent that some governments across the world have made it mandatory in certain foods (Williams *et al.*, 2002). This is because it is essential in preventing neural tube disorders such as anencephaly and spina bifida that develop in the



first 28 days of pregnancy, before a woman knows she is pregnant. The exact process by which it does this remains unknown however the evidence is substantial, with studies reporting incidence reductions of 72-100 % (Wehby and Murray, 2011).

The theory is that because neural tube disorders develop at similar gestation periods to OFCs, prevention methods could correlate. There are contradictory reports from studies with some indicating a 50 % decrease in the risk of CP although not CL/P and others reporting a 50 % decrease in CL/P but not CP whilst others report no change at all (Shaw, 1995; Czeizel, 2004; Johnson and Little, 2008). This could be explained by gene- environment interactions where two different genotypes in the same environment can produce phenotypic differences. Another explanation is the poor experimental designs observed which included patient self-selection, a lack of measurement or report of dose given and sample selection biases which will need to be amended for future studies (Wehby and Murray, 2011).

#### 2.1.4. Effects of Cleft Palate

CP and CL/P are easily identifiable at birth from the obvious structural anomalies but SMCP requires closer examination along the mid-line of the palate for transparency, discolouration or notching. The severity of these conditions should not be understated as they are known to adversely affect the child's feeding, breathing, speech, hearing and have psychosocial implications. Any single one of these affects would greatly affect the quality of a fully-grown healthy adult, let alone a neonate.

#### 2.1.4.1. Feeding

The most severe complication caused by CP is difficulty in breastfeeding which increases the mortality risk due to malnutrition and dehydration within days if the neonate cannot successfully feed. CP makes breastfeeding much more difficult as the vacuum over their mother's breast, the process by which milk is drawn from the mammary glands when sucking, cannot be created. This is a considerably stressful time for both mother and child when considering that feeding is a very calorie-intense exercise for new-borns, so failed feeding attempts will contribute to weight loss and weakness. The most common solution when children struggle to feed is to use a specially designed CP bottle that allows for squeezing, to assist the new-born which prevents food entering the nasal cavity as seen in Figure 2.8.



*Figure 2.8: Nasal regurgitation of food in an infant with cleft palate (Garrett, 2012).*

In more severe cases a nasogastric tube may be used to minimise the amount of food which enters the nasal cavity or the lungs. Although these simple solutions are easily

implemented, low-income countries within the Indian sub-continent and Asia typically have limited access to them. In China, for example, one study has reported that children born with isolated and syndromic OFCs have a mortality rate of 6.46 % and 32.15 % respectively in the first week compared to 0.37 % for the overall population (Carlson, Hatcher and Burg, 2013). Frustratingly, much of the research conducted in this area is limited to high-income countries which represents a large hole in the knowledge of the extent of the problem. By not knowing the extent of the problem it is difficult for researchers and medical professionals to address it effectively.

#### 2.1.4.2. **Speech**

Of the 44 separate phonemes (sounds) in the English language only three (/m/, /n/ and /ng/) project air solely through the nasal cavity during correct pronunciation. For correct pronunciation for the remaining 41 phonemes the velum controls resonance and airflow at least partly through the mouth. Velopharyngeal insufficiency or incompetence (VPI) is inadequate closure of the velopharyngeal sphincter through either improper controls of the palatal muscles or the palate not being long enough. This undermines the proper direction of air and allows air to leak into the nasal cavity which produces hyper-nasal speech, a typical symptom of CL/P patients. CP is more likely than CL to present VPI following primary surgery, which is often found in up to 30 % of cases (Mitchell and Wood, 2000; Phua and de Chalain, 2008).

The term 'cleft palate speech' has even been coined, which describes incorrect production of consonants, altered laryngeal voice quality, nasal/ facial grimaces or abnormal nasal resonance and airflow (Nagarajan, Savitha and Subramaniyan, 2009). The current treatment procedure is unideal as surgery occurs at about 12 months old however by 5-6 months the child has already been practising voice intonation/sounds which become multiple consonants and vowels e.g. "bah-bah" or "no-no" by 8-12 months (Tibesar, Black and Sidman, 2009). Results have shown that operating earlier at 8-10 months improves speech

results due to less relearning being necessary post-surgery (Tibesar, Black and Sidman, 2009). When considering speech by itself, an ideal treatment would be one that occurs before 5-6 months so that no babbling has begun and no relearning is necessary at all.

### 2.1.4.3. Hearing

Conductive hearing loss is also commonplace amongst CL/P patients due to problems with the middle ear and the eustachian tube which connects it to the nasopharynx to allow pressure equalisation and drainage *via* a muscular nasopharyngeal opening. The orientation of the eustachian tube in infants is much more horizontal compared to later in life as an adult (Figure 2.9) which can hinder drainage during infancy.

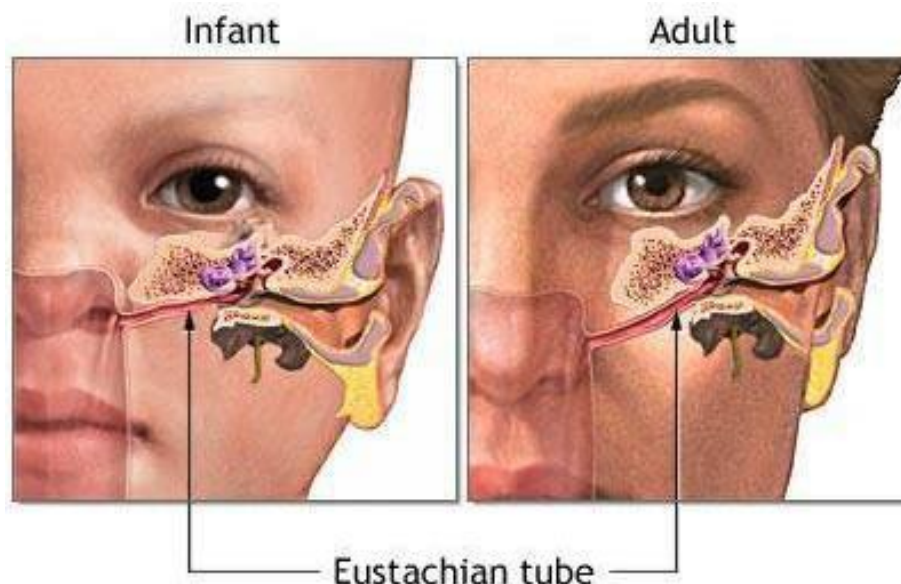


Figure 2.9: Differences in eustachian tube anatomy between infants and adults (A.D.A.M., 2015).

When drainage is insufficient, middle ear fluid accumulation occurs causing excessive bacterial growth and infection. This is known as chronic otitis media with effusion (COME), which poses a risk of hearing loss due to perforation of the tympanic membrane or presence of a cholesteatoma/granulation tissue (Costa, Rosito and Dornelles, 2009). CL/P further increases the risk due to reduced opening and closing of the Eustachian orifice when yawning, swallowing or speaking because the muscles responsible for this mechanism, the tensor and levator veli palatini, are not intact or able to function correctly. Hearing problems

in children with CP or CL/P is generally found to be quite high with studies reporting 32.5 - 45 % of patients developing COME (Sheahan *et al.*, 2003; Subramaniam *et al.*, 2015). There are, however, large variations due to ethnicity where Chinese and Japanese CP patients have incidences of 23 % and 69 % respectively (Sharma and Nanda, 2009). When eustachian tube orientation changes with age (Figure 2.9) the audiological status of patients has been reported to improve due to increased drainage however other studies have reported contradictory evidence that states there is no change or conditions even worsened (Chu and McPherson, 2005).

#### **2.1.4.4. Psychological and Social Implications**

The face serves as the most important social aspect of the body due to its critical role in attractiveness, emotional expression and communication. It is therefore no surprise that when craniofacial defects are present in children, particularly those between the ages of 11-18 years old, increased incidence of shyness, depression and social isolation has been documented (Hickey and Salter, 2006). Another study that analysed parent/patient self-awareness, social competence and satisfaction of facial appearance found that children between the ages 8-15 with OFCs have the same psychosocial development as non-cleft children (Slifer *et al.*, 2003). Both children with and without OFCs reported dissatisfaction with facial appearance but only parents of children with OFCs concurred. This meant that they may have responded to this by improving the quality of life for their children which may have contributed to retaining normal psychosocial status.

Cultural differences also have a significant role to play in this scenario as, although the western world may be more accepting of birth defects, developing countries with greater traditional, religious and community influences are known to hold greater stigmas for defects and consider them punishment for previous sins (Kimotho and Macharia, 2020). Other studies have found that CL/P patients have lower self-concept scores and express greater dissatisfaction with their appearance compared to CP patients (Hunt *et al.*, 2005).

## 2.2. Cleft Palate Treatment

It is important to know how CP is treated and what the success rates and other outcomes of these treatments are in order to identify areas that can be improved upon. The following sections will detail the surgical and various non-surgical methods of treating CP and evaluate the outcomes of these.

### 2.2.1. Surgical Treatment

In ancient times the presence of congenital deformities at birth were explained through superstition, religion and charlatanism which led to infants being condemned and often either abandoned in the wild or killed (Bhattacharya, Khanna and Kohli, 2009). The first reported successful CL surgery dates back to 390 BCE in China whereas in stark contrast the first successful CP surgery was in 1816, over 2,000 years later (Perko, 1986; Bhattacharya, Khanna and Kohli, 2009). The delay is credited to the belief during The Renaissance that CP was secondary to syphilis (hence surgery was not advised) and that surgery without anaesthetic was too difficult and painful (Perko, 1986). Since then, several surgical techniques have been practiced, each with many of their own variations, but only a few are relevant on the grand scale. Virtually all of these procedures rely on the original idea of using raised mucosal flaps, relaxing incisions and suturing to achieve primary closure of the defect (Navarro-Gasparetto, 2007).

The von Langenbeck technique (1859) is the oldest of these techniques which is still popular today in treating isolated CP, seen in Figure 2.10 (Agrawal, 2009; Katzel *et al.*, 2009). Two bipediced mucoperiosteal flaps are elevated on both the medial and lateral sides of the cleft, the latter of which is a relaxing incision. The flaps are then elevated from the hard palate and moved medially to close the cleft whilst avoiding tension and not lengthening the palate. A bipedicle flap is one where a narrow base of tissue is still attached to the donor site so

that the grafted tissue retains its own blood supply after being transferred.

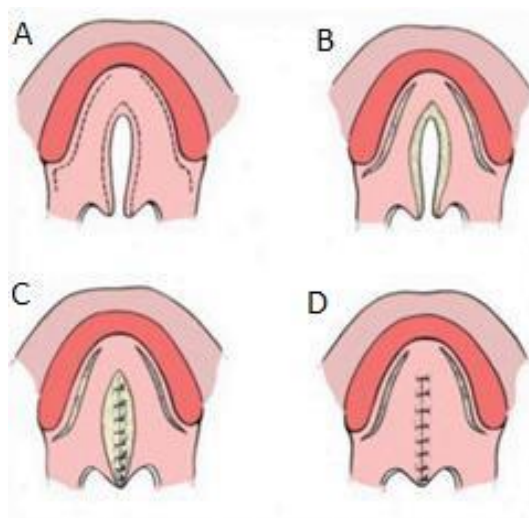


*Figure 2.10: Von Langenbeck palatoplasty: (A) Planned flap incisions, (B) Surgical incisions, (C) Nasal mucosa sutured and (D) Oral mucosa sutured with relaxing incisions unaltered (Basuki, 2013).*

The Veau-Wardill-Kilner (VWK) V-Y Pushback technique (1936) was a modification of the von Langenbeck technique designed to lengthen the velum by repositioning full- thickness mucoperiosteal flaps rearwards, seen in Figure 2.11 (Ravishanker, 2006). This was the most common form of palatoplasty and considered the gold standard until the 1980's. (Ravishanker, 2006; Navarro-Gasparetto, 2007; Agrawal, 2009). The cause of its demise was the excessive raw area of denuded bone created which could retract when healing by secondary intention, thereby undoing any previously achieved velum lengthening.

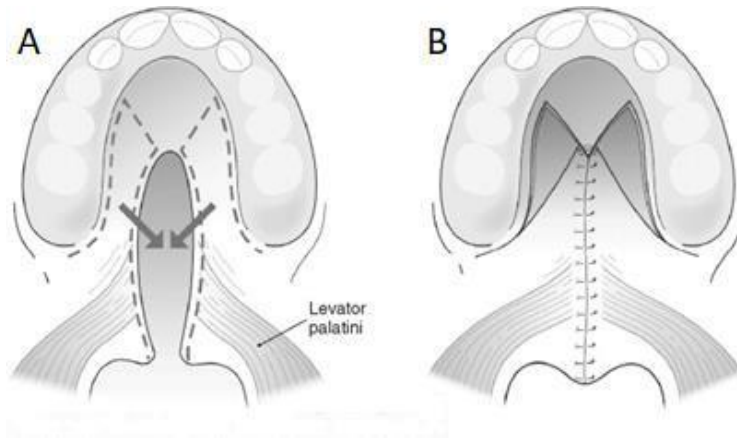


Figure 2.11: Veau-Wardill-Kilner Palatoplasty: (A) Planned incisions with pullback direction and (B) suturing complete leaving significant denuded areas (Karl, 2016).

The Bardach two-flap technique (1967) is another modification of the von Langenbeck technique also uses two full-thickness mucoperiosteal flaps which are elevated to improve access and visibility for nasal and velar muscular repair, seen in Figure 2.12 (Bardach, 1995). Once this has been achieved, they are attached at the midline, not causing significant denuding of bone. These flaps (and those of the VWK V-Y pushback) are axially pedicled on the greater palatine arteries, seen clearly in Figure 2.12C. CL is treated secondary to the successful outcome of the procedure.

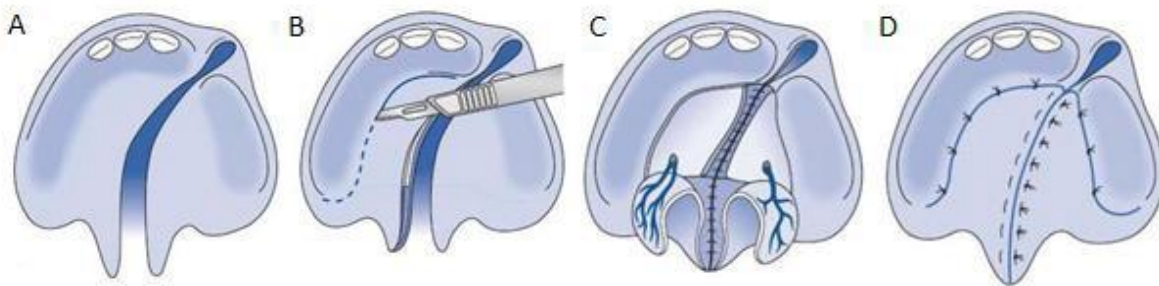


Figure 2.12: Bardach two-flap palatoplasty: (A) Unilateral CLP, (B) Cutting flaps, (C) Complete elevation of flaps with greater palatine arteries seen and (D) Suturing complete with remnant CL (Hosein and Motamedi, 2013).

Furlow double-opposed Z-plasty (1986) was also designed with the specific intention of lengthening the velum by sacrificing width and avoiding longitudinal scar contracture, to improve speech results (Furlow, 1986; Khosla, Mabry and Castiglione, 2008). Four flaps are created in total of which two are made from the nasal mucosa and two from the oral mucosa as seen in Figure 2.13. By rearranging this in an opposed-Z fashion the levator veli



palatini sling can be reconstructed through the use of transpositioning flaps alone, without transection of the muscular layer (Ravishanker, 2006).

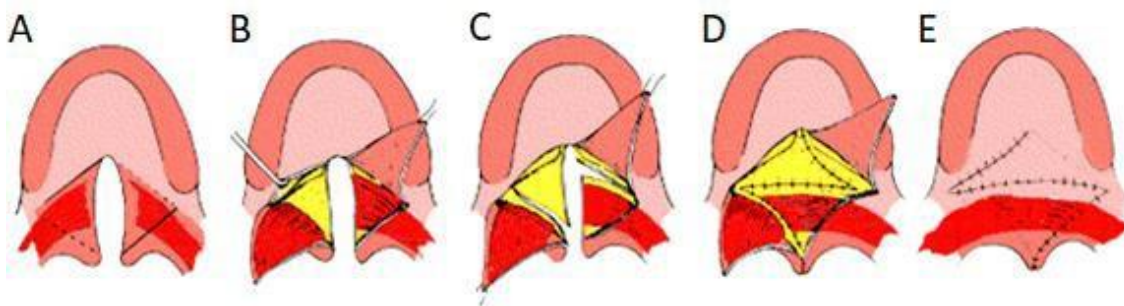


Figure 2.13 Furlow double-opposed Z palatoplasty: (A) Soft palate CP with incomplete levator veli palatini, (B) Oral mucosa flaps produced, (C) Nasal mucosa flaps produced, (D) Nasal mucosa flaps rearranged and sutured and (E) oral mucosa flaps rearranged and sutured to produce the complete levator veli palatini sling (Patel, 2016).

#### 2.2.1.1. Outcomes

Early surgical complications include haemorrhaging, obstructed respiration, wound dehiscence and formation of non-healing oronasal fistulas (ONF). Late complications include bifid (separated) uvula, VPI, hypernasal speech, maxillary hypoplasia, COME and poor dental alignment/positioning (Agrawal, 2009). ONF is the most common of these occurring in approximately 25 % of primary palatoplasties (Sadhu, 2009). Some of these will spontaneously heal over months or years, particularly soft palate ONFs, although if this does not occur, revision surgery will be necessary. The incidence of post-operative ONF development is comparative to the difficulty of closing the cleft which is primarily influenced by the cleft extent (Phua and de Chalain, 2008). The tension on the sutures is considered one of the biggest risk factors for failure which is why tension-free closure is considered the gold standard (Losken *et al.*, 2011). Figure 2.14 shows the incidence of anterior/posterior ONFs and hypernasality severity amongst patients according to the Veau classification system.

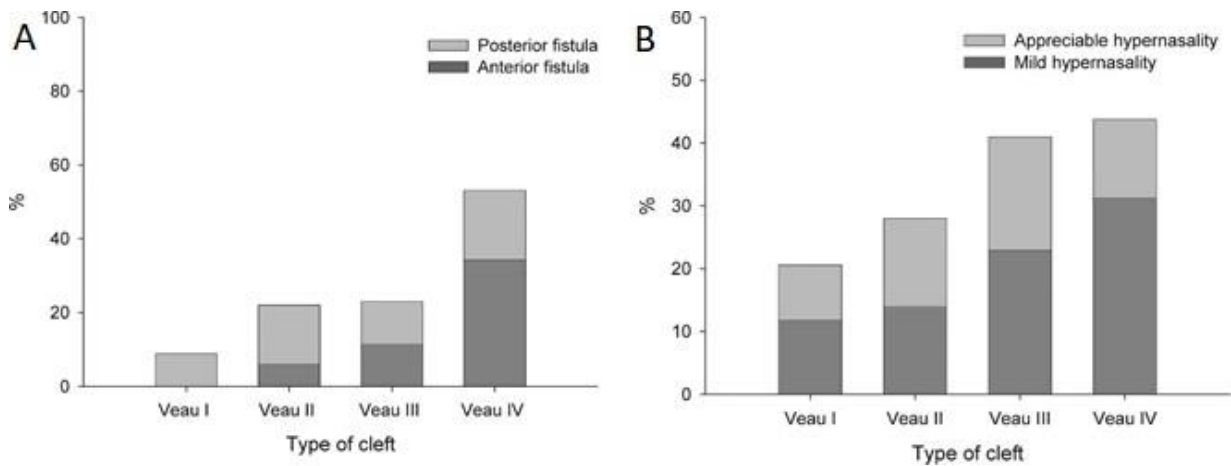


Figure 2.14: (A) Incidence of anterior and posterior fistulas and (B) degrees of hypernasality recorded following palatoplasty of different Veau classifications (Phua and de Chalain, 2008).

Regardless of the technique used, there are three universal objectives for CP surgery: anatomical closure of the defect, normal midfacial growth and development of normal speech (Hassan and Askar, 2007; Agrawal, 2009). The timing of surgical intervention is a controversial topic because of this as earlier reparation leads to better speech development whereas delayed reparation may improve maxillofacial growth in later years (Tibesar, Black and Sidman, 2009). This is because the child will learn how to use the palatal muscles to speak, eat, etc. in their incorrect position as previously mentioned in section 2.1.4.2 which will all need to be relearnt, often requiring a speech therapist. On the other hand, the more one can delay surgery and its corresponding site scarring, which causes maxillary retrusion, the lesser an adverse effect it will have on the patient. The compromise that surgeons seldom deviate far from is operating at the age of 12 months although some authors have suggested as old as 15 years so that the patient is nearly fully grown (Katzel *et al.*, 2009; Shi and Losee, 2010).

Development of normal speech is also closely connected to correct repositioning of velar musculature, a process known as intra-velar veloplasty (IVV), to reform the functional 'sling' of the levator veli palatini. This has been shown to reduce incidence of VPI and COME however increases the incidence of ONF (Hassan and Askar, 2007). When introducing IVV to any of the previously mentioned techniques, they can become a 'three-layer'

technique. This is one example of different versions of the core palatoplasties but many surgeons tweak small details depending on their own preferences and experiences which has led to numerous types of palatoplasties today, making comparisons difficult (Agrawal, 2009).

Furlow Z-plasty results in ONF incidence of 0-3.6 % and 77.2-84 % of patients being rated normal speech or completely free from VPI whereas the VWK pushback has 6.6 % incidence of ONF and only 50 % normal speech results (Khosla, Mabry and Castiglione, 2008; Abdel-Aziz and Ghandour, 2011). In contrast to this, other reports state incidences significantly higher at 40.6 % when using the Furlow Z-plasty when used for Veau classifications II, III and IV (Losken *et al.*, 2011). The Bardach method similarly found results of 75-80 % of normal speech in patients and ONFs in 5.2 % of patients (Bardach, 1995). A poll of 288 cleft surgeons in the US showed the Bardach and Furlow methods were massively preferred, having been used in 45 % and 42 % of cases respectively which was in stark contrast to the Von Langenbeck technique at 2 % and the VWK pushback at 1 % (Katzel *et al.*, 2009).

Additionally, difficulties lie when conducting reviews between different surgeons who each have their own preference for when to use certain methods, which introduces bias. The lack of definitive data from prospective trials is also a limiting factor which means retrospective studies are relied upon with their varying description qualities (Khosla, Mabry and Castiglione, 2008). Another problem is that techniques are not compared on the same clefts e.g. Furlow repairs are popular when repairing Veau I's which are known to have lower risk of ONF and VPI regardless of technique used, producing potentially misleading positive results (Phua and de Chalain, 2008). Future reviews should aim to be prospective in nature to avoid problems with inconsistent patient records which often lack detail, making evaluation difficult.

Despite extensive evaluation of these techniques over decades there is still no definitive answer to which is the 'gold standard' as complication rates vary vastly between surgical

technique, timing of repair, surgeon, centre and post-surgical management (Zhang *et al.*, 2017). Other factors previously discussed are the cleft classification and morphology however whether the surgery is a primary palatoplasty or revision is also key. This is because post-operative fibrosis has made the palatal tissue less workable, increasing the difficulty and subsequently the failure rate due to ONF development increases with each additional surgery (Langdon, 2011). Ultimately, it is widely believed that further research is required into the efficacy of the various palatoplasties and the other risk factors that surround them in order to fully understand how to optimise clinical success (Sitzman *et al.*, 2017).

## 2.2.2. Alternative Treatments

### 2.2.2.1. Obturators

The difficulty that surgeons and dentists encountered when attempting to surgically repair CP also led to the development of other treatment types. The most notable of these were obturators which were first described in 1560 as a gold plate held in place with a sponge to restore speech as seen in Figure 2.15 (Rogers, 1976). These are removable devices that temporarily close the opening between the oral and nasal cavities during activities like feeding or eating to prevent nasal regurgitation and reduce hypernasality.

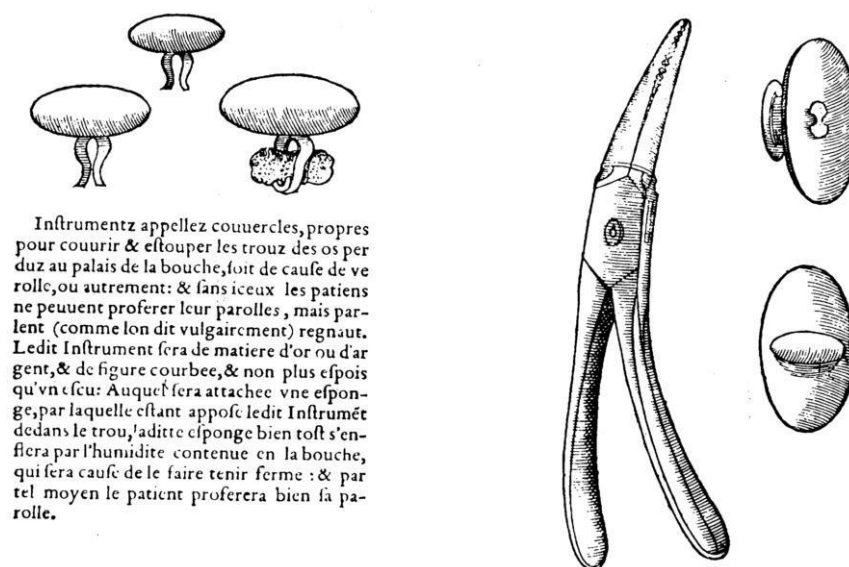


Figure 2.15: Original illustrations and notes of some of the first palatal obturators with sponge from 1564 (Rogers, 1976).

The critical advantages obturators have is that they do not require surgery to separate the oral and nasal cavities which is particularly useful in CP cases with irregular morphology. CP typically displays itself as a unidimensional defect which is characterised by a width to length ratio of  $< 1:3$  however bidimensional defects with a ratio of  $> 1:3$  can also occur as seen in Figure 2.16 (Richardson and Agni, 2014). These are much harder to treat with the conventional flap surgeries because there is less palatal tissue available to construct flaps with and a larger distance to mend which causes greater suture tension and higher ONF rates (Richardson and Agni, 2014).



Figure 2.16: (A) Unidimensional CP case and (B) Bidimensional CP case (Richardson and Agni, 2014).

Modern obturators can be used as either a modification obturator for an immediate, short-term seal of the breach or as an interim obturator for use post-surgery to aid with closing ONFs. They are rarely used as a definitive (semi-permanent) obturator however one example of these is the Nance device, which is used when surgery is not feasible and temporary devices have previously failed. These have relatively low-costs and low-maintenance compared to surgery whilst producing excellent speech results (Borzabadi-Farahani *et al.*, 2012). On the other hand, if treating children, their deformity morphology changes as they grow and replacement devices are needed regularly which becomes expensive and the device can also irritate the palate (Agarwal, Rana and Shafi, 2010). As anything other than surgery is seldom used as a permanent treatment there is very limited data on the popularity of obturators other than as feeding aids in infants prior to surgery

(Chandna, Adlakha and Singh, 2011).

#### 2.2.2.2. **Regenerative Medicine Approaches**

Acellular dermal matrices (ADMs) such as AlloDerm are implants that have recently been successfully used with palatoplasty to cover bony defects and nasal mucosa suture sites at the junction of the soft and hard palate, a notorious point for ONF development (Albanna *et al.*, 2016). They are also useful when palatoplasty fails and ONFs form as they support spontaneous healing without the need for secondary surgery. In a recent review, the weighted average for ONF incidence after primary palatoplasty with ADMs was found to be 5.4 % compared to 10.6 % in a non-ADM group (Aldekhayel, Sinno and Gilardino, 2012). This was also seen in secondary palatoplasty surgeries where the ADM group had a persistent ONF incidence of 8.1 % compared to 12.9 % (Aldekhayel, Sinno and Gilardino, 2012). Although promising, there is insufficient evidence currently to recommend this as routine but there is a potential benefit that needs to be supported with randomised evidence.

Other promising scaffolds that have been developed and may be used to treat CP are electrospun bilayer and trilayer membranes made from polyhydroxybutyrate-co-hydroxyvalerate, PLA and polycaprolactone (PCL) which are biocompatible and biodegradable (Bye *et al.*, 2013). The use of polymers with different properties has been used to successfully segregate different cell cultures on the membrane which could be used for harmonious soft and hard tissue repair in CP deformities (Puwanun *et al.*, 2016). These electrospun membranes are only 600 µm thick however so are not suitable to occupy the cleft void although their manufacture could be optimised to scale this up to mm thickness scales.

Additionally, electrospinning as a production technique is known for having variation in diameters of the produced polymer fibres which would produce varying porosities and densities across different areas of the membrane. In summary, surgical intervention is a difficult compromise between avoiding maxillofacial growth disruption and attaining high

speech quality for a patient. Surgery has not seen significant modernisation for decades despite it being considered the sole practical treatment option. Obturators are primitive in their design and are not popular however offer unique advantages by avoiding surgery and corresponding maxillary growth problems.

There is a pressing need for the development of new devices for treating cleft palate and the development of new biomaterials is key for achieving this task. In section 2.3 the concept of biomaterials is explored which focuses on the use of hydrogels since they have been reported as great candidates for tissue engineering applications.

## **2.3. Biomaterials**

A biomaterial is broadly defined by the journal of biomaterials as "a substance that has been engineered to take a form which, alone or as part of a complex system, is used to direct, by control of interactions with components of living systems, the course of any therapeutic or diagnostic procedure" (Biomaterials, 2017). The use of biomaterials dates back to 1,000 CE in ancient Egypt and South America where artificial teeth made out of stone have been found (Saini, 2015). Biomaterials have been used in a vast range of medical applications to date including cardiovascular stents, heart valves, dental implants, orthopaedic implants, burn dressings, sutures, drug delivery systems, biosensors and contact lenses (Rezaie, Bakhtiari and Öchsner, 2015). When selecting a biomaterial to use in the body, specifically the oronasal cavities in this instance, many qualities must be considered which are all important for the success of an implanted device.

### **2.3.1. Biomaterial Classification**

Biomaterials are fundamentally grouped as metals, ceramics, polymers and composites but they can also be classified in relation to their synthetic or natural origins (Table 2.2). Natural polymers that are used as biomaterials can be further classified dependent on their precise

origin. Autogenic materials are derived from the same individual they are used to treat whereas allogenic materials are from members of the same species. Xenogeneic materials are derived from different species, commonly cows (bovine) or pigs (porcine), and plant derived biomaterials are sourced from flora such as trees, kelp and algae. Each class of biomaterial offers specific advantages and disadvantages that, as a collective, enable a vast range of applications (Table 2.2).



Table 2.2: Table of biomaterial groups used in medicine with common advantages, disadvantages and applications.

Group	Examples	Advantages	Disadvantages	Applications	References
Metals	Gold, stainless steel, cobalt-chromium-molybdenum alloys, nickel-titanium, other titanium alloys and silver.	Hard, strong, castable, alloyable, shape-memory and fatigue resistance.	Stress shielding, aseptic loosening, wear particle toxicity, radiopacity and corrosion.	Load bearing orthopaedics, temporary devices, fixings, pacemakers, orthodontic archwires, vascular stent, vena cava filter, intra-cranial aneurysm clips, heart valves, catheter guide wires and orthopaedic staples.	(Chen and Thouas, 2015; Mahyudin, Widhiyanto and Hermawan, 2016) (Williams, 2008).
Ceramics	Alumina, zirconia, bioactive glass, glass-ceramics, tricalcium phosphate, hydroxyapatite and carbon fibre.	Wear resistance, high compression strength, corrosion resistance and chemical similarity to bone.	Poor tensile strength, low fracture toughness and brittle failure.	Orthopaedic cement, filler, total hip replacement surface, bone graft, heart valves and bearing surfaces.	(Mahyudin, Widhiyanto and Hermawan, 2016) (Williams, 2008).
Synthetic Polymers	Silicone rubber, acrylic resins, nylon, PLA, polyglycolic acid, polylactic-co-glycolic acid, polymethyl methacrylate, PCL, polyethylene, polyethylene terephthalate, polyvinyl chloride and polyetheretherketone.	Resilient, easily mass produced, tailorable properties and biodegradable (some).	Weak, made from non-renewable oil and non-biodegradable (some).	Load bearing orthopaedics, vascular grafts, heart valves, spinal cages, cranial implants, bearing surfaces, sutures, drug delivery, soft tissue augmentation and cell scaffolds.	(Mahyudin, Widhiyanto and Hermawan, 2016) (Williams, 2008).
Natural polymers	Hyaluronic acid, collagen, gelatine, fibrin, natural rubber, cellulose, chitin, alginate, silk, agarose and decellularised tissues.	Form hydrogels, biocompatible, biodegradable, bioactive, non-toxic, mimics tissue, acts as extracellular matrix and nutrient/waste diffusion.	Poor mechanical strength, contamination risk, batch variability and potential impurities.	Drug delivery, soft tissue augmentation, spinal cages, other cartilage replacement, sutures and cell scaffolds.	(Drury and Mooney, 2003; FMC Corporation, 2003; Nair and Laurencin, 2007; Croisier and Jérôme, 2013)
Composites	Fibreglass, carbon fibre/ polyethylene, carbon fibre/ polyetheretherketone, hydroxyapatite/ polyethylene, polyethylene terephthalate /gelatine and polyethylene terephthalate /collagen.	Combining beneficial properties of individual materials, satisfying niches and weight reduction.	Expensive, complex manufacture and difficult to detect weakening.	Load bearing orthopaedics, bone filler, vascular grafts, orthopaedic cement, fixings and dental implants.	(Ramakrishna <i>et al.</i> , 2001; Hak <i>et al.</i> , 2014; Mahyudin, Widhiyanto and Hermawan, 2016).

### 2.3.1.1. Synthetic Biomaterials

Metals are a popular choice for load bearing application due to their favourable mechanical properties including toughness (resistance to deformation), Young's modulus (stiffness) and ultimate tensile strength and are often used in orthopaedic load bearing applications such as joint replacements. The high Young's modulus of metals can, however, cause stress shielding which lowers bone density and can lead to fracture and failure (Chen and Thouas, 2015). In comparison, ceramics such as zirconia or alumina are also high strength but brittle which can lead to sudden, unexpected device failure. They are the preferred material for movement surfaces in devices due to their excellent wear resistance. Calcium phosphate ceramics are also useful as bone grafts due to their chemical similarity to bone and osteogenic porosity (100-300  $\mu\text{m}$ ) (Hannink and Arts, 2011). Composites are comprised of separate regions of two or more materials that exhibit a compromise of their physical and chemical properties which often fill niches. Carbon-fibre-reinforced polyether etherketone (PEEK), for example, is a composite that could replace metals in load bearing applications as it has a Young's modulus significantly closer to that of cortical bone which can prevent stress shielding (Hak *et al.*, 2014).

Polymers are large macromolecule chains composed of many repeating subunits (monomers) that formed from polymerisation. This is unlike metals and ceramics that have a combination of dense, lattice structures and crystals regions called grains. Synthetic polymers offer a diverse selection of physical and chemical properties through use of monomer variety, different polymerisation methods (condensation or addition) and the use of copolymers, where multiple monomer types are combined (Lendlein, 2010). Polylactic-co-glycolic acid (PLGA) is one such biodegradable copolymer where hydrophilic, crystalline polyglycolic acid (PGA) and hydrophobic PLA monomers are used. By using different ratios of these monomers certain material properties like biodegradation rate can be tailored for applications with differing *in vivo* time requirements such as sutures, drug eluting surface coatings and blood vessel stents (Maitz, 2015). PCL is popular as a biomaterial because it

is easy to process, has clinically relevant degradation times and is approved by the US Food and Drug Administration (FDA) for multiple applications (Mondal, Griffith and Venkatraman, 2016).

### 2.3.1.2. **Natural Biomaterials**

#### 2.3.1.2.1. **Autogenic & Allogenic Biomaterials**

Natural materials are produced by living organisms hence can offer many advantages over synthetic materials. For instance, they can mimic the complex biomechanics of non-Newtonian tissues in the body which are a result of intricate organisation of components and presence of living cells. Autogenic materials such as bone grafts represent the 'gold standard' of biocompatibility where the unimpeded host immune system does not respond to the implanted tissue antigens as they are genetically identical to the host (McKay, Park and Perkins, 2010). Antigens are surface-embedded and excreted proteins which have a unique 'thumbprint' that is recognised by the immune system. If identified as foreign, a complicated immune response is triggered which isolates and destroys the donor tissue (rejection) (McKay, Park and Perkins, 2010). Nerve grafts and skin grafts are common uses of autogenic material however any large scale use is limited by excessive donor site morbidity, patient discomfort and a lack of availability (Yuan, 2010).

This has led to the popularity of allogenic biomaterials where either tissue or whole organs are transplanted to the patient from other humans. This allows damaged or diseased organs and tissues to be replaced with fully functioning alternatives from healthy donors to alleviate patient symptoms. Allogenic transplants provide the correct overall morphology, functionality and complex microstructure of living material which is otherwise difficult to replicate (Esch, Bahinski and Huh, 2015). Unfortunately, transplant recipients will require lifelong immunosuppression therapy to prevent their immune system attacking the transplant which leaves patients susceptible to infections, the leading cause of morbidity and mortality following transplantation, particularly for children (Duncan and Wilkes, 2005; Meyer *et al.*,

2005). Moreover, transplants have limited availability because there are few opportunities where a healthy, viable donor can be matched with a recipient at a suitable time. The number of patients on the waiting list for transplants has also significantly increased in recent years, whereas donations have not (Figure 2.17) (OPTN, 2016). This shortage of donors means that unfortunately many patients will pass away without receiving a transplant, indicating a clear need for alternative, scalable methods for replacing organs and tissues.

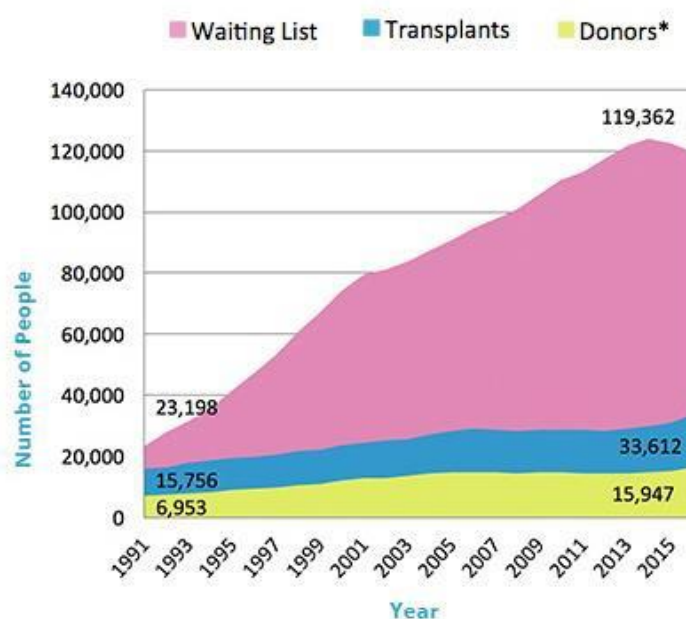


Figure 2.17: Number of donors and transplantations in the US from 1991 to 2015. \* Includes live and dead donors (OPTN, 2016).

### 2.3.1.2.2. Xenogeneic & Plant Derived Biomaterials

Animal and plant derived biomaterials are capable of being easily upscaled to provide large amounts of biomaterial which is one of many reasons why they are popular. Animal- derived polymers such as collagen, hyaluronic acid (HA), gelatine, fibrinogen and chitosan have been used in many medical applications (Drury and Mooney, 2003). Collagen is highly versatile, abundant in many fibrous tissues, provides integrin binding sites and is very similar between species. Collagen has been used extensively for burn/wound dressings, bone grafts and antithrombogenic surfaces (Khan and Khan, 2013). HA is a glycosaminoglycan which is abundant in skin that displays interesting viscoelasticity

properties and is used as a scaffold in cartilage repair and bone grafts (Menaar, Menaar and Menaar, 2013). Chitosan is derived from crustacean shells and exhibits excellent antimicrobial, antifungal, mucoadhesive and haemostatic properties which is why it is very popular in wound dressings and skin replacement (Croisier and Jérôme, 2013).

De-cellularised tissues are another form of xenogeneic biomaterial where tissues such as porcine heart valves have been treated before implantation in humans. By removing cellular components of a tissue and leaving the ECM intact the immune response can be significantly reduced although further long term studies are required to translate these results into improved clinical results (Meyer *et al.*, 2005). Unfortunately, the exposed ECM proteins have been shown to cause blood clotting (thrombosis) which is a significant cause of transplant failure (Jiang *et al.*, 2016). The size and structure of the tissues are also extremely difficult to tailor to specific patients in some cases such as small children or patients that have surgical complications affecting aortic geometry. Both xenogeneic and allogenic materials also carry risk of infections including human immunodeficiency virus, hepatitis and transmissible spongiform encephalopathy which is worsened because transplantation breaches normal host defences (Boneva, Folks and Louisa, 2001).

Plant-derived materials do not pose these risks but do still provide the benefits of being a natural material such as excellent biocompatibility, biodegradability and remodelling (Bao Ha *et al.*, 2013). They are also the easiest source of biomaterial for economic upscaling and can be monitored in a controlled environment from the start to finish of their growth cycle which is valuable for reliability and regulation. Cellulose is a structural component in cell walls of many plants which has been studied as a biomaterial for bone grafting and has interesting chemoattractant properties that aid migration of cells (Tommila *et al.*, 2013). Agarose is a polysaccharide found in agar which is commonly extracted from seaweed which has been used for bone grafts, cartilage repair and nervous tissues (Varoni *et al.*, 2012). Finally, alginate is one of the most popular plant derived materials which has been used

extensively as a biomaterial for microencapsulation and therapeutic drug delivery (Goh, Heng and Chan, 2012).

In summary, there are many biomaterials available for use however deciding which is best depends on the specific requirements and limitations of the application in question.

### 2.3.2. Biomaterial Requirements

The most critical quality of any biomaterial is their biocompatibility, defined as the ability to coexist with a living system without causing an unacceptable degree of harm to the body (Williams, 2008). Bioactivity and bioinertia are similar terms that are used in parallel to define introducing deliberate biological effects or avoiding interactions altogether with the living system respectively (Williams, 2008). First generation biomaterials (60's and 70's) were designed primarily for their physical properties whilst remaining bioinert however second generation (80's) showed a shift of focus to bioactive principles (Hench and Polak, 2002). Third generation biomaterials are now being designed as bioactive, to stimulate specific cellular infiltration and proliferation at a molecular level whilst biodegrading, a key concept in tissue regeneration (Hench and Polak, 2002).

Biodegradation is the ability to break down over extended times *in vivo* which is also termed bioresorbable if full excretion of degradation macromolecules by the body is achieved (Liu, Zheng and Hayes, 2017). Using biodegradable materials offers many advantages including avoiding complications with long-term biocompatibility of permanent devices and removing the need for follow-up surgery to remove non-permanent devices. The degradation rate can be fine-tuned for specific applications such as drug delivery treatment lengths or to match the in-growth rate of the hosts own cells to optimise tissue regeneration (Sun and Tan, 2013). Polymer biodegradation *in vivo*, for example, is achieved *via* chemical degradation, typically with hydrolysis reactions where hydrolytically unstable bonds in the polymer backbone (including esters, anhydrides, acetals and carbonates) are cleaved *via* the addition of a water

molecule (Figure 2.18) (Ulery, Nair and Laurencin, 2011). Most natural polymers undergo enzymatical degradation too although this depends on the availability and concentration of naturally occurring enzymes (Nair and Laurencin, 2007).

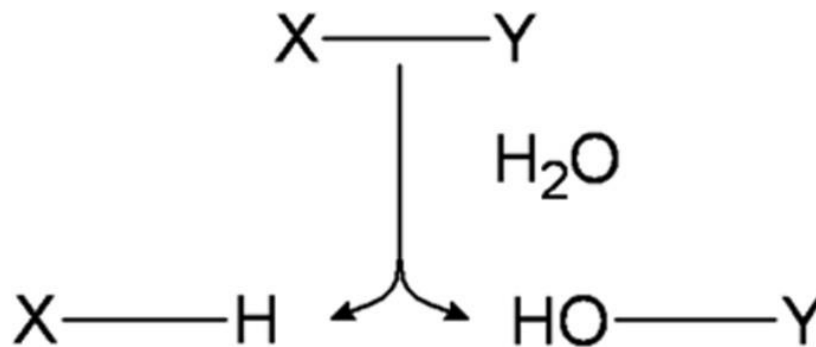


Figure 2.18: Hydrolytically sensitive bond between X and Y monomers in a polymer backbone hydrolysed with a water molecule (Ulery, Nair and Laurencin, 2011).

Amorphous regions are hydrolysed first which reduces molecular weight and mechanical properties but the polymer remains physically unchanged initially due to crystalline regions holding it together. Eventually fragmentation of the whole structure produces low molecular weight oligomers (chains of only a few monomers) which can be resorbed by cells and excreted by the body (Gajjar and King, 2014). Biodegradation of a biomaterial is also classified on which erosion mechanism is exhibited, either surface or bulk. Surface erosion is characterised by the rate of degradation and mass relief exceeding the rate of water diffusion into the bulk volume of the material whereas bulk erosion is *vice versa* where all material is simultaneously degraded (Ulery, Nair and Laurencin, 2011).

A biomaterial must also possess the sufficient mechanical properties necessary for its specific application such as high wear resistance for movement surfaces, high strength for load bearing applications or high malleability for flexibility. In applications like hip or knee joint replacements these mechanical properties need to be sustained for decades *in vivo*, so the materials must also be resistant to fatigue from cyclic loading caused by walking in this instance (Micheli, Wannomae and Muratoglu, 2017). One of the biggest challenges that

the biomaterials field faces is the difficulty in reproducing materials with the complex biomechanical properties of living tissues which are highly organised natural composites comprised of ECM components and multiple cell types (Murphy and Atala, 2014). Directional dependencies (anisotropy) in long bones are one example of this complexity, which are much stronger under compression longitudinally than transversely due to the arrangement of ossified constructs. The variety of applications that biomaterials are required for has led to a wide selection of biomaterials that have been used with very different properties.

When considering these requirements, alginate stands out as the primary biomaterial candidate for designing a novel regenerative treatment for CP, discussed in detail in the next section.

### 2.3.3. Alginate

Alginate, or alginic acid, is a polysaccharide commonly derived from the cell walls of brown algae (kelp) or sometimes microorganisms. 30,000 tonnes of alginate are produced annually, at a relatively low cost, which is estimated to be below 10 % of the total biosynthesised alginate available, indicating both its affordability and suitability as a biomaterial (Pawar and Edgar, 2012; Raman, Gurikov and Smirnova, 2015). Farming alginate for use as a biomaterial also allows greater quality assurance of the final product compared to other sources as producers can choose which specific algae species to grow and monitor it throughout its lifetime.

Historically, it has been regularly used in the food industry as a thickener or gelling agent, in pharmacology as an acid-reflux treatment and in dentistry as an impression material to create moulds of a patient's mouth (Augst, Kong and Mooney, 2006). Recently, alginate has been the focus of research for medical applications including wound healing, cell transplantation and delivery of bioactive agents (Liberski, 2016). These are not limited to research, however, demonstrated by the clinical use of alginate as a drug delivery



mechanism to promote regeneration of mineralised tissue in intra-bony defects in adult patients with periodontitis (Bratthall *et al.*, 2001).

Alginate has a well-established biocompatibility which has been extensively evaluated both *in vitro* and *in vivo* which typically reports little or no foreign body response following implantation of the material (Lee and Mooney, 2011). Impurities such as heavy metals, endotoxins, proteins and polyphenolic compounds could be the cause of this which is supported by products with higher degrees of purification showing no significant response (Orive *et al.*, 2002). The lack of mammalian integrins present in alginate can be seen as disadvantageous due to reduced cell adhesion however it can also be helpful because the material can serve as a 'blank slate' to which specific, quantified levels of cell-adhesive proteins such as Arginylglycylaspartic acid can be added (Lee and Mooney, 2011). Alginate is also biodegradable but due to its large molecular weight is difficult to clear from the body so partial oxidation can be used to cleave molecules and accomplish this without significantly altering gel properties (Bouhadir *et al.*, 2001).

The practicality of alginate as a biomaterial can also be attributed to its interesting mechanical properties which are governed by its chemical composition. Alginate is formed of unbranched copolymers comprised of covalently bound  $\beta$ -D-mannuronic acid (M) and  $\alpha$ -L-guluronic acid (G) in repeating blocks of GG, MM or alternating GM as seen in Figure 2.19 (Pawar and Edgar, 2012). The relative ratios of these blocks varies between which seaweed species the alginate was extracted from and the location this was grown in beforehand, with cold and rough waters facilitating high G-block content (FMC Corporation, 2003). Interestingly, the foreign body reactions observed with alginate have also been attributed to high M-block-containing varieties (Otterlei *et al.*, 1991).

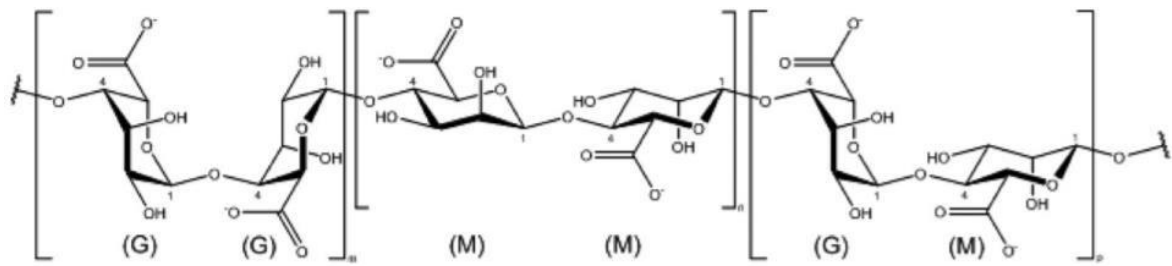


Figure 2.19: Diagram of an alginate molecule with distinct regions of G, M and GM blocks (Agulhon et al., 2012).

Alginate, like many naturally occurring polymers, can form hydrogels which are hydrophilic networks of crosslinked polymer chains which readily absorb and retain water. Hydrogels offer many advantages over other polymeric scaffolds as the high water content mimics the composition and viscoelastic mechanical properties of soft tissue whilst enabling diffusion of nutrients and cellular waste (Zhu and Marchant, 2011). The density of alginate crosslinking can be controlled to determine the porosity which can be used both to allow cell migration as a biodegradable scaffold or to encapsulate cells as a therapeutic application that is isolated from the patient immune system (Varoni *et al.*, 2012). The G- block content of alginate heavily influences the strength of gels formed by alginate as they contain the location for binding sites of the divalent cations such as  $Mg^{2+}$  and  $Ca^{2+}$  which are used to ionically crosslink molecules in hydrogels (Paques *et al.*, 2014). This is described as an 'egg-box' model as seen in Figure 2.20.

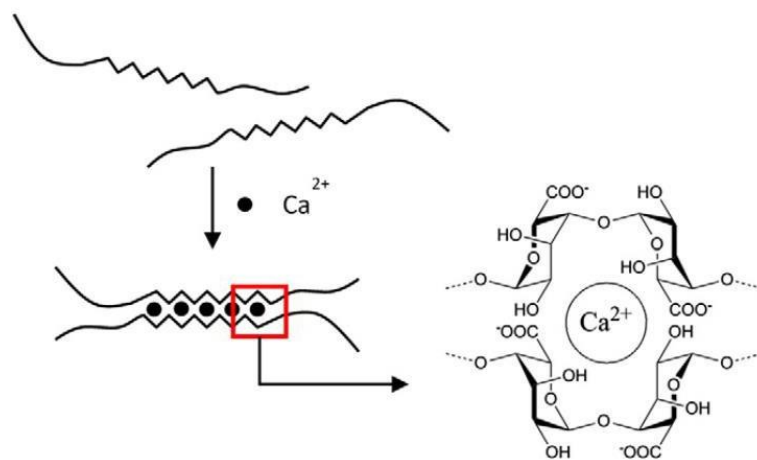


Figure 2.20: Addition of  $Ca^{2+}$  ionically binds G-block regions in adjacent alginate molecules to form the hydrogel (Paques et al., 2014).

Alginate also has recently been a popular choice in medical 3D printing applications because of the viscoelastic nature of the material which can behave as both a solid and a liquid depending on the conditions. Specifically, aqueous alginate exhibits thixotropic shear-thinning properties whereby viscosity is reduced when subjected to shear forces because polymer chains align parallel to the force, reducing the resistance to flow (Dávila and d'Ávila, 2017). As it is thixotropic, the viscosity increases when the shearing force stops and the hydrogel network returns to its normal solid, elastic structure. In comparison, other biomaterials such as agarose are thermosetting and thus limited by severe temperature dependency over material properties (Varoni *et al.*, 2012). Additionally, the heat required to manipulate agarose or dissolve it initially is 60 °C which would destroy any delicate biological materials intended to be used in conjunction with it.

Alginate's rheological properties have seen it used to satisfy biomaterial niches such as injectable drug delivery systems which provide minimally invasive but robust implantation treatments that have good survivability *in vivo* (Yan *et al.*, 2016). 3D printing in medicine is another emerging field that alginate has been utilised within as it can be extruded through a narrow nozzle and then display the elastic properties necessary to support additional material (Ventola, 2014). A variety of alginate compositions and combinations with other biomaterials have been tested as scaffolds to better optimise the established compromise between mechanical strength and cytocompatibility as seen in Table 2.3 (Malda *et al.*, 2013).

Table 2.3: Alginate compositions that have been used to produce scaffolds with 3D printing. Print quality of 1 = poor, 2 = intermediate and 3 = high. \*Specific fibrin concentrations omitted from literature (Malda et al., 2013).

Materials	Polymer Concentrations (w/v)	Gelation method	Cytocompatibility	3D Printing Quality
Alginate	10 %	Ionic	89 % day 1	2
Alginate	4 %	ionic	94-95 % day 7	2
Alginate/collagen	1 %/0.3 %	Ionic	90 % day 7	2
Alginate/fibrin	6.3 %/? %*	Ionic/enzymatic	Not studied	1
Alginate/gelatine	7.5 %/5 %	Thermal/ionic/chemical	95 % day 0	2
Gelatine/alginate	6 %/5 %	Thermal/ionic	82 % day 7	3
Gelatine/alginate/chitosan	15 %/1.25 %/2.5 %	Enzymatic/ionic/chemical	Cells proliferating on day 7	2
Gelatine/alginate/fibrinogen	15 %/1.25 %/0.5 %	Thermal/enzymatic/ionic/chemical	Cells proliferating on day 7	2
Gelatine/alginate/fibrinogen	2:1:1	Thermal/ionic/enzymatic	Differentiating cells	2
Poly(ethylene glycol) (PEG) diacrylate/alginate	20 %/12.5 %	Photo	~100 % day 21	3

The combination of favourable biological and mechanical properties was the reason that alginate was chosen as the primary material in this project for producing obturators. The properties of the material will dictate their most appropriate manufacturing route, in this sense, 3D printing has become a rapidly evolving field in the development of the new generation of medical devices.

## 2.4. 3D Printing

In recent years the popularity of 3D printing has increased massively with the introduction of affordable printers for consumers. 3D printing allows people to produce their own designs at home but also is very popular commercially within the automotive and aerospace industries. The following sections will provide an introduction to 3D printing, compare it to traditional manufacturing and discuss how it is also used within the medical industry.







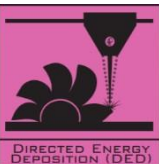
### 2.4.1. Introduction to 3D Printing

The popular perception of the term '3D printing' is synonymous with its technical term,

Additive Manufacturing (AM) which was invented in 1984 by Chuck Hull (Schubert, van Langeveld and Donoso, 2014). For the purposes of this report, the terms 3D printing and AM are used interchangeably. Since 1984, many different forms of AM have been developed which have been grouped into 7 distinct families as per American Society for Testing and Materials (ASTM) standard F2792 as seen in Table 2.4: Vat photopolymerisation, powder bed fusion, binder jetting, material jetting, sheet lamination, material extrusion and direct energy deposition. These 3D printing methods all hold to a fundamental layer-by-layer approach where layers, or slices, in one axis of a 3D object are individually produced one-by-one, fusing as they do this, to eventually produce the completed object.

Although 3D printing encompasses 7 families, one specific type of binder jetting is also termed 3DP™ for 3D printing which is confusing and can cause inconsistencies in terminology. Other instances of inconsistencies are in the amount of families that exist such as in a review where 9 were described, where powder bed fusion was divided and a new process called Prometal was included (Wong and Hernandez, 2012). One of the most popular forms of 3D printing is FFF, seen in Figure 2.21, which is part of the material extrusion family (Ventola, 2014). This term was coined by The RepRap Project, a community dedicated to an open-source 3D printing philosophy, as a synonymous term for fused deposition modelling (FDM™) which was not legally constrained (Reprap, 2017).

Table 2.4: The 7 AM families (Hybrid Manufacturing Technologies, 2012; Ernst & Young, 2016).

Family	Brief Description	Other Names	Materials	State	Advantages
	An ultraviolet laser selectively cures a vat of photopolymer which polymerises on a submerged platform. This is then incrementally lowered to produce new layers.	Stereolithography apparatus, & digital light processing.	Photopolymers & ceramics.	Liquid.	High levels of accuracy and complexity, Smooth surface finish & large build areas.
	Uses an electron beam or laser to melt and subsequently fuse particles. A hopper and roller disperse a thin fresh layer of material afterwards for the next layer.	Selective laser sintering, electron beam melting, selective heat sintering & direct metal laser sintering.	Metals, sand, ceramics & polymers.	Powder.	High level of complexity, support material not required & wide range of supported materials.
	Binder material droplets are selectively deposited onto a bed of loose powder to fuse it and produce layers. A hopper and roller disperse a thin fresh layer of powder afterwards for the next layer.	3DP™, powder bed and inkjet head & plaster-based 3D printing.	Polymers, sand, metals, glass & ceramics.	Powder.	Colour printing, high productivity & wide range of supported materials.
	Droplets of print material are selectively deposited onto a print surface using a piezoelectric or thermal method, much like a modern-day home printer.	Multi-Jet modelling, polyjet™ & smooth curvature printing.	Photopolymers, polymers & waxes.	Liquids.	High level of accuracy, colour printing & can use multiple materials in a single part.
	Material spool provides consecutive sheets over the entire print surface where the desired layer cross section is fused, typically by ultrasonic welding or using an adhesive. Unused sheet material is removed onto a secondary spool.	Laminated object manufacture, selective deposition method & ultrasonic additive manufacturing.	Paper, polymer & metals.	Solid sheets.	High volumetric build rate, relatively low cost for metals & can combine sheets of different metals.
	Material is selectively dispensed through a nozzle or orifice which combine to form multi-layer models. Usually nozzle moves in 2 dimensions and print platform in 1.	FFF & FDM™.	Polymers, food & cells.	Filaments & Pastes.	Inexpensive, economical, multiple colours, desktop applications & good mechanical properties of prints.
	Controls deposition via a robotic arm which offers 4-5 axes of movement instead the conventional 3. The arm supplies material which is immediately melted upon contact using a laser, electron beam or plasma arc.	Laser metal deposition.	Metals & ceramics.	Powder.	Less limited by axes movement, Useful when making repairs and additional features, can use multiple material in a single part & highest single-point deposition

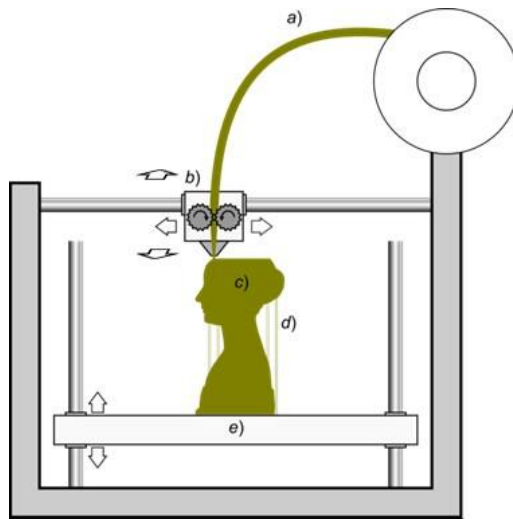


Figure 2.21: Conventional fused filament fabrication setup: (a) Filament, (b) Heated nozzle that controls X/Y axes, (c) Previously deposited material, (d) Support structures for overhanging areas, (e) Print surface which controls Z axis (Reprap, 2014).

## 2.4.2. 3D Printing vs Traditional Manufacturing

The four-traditional manufacturing, or material processing, families are: casting, material removal, deformation and consolidation. These all function to convert a raw material into a shape with useful structure and properties. Table 2.5 contains a brief description and comparison for typical features of each family.

Table 2.5: Comparison of TM processes (Sculpteo, 2017).

Family	Description	Advantages	Disadvantages
Casting	Molten material is poured into a previously constructed mould of the desired product then allowed to cool and solidify before the mould is removed.	Moulds can be tailored to produce extremely complex shapes.	Imperfections can arise from shrinkage and bubbles forming (porosity) on the surface or in the core as the material cools and solidifies. Gates which feed material to the mould must be removed as post-processing.
Material Removal	the broadest of the families, can also be referred to as machining and involves, as the name suggests, removal of material to change its shape by milling, turning, drilling, planing and several types of finishing etc.	Excellent precision and smooth Finish.	Generates scrap/waste material.
Deformation	using forces to change the shape of a material and includes forging, rolling, extrusion, pressing, stamping, bending, shearing etc.	High rates of production and large parts lowers cost.	Requires powerful, expensive equipment and dedicated tools or dies. Thin walled parts only. Limited shape complexity from the one side control.
Consolidation	or joining involves the use of combining two separate materials via methods including welding, brazing, soldering, adhesion and fastening.	Can produce large and complex shapes. Can use all materials.	Joints may possess properties different to the base material. Time consuming. High labour cost.

Effective TM processes are heavily reliant on the economy of scale to be economically viable i.e. the more one produces, the lower the average cost. This is due to the start-up costs such as in high pressure die casting (HPDC) where a very high-quality mould is required which is expensive prior to production commencing. One report demonstrates this by analysing the production of a scaled-down aluminium aircraft landing gear using HPDC and selective laser sintering (SLS) (Atzeni and Salmi, 2012). When considering all of the production and assembly costs, the total cost per unit for HDPC was  $\text{€ } 21.29 + (\text{€ } 21,000/N)$ , where N is the production volume and € 21,000 is the cost of the mould (Atzeni and Salmi, 2012). SLS on the other hand is an invariable cost of € 526.31 regardless of N and these two cross-over at  $N = 42$  as seen in Figure 2.22. Hence, HPDC is preferable at high production volumes compared to SLS at low volumes.



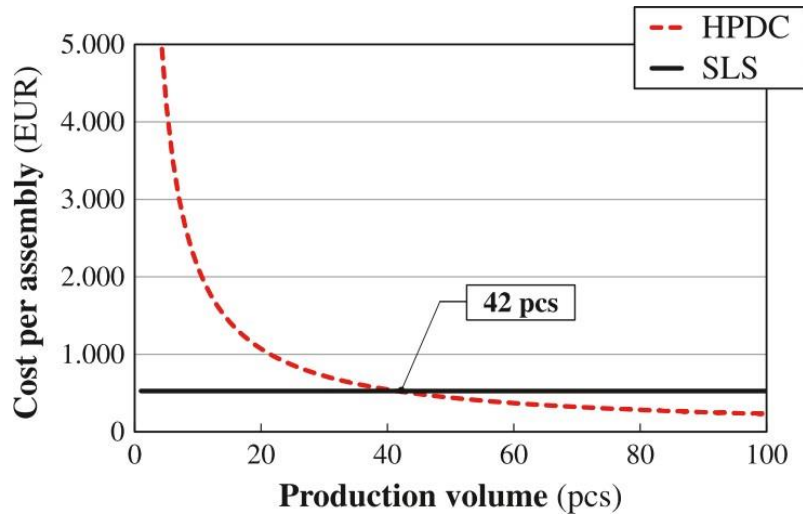


Figure 2.22: Comparison of costs of producing a landing gear assembly between HPDC and SLS techniques (Atzeni and Salmi, 2012).

However, the flexibility of production was overlooked in this comparison which is where 3D printing methods greatly out-perform TM methods such as die casting. For a die casting operation to change products, a new mould is needed which costs € 21,000 and can take months to produce along with the necessary tools (Atzeni and Salmi, 2012; Sculpteo, 2017). 3D Printing methods, however, only require a new computer-aided design (CAD) file which would only entail approximate wage costs of € 560 and a lead time of 2-3 days (Atzeni and Salmi, 2012).

Another area 3D printing is disadvantaged is sometimes the surface finish quality of products is poor. The resolution is limited by the layer height which, in FFF for example, is usually 0.2 – 0.4 mm. This means that in curved sections the layers form ‘steps’ which leaves a rough and unprecise finish, particularly in places with acute angles as seen in Figure 2.23. This can be reduced by using thinner layers although this increases production time significantly, often by a factor the layer height was reduced by i.e. layer height halved = production time doubled. Alternatively, post-processing methods can be used such as vibratory bowl abrasion and ultrasonic abrasion finishing however these also add on to the production time and costs for parts (Kumbhar and Mulay, 2016). The manufacturing duration is generally a disadvantage of 3D printing compared to TM, which is considered one of the key parameters

that limits 3D printing's mass productive capabilities (Thomas and Gilbert, 2014).

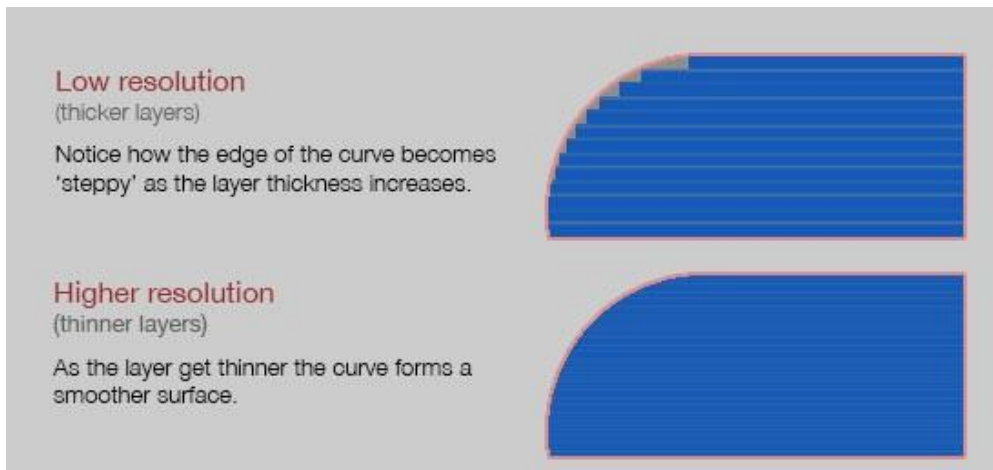


Figure 2.23: Demonstration of steps in layer resolution (3dprinterprices.com, 2017).

Material costs of 3D printing are also disadvantageous, with polymers being 20-100 times the price of their injection moulding counterpart (Atzeni and Salmi, 2012; Ernst & Young, 2016). This is most expensive for SLS systems where materials costs have been found to represent 74 % of the overall production costs compared to 25 % with stereolithography and 39 % with FFF (Hopkinson and Dickens, 2003). It is important to note, however, that this is likely to decrease as 3D printing becomes more popular at an industrial level and more suppliers begin to compete (Thomas and Gilbert, 2014). The specific energy consumption is also considerably higher in 3D printing compared to TM with an estimated 100-fold increase in the specific energy consumption (energy used per kilogram of finished product). Specifically, these have been found to be  $36.04 \text{ kWhkg}^{-1}$  for SLS,  $148.89 \text{ kWhkg}^{-1}$  for FFF,  $6.8\text{-}14.5 \text{ kWhkg}^{-1}$  for milling,  $1.47 \text{ kWhkg}^{-1}$  for injection moulding and  $4.72 \text{ kWhkg}^{-1}$  for metal casting (Baumers *et al.*, 2011; Yoon *et al.*, 2014).

The layer-by-layer process that 3D printing is characterised by unfortunately causes anisotropies, or directional dependencies, within prints depending on their orientation on the print surface with respect to the layering direction (Torrado and Roberson, 2016). As seen in Figure 2.24, which illustrates tensile strength of an FFF print, this is due to different amounts of fused areas between volumes in the design. This is macro-anisotropy however

it is important to note that micro-anisotropy can also occur. This is best described in metals, where in a 3D printed object, volumes will be subject to different temperature gradients depending on their location e.g. edge or centre of design. These two locations will therefore cool at different rates and in different directions which will influence grain size and morphology as well as which phases form, ultimately having large influences on the properties of the overall object (Collins *et al.*, 2016).

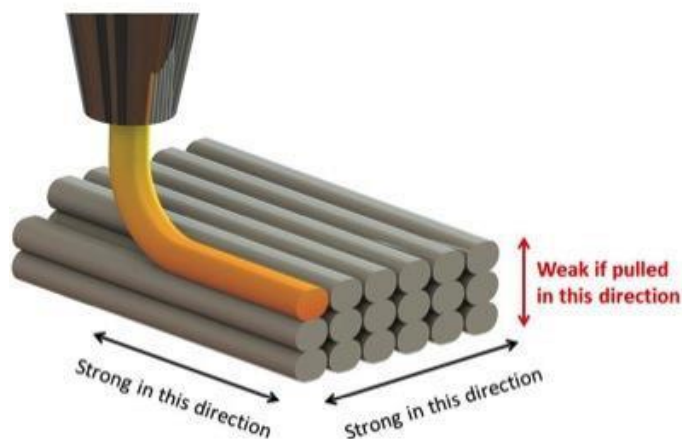


Figure 2.24: FFF example of structural anisotropy due to object orientation (Maroni, 2016).

Ultimately, more definitive comparisons between 3D printing and traditional manufacturing processes must be undertaken based on individual systems as there are too many families and processes whose properties vary greatly. When choosing which process would be best for a specific manufacturing job it is therefore a multi-factorial decision which incorporates print volume required, lot number required, quality required, time allowed, available funds, etc.

### 2.4.3. 3D Printing in Medicine

#### 2.4.3.1. Hard Materials

The concept of utilising 3D printing for medical applications began in the early 2000's with printing of dental implants out of hydroxyapatite, along with prosthetics and discussing how organ printing could be successfully achieved (Mironov *et al.*, 2003; Leukers *et al.*, 2005).

Since then, medical 3D printing has become an ever-increasingly popular research field which boasts previously unavailable opportunities including production of custom made implants, prosthetics, jigs, stents, fixtures and surgical tools. This can improve not only the success rate of the surgery or implant but also reduce surgical and patient recovery times (Ventola, 2014). Another benefit is the improved cost efficiency as these patient/surgery-specific products will be required on a very small scale compared to the larger scales seen with TM as previously discussed in Section 2.4.2.

A further use of 3D printing in medicine is production of anatomical models for use prior to surgical intervention such as mandibular reconstruction where computed tomography (CT) imaging data can be used to 3D print a model of the affected jaw (Cohen *et al.*, 2009). This allows surgeons to plan the resection cuts and pre-contour the titanium locking bone plate as seen in Figure 2.25 that preserve jaw strength. This reduces operation time considerably through minimising mid-operation adjustments when achieving the desired (and original) facial symmetry (Cohen *et al.*, 2009). This reduces time under general anaesthetic, blood loss and wound exposure time. The titanium locking plate is only temporary whereas autogenic bone graft reconstruction is considered the permanent treatment. The amount of graft required, usually taken from the ilium, is often estimated but by producing a model of the 'negative space' from a postoperative CT scan the exact shape and size of the required graft can be planned as well as its placement, which is important for later prosthodontic rehabilitation (Cohen *et al.*, 2009). SLA has also been used to produce patient-specific mandibular moulds which are then used to cast titanium trays, an alternative to locking bone plates which has proven a better fit and aesthetic results, reducing the need for revision surgery.

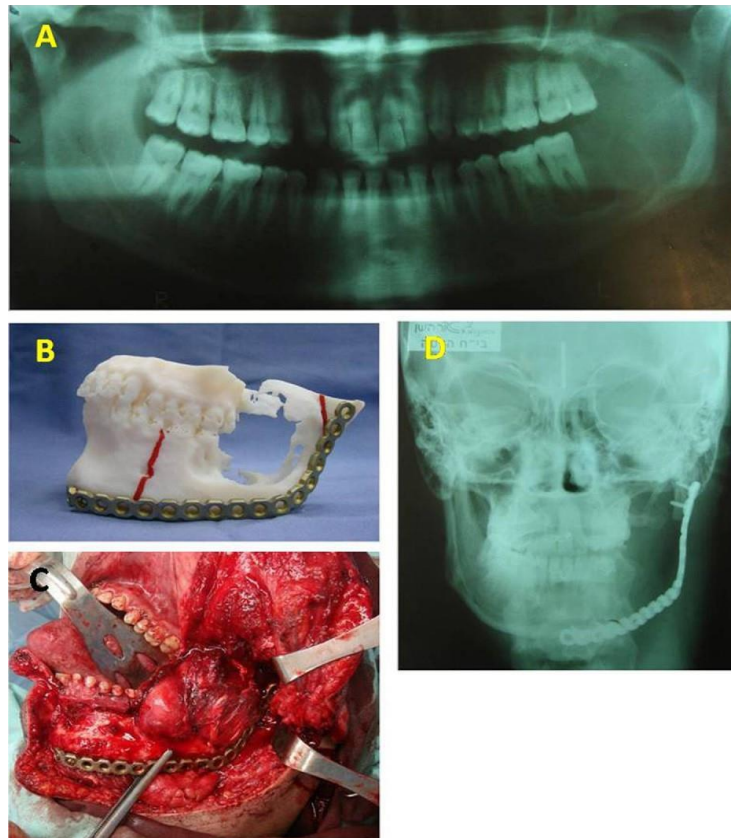


Figure 2.25: (A) Pre-operative CT scan (B) Printed model fitted with locking bone plated pre-contoured (C) Surgical attachment and (D) Post-operative CT scan showing symmetrical results (Cohen et al., 2009).

There are also uses for 3D printing for the musculoskeletal system such as production of models for patients with hard tissue abnormalities using CT data to better understand anatomical dimensions of the lesion (Tam *et al.*, 2012). Such models can also be utilised as a reference within the operating theatre (Singare *et al.*, 2004).

Electron beam melting (EBM), has been used to produce a titanium calcaneus prosthetic following total calcanectomy due to osteolytic lesion removal, designed specifically for that patient (Imanishi and Choong, 2015). This is a load bearing application hence structural strength and ability to withstand compressive forces are paramount to prosthesis success. EBM allowed flexibility of design such that load bearing struts could be solid titanium whilst the rest of the design could be hollow to reduce weight. In addition, small round holes could be produced on the implant surface both to promote tissue integration and as anchor points for attachment of the Achilles tendon, plantar fascia and spring ligament. Lastly, the

prosthetic was available within days, taking approximately two days to design, a day for printing and then two days for post-processing (Imanishi and Choong, 2015).

### 2.4.3.2. Soft Materials

Biofabrication, is a specific type of 3D printing used in tissue engineering and regenerative medicine where biological materials and biochemicals are used to produce organised, functional 3D structures to replace tissues and organs within the body (Murphy and Atala, 2014). When living cells are included within this, it is known as bioprinting. Due to the delicate nature of natural proteins and cells, many of the regular 3D printing technologies, such as SLS with its extreme heats, are inappropriate for biofabrication and bioprinting. As a result, three primary methods have emerged as seen in Figure 2.26. The inkjet and laser-assisted bioprinters are used to produce droplets of biological material whereas microextrusion bioprinters can dispense continuous streams.

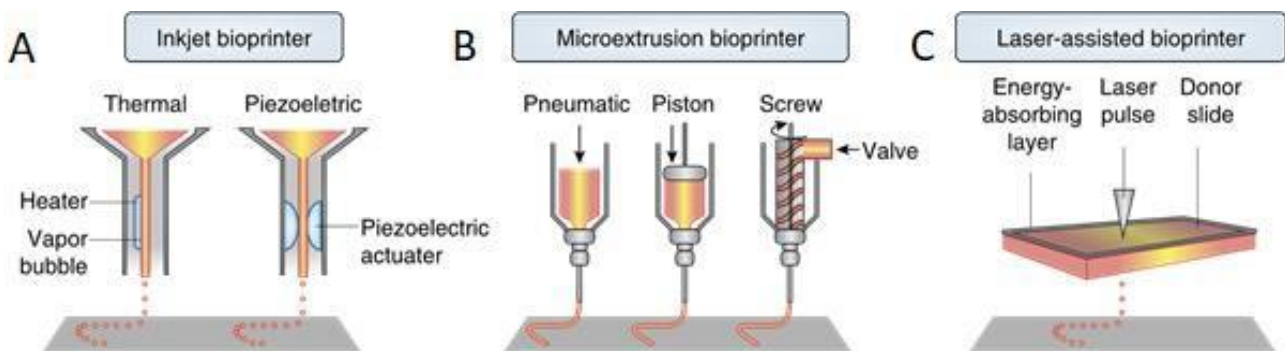


Figure 2.26: Bioprinting methods: (A) Inkjet bioprinting using thermal energy or piezoelectric actuators, (B) Microextrusion bioprinting using pneumatic, piston or screw driving forces and (C) Laser-assisted bioprinting controlled by laser (Murphy and Atala, 2014).

Biofabrication and bioprinting have the potential to improve the medical industry as many kinds of organ could theoretically be produced. By using autologous materials, complications with allogenic and xenogeneic materials including immune responses, inflammation and rejection could be avoided entirely thereby removing the need for lifelong immunosuppressant treatment (Schubert, van Langeveld and Donoso, 2014). In tissue regenerative medicine the following types of tissue have been studied in animal models: bone, cardiac (including valves), cartilage, liver, lung, neural, skin and pancreatic (Ozbolat,



Peng and Ozbolat, 2016). These animal models assess differentiation of cells *in vivo* and the function of implanted constructs however their long term functionality and performance is still a concern that needs to be evaluated before human clinical trials can begin (Ozbolat, Peng and Ozbolat, 2016).

The central problem of bioprinting and the replacement of human tissue is in reproducing their complex biomechanical properties which arise from the complex microarchitecture of ECM components and multiple cell types present (Murphy and Atala, 2014). For bioprinting to be successful many different steps must be considered as seen in Figure 2.27.

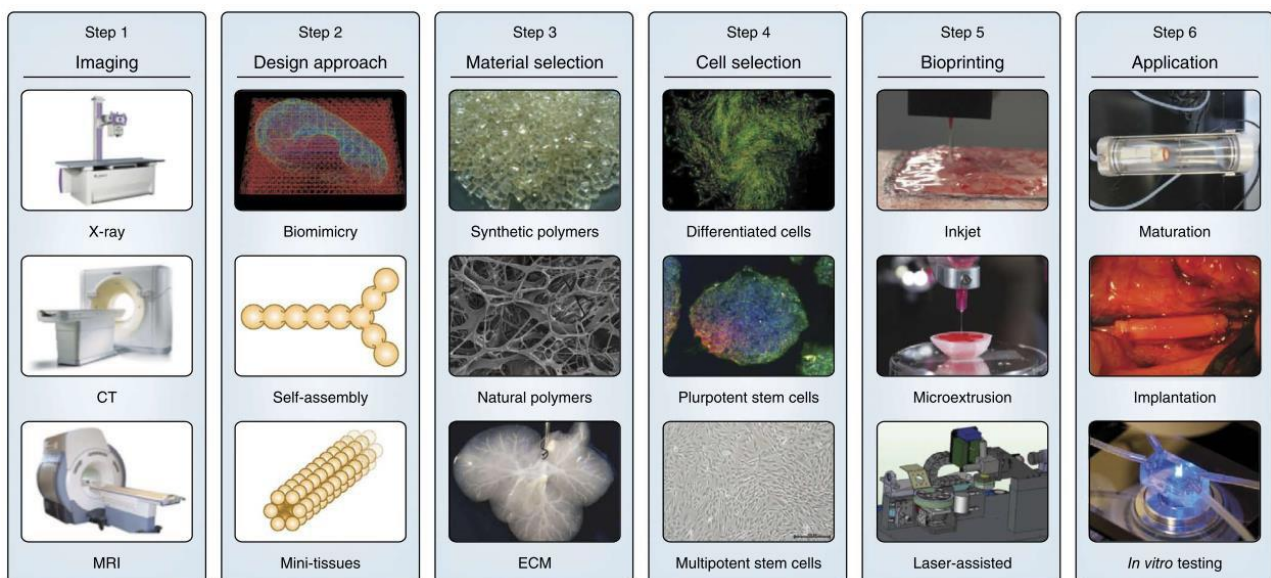


Figure 2.27: A typical 6-step bioprinting process: (1) Imaging the damaged tissue and its environment, (2) Design approach method, (3) Selecting the materials, (4) Selecting the cells, (5) Bioprinting method and (6) The application of the product either implantation (maturation may be necessary prior to this) or for *in vitro* testing (Murphy and Atala, 2014).

In general, 3D printing is emerging as a powerful tool within medicine and especially when used in accordance with patient imaging data which has been shown to improve clinical outcomes, educate trainees on delicate procedures and creation of patient-specific custom prosthetics (Marro, Bandukwala and Mak, 2016). Bioprinting also offers very interesting opportunities which could be used to offer novel solutions to modern day medical problems however significant work is required to develop these processes into clinical stage work.

## 2.5. Requirements for Proposed Biomaterials Approach to Treating Cleft Palate

The literature review revealed a number of different requirements that an ideal biomaterials approach should have to function correctly whilst successfully improving upon the current treatment methods. These are summarised below along with proposed concept ideas for this biomaterials approach.

- Oral and nasal cavity separation – This is the primary aim of all CP treatment methods from traditional surgical approaches to temporary approaches such as obturators (Burg et al., 2016). Unlike surgery, where flaps are raised with neighbouring tissue, a biomaterials approach would use exogenous biomaterials as the bulk material for a device to achieve said separation. An ideal solution would be to model an obturator-like device that corresponds with local geometry of the patient to only occupy the volume affected by the CP when implanted, thereby only occupying ‘missing’ tissue. This would restore function and patient oronasal geometries to those of a person unaffected by CP.
- Mechanical strength – Any implanted biomaterial device will be subject to forces from bodily functions such as sneezing, breathing, eating etc. and will need to be mechanically robust enough to retain positioning and integrity. An ideal outcome would be to engineer a material that matches the mechanical properties of the neighbouring soft tissue to achieve this. Additionally, an elastic material would allow the device to ‘flex’ with forces and then return to its original status after the mechanical stimuli has ceased (Chen et al., 2022).
- Fixation mechanism – As suturing has been linked to several disadvantages of traditional surgical methods such as scarring, it is important to avoid the use of sutures in securing the device in place (Fayyaz et al., 2018). Alternatives such as the usage of fibrin glue have previously been used for soft tissue adhesion and present an alternative approach which minimises bleeding and has the potential to reduce failure rate (Feldman &



Osborne, 2018). Fibrin glue also has the benefit of being a natural material whereas alternatives such as n-butyl-2-cyanoacrylate are synthetic and promote inflammation, so are only suitable for use *ex vivo*. Fibrin by comparison can be derived from non-related individuals or a patient's own blood to form either an allogenic or autogenic tissue glue (Panda et al., 2009).

- **Biocompatibility** – This is an extremely important characteristic of any biomaterials approach within bioengineering. When putting non-native materials inside the body, the effects of an implanted material need to be fully understood to ensure that a material is having an overall beneficial effect and does not pose a significant risk to patient health (Augst et al., 2006). The primary when using exogenous material is inciting an immune response which, depending on the severity, can lead to inflammation, fibrous encapsulation eventually implant rejection. A biomaterial-oriented approach will include a device that not only minimises immune response, but also acts as a scaffold to actively encourage patient's cells to migrate into the biomaterial. The aim would be for native cells to invade the scaffold, proliferate and remodel the scaffold over time to eventually generate new host tissue (O'Brien, 2011).
- **Biodegradability & degradation rate** – As host cells invade the material, a secondary aim of a biomaterials approach would be for the material to be fully biodegradable so that any originally implanted exogenous material is eventually completely replaced native tissue. The rate of degradation needs to be engineered to work synergistically with the rate that patient cells will invade and proliferate within the device. If the rate is too fast, the device will lose mechanical strength before cells invade, proliferate and remodel correctly to form new tissue. If it is too slow, the material may inhibit tissue generation. Previous studies have shown that similar scaffolds require up to 12 weeks for cell invasion and proliferation to occur (Maxson et al., 2019; Modulevsky et al., 2014). This is highly dependent on scaffold size, clinical requirements and a variety of other factors so the desired degradation timeframe will need to be validated. A material that is able to be altered to

extend or reduce degradation rates is therefore highly preferable.

- Device design – As previously mentioned, an ideal solution would be one where the device geometry occupies only the area affected by the cleft so that long-term, this would be regenerated as new tissue. Medical imaging data such as CT or MRI could be utilised in a CAD/CAM workflow to produce bespoke devices to provide unique geometries for each patient to ensure optimal obturator geometries (Leukers et al., 2005). The chosen 3D printing method would need to provide a suitable fidelity to allow for precise deposition of printed material which remains in-place post-printing.

### 3. Aims and Objectives

A review of the literature has shown that there is a clear clinical need for a novel strategy for treating children affected by CP. Whilst traditional surgical palatoplasties generally show acceptable results there is a small but significant number of cases that require secondary revision surgery due to ONF formation and dehiscence (Cohen *et al.*, 1991; Sadhu, 2009; Landheer, Breugem and van Mink Der Molen, 2010). Additionally, the trauma of invasive palatoplasty not only gives rise to an unacceptable distortion of the mid-face from scarring and abnormal growth but also makes delaying treatment a necessity for the child to be able to tolerating surgery, negatively affecting speech results (Katzel *et al.*, 2009). Obturators could provide a significantly less invasive treatment option that may then be used on patients of a younger age and give rise to improved speech results whilst avoiding scarring caused by using palatal flaps (Tibesar, Black and Sidman, 2009). At young ages cleft sizes, a significant risk factor in palatoplasty, are much smaller as the child has not grown hence there will also be a greater chance of successful repair (Parwaz *et al.*, 2009; Bye *et al.*, 2013).

Therefore, the aim of the project is to employ recent advancements in 3D printing technology to develop suitable alginate-based materials that can be 3D printed with high fidelity for potential use as palatal obturators. The individual objectives for the project were as follows:

- To investigate the chemical structure of different commercial alginate strains.
- To explore which alginate hydrogel compositions were suitable for 3D printing.
- To characterise the rheological viscoelastic properties of alginate hydrogels that are relevant to 3D printability.
- To test the fidelity of shortlisted hydrogels in 3D printing.

- To modify the physical properties of printed samples to create a mechanically viable obturator.

## 4. Materials & Methods

The following section details the materials that were used and the methodology. Figure 4.1 provides an overview for the flow of the experimental work. Both chemical and physical characterisation of alginate was essential to better understand advantages and limitations of 3D printing with sodium alginate through successive experiments. Proton nuclear magnetic resonance ( $^1\text{H}$  NMR) was used to explore chemical differences between alginate strains to select the most suitable one for this project. Optimisation of hydrogel composition was then performed to understand how physical properties changed between hydrogels of different alginate concentrations and primary-crosslinking amounts. Rheological characterisation of promising hydrogels was then undertaken to better understand the viscoelastic nature of these uncrosslinked (UC) and primary-crosslinked (PC) hydrogels. These were then used to 3D print a variety of geometries and the quality of this printing was reported on. The best composition was then used to create secondary- crosslinked and tertiary-crosslinked scaffolds, the mechanical properties of which were assessed.

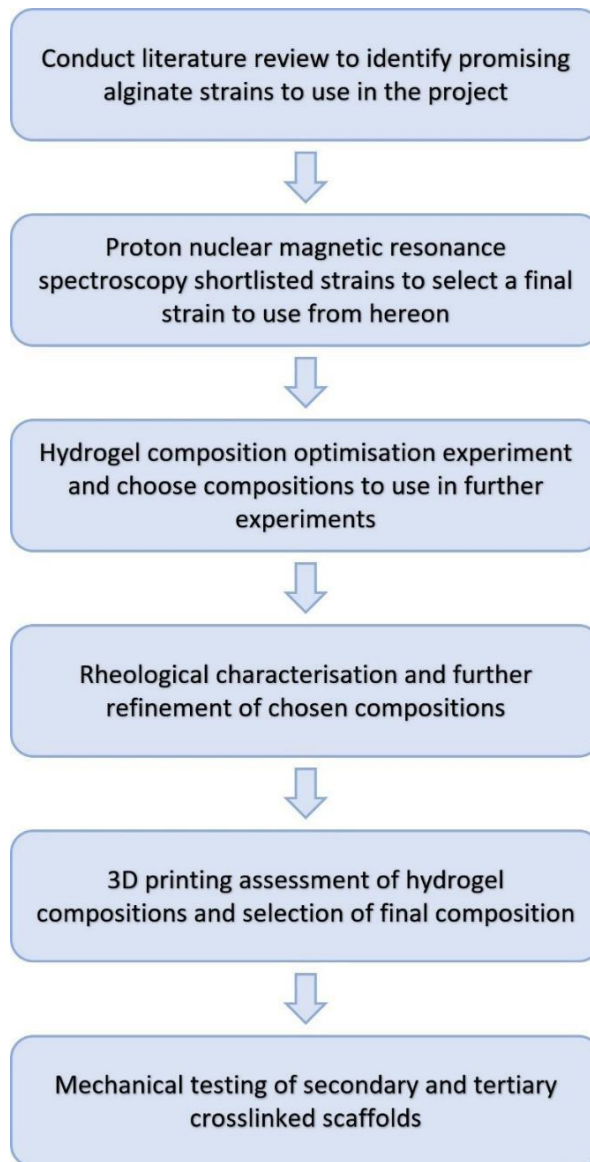


Figure 4.1: Experimental overview of the project.

## 4.1. Materials

All of the details for the commercial materials used in the project can be seen in Table 4.1.

Table 4.1: A list of all materials used in the project.

Material	Supplier and Code	Stock volume and concentration	Storage conditions
Alginate Strain 1	Sigma 180947	500 g	4 °C, out of direct sunlight
Alginate Strain 2	Sigma W201502	250 g	4 °C, out of direct sunlight
Alginate Strain 3	Sigma A2033	1 kg	4 °C, out of direct sunlight
CaCl <sub>2</sub>	Sigma C3306	500 g	20 °C, in a dry/cool place and well-ventilated area
Hydrochloric acid (HCl)	Sigma 2104	50 ml, 0.1 M	20 °C, non-metal container, tightly closed and well-ventilated area
Sodium Hydroxide (NaOH)	Fisher Scientific 10141860	1 l, 0.1 M	20 °C, tightly closed, in a dry/cool place and well ventilated
Deuterium Oxide (D <sub>2</sub> O)	Sigma 151882	50 ml	20 °C and tightly closed
Triethylenetetramine-hexaacetic acid (TTHA)	Sigma T7633	5 g	20 °C, tightly closed, in a dry/cool and well-ventilated area
70 % isopropanol	Sigma 563935	1 l	20 °C, tightly closed, in a dry place, well ventilated and keep away from heat

The 3D Printer that was used for this project was the Allevi 2 (Allevi) which can be seen in Figure 4.2 below. It was a pneumatically controlled printer that could operate at pressures from 1 to 120 psi and featured two extruders designed to fit 10 ml syringes. It boasted a print volume of 9 × 6 × 13 cm (702 cm<sup>3</sup>) alongside a precision of 5 μm in the X- & Y-axis and 1 μm in the Z-axis.

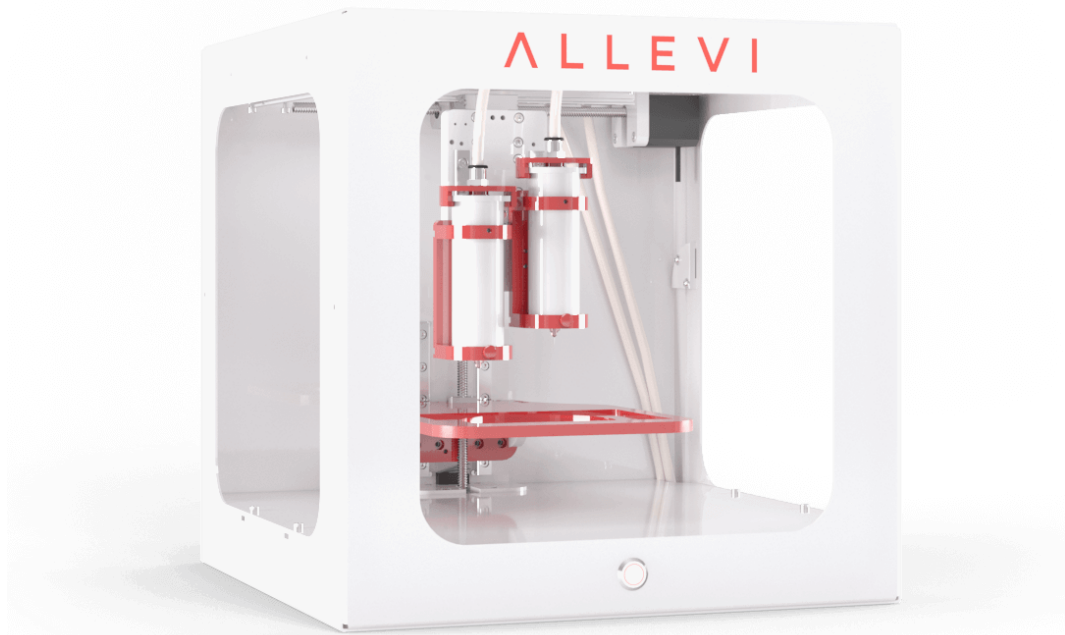


Figure 4.2: Allevi 2 3D Bioprinter (Allevi, 2022)

## 4.2. Hydrogel Preparation

Alginate was commercially available in salt form, most commonly as sodium alginate which readily dissolved in water to form aqueous sodium alginate, a naturally occurring hydrogel network. When dissolved, the alginate molecular chains spread out over the solution, increasing the viscosity and changing the appearance of the solution. The high water content of sodium alginate hydrogels allows them to mimic the structure of many soft tissues in the body which share this characteristic. Combined with alginate's biocompatibility and the many ways it can be modified to tailor specific physical or chemical needs, alginate has become the focus of much biomedical and regenerative research (Lee and Mooney, 2011). The principal way alginate hydrogels are enhanced are by crosslinking their individual molecular chains together, most commonly through ionic gelation using divalent cations such as  $\text{Ca}^{2+}$ . This, however, was limited by rapid gelation which must be controlled if a homogenous hydrogel is going to be produced, something critical to the reliability and mechanical stability of 3D prints.



## 4.2.1. Aqueous Sodium Alginate

Whilst sodium alginate readily dissolves in water at a room temperature, in practice 'clumps' form and areas of undissolved alginate can persist. For this reason, a mechanical stirrer was used with a 30 mm diameter pitched blade impeller. 200 ml of deionised water was added to an 80 mm diameter Pyrex beaker. This ratio of impeller diameter, beaker diameter and water volume were important as it ensured an axial flow throughout the contents of the beaker for proper mixing and homogenous hydrogel production.

The required amount of sodium alginate was measured onto a weighing boat using a balance (+/-0.1 mg). The stirrer was set to 1000 rpm to create a vortex in the beaker and then the alginate added to the centre of the vortex to disperse. After 5 minutes, the stirrer speed was set to 300 rpm for a further 16 hours to allow the alginate to completely dissolve into a homogenous solution. If sodium alginate was added when a vortex was not present, large masses of alginate would aggregate and fail to dissolve. A lid was added to minimise the effects of water evaporation from the beaker and the beaker was held in place with a clamp to prevent it from spinning as alginate dissolved and viscosity increased.

There was an upper limit to the concentration of aqueous sodium alginate that could be produced using this method as solutions would become too viscous which would allow undissolved sections of the alginate powder to persist. The exact concentration this occurred varied between the different sodium alginate varieties but as an example, the medium viscosity (A2033, Sigma) could not be produced at concentrations over 10 % (w/v).

After 16 hours, the aqueous sodium alginate solutions were transferred to 50 ml conical centrifuge tubes and centrifuged at 2500 × g for 60 minutes at 20 °C to remove trapped air bubbles from the hydrogels. These were then removed and stored refrigerated at 4°C until required for experiments. As a precaution, aqueous sodium alginate solutions were kept for a maximum of 4 weeks post-hydration as microorganisms could be present. When needed

for experiments, solutions were removed from the fridge 30 minutes prior to allow them to return to room temperature, 20 °C.

#### 4.2.2. Primary Crosslinking of Alginate Hydrogels

Individual UC alginate chains can crosslink together when treated with divalent cations such as  $\text{Ca}^{2+}$  to form PC hydrogels with different characteristics. This ionic crosslinking has a time dependent gelation mechanism, so it was crucial to ensure an effective mixing technique was used to avoid areas with different degrees of crosslinking within hydrogels, heterogeneity.  $\text{CaCl}_2$  was used as the primary-crosslinking agent although when added to aqueous sodium alginate post-production or dissolved in the water prior to alginate mixing these yielded poor results and a non-homogenous hydrogel.

A separate solution of  $\text{CaCl}_2$  was therefore produced.  $\text{CaCl}_2$  (147.01g/mol) was measured out using a Mettler AJ100 balance ( $\pm 0.1$  mg) and added to a Pyrex beaker containing 100 ml of deionised water and gently shaken for thirty seconds until the powder had fully dissolved. Solutions were produced in concentrations between 10 and 100 mM.

To mix the aqueous sodium alginate and crosslinker solution, a method was devised that used two half-filled 10 ml Luer lock syringes, one containing 5 ml of crosslinker solution and one containing 5 ml of aqueous sodium alginate. The crosslinker solution was easily drawn into the syringe however the high viscosity of aqueous sodium alginate meant that a spatula was required to load the syringe from the rear. Luer lock caps were then attached and the syringes were centrifuged with tips facing up at  $2500 \times g$  for 30 minutes at 20 °C to remove bubbles.

Both syringes were then refrigerated at 4 °C for at least 1 hour before mixing to lower solution temperatures and thereby decrease crosslinking speed. These were joined with a female-to-female Luer lock connector taking care not to re-introduce any air bubbles to the system

and then rapidly mixed 'back and forth' repeatedly to combine the two solutions. Rapid mixing was emphasised as crosslinking was time dependent and if the solution were not mixed sufficiently this would create heterogeneous areas with greater crosslinking and *vice versa*. This was done 100 times over 90 seconds to create the final product, a 10 ml PC hydrogel solution with an alginate and  $\text{CaCl}_2$  concentration of half its constituent parts (due to a 1:1 dilution). This process can be seen detailed in Figure 4.3.

The final PC product was transferred to one syringe, fitted with a Luer cap and then allowed to rest for 30 minutes prior to use in any experiments to allow the material to rest.

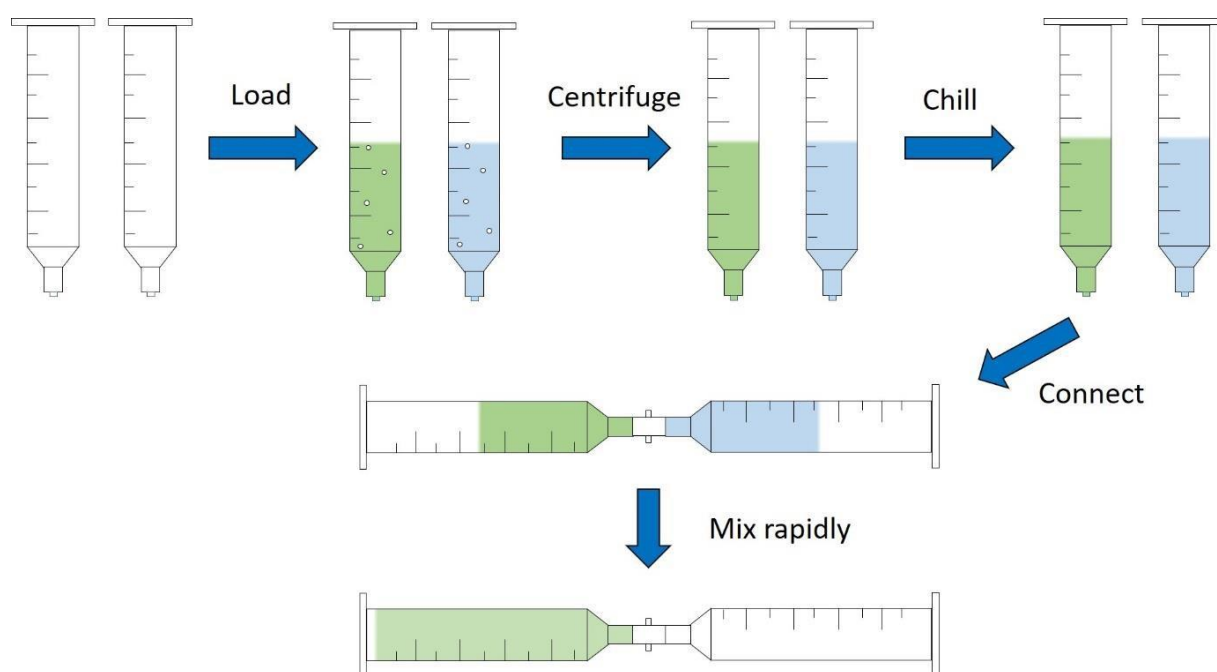


Figure 4.3: Process of producing homogenous primary-crosslinked hydrogels (light green) with aqueous sodium alginate (dark green) and calcium chloride crosslinker solution (blue).

The ideal volumes for each constituent part were 5 ml each which meant that, due to the previously mentioned limits of dissolution, only hydrogels up to 5.0 % w/v could be produced for the medium viscosity alginate strain. By using 6 ml of 10 % w/v alginate and 4 ml of crosslinker solution (with corresponding concentrations) this allowed an expanded production up to 6.0 % w/v which improved the scope of PC hydrogels that could be assessed. Using more unequal volumes would eventually lead to problems with homogeneity as volumes would not mix sufficiently. Also, the use of increased crosslinker

concentration would increase speed of crosslinking but at the ratio of 6 : 4 there was no noticeable compromise in the quality of product.

It was important to inspect the final product of this crosslinking method as homogeneity of the PC hydrogel and general quality control was vital. Firstly, a visual inspection was performed as aqueous sodium alginate has a green tint whereas the crosslinking solution was transparent. Any differences in colour throughout the volume would be a clear indicator of areas with differing amounts of crosslinker and alginate. Additionally, the final volume was checked for bubbles which would create differences in density, a further source of heterogeneity.

A simple test for homogeneity was to gently extrude the syringe contents from one syringe to another with the Luer lock connector at the end of mixing to feel if the same amount of force was required throughout the exchange. This was because areas of uneven crosslinking had different viscosities which were easily felt when extruded through a small channel like the diameters of the dispensing tip and Luer lock connector. It was rare that any PC hydrogels failed these inspections as the crosslinking method was reliable and robust however any products that did were discarded and reproduced. PC samples were produced with alginate concentrations from 0.5 – 6.0 % (w/v) alginate and 5 – 50 mM CaCl<sub>2</sub>.

### **4.3. Proton Nuclear Magnetic Resonance Spectroscopy of Alginate**

Limited Information was provided from suppliers about the chemical composition of alginate strains so <sup>1</sup>H NMR was used to determine the chemical composition. ASTM F2259 was used as the standard for this method. Three different strains of sodium alginate that had previously been cited for use in 3D printing were used: 180947, W201502 and A2033 (Sigma). A 10 ml, 1 % (w/v) solution was prepared for each one using the technique

previously described in Section 4.2.1.

0.1 M of HCl was pipetted into each solution until a pH of 5.6 was recorded with a pH meter that had been calibrated beforehand. When swapping between samples, the pH meter was rinsed with deionised water to avoid cross contamination. The samples were then added to a water bath set to 95 °C for 1 hour. HCl was added until the pH reached 3.8 and returned to the water bath for a further 30 minutes. 0.1M of NaOH was then added to return the samples to a pH of between 7 and 8.

The samples were put into a -80 °C freezer for 30 minutes to pre-freeze them before freeze drying to avoid spillage when they boil in vacuum conditions. Prior to freeze-drying lids were removed from the samples. The freeze dryer lid was then closed and the vacuum pump turned on. After 5 minutes the generated vacuum reached a steady pressure of -0.95 bar and samples began to bubble. The samples were left under vacuum for 16 hours overnight. The next day 5 ml of D<sub>2</sub>O was added to each sample and gently mixed for a few minutes using a spatula until completely dissolved. The samples were then freeze dried overnight again.

The next day, 10 to 12 mg of each dried sample was weighed out and added to new, individual containers. 1 ml of D<sub>2</sub>O was then added and a spatula used again to completely dissolve the material. Separately, 14.83 mg of TTHA was dissolved into 0.1 ml of D<sub>2</sub>O to form a 0.3 M solution. 28.57 µl of this solution was then added to each of the 1 ml alginate samples.

<sup>1</sup>H NMR data was acquired using a 500 MHz Bruker AVIIIHD 'Millicent'. A full list of acquisition parameters can be seen in Table 10.1 in the appendix. Data was then loaded into MestReNova software for processing and analysis. Within MestReNova, an exponential line broadening setting of 0.3 Hz was selected and a zero-fill setting of 64k that allowed for a spectrum of 65536 data points. MestReNova automatically applies a Fourier transform to

convert the recorded free induction decay signals into NMR spectra. Phase correction was then applied using the biggest peak on each spectrum as the respective pivot points and automatically determined zero-order and first-order values which were deemed suitable. Baseline correction was then performed using the Whittaker smoother method using automatically determined filter and smoothing factor parameters which was satisfactory. A range of 4.3 – 5.3 ppm was then selected for further analysis. Peak labelling was completed automatically using the MestReNova function which was inspected for errors and any adjustments made to the location of the peaks and their corresponding intensities. After labelling, signal intensities of each peak were recorded.

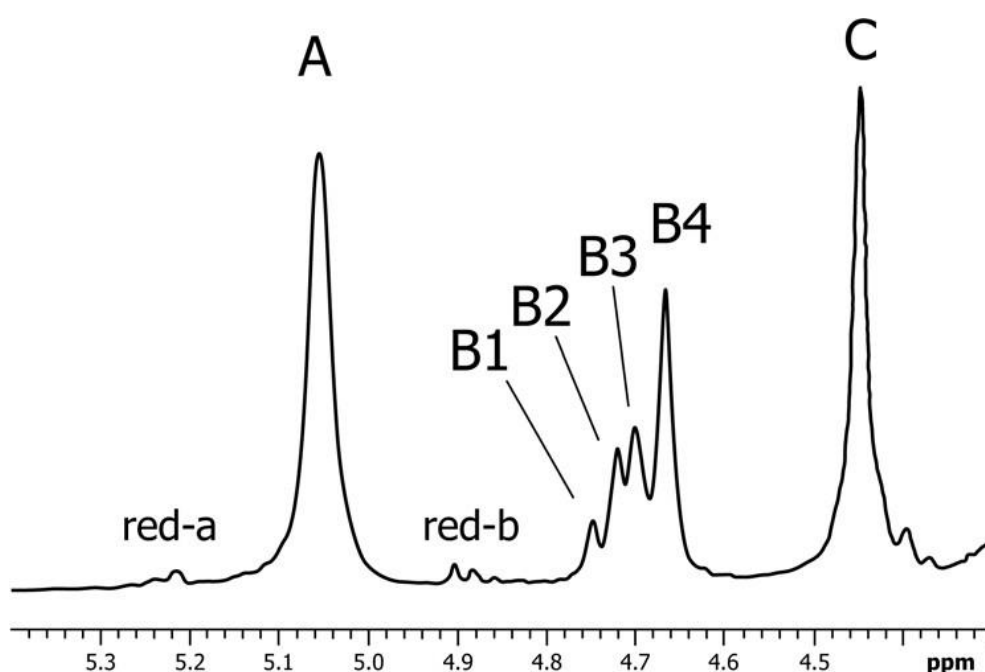


Figure 4.4: Example  $^1\text{H}$  NMR spectra of alginate with labelled peaks. Source: (ASTM F2259-10, 2012).

Figure 4.4 shows the expected resultant spectra of alginate. Each labelled peak was a distinct proton signal that corresponds to a specific part of an alginate chain sequence which is comprised of mannuronic acid and guluronic acid. Sequences were represented the following way: MMM (mannuronate only), GGG (guluronate only) and GMG/MGM (alternating blocks). Where a signal or variable is attributed to an individual element of a specific sequence, this is denoted using underlining.

Signal A was H-1 of any G, signal B1 was H-5 of GGM, signal B2 was H-5 of MGM, signal B3 was H-1 of MG, signal B4 was H-1 of MM and signal C was H-5 of GG (ASTM F2259-10, 2012). Red- $\alpha$  and red- $\beta$  correspond to alpha and beta reducing ends respectively although these extend beyond the scope of this project. Using these signals, variables were produced with the following equations that correlate to structural composition:

$$G = 0.5(A + C + 0.5(B1 + B2 + B3)) \quad \text{Equation 4.1}$$

$$M = B4 + 0.5(B1 + B2 + B3) \quad \text{Equation 4.2}$$

$$GG = 0.5(A + C - 0.5(B1 + B2 + B3)) \quad \text{Equation 4.3}$$

$$MG = GM = 0.5(B1 + B2 + B3) \quad \text{Equation 4.4}$$

$$MM = B4 \quad \text{Equation 4.5}$$

$$GGM = MGG = \frac{B1(0.5(B1 + B2 + B3))}{B1 + B2} \quad \text{Equation 4.6}$$

$$MGM = \frac{B2(0.5(B1 + B2 + B3))}{B1 + B2} \quad \text{Equation 4.7}$$

$$GGG = GG - GGM \quad \text{Equation 4.8}$$

These variables were then used to calculate the true percentage values of constituent parts of alginate:

$$\%G = \frac{G}{M + G} \quad \text{Equation 4.9}$$

$$M = \frac{M}{M + G} \quad \text{Equation 4.10}$$

$$\%GG = \frac{GG}{M + G} \quad \text{Equation 4.11}$$

$$\%MG = \%GM = \frac{MG}{M+G} \quad \text{Equation 4.12}$$

$$\%MM = \frac{MM}{M+G} \quad \text{Equation 4.13}$$

$$\%GGM = \%MGG = \frac{GGM}{M+G} \quad \text{Equation 4.14}$$

$$\%MGM = \frac{MGM}{M+G} \quad \text{Equation 4.15}$$

$$\%GGG = \frac{GGG}{M+G} \quad \text{Equation 4.16}$$

Additionally, the average block lengths of M-blocks, G-blocks and G-blocks excluding singlets (i.e. MGM and GMG) can be calculated (Grasdalen, Larsen and Smisrod, 1981):



$$N_G = \frac{\%G}{\%GM} \quad \text{Equation 4.17}$$

$$N_{G > 1} = \frac{\%G - \%M}{\%GM} \quad \text{Equation 4.18}$$

$$N_M = \frac{\%M}{\%MG} \quad \text{Equation 4.19}$$

Equations 4.1 to 4.19 were then applied to the peak intensity data collected within MestReNova to form quantified results of the chemical composition and sequencing of the three alginate strains as per (ASTM F2259-10, 2012).

## 4.4. Hydrogel Composition Optimisation

A2033 medium-viscosity alginate was selected for use in future sections of the project. Reported compositions for hydrogels that are suitable for such 3D printing vary considerably either due to strain differences, batch variation or different success criteria between authors. Compositions of both UC and PC A2033 alginate hydrogels therefore needed to be evaluated for their suitability in 3D printing. A hydrogel composition optimisation experiment was performed to determine a broad understanding of how physical properties changed with differing sodium alginate and CaCl<sub>2</sub> concentrations.

### 4.4.1. Experimental Design

Hydrogels were produced as per Section 0 and were subdivided into two groups: UC and crosslinked. There were 12 UC samples between 0.5 % and 6.0 % w/v sodium alginate concentration. Crosslinking solutions were produced between 10 and 125 mM to enable production of PC hydrogels with 10 different concentrations between 5 – 50 mM. To test every combination of alginate and CaCl<sub>2</sub> concentration would require 132 samples: 12 UC and 120 PC possibilities. For that reason, a fractional factorial experimental design was

employed to decrease the workload to a practical level without any meaningful loss of understanding of how these variables interact (Gunst and Mason, 2009).

Per individual alginate concentration, every other crosslinking concentration was tested. When testing the following alginate concentration, the alternate concentrations were then used to form a checkerboard pattern as seen in Table 4.2. UC samples were tested individually without any omissions as they were a sub-group with fewer variables which did not meet the same criteria for the fractional factorial experimental design method.

Table 4.2: Chosen samples for the hydrogel composition optimisation experiment as per the fractional factorial experimental design.

		Calcium Chloride Concentration (mM)										
		0	5	10	15	20	25	30	35	40	45	50M
Alginate Concentration w/v (%)	0.5	Yes	Yes	-	Yes	-	Yes	-	Yes	-	Yes	-
	1.0	Yes	-	Yes	-	Yes	-	Yes	-	Yes	-	Yes
	1.5	Yes	Yes	-	Yes	-	Yes	-	Yes	-	Yes	-
	2.0	Yes	-	Yes	-	Yes	-	Yes	-	Yes	-	Yes
	2.5	Yes	Yes	-	Yes	-	Yes	-	Yes	-	Yes	-
	3.0	Yes	-	Yes	-	Yes	-	Yes	-	Yes	-	Yes
	3.5	Yes	Yes	-	Yes	-	Yes	-	Yes	-	Yes	-
	4.0	Yes	-	Yes	-	Yes	-	Yes	-	Yes	-	Yes
	4.5	Yes	Yes	-	Yes	-	Yes	-	Yes	-	Yes	-
	5.0	Yes	-	Yes	-	Yes	-	Yes	-	Yes	-	Yes
	5.5	Yes	Yes	-	Yes	-	Yes	-	Yes	-	Yes	-
	6.0	Yes	-	Yes	-	Yes	-	Yes	-	Yes	-	Yes

This checkerboard formation meant that each excluded sample would be neighboured exclusively by four samples that had been tested, reducing the severity of any individual gap. This meant that any potential loss of overall understanding of the sodium alginate and CaCl<sub>2</sub> relationship was minimised. In total 72 samples were tested: 12 UC and 60 PC as seen in Table 4.2.

#### 4.4.2. Visual Assessment

The first stage of the experiment was to produce all the required samples as per the methods described in Section 4.2. The samples were allowed to rest for 30 minutes and then visually assessed for any undesired characteristics such as presence of solids, undissolved sediment or distinct colours/phases throughout the volume. Either of these qualities would indicate severe heterogeneity which would adversely affect 3D printing as a constant pressure was supplied, under the assumption that the printed material was homogenous. Regions of higher or lower viscosities would reduce or increase the flow rate of extrusion, causing incorrect amounts of material to be deposited which would greatly diminish print fidelity. Samples were grouped based on alginate concentrations and group photos were taken using a digital camera with an 18 – 55 mm lens.

#### 4.4.3. Extrudability

The next stage was to assess how well these various hydrogel compositions could be extruded through a narrow-gauged nozzle, commonly a dispensing tip, an essential requirement for 3D printing suitability. All original 72 samples were tested.

The Allevi 2's air compressor was turned on and allowed to reach capacity whilst the controlling computer was booted up. Bioprint (Allevi software) was launched and used to connect to the printer then the X-, Y- and Z-axis motors were individually calibrated using the 'home' functions. Next, samples were taken to the printer and the syringe plungers were carefully removed, taking care not to disturb the hydrogels within. The Luer caps were then removed and replaced with a 0.25" long, 22-gauge dispensing tip with an internal diameter of 0.41 mm (Intertronics FIS5601078). The open-ended syringes were connected to the compressor air-supply, loaded into the extruder assembly and secured using the upper locking mechanism. The nozzle was then positioned 10 mm above the print bed and paper towel laid over it to collect extruded material.

The extruder was turned on and the pressure functions used to incrementally toggle the pressure up or down as required to produce a fibre flow-rate of approximately  $10 \text{ mms}^{-1}$  (or equivalent volume within a droplet) or until the pressure limit of 100 psi was reached. Samples that did not achieve sustained flow by this pressure limit were marked as non-extrudable. For samples that achieved flow, extrusion was permitted for 60 seconds to observe if flow varied during this time, indicating differing localised properties within the bulk material, after which extrusion was halted. Specific signs of this were observable differences in flow rate, temporary blockages or sputtering. Samples that displayed any of these characteristics were labelled as unstable flow whereas if no changes were observed they were labelled as stable flow.

#### 4.4.4. Extrusion Form

Another material requirement was the ability of extruded material to form distinct fibres so that high accuracy and resolution can be achieved. However, liquid-like materials such as some weaker hydrogels were prone to forming droplets due to water cohesion that adhere together and 'blob up'. 14 samples that were labelled as non-extrudable from Section 4.4.3 were excluded as they could not reliably be used with Allevi 2. Additionally, 7 unstable-flow samples were further excluded as their heterogeneity would produce over/under-extrusion as weaker/stronger sections of the material approach the nozzle. The remaining 51 stable flow samples shown in Figure 5.4 were tested for their extrusion form.

The previous experimental setup from Section 4.4.3 was retained, the dispensing tip was wiped clean and extrusion was turned on again. Focus was now on observing the material at the dispensing tip specifically, immediately post-extrusion. Extrusion was toggled 'off'

and 'on' over the course of 20 seconds and the dispensing tip was routinely cleaned to confirm the form was consistent. A clean dispensing tip was important as excess material at the tip may prevent further extrusion or alter the extrusion form. Observation of a thread or loop hanging from the tip post-extrusion indicated a solid-like fibre form whereas material pooling (forming a spherical or tear-drop shape at the dispensing-tip) was evidence of a liquid-like form. Observations of these extrusion forms were recorded, further extrusion halted and then the extrusion pressure returned to the original value.

#### 4.4.5. 3D Printed Stress Test

During this part of the hydrogel composition optimisation experiment, samples were used to 3D print a 'stress test' model. 3D printing is, by definition, a layer-by-layer manufacturing process hence it was imperative that any printing material must form and retain distinct layers. Stress tests contain purposefully difficult-to-print geometries such as overhangs and bridges that provide minimal support which may lead to slumping or collapse of deposited material.

The steps below outline the typical start-to-finish 3D printing process including STL design, G-code generation and operation of the Allevi 2 bioprinter used in this project. Following this, the 51 previously mentioned hydrogel compositions that exhibited stable flow were used to 3D print this stress test. The outputs from this stress test were the extrusion pressure required to print each sample consistently and the layer formation & retention of the printed stress test.

##### 4.4.5.1. STL Design

Fusion 360 (Autodesk) was the software used to create any models that were required during the project. A sketch was first used to create a 2-dimensional (2D) outline for the base shape of the model which could then be expanded into a 3D shape. Any necessary modifications were then applied to create the finished 3D model. The model was then

exported as an STL file using Fusion 360's high-quality settings. This was important as an STL is only ever an approximation of the true surface geometry of a model. Hence, by maintaining high settings, minimal dimensional accuracy was lost in the output STL file.

A lattice design was chosen as the design for the hydrogel composition optimisation stress test. Individual rectangular lines were created that were 20 mm long and 0.5 mm wide. Five of these were equally spaced 1.875 mm apart across a 10 mm segment in parallel as seen in Figure 4.5A and then extruded by 0.2 mm to form the first layer. 5 copies of this were placed on top of each other in a sequential perpendicular layout to form the final lattice design as seen in Figure 4.5B. This model was then exported from Fusion 360 into an STL file for use in other 3D printing applications.

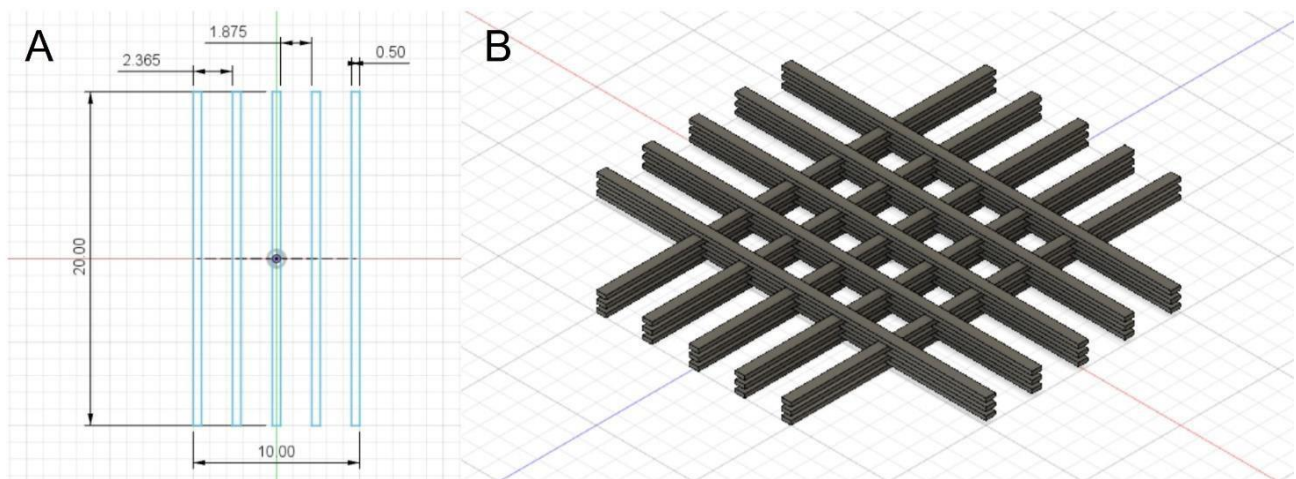


Figure 4.5: A 2D sketch of a single layer of the lattice design showing five individual, unconnected straight segments that run parallel. The final design of the 3D lattice structure which featured six layers, each 0.2 mm tall.

#### 4.4.5.2. G-Code Generation

Repetier-Host (Hot-World GmbH & Co. KG) was used as the primary software for managing 3D printing which included Slic3r (Alessandro Ranellucci) as the slicer software. Slicing software combines the STL file geometry and several user-defined parameters to produce a series of individual printer commands that 3D printers utilise, known as G-code. This G-code includes commands such as axis movement, extrusion rates and temperature control. Over time, this series of commands causes the 3D printer to deposit material line- by-line

and layer-by-layer until the print is completed.

Repetier-Host was used to import the previously produced lattice STL which was then orientated correctly and the size checked. If multiple objects were being printed simultaneously, they would be arranged so that there was sufficient space between them. Within the embedded Slic3r tool, the layer height was set to 0.2 mm, infill to 100 % and print speed to 10 mms<sup>-1</sup>. As previously mentioned in Section 4.4.3, a 0.5" long, 22-gauge dispensing tip was used which had an internal diameter of 0.41 mm. To complement this, a line width of 0.5 mm was also chosen.

Once slicer settings had been chosen, slicing was performed and the G-code was visualised within Repetier-Host. The G-code was evaluated to confirm the commands were as intended and that no errors were present. If changes or corrections were required these were performed with Repetier-Host and Slic3r and slicing performed again. G-code was then exported and saved.

#### **4.4.5.3. Operating the Allevi 2 Bioprinter**

Before printing could commence, the chosen hydrogel composition needed to be loaded into the printer. The 10 ml syringes that they were produced and stored within (Section 4.2.2) had their plunger components removed. By using Luer lock caps on the syringes, air bubbles were not able to enter the syringe as this occurred or disturb the print material. The pneumatic supply hose was then attached to the syringe before it was inserted into the syringe sleeve on the printer and locked in place. The air compressor was then turned on and allowed to reach capacity whilst the dispensing tip was attached to the syringe.

The chosen printing surface was then loaded onto the Z-platform. The Allevi 2 was designed to be used with well plates and petri dishes however those tested were found to have warped surfaces that did not present a level surface which would be detrimental to printing. For that reason, bespoke acrylic inserts were designed and produced to perfectly fit the Z-

platform and create a level surface (127 × 85 × 5 mm, 3 mm radius rounded corners).

Once set up, the Allevi 2 was controlled using Bioprint. Once this was connected to the 3D printer, the X-, Y- and Z-axis motors were calibrated *via* a 'zeroing' process. An extruder 'calibrate' function was executed to centre the X- and Y-axis over the Z-platform. Then, using the movement controls for the Z-axis, the Z-platform was raised until the end of the dispensing tip only just touched the acrylic insert print surface lightly. Here the 'update' and 'calibrate' functions were used to save this positioning and finish spatial calibration. It was vital to 3D printing efficacy to correctly complete this so extra caution was always taken during this step. Each time a new syringe was added, extruder calibration was repeated.

Extrusion pressure and temperature were then set. The previously produced G-code was then uploaded to Allevi Bioprint and initiated. It was good practice to watch deposition of the first few layers of printing to ensure that everything was functioning correctly. Once a print had been completed, acrylic inserts were carefully removed to not disturb printed material and taken to the following steps of the experiment. An insert could later be re-used after a thorough clean with 70 % isopropanol and being allowed to dry.

#### 4.4.5.4. **Extrusion Pressure**

As per the Section 4.4.5.3, the Allevi 2 was setup syringes with different hydrogel compositions were loaded up and calibrated. Extruder temperature was set to 20 °C whilst extruder pressure was set to individual values that corresponded to an approximate flow rate of 10 mms<sup>-1</sup>, previously measured in Section 4.4.3. Manual extrusion was performed for approximately 10 seconds to prime the dispensing tip with material. This was important as the dispensing tip introduces some air to the system which was unavoidable.

As the previously established extrusion pressure was only an approximation for a flow rate of 10 mms<sup>-1</sup>, it was expected that over-extrusion or under-extrusion would occur at this stage which needed to be corrected. Visual inspection of extruded filaments during printing was



used to determine an appropriate flow rate. Low pressure during printing was characterised by noticeably thin or stretched lines. In extreme cases, intermittent extrusion occurred which resulted in a disrupted line formation. In contrast, a high pressure would produce globular, rounded lines that exceed the planned deposit area, potentially leading to a 'ploughing' effect. It was important to establish a correct extrusion pressure as incorrect amounts of deposited material would otherwise incorrectly indicate poor layer formation and retention.

The extrusion pressure was modified empirically during initial trial prints of the lattice design until the flow rate was correct. This was necessary to provide consistent conditions across the many samples so that comparisons could reliably be made. This pressure was recorded for each sample and then a final lattice structure printed with the correct settings.

#### **4.4.5.5. Layer Formation and Retention**

A lattice stress test 3D print was executed for each hydrogel composition using their corrected extrusion pressure as per Section 4.4.5.4.

A photography area had previously been prepared to capture image of 3D printed stress tests for analysis. A lightbox was setup overhead and a black cardboard paper used on the work surface to use as a background. A digital camera was setup with an 18 – 55 mm lens along with a 55 mm polarising filter to help contrast the semi-transparent hydrogels and reduce glare from the acrylic inserts.

As soon as a print completed, a timer was started and the acrylic insert was gently removed and taken to the photography area to not disturb the printed structure, whilst being observed for changes. Using a timer ensured that observations could be made at referenced times after print completion. Samples were graded on if clearly distinct layers could be seen or not on the printed structure. One label was applied if distinct layers were not seen at any point after print completion. Two other labels were applied if distinct layers were initially seen after printing however these merged after either  $< 2$  s or between 2 – 10 s. A final label was given

to samples where distinct layers were seen and did not merge for the 10 s observation period. Pictures were taken in an orthographic style of each sample 10 s after print completion for later reference.

## **4.5. Rheology**

Of the 72 samples initially tested within the hydrogel composition optimisation, 7 of these were selected for rheological characterisation. UC 1 %, 3 % and 5 % were chosen to observe how different concentrations of uncrosslinked alginate behave. PC 2 %/30 mM, 3 %/30 mM, 4 %/30 mM and 5 %/30 mM were also chosen as diverse results had been found at this CaCl<sub>2</sub> concentration, particularly in the layer formation and retention section. Using these samples would therefore continue to test from a large range of the overall properties of the previous sample pool.

### **4.5.1. Introduction**

Rheology is the study of flow or deformation of a material which can be used to measure the viscoelastic properties of materials that were candidates for 3D printing. A popular method used to obtain rheological data is to use a rotational rheometer, such as the Anton Paar Physica MCR 301 which was used in this project (Figure 4.6).



Figure 4.6: Anton Paar Physica MCR 301 with a 50mm plate-plate measuring system attached in the raised position.

Rheometers can be configured with a variety of measuring systems that have different geometries which induce shear forces on different planes within a sample (Figure 4.7). Each configuration is comprised of a stationary component that typically connects to the rheometer frame and a kinetic component, or measuring system, that connects to the upper housing of the rheometer where the majority of the instrument's sensors are housed and forces measured. A sample is loaded between the stationary and kinetic parts, a shear force is applied through movement of the kinetic component and corresponding forces are measured and then outputs are calculated from that.

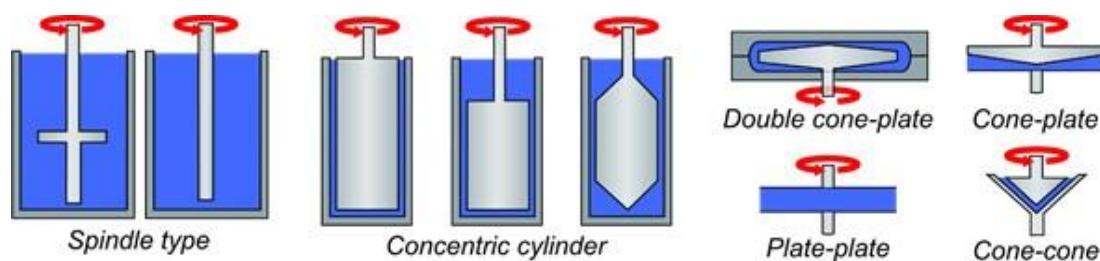


Figure 4.7: Different rotational rheometer configurations and their subsequent stationary and kinetic component variations (Martin, 2017)

Deciding which configuration and measuring system to use largely depends on the consistency of the sample being tested although other limitations such as the amount of sample available may also play a role. As detailed in Figure 4.8, large surface-area configurations such as double-gap and concentric cylinder are generally reserved for low-viscosity liquid samples. Whereas solid rectangle fixture, Sentmanat extensional rheology and universal extensional fixture techniques are employed for testing solids. Between these two polars lie the varying degrees of viscoelastic materials which generally recommend cone-plate (CP) and plate-plate (PP) configurations. Generally, the lower the sample viscosity, the larger the testing surface of the measuring system should be to maximise the signal to noise ratio (SNR) so that valid data can be collected reliably. However, the recommended diameter of measuring system also decreases as sample viscosity increases to prevent the rheometer becoming jammed by excessive resistant forces.

Low-viscosity liquids	Viscoelastic liquids	Melts	Paste-like materials	Gel-like materials	Soft solids	Reactive systems	Solids
almost 100 % liquid		←—————→				almost 100 % solid	
Rotation	Rotation	Rotation	Rotation				Extension
Oscillation	Oscillation	Oscillation	Oscillation	Oscillation	Oscillation	Oscillation	Torsion
DG, CC	CP & PP (50-25)	CP 25-3 & PP 25	CP & PP (25-50)	CP & PP (25-50)	PP 25	PP 15	SRF, UXF
CP & PP (60) Ti	DG or CC	CP 35-3 & PP 35	Special	DG, CC	PP 15		SER

Figure 4.8: Suitability of configurations and measuring systems for different sample consistencies. Numbers represent diameters in mm, CP = Cone-plate, PP = Plate-plate, DG = Double-gap, CC = Concentric Cylinder, SRF = Solid Rectangle Fixture, SER = Sentmanat Extensional Rheology and UXF = Universal Extensional Fixture (Anton Paar, 2015)

This project involved testing gel-like hydrogels across a wide variety of compositions intended for use as printing inks. For this reason, PP and CP systems were considered as they were the most versatile across ranges of consistencies. These systems use a flat stationary lower plate, which contains the Peltier temperature control system and a rotating upper plate which could either be flat or conical.

A CP system was preferred as it could provide a uniform shear rate throughout the sample as distance from the centre changed due however a PP could not. This is achieved with diameter-dependant gap angles on the conical upper plate which operate on smaller, predetermined gap heights that fulfil the mathematical criteria for uniform shear rates. However, CP systems increase the risk of is aggregation where sample particles accumulate in the narrow gap, effecting sample structure and voiding a test. Hence, gap height should be several times larger than sample grain size to avoid aggregates combining and truncating at the gap (Ghanbari *et al.*, 2020). A 50 mm CP would offer an improved SNR however the more-crosslinked materials would have been likely to cause jam by exceeding the machine's torque tolerance. In comparison, a 25 mm diameter CP could offer the best compromise for testing a wide range of gel-like and paste-like materials and was selected as the final system. As part of the series of complex equations that govern the calculations of the rheometer, a uniform shear rate is provided through specific, non-changeable values for gap height and gap angle depending on diameter. 25 mm, for example, is manufactured with a 1 ° gap angle and Rheoplus locks the gap height to 0.104 mm prior to testing.

Gap angle, gap height and measuring system diameter were important parameters in testing. However, other variables including temperature, shear rate, strain, oscillation frequency and test duration also varied between experiments. It was critical that these variables were correctly calibrated during setup to provide accurate and reliable rheological data. The results obtained from rheological studies were used to quantify complex material properties and form a comprehensive rheological profile for materials.

#### 4.5.2. Setup

First, a constant air pressure was connected to the rheometer, supplying the air-bearings and allowing for near-frictionless actuation. The rheometer was then powered up whilst Rheoplus software (Anton Paar) was launched to control the device. The rheometer motor

housing was stored in a lowered position surrounded by the transport protection which was removed by using the 'Ref' function on the rheometer control panel to lift the head to its maximum position.

Within Rheoplus, the chosen job template was then opened and the 'Initialize' function used to connect Rheoplus to the rheometer. The sleeve of the measuring system coupling was raised and the alignment mark lined up with the corresponding marker on the 25 mm CP measuring system before being fixed in place by lowering the sleeve again. Using Rheoplus, the 'Zero Gap' function was then used to calibrate the height between the upper and lower plates of the measuring system. The 'Reset Normal Force' function was then used to calibrate the normal force with the new weight of the assembled measuring system to 0 N.

Once the rheometer was setup, the warmup protocol was run at a shear rate of  $400 \text{ s}^{-1}$  for at least 30 minutes at the start of a session before a long motor calibration was performed. Over prolonged usage times the normal force may deviate from zero whilst at rest, indicating a change in air supply pressure and the need for recalibration of normal force. It was important that prior to loading, samples had been allowed at least 12 hours to rest so that excitation from previous shearing, mixing or centrifuging (as detailed in sections 4.2.1 and 4.2.2) did not carry forward. If not, samples would have been tested at a non-resting rheological state which would have affected results.

Samples were loaded by adding approximately 0.5 ml to the centre of the bottom plate and then lowering the upper plate. The plate was programmed to stop 0.01 mm above the measuring height (0.104 mm), known as the 'trim height' (0.114 mm). Here, a visual inspection was carried out to ensure the entire area between the plates contained sufficient sample (i.e. excess material had been ejected from the entire plate circumference) and it had not been underloaded (Figure 4.9).

Then, a straight-edged spatula was used perpendicular to the plate direction to correctly

remove excess sample. This was important as if the excess would otherwise contribute to resistant forces within the sample area. Likewise, a lack of material would cause the rheometer to calculate erroneous rheological data due to incorrect sample volume assumptions. In practice, surface tension of liquid-like samples formed minor outward slopes as seen in Figure 4.9C. The plate was then further lowered to the measuring height and the test performed. After a test, the sample was removed and discarded, both plates wiped clean and prepared for the next sample.

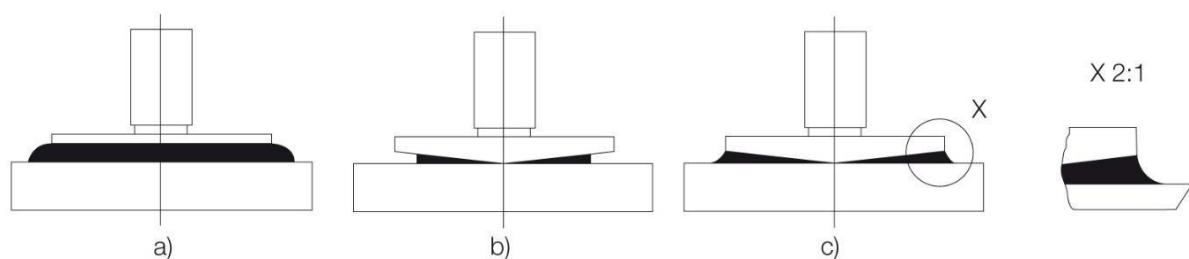


Figure 4.9: Overloading (A), underloading (B) and correct loading (C) of a rheometer (Paar, 2017)

### 4.5.3. Constant Shear

A constant shear rotational experiment is commonplace in 3D printing literature (He *et al.*, 2016) and provides a rudimentary value of viscosity.

Here seven separate samples were tested in triplicate from the UC and PC groups. The UC samples were 1 %, 3 % and 5 % w/v sodium alginate and the PC samples were 2 %/ 30 mM, 3 %/ 30 mM, 4 %/ 30 mM and 5 % /30 mM (w/v) sodium alginate with CaCl<sub>2</sub>, all produced as per methodology in section 4.2.2.

The rheometer was setup and allowed to warm up as detailed in Section 4.5.2 before the temperature was set to 20 °C and allowed to reach equilibrium  $\pm 0.2$  °C before samples were loaded. A 25 mm CP with a 1 ° angle and a 0.104 mm testing gap height was used. After each sample was trimmed and loaded a 30 second pause was allowed for sample temperature equilibration and to mitigate any undue excitation caused from the loading and

trimming processes. A shear rate of  $1 \text{ s}^{-1}$  was then applied and a measurement taken every 0.5 seconds for 10 seconds which provided a value for viscosity,  $\mu$  (Pa·s).

The final reading of the test was taken as the ‘true’ viscosity as a precaution for cohesive effects described in literature review section 4.2.2. Coefficient of variance (CoV) was used to verify and quantify if suspected cohesive effects had any effect on results by comparing the first measurement, at  $t = 0.5 \text{ s}$ , versus the last, at  $t = 20 \text{ s}$ . An acceptable value of CoV was 10 % or below. CoV calculation is seen below in Equation 4.2.

$$CoV = \frac{\sigma}{\mu} \times 100 \quad \text{Equation 4.20}$$

Additionally, all 51 stable flow samples from the previous hydrogel composition optimisation experiment in section 4.2.2 were also included in a separate, identical constant shear experiment to add an additional layer of understanding of the hydrogel optimisation as reported in Section 5.2.6.

Due to the limitations of rotational rheology as discussed in literature review section 4.2.2, oscillatory experiments were used in all further experiments.

#### 4.5.4. Amplitude Sweep

When building a comprehensive rheological profile, an amplitude sweep should be conducted early in the process to understand the effect of a broad range of shear rates on the test material. More specifically, an amplitude sweep was used to identify the LVER if there was one and its corresponding limits for future non-destructive testing.

Seven separate samples were produced as per methodology in section 4.2.2 and tested in triplicate. These were divided into two distinct groups, UC and PC. The UC samples were 1 %, 3 % and 5 % w/v sodium alginate and the PC samples were 2 %/30 mM, 3 %/30 mM, 4 %/30 mM and 5 %/30 mM sodium alginate &  $\text{CaCl}_2$ . An amplitude sweep was then conducted between 0.01 % and 1,000 % strain, using a logarithmic ramp which allowed for



6 measuring points per decade at a frequency of 1 Hz.

The primary outputs of the experiment were dynamic storage modulus ( $G'$ ) and dynamic loss modulus ( $G''$ ) which indicated the measured quantity of stored deformation energy (solid behaviour) and energy lost to internal friction (viscous behaviour) respectively. These were a function of applied strain amplitude ( $\gamma_0$ ) and resultant stress amplitude ( $\sigma_0$ ) at a given time however these do not occur at the same time within viscoelastic materials. Instead, there is a characteristic phase lag ( $\delta$ ) between the deformation and response of  $0 - 90^\circ$  which is measured by the rheometer. Calculations for  $G'$  and  $G''$  can be seen in Equation 4.21 and Equation 4.22 respectively.

$$G' = \frac{\sigma_0}{\gamma_0} \times \cos(\delta) \quad \text{Equation 4.21}$$

$$G'' = \frac{\sigma_0}{\gamma_0} \times \sin(\delta) \quad \text{Equation 4.22}$$

$\tan(\delta)$  was also calculated as per Equation 4.23 which describes the ratio between relative  $G'$  and  $G''$  moduli. A material with equal amounts would have a  $\tan(\delta)$  of 1 whereas as a material becomes more  $G'$  or  $G''$  dominant  $\tan(\delta)$  would approach 0 or infinity respectively. Finally, complex viscosity ( $\eta^*$ ) was calculated as it was the appropriate viscosity measurement for an oscillatory experiment, factoring in angular frequency ( $\omega$ ) as seen in Equation 4.24.

$$\tan(\delta) = \frac{G''}{G'} = \frac{\frac{G'' = \frac{\sigma_0}{\gamma_0} \times \sin(\delta)}{\gamma_0}}{\frac{G' = \frac{\sigma_0}{\gamma_0} \times \cos(\delta)}{\gamma_0}} \quad \text{Equation 4.23}$$

$$|\eta^*| = \frac{\sqrt{G''^2 + G'^2}}{\omega} \quad \text{Equation 4.24}$$

Analysis was performed within RheoPlus (Anton Paar) to determine the limit of the LVER ( $\gamma_L$ ) using a tolerance of  $\pm 10\%$  of  $G'$  as per ASTM D7175 and the Deutsches Institute for Normung (DIN) 51810-2. The first data point that deviated by more than 10% of the plateau-value of  $G'$  was used to confirm the  $\gamma_L$ . To gather a more precise estimate for the LVER location, a linear equation was formed between these two points and using the known values of  $\pm 10\%$  of the  $G'$  plateau-value, a corresponding amplitude value can be found. As the area between these two data points was a curve and not a straight line, this was an approximation although is used in the methods of previously cited standards. Additionally, Rheoplus provided a recommended strain value located within the LVER for non-destructive testing in further experiments.

#### 4.5.5. Frequency Sweep

Frequency sweeps were used to determine time-dependent behaviour of materials within the LVER. High frequencies simulate fast movement whereas low frequencies simulate slow movement. Results of LVER analysis in section 4.5.4 indicated that all tested samples were suitable for non-destructive testing at a 1% strain within all sample's LVERs. This was an optimal value to maximise SNR because strain was at the upper limit of what could be tested within the LVER.

A frequency sweep was conducted using a strain of 1% and measured between 0.01 Hz to 100 Hz with a logarithmic ramp which allowed for 5 measuring points per decade. Frequencies were measured from 100 Hz to 0.01 Hz as this significantly reduced testing time without impairing the quality of results.

#### 4.5.6. Temperature Sweep

A temperature sweep was used to analyse the effects of temperature viscoelastic properties

of materials change with different thermal parameters. A temperature sweep was conducted from 5 °C to 70 °C using a frequency of 1 Hz and applied an LVER-strain of 1 % to simulate resting conditions. A sampling time of 5 seconds was used and a temperature increase of 0.2 °Cs<sup>-1</sup> employed over a 330 second test period.

Because the starting temperature of the test was different to the normally used 20 °C, which was very similar to the room temperature ~20 °C of samples prior to testing, a 30 second time was given after setup to allow the hydrogel to cool down to 5 °C and thermal equilibration be reached. This was important as not only would the sample temperature be incorrect, hence the test void, but the sensor would also be warmed up and be temporarily unable to reach the desired 5 °C start temperature. After each test, the temperature was manually reset to 5 °C and allowed to find thermal equilibration before the next sample was loaded onto the rheometer.

#### 4.5.7. 3-Interval Thixotropy Test

A 3-interval thixotropy test (3ITT) was performed to further understand the thixotropic (time-dependent) nature of sample viscoelastic properties. A frequency of 1 Hz was used as a zero-shear approximation within the LVER and a sampling time of 5 seconds selected to reliably record data at this frequency. Interval 1 utilised a 1 % strain for 120 seconds, whilst interval 2 used a logarithmic ramp with 4 points per decade to increase the strain from 1 % to 1,000 % over 65 seconds. Interval 3 also used a 1 % strain like interval 1 so that comparisons could be drawn between these resting states before and after destructive testing although this was over an extended time period of 300 seconds.

#### 4.5.8. Post-Mix Time Sweep

As discussed in section 4.2.2, PC samples were produced *via* a rigorous mixing process that exchanged materials back and forth between syringes a total of 100 times over

approximately 90 seconds. This induced higher shear forces and it was unclear when samples would return to resting states. It was important to know this as otherwise experiments could have been using materials at different states, leading to systematic errors.

Typically, samples were allowed to rest for at least 30 minutes after the crosslinking process before use. However, this test sought to analyse what occurred immediately after crosslinking. As such, the 30 minute rest-period was omitted from this study. In addition to the 90 seconds mixing process required, a further 60 seconds of sample manipulation was required to correctly load the rheometer as per section 4.5.2. This meant the testing started a total of 150 seconds after crosslinking began which was a known limitation.

A frequency of 1 Hz and 1 % strain was applied to test within LVER limits while measurements were taken every 5 seconds for a total of 30 minutes. As this was an extended test duration, a solvent trap was used and filled with water to mitigate the hydrogel evaporation which would likely occur and affect results.

#### 4.5.9. Data Presentation

Graphical representations of rheological data from the tests listed above typically do not include error bars for the groups of technical repeats for the samples due to the largely systematic insignificant size of the errors relative to signal size. When plotted, these error bars were seldom visible as they were 'hidden' behind the mean data point due to the lack of variance hence offer little value when viewing data as a graph. For these reasons, the following presentations of rheological data from this project plot only the mean with no error bars for groups.

### 4.6. Evaluation of 3D Printed Hydrogels

Now that a full optimisation and assessment of a wide range of hydrogels had been completed, alongside further rheological characterisation, further 3D printing quality could

be assessed. Three promising PC samples (2 %/30 mM, 3 %/30 mM and 5 %/30 mM) were chosen to demonstrate 3D printing quality of hydrogels with a range of viscous and elastic moduli ratios. Some 3D printing was previously conducted in Section 4.4.5 for the stress test, however, these studies focused on material properties rather than print quality. This following evaluation will further assess the quality of the 3D printing exclusively.

#### 4.6.1. Advanced G-code Generation

The processes of STL production, G-code generation and 3D printing were previously introduced in the project although this was for a rudimentary stress test. Previously mentioned settings used during 3D printing of stress tests were fundamental in extruding material at the correct rates for desired heights and line widths of individual 3D printed fibres. Previously, few slicer settings were relevant when printing these simple lattice models however were now used to fine-tune print quality. A full list of the slicer settings can be found in Table 4.3.

*Table 4.3: List of complete settings for 3D printing primary-crosslinked alginate.*

	Parameter	Setting
Previous Settings	Layer height	0.2 mm
	Default Print Speed	10 mms <sup>-1</sup>
	Extrusion width	0.5 mm
	Extrusion Pressure	4.6 psi (2 %/30 mM), 10.4 psi (3 %/30 mM) and 30.2 psi (5 %/30 mM)
Additional Settings	Perimeters	2
	Seam position	Aligned
	Skirt loops	1
	Infill pattern (angle)	Alternating rectilinear (45 °)
	Infill	100 %

Perimeters were useful in larger connected surfaces to smooth out the exterior edges, 2 was sufficient. A seam position was the start point for each new layer on an object, specifically the point where perimeters would start and minor surface inaccuracies may occur. This was set to aligned, so that all material behaviour could be observed. A skirt loop was a detached

extruded line that extended around the perimeter of printed objects. This purged material to ensure it was properly flowing prior to printing the model area, a process known as priming. A 45 ° alternating rectilinear infill pattern was used to minimise crossings areas and prevent associated material accumulation at these crossings while ensuring efficient print speeds. Finally, a 100 % infill was selected so that any solid areas of a designed STL were correctly printed as such.

#### 4.6.2. Line Width

The most important aspect in producing accurate 3D printed structures is ensuring accurate material deposition at the most fundamental level. In FFF this is the individual lines produced by the dispensing tip or nozzle. The chosen slicer used a line width of 0.5 mm however if, in practice during printing, a wider line is produced, material will be incorrectly deposited in neighbouring areas. Likewise, if a thinner line is being produced, sections of the printed object are effectively skipped and voids will be present.

In Fusion 360, a rectangle prism measuring 50 × 0.5 × 0.2 mm was produced to test the single line width of each of the three PC samples. Three of these were arranged in parallel with a 5 mm spacing as seen in Figure 4.10. To better understand the relationship of pressure and print speed and how they impact line width, a range of each was used. Print speeds of 6, 8, 10, 12 & 14 mms<sup>-1</sup> were used alongside the previously recorded default pressures of each of the three PC hydrogels and both ±10 % & ± 20 % of this.

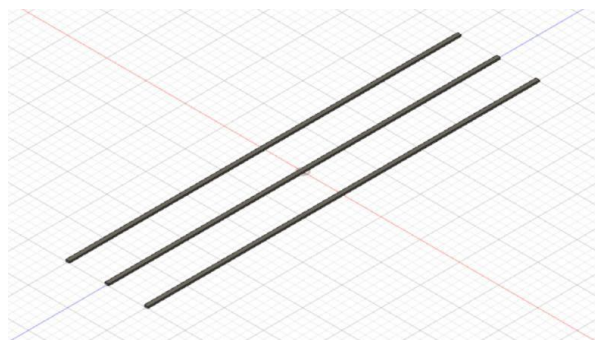


Figure 4.10: Line width model seen in Fusion 360. Dimensions were 50 × 0.5 × 0.2 mm arranged in parallel with a 5 mm spacing.

G-code was generated using the changes to print speed whereas other settings remained the same. The Allevi 2 was setup and calibrated as previously discussed in Section 4.4.5 however prior to printing, the extrusion pressures were increased or decreased by 10 % or 20 % if required. 3D printing was then performed for 2 %/30 mM, 3 %/30 mM and 5 %/30 mM PC samples using these multiple print speed and extrusion pressure settings.

After print completion, acrylic inserts were immediately removed and taken to a Mitutoyo toolmakers microscope and arranged along the Y-axis. The crosshair within the eye piece was positioned in the centre of each line along the Y-axis and on one of edges along the X-axis. The digital X-axis micrometre was then zeroed and micrometre tools used to move the XY stage so that the crosshair moved to the other edge along the X-axis where the measurement was recorded as the line width. This was repeated for each of the lines. Results were then arranged in a 3-colour graded heatmap using 0 mm as red, 0.5 mm as green, and 1.0 mm or above as blue.

### 4.6.3. Single Layer Infill

Single layers were next 3D printed and evaluated as the next level in the progression scales of 3D printing. A single layer is produced through the fusion of multiple individual lines that have been deposited adjacent to each other. It was necessary to assess the ability of these many individual 3D printed lines to successfully fuse to form a uniform, solid layer.

Using Fusion 360, a 30 × 30 × 0.2 mm STL was produced as seen in Figure 4.11. As in Section 4.6.2, print speeds of 6, 8, 10, 12 & 14 mms<sup>-1</sup> were used alongside the previously recorded default pressures of each PC hydrogel and both ±10 % & ± 20 % of these. Repetier-Host and Slic3r were used to produce G-code with these varied print speeds and the Allevi 2 was setup as previously discussed in Section 4.4.5. 3D printing was then performed for 2 %/30 mM, 3 %/30 mM and 5 %/30 mM PC samples using these multiple print speed and

extrusion pressure settings.

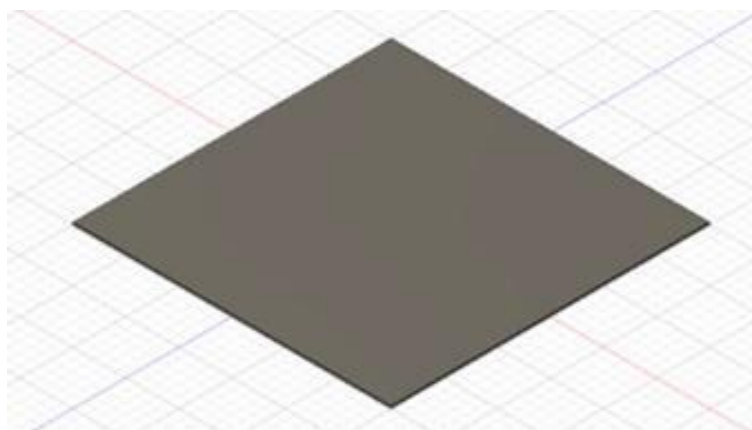


*Figure 4.11: Single layer infill model seen in Fusion 360 with dimensions 30 x 30 x 0.2 mm.*

Once a print had been completed, the acrylic inserts were taken over to a photography area with a matte black background. A digital camera and polarising filter were then used to capture images of each print in an orthographic style to compare line fusion and layer formation.

Resulting images were assessed and given a score category depending on the outcome of any flaws present. A score of 0 was given for 3D prints that contained a complete layer formation with no exposed areas at all. 3D prints that contained very minor, dot-like defects were given a score of -1. Those that contained larger flaws that formed line-like defects were given a score of -2 if these were limited in their location to outer regions of the 3D print. A score of -3 was given to 3D prints that contained larger line-like flaws across central areas of the printed area if significant sections of material that were correctly fused were present. Finally, a score of -4 was given to severely flawed 3D prints that contained large line-like defects across the whole print area with no discernible fused section being present.

#### 4.6.4. Multi-Layer Geometries

The line width and single layer infill tests provided information on how the fundamental stages of 3D printing hydrogels performed at different extrusion pressures and printing



speeds. The aim of this experiment was to investigate how these materials would perform on a larger scale with multiple layers, a true 3D print.

Four separate models were produced in Fusion 360 to evaluate how applicable the three primary-crosslinked samples (2 %/30 mM, 3 %/30 mM and 5 %/30 mM) to evaluate more complex 3D printing. The first of these was a cube measuring  $10 \times 10 \times 5$  mm seen in Figure 4.12A. The second was a hollowed-out model also measuring  $10 \times 10 \times 5$  mm with a wall thickness of 1 mm seen in Figure 4.12B. The third and fourth models were  $10 \times 10 \times 5$  mm cubes that had been extruded at an angle to provide  $22.5^\circ$  and  $45^\circ$  overhangs respectively. These can be seen in Figure 4.12C and Figure 4.12D.

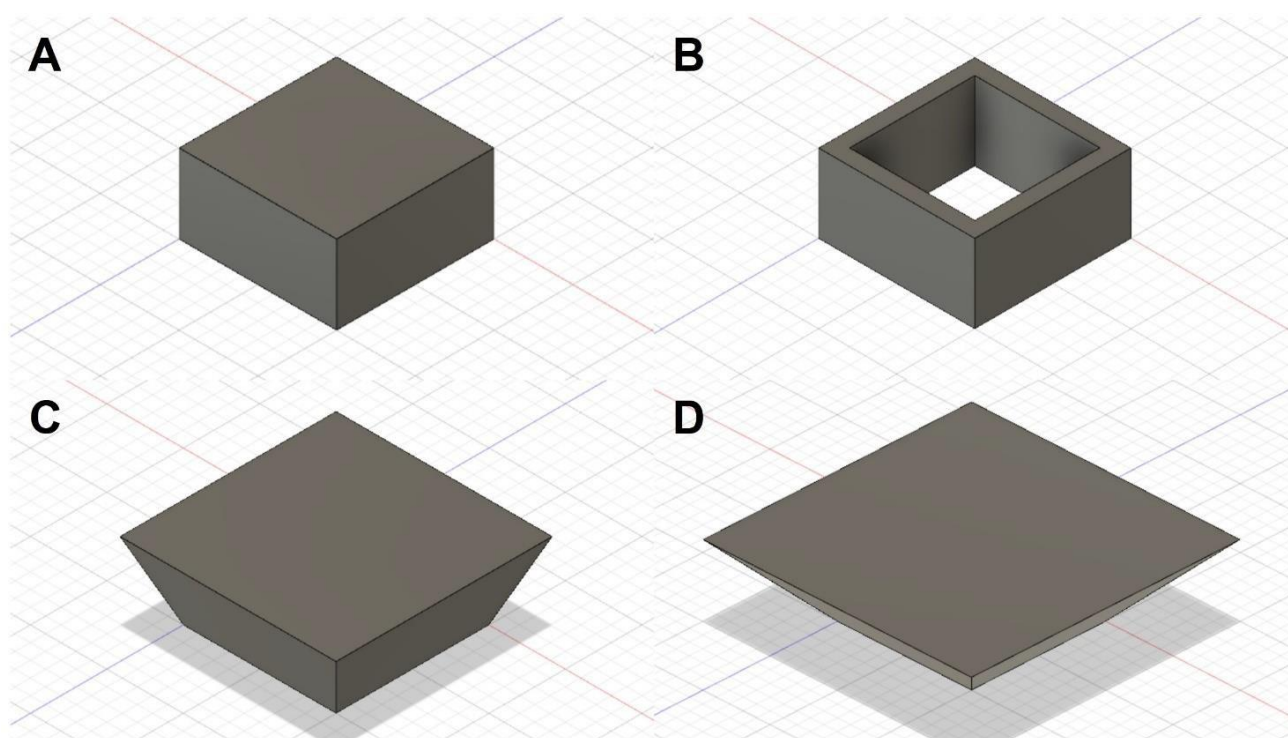


Figure 4.12: Multi-layer geometry models seen in Fusion 360. (A) Solid cube with dimensions  $10 \times 10 \times 5$  mm. (B) Hollowed-out cube with dimensions  $10 \times 10 \times 5$  mm with a wall thickness of 1 mm. (C)  $22.5^\circ$  overhang cube with base dimension of  $10 \times 10$  mm and 5 mm tall. (D)  $45^\circ$  overhang cube with base dimension of  $10 \times 10$  mm and 5 mm tall.

G-code was generated for each model using the original print speed of  $10 \text{ mms}^{-1}$  and the Allevi 2 was used to execute G-code for the models. Originally calibrated extrusion pressures were used for each material: 4.6 psi for 2 %/30 mM, 10.4 psi for 3 %/30 mM and 30.4 psi for 5 %/30 mM.

After printing, as before, samples imaged with the digital camera and polarising filter. Multiple angles of 3D printed samples were collected for each hydrogel composition.

## **4.7. Mechanical Testing of 3D Printed Hydrogels**

Three candidate PC hydrogels had been evaluated for multi-layered 3D printing whereby the 5%/30 mM composition produced the highest fidelity prints. As noted in literature, these 3D printed hydrogels lacked mechanical strength and required further development to generate robust structures. Since the 3D printed objects were designed as theoretical palatal obturators, it was vital that they were capable of withstanding physical forces between the oral and nasal cavities. The 5%/30 mM hydrogel was therefore evaluated with regards to secondary-crosslinking and mechanical testing performed.

### **4.7.1. Secondary Crosslinking**

3D printed alginate objects had previously been primary-crosslinked however they can be further crosslinked to form secondary-crosslinked hydrogels by exposing them to further amounts of divalent cationic ions.

Secondary crosslinking solutions were prepared by dissolving  $\text{CaCl}_2$  in deionised water as in section 4.2.2 to form molarities between 50 – 300 mM. Once a 3D print had been completed, the acrylic insert was removed and transferred into a crosslinking bath. This was then gently filled with approximately 100 ml of the secondary crosslinking solution so that the entire object was completely submerged. It was important not to disturb the printed object with the flow of liquid by pouring into the corners of the crosslinking bath.

A timer was started and objects were left submerged in the crosslinking solution for the required amount of time between 15 – 240 mins. One of the disadvantages of this method

for secondary crosslinking was that the surface of the printed object that was in contact with the acrylic insert was not in contact with any secondary crosslinking solution. To overcome this, after 60 seconds of crosslinking, objects were gently released from the print bed using a spatula. Printed objects came away easily and were not deformed during this process. They were then placed on an elevated mesh surface within the bath to ensure all sides were being crosslinked for the remainder of time. After the allocated crosslinking duration, printed objects were removed and gently washed with deionised water to prevent further crosslinking. After each secondary crosslinking reaction, the secondary-crosslinking solution was replaced.

#### 4.7.2. Compressive Testing

Now that the printed objects had been secondary-crosslinked, a method was required to measure their final mechanical properties. Compressive testing is a well-established method for determination of mechanical properties. The precise methodology to follow can be found in International Organisation for Standardisation (ISO) standard 604:2003.

ISO 604:2003 details the ideal requirements for a compressive test specimen that has a diameter at least 2.5 times the size of the specimen length. To satisfy this requirement, a circular prism was designed within Fusion 360 that had a diameter of 15 mm and length of 5 mm, seen in Figure 4.13.

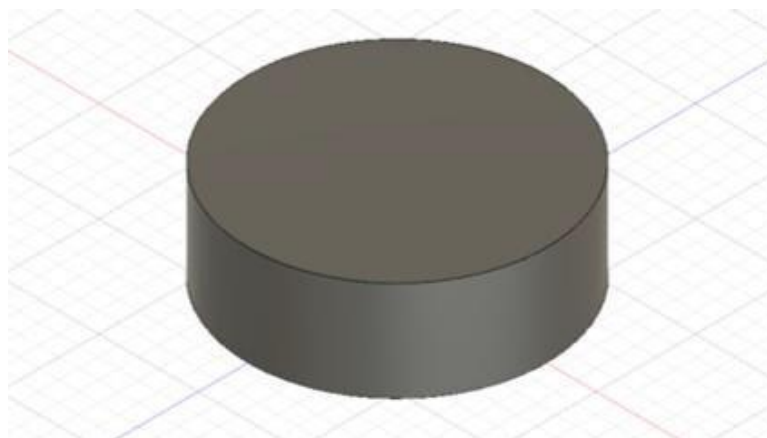


Figure 4.13: Compressive test specimen seen in Fusion 360 with a 15 mm diameter and length of 5 mm.

Models of the compressive test specimen were printed in triplicate using the previously defined G-code in Section 4.6.1. The 5 %/30 mM hydrogel composition was used at a print speed of  $10 \text{ mms}^{-1}$  and extrusion pressure of 30.4 psi to produce optimal 3D printing results. Once printed, models were secondary crosslinked with 50 – 300 mM of  $\text{CaCl}_2$  solution for 15 – 240 mins as per Section 4.7.1.

Post-crosslinking, the diameter of models was measured in triplicate using a digital micrometre from equally spaced sections along the circumference of the specimen. The previously used Anton Paar Physica MCR 301 rheometer was used to conduct the compressive test which had a normal force limit of 40 N. It had been setup as per Section 4.5.2 although a 50 mm PP measuring system was used. This was attached and zeroed to the testing surface before being raised to a height of 10 mm above the testing surface. Specimens were then loaded into the centre of the testing surface and orientated correctly in the flat position.

A compressive test was designed within Rheoplus from a tack test template. The test height was set to 10 mm and travel speed of the 50 mm measuring system set to  $1 \text{ mmmin}^{-1}$  (or  $0.016 \text{ mms}^{-1}$ ) as per recommendations from ISO 604:2003. Prior to the start of each test, the normal force was re-zeroed as this value could vary slightly during prolonged rheometer usage. The test was then run and a data point was recorded for every second for 600 seconds. This was repeated for each tested sample in triplicate.

The data sets comprised of normal force (N) and the gap height (mm) were exported to Excel for analysis. Within each dataset, the results were refined according to the following two criteria. The first was removal of data with a normal force of  $< 0.05 \text{ N}$  which was defined as the pre-loading region which also functioned as a standardising method to accurately determine the length of the specimens. Secondly, data after the first data point to register  $> 40 \text{ N}$  was also removed as the limits of the rheometer had been reached and following data was invalid.

Next, stress and strain values were calculated from which stress-strain curves could be produced. The equation for stress,  $\sigma$  (KPa), can be seen in Equation 4.25 where  $F$  was the normal force recorded on the rheometer (N) and  $d$  (mm) was the previously recorded median sample diameter. The equation for strain,  $\varepsilon$ , can be seen in Equation 4.26 where  $L_0$  (mm) was the specimen height, taken as the rheometer gap height at the first recorded data point to have  $N \geq 0.05$ , and  $\Delta L_0$  (mm) was the displacement of this.

$$\sigma = \frac{F \times 10^3}{A} = \frac{F \times 10^3}{\pi \times \left(\frac{d}{2}\right)^2} \quad \text{Equation 4.25}$$

$$\varepsilon = \frac{\Delta L_0}{L_0} \quad \text{Equation 4.26}$$

These equations were applied to all trimmed data sets and the resulting data plotted as line graphs in GraphPad Prism. An example stress strain curve of compression of a hydrogel can be seen in Figure 4.14. The initial part of the curve (A) was the loading region where the hydrogel was gradually exposed to more stress and the linear section that follows (B) was the elastic region. The elastic modulus was the gradient within the linear region. The elastic modulus was the gradient within the linear region.

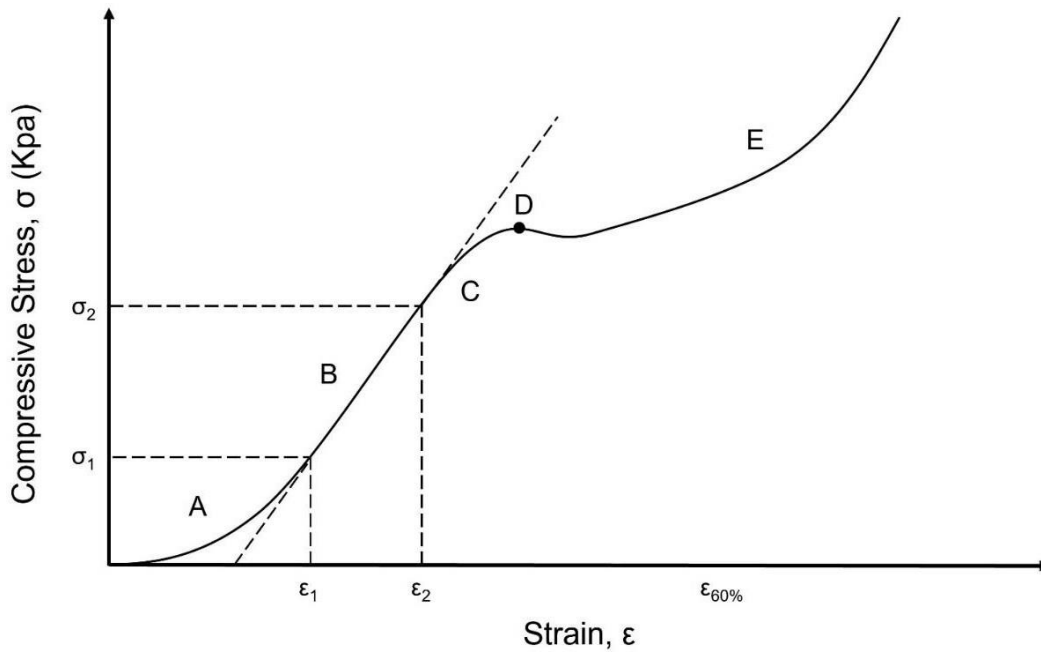


Figure 4.14: Diagram of a representative compressive stress strain graph of alginate hydrogels. Shown on the diagram are the toe region (A), linear region (B), plastic deformation region (C), ultimate compress stress (D) and post-ultimate compressive stress region (E). Locations were also labelled at the start and end of the linear region that can be used to calculate elastic modulus. Not to scale.

Each stress strain graph was visually assessed to locate this linear region and record the coordinates of suitable start and end locations. The elastic modulus for each sample was calculated using the data from these two locations as seen in Equation 4.25 and then plotted as a bar chart.

$$E = \frac{\sigma_2 - \sigma_1}{\epsilon_2 - \epsilon_1} \quad \text{Equation 4.27}$$

The area under the curve of the stress strain graph represents the total energy required to deform the material per unit volume or toughness. Calculating toughness was valuable as it includes information from a broader range of strain values, thus deformation, than just the elastic region. In this instance, toughness calculation was limited to include values up until 60 % strain to allow for proper comparisons between samples. To calculate this area, the curve was divided into multiple rectangles as seen in Figure 4.15, known as a Riemann sum. Rectangle width was equal to the difference in strain values between two data points whilst the height was taken as an average of the two points' stress values.

Within Excel, the sum the area of all rectangles up to a strain value to 60 % was then calculated and the results plotted as a new bar chart.

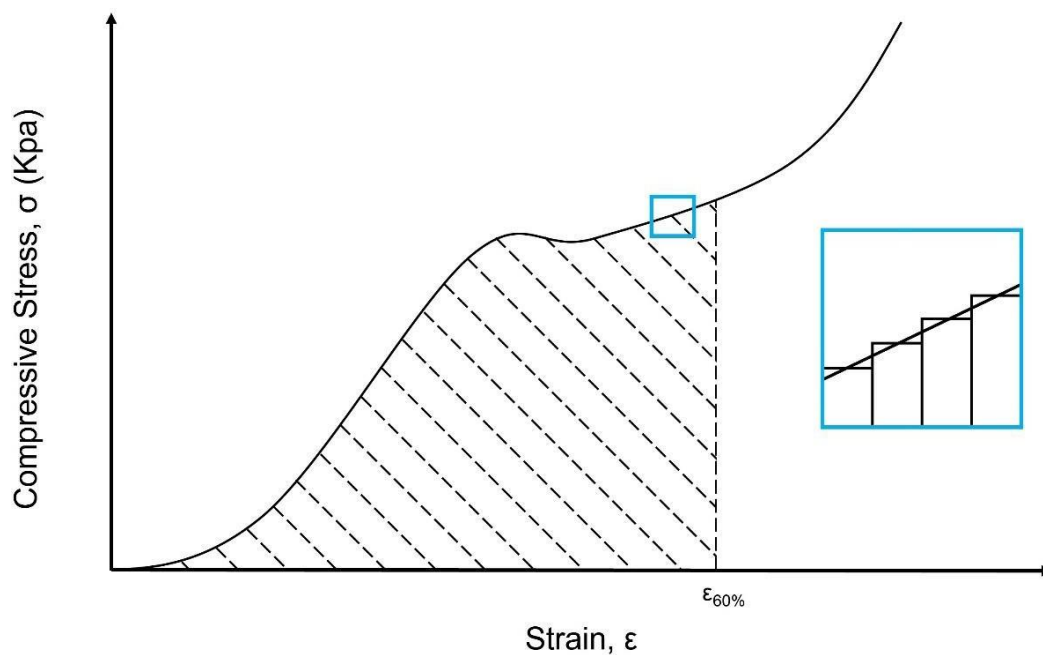


Figure 4.15: Using a Riemann sum to calculate area under a stress strain curve, or toughness, using a 60 % strain limit.

2-way analysis of variance (ANOVA) statistical tests were performed using the Tukey multiple comparison technique on both the elastic modulus and toughness to determine statistical significance.

## 5. Results

### **5.1. Proton Nuclear Magnetic Resonance Spectroscopy of Alginate**

As per Section 4.2, three separate alginate strains were prepared and then analysed using  $^1\text{H}$  NMR. MestReNova was used to view the raw data and apply post-processing steps to produce correctly formed NMR spectra. Three repeats were conducted to produce three separate  $^1\text{H}$  NMR spectra of each alginate strain. Representative images for each alginate strain can be seen in Figure 5.1. The remaining technical repeats for each alginate are found in the appendix (Figure 10.1 – Figure 10.3).



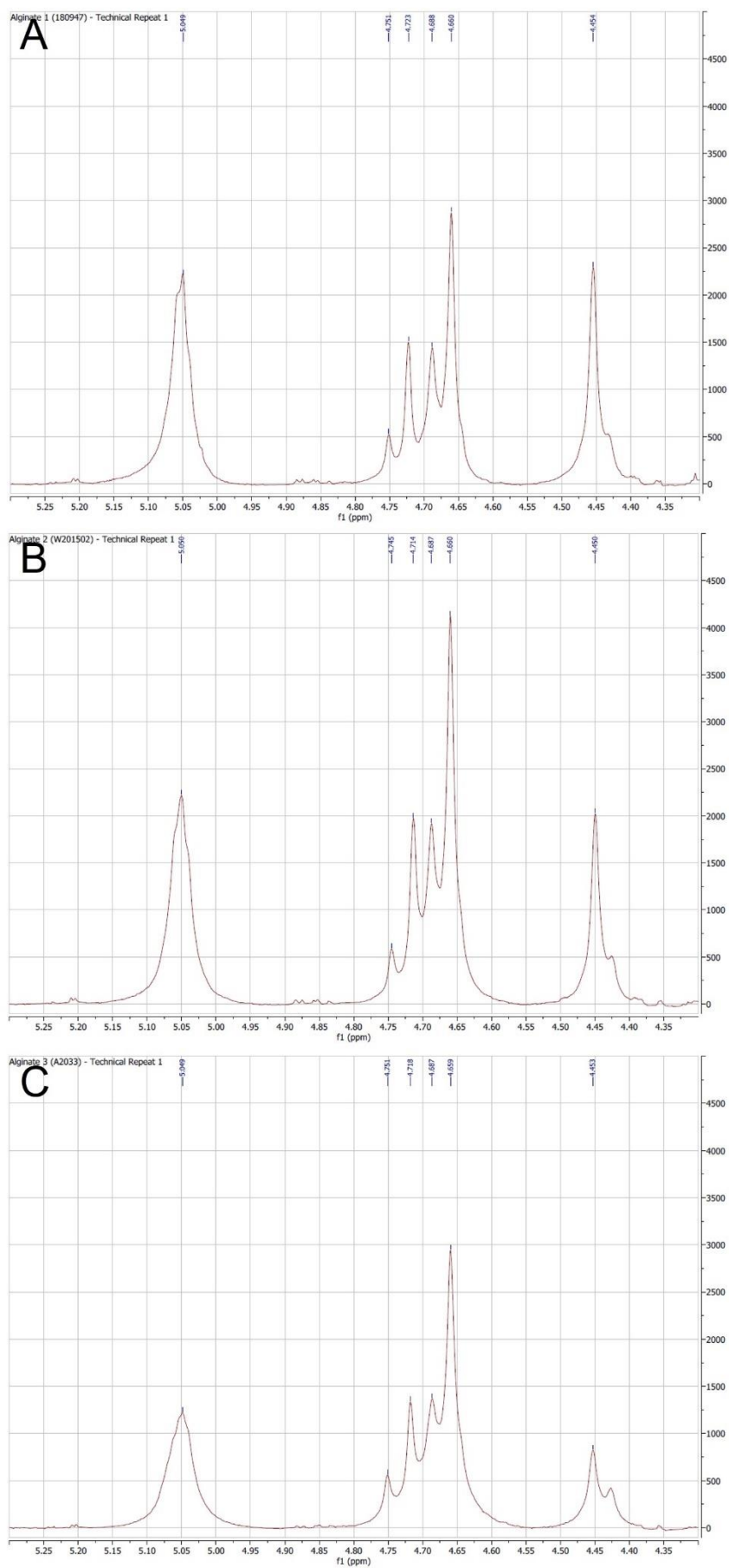


Figure 5. 1: <sup>1</sup>H NMR Spectra of three separate alginate chains that were labelled with their supplier product codes: alginate 1 (180947), alginate 2 (W201502) and alginate 3 (A2033). Representative images were taken from three technical repeats (n = 3). MestReNova was used to apply Fourier transform, phase correction, baseline correction and peak labelling.

All three alginate strain NMR spectra correctly matched the overall expected layout between 4.3 – 5.3 ppm as per the template in ASTM F2259-10. Each spectrum clearly contained six dominant peaks at approximately 4.45, 4.66, 4.69, 4.71, 4.75 and 5.05 ppm. Average intensity values recorded for each peak post-labelling can be seen in Table 5.1.

Table 5.1: Average intensity values and standard deviation of peaks located from the <sup>1</sup>H NMR spectra of three strains of alginate (n = 3).

Peak Label (Location)	Alginate 1 (180947)	Alginate 2 (W201502)	Alginate 3 (A2033)
C (4.45 ppm)	1758.17 ± 253.67	2147.80 ± 72.86	1326.50 ± 151.84
B4 (4.66 ppm)	429.13 ± 88.10	505.27 ± 45.67	469.93 ± 79.43
B3 (4.69 ppm)	902.57 ± 521.78	1822.33 ± 72.54	1127.87 ± 145.15
B2 (4.71 ppm)	1278.97 ± 300.93	1623.07 ± 157.78	950.00 ± 374.55
B1 (4.75 ppm)	2652.20 ± 580.81	3998.00 ± 413.77	2932.90 ± 370.1
A (5.05 ppm)	2208.10 ± 467.79	2066.57 ± 50.53	867.83 ± 111.68

There is no clear overall trend for peak intensity between alginates 1, 2 and 3. Alginate 2 had noticeably higher intensity peaks on its B4, B3 and B2 peaks than its counterparts. Alginate 3 displayed the lowest intensity at peaks C, B2 and B4. Alginate 1 showed the weakest intensities on peaks B1 and B3. These peak intensities were used to produce average variables seen in Table 5.2.

Table 5.2: Average intensity values and standard deviation of variables created using <sup>1</sup>H NMR peak intensity data for quantifying structural elements of alginate. M = mannuronate and G = guluronate (n = 3).

Variable Name	Alginate 1 (180947)	Alginate 2 (W201502)	Alginate 3 (A2033)
G	2635.80 ± 410.7	3094.85 ± 105.79	1734.12 ± 105.79
M	3957.53 ± 663.36	5973.33 ± 516.27	4206.80 ± 516.27
GG	1330.47 ± 320.54	1119.52 ± 40.94	460.22 ± 40.94
MG & MG	1305.33 ± 221.61	1975.33 ± 116.68	1273.90 ± 116.68
MM	2652.20 ± 580.81	3998.00 ± 413.77	2932.90 ± 413.77
GGM	420.64 ± 228.07	428.80 ± 47.14	374.67 ± 47.14
MGM	884.70 ± 346.65	1546.54 ± 69.83	899.23 ± 69.83
GGG	909.83 ± 124.12	690.72 ± 76.49	85.55 ± 76.49

These variables were then used to quantify the percentage of constituent parts of the alginate strains, seen in Table 5.3. These were separated into groups based on the block

length of the quantified element.

Table 5.3: Quantified average mannuronate (M) and guluronate (G) block sequences of alginate strains with standard deviation (n = 3).

Quantified Block Sequence	Alginate 1 (180947)	Alginate 2 (W201502)	Alginate 3 (A2033)
%G	39.98 ± 0.59	34.13 ± 1.23	29.19 ± 0.06
%M	60.02 ± 0.59	65.87 ± 1.23	70.81 ± 0.06
%GG	20.18 ± 2.34	12.35 ± 0.98	7.75 ± 1.56
%GM & %MG	40.23 ± 3.52	44.09 ± 1.68	49.37 ± 1.67
%MM	19.80 ± 2.93	21.78 ± 0.62	21.44 ± 1.61
%GGM & %MGG	13.80 ± 0.35	7.62 ± 1.22	1.44 ± 2.24
%MGM	13.42 ± 5.58	17.05 ± 0.55	15.14 ± 0.94
%GGG	6.38 ± 2.65	4.73 ± 0.28	6.31 ± 0.68

The quantification of alginate constituent blocks revealed clear differences between the strains. Alginate 1 had highest overall guluronate content at 39.98 % followed by alginate 2 and alginate 3 with 34.13 % and 29.19 % respectively. *Vice versa*, alginate 3 possessed the highest quantity of mannuronate at 70.81 % followed by alginate 2 and alginate 3 at 65.87 % and 60.02 % respectively.

When considering two-length sections of the alginate block sequence, Alginate 1 also had the highest concentration of homogenous guluronate (20.18 %) compared to alginate 2 and alginate 3 which were 12.35 % and 7.75 % respectively. Interestingly, all 3 alginate strains had similar amounts of heterogeneous two-length sections of between 40.23 – 49.37 %. Alginate 3 was also measured as having 21.44 % homogenous mannuronate where alginates 2 and 3 had 21.78 % and 19.80 % respectively.

Of the quantified three-length alginate blocks, a clear difference was seen in calculated amounts of the heterogeneous GGM and MGG block sequences which constitute between 1.44 – 13.80 % of the block sequences. In contrast, there is little difference in MGM block sequence values which ranged from 13.42 to 17.05 %. Lastly, large differences were observed in the homogenous GGG block sequences between alginate 1 & 3 versus alginate 2. Alginate 2 contained 4.73 % whereas alginates 1 and 3 contained 6.38 % and 6.31 %

respectively.

Finally, the average length of some blocks could also be quantified, the results from which can be seen in Table 5.4.

Table 5.4: Average block lengths within alginate strains ( $n = 3$ ).  $N_G$  represents homogenous guluronate sections,  $N_{G > 1}$  denotes homogenous guluronate sections excluding individual guluronate blocks and  $N_M$  represents homogenous mannuronate sections.

Block Type	Alginate 1 (180947)	Alginate 2 (W201502)	Alginate 3 (A2033)
$N_G$	$2.02 \pm 0.29$	$1.57 \pm 0.05$	$1.36 \pm 0.10$
$N_{G > 1}$	$3.03 \pm 0.52$	$3.02 \pm 0.13$	$3.30 \pm 0.26$
$N_M$	$4.16 \pm 0.69$	$3.61 \pm 0.33$	$2.23 \pm 0.40$

Alginate 1 contained the highest average length of homogenous guluronate sections ( $N_G$ ) measured as 2.02 blocks whereas alginates 2 and 3 measured 1.57 and 1.36 respectively. When excluding single guluronate blocks in calculations ( $N_{G > 1}$ ), this trend interestingly disappears and insignificant differences were observed between alginates with values of 3.02 – 3.30. This indicates that alginate 3 had a disproportionately large amount of single G blocks as part of its overall G content. The same trend can be seen in average length of homogenous mannuronate sections ( $N_M$ ) in alginate strains, however the differences between values were smaller. Alginate 3 had a recorded average  $N_M$  length of 2.23 blocks whereas alginates 2 and 1 were 3.61 and 41.16 respectively.

Following on from the 1H NMR Spectroscopy of these three alginate strains it was decided that alginate 3 would be used for further experiments within the project. This was because it contained the highest relative amounts of double guluronate blocks which have been shown to perform well in 3D printing.

## 5.2. Hydrogel Composition Optimisation

### 5.2.1. Visual Assessment

Figure 5.2(A – F) and Figure 5.3(A – F) show pictures of hydrogel compositions with alginate concentrations of 0.5 to 3.0 % and 3.5 to 6.0 % respectively, and corresponding  $\text{CaCl}_2$  concentrations of 0 – 50 mM. At this stage, samples were produced and PC as per Section 4.2 and then arranged in front of a black background and their image captured with a digital camera.

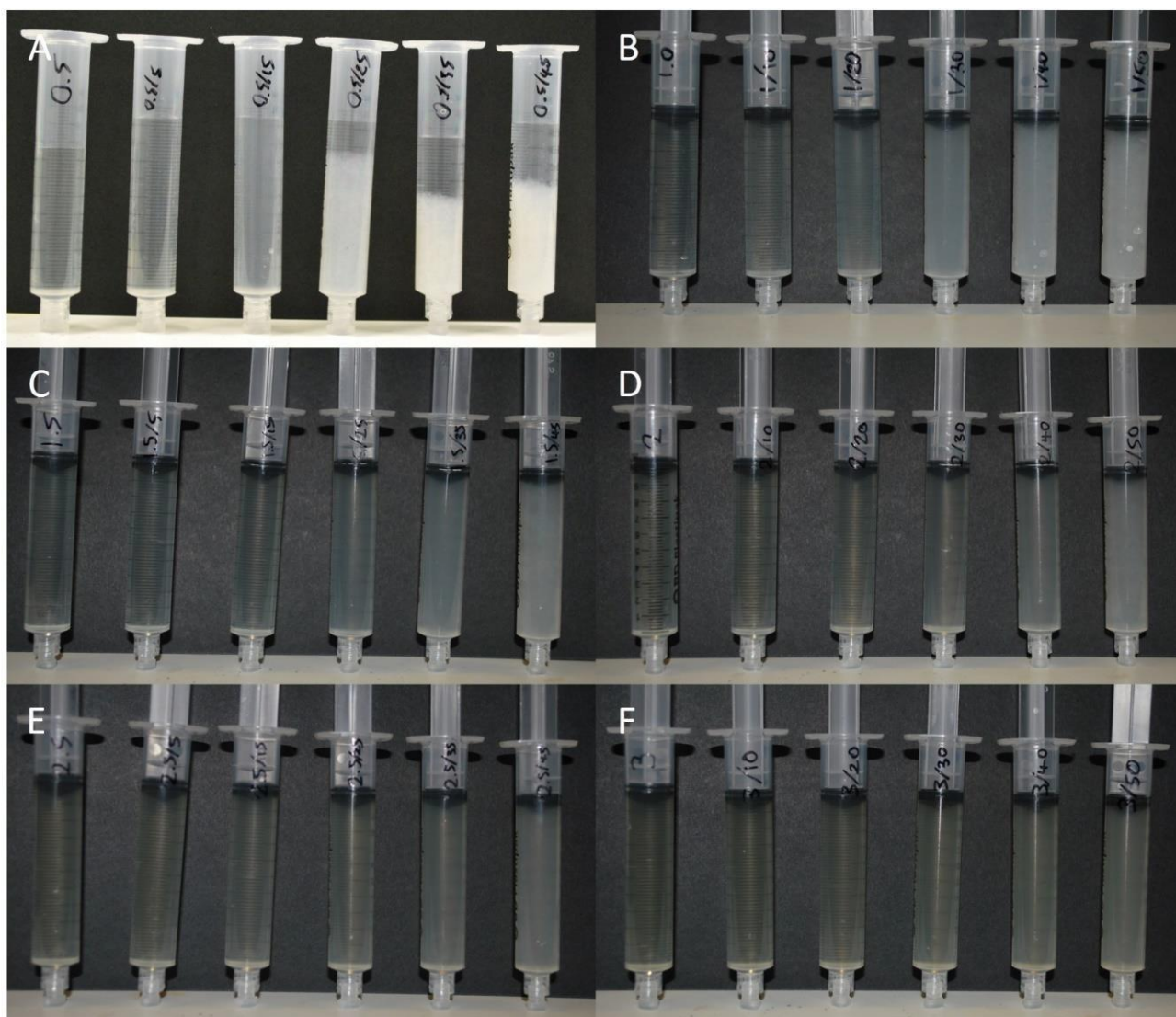


Figure 5.2: Images of hydrogel compositions 30 minutes post-production grouped per sodium alginate concentration (w/v): 0.5 % (A), 1.0 % (B), 1.5 % (C), 2.0 % (D), 2.5 % (E) and 3.0 % (F). From left to right within each group the calcium crosslinking amounts are: 0 mM, 5/10 mM, 15/20 mM, 25/30 mM, 35/40 mM, 45/50 mM (groups A, C and E contain odd values whereas B, D and E contain even values). Syringe diameter = 15 mm.



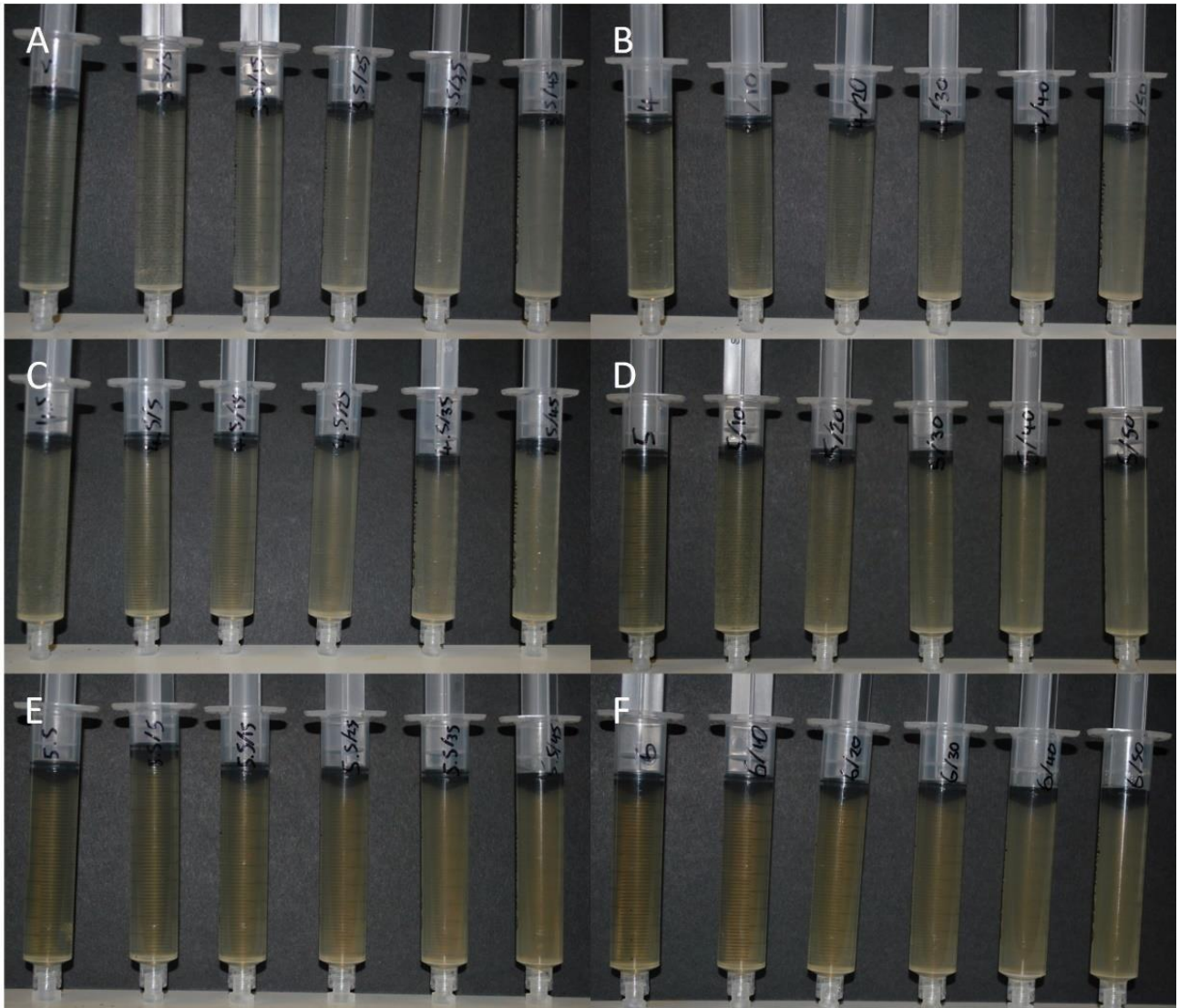


Figure 5.3: Images of hydrogel compositions 30 minutes post-production grouped per sodium alginate concentration (w/v): 3.5 % (A), 4.0 % (B), 4.5 % (C), 5.0 % (D), 5.5 % (E) and 6.0 % (F). From left to right within each group the calcium crosslinking amounts are: 0 mM, 5/10 mM, 15/20 mM, 25/30 mM, 35/40 mM, 45/50 mM (groups A, C and E contain odd values whereas B, D and E contain even values). Syringe diameter = 15 mm.

As alginate concentration increased from 0.5 % to 6.0 % the overall colour of compositions transformed from white to olive with varying degrees of translucency depending on  $\text{CaCl}_2$  concentration. Within each grouped image, as  $\text{CaCl}_2$  concentration increased the compositions become increasingly less translucent. This was most noticeable in the lower alginate concentrations such as 1.0 % although the trend was visible in each grouped image, including the highest concentrations, albeit less obvious. Figure 5.2A was distinctive as the three compositions with the highest  $\text{CaCl}_2$  concentration (0.5 %/25 mM, 0.5 %/35 mM and 0.5 %/45 mM) exhibited phase separation. The upper translucent phase was liquid whereas the lower opaque phase contained several small solid particles that settled at the bottom of

the syringe. No other compositions displayed distinctive phase separation.

### 5.2.2. Extrudability

Figure 5.4 shows the results of the extrudability section of the hydrogel composition optimisation experiment with alginate concentrations between 0.5 and 6.0 % w/v and  $\text{CaCl}_2$  concentrations between 0 and 50 mM.

As the Allevi 2 extrusion pressure was incrementally increased to a limit of 100 psi, samples exhibited one of three extrusion behaviours: stable flow (green), unstable flow (light grey) or non-flowing (dark grey). All alginate concentrations that were tested had stable flow when combined with  $\text{CaCl}_2$  concentrations of 20 mM or less. Specifically, the UC sample group was made up of entirely stable flow results regardless of alginate concentration. Each alginate concentration of PC samples that contained a  $\text{CaCl}_2$  concentration between 25 and 50 mM caused either unstable flow or flow prevention.

It was observed that, as alginate concentration increased, the concentration of  $\text{CaCl}_2$  could also be increased whilst maintaining stable flow. For example, 5.5 % w/v alginate produced stable flow with  $\text{CaCl}_2$  concentrations up to 45 mM whereas for 0.5 % w/v alginate, exceeding 15 mM  $\text{CaCl}_2$  concentration resulted in non-flow. Certain alginate concentrations such as 2.0 and 3.5 % w/v contained outliers of this trend whereby unstable flow was observed in high  $\text{CaCl}_2$  concentrations however no flow was achieved in neighbouring samples with increased alginate concentrations (using the same  $\text{CaCl}_2$  concentration). Once an alginate concentration produced either unstable flow or no flow, further increases of  $\text{CaCl}_2$  did not produce stable flow. Instances of unstable flow in 1, 2 and 3 % alginate stopped flowing altogether with further  $\text{CaCl}_2$  concentration increase.

## Extrudability

		Calcium Chloride Concentration (mM)										
		0	5	10	15	20	25	30	35	40	45	50
Alginate Concentration (% wt/v)	0.5	Green	Green	White	Green	White	Dark Grey	White	Dark Grey	White	Dark Grey	White
	1	Green	White	Green	White	Green	White	Light Grey	White	Dark Grey	White	Dark Grey
	1.5	Green	Green	White	Green	White	Green	White	Dark Grey	White	Dark Grey	White
	2	Green	White	Green	White	Green	White	Green	White	Light Grey	White	Dark Grey
	2.5	Green	Green	White	Green	White	Green	White	Dark Grey	White	Dark Grey	White
	3	Green	White	Green	White	Green	White	Green	White	Light Grey	White	Dark Grey
	3.5	Green	Green	White	Green	White	Green	White	Light Grey	White	Light Grey	White
	4	Green	White	Green	White	Green	White	Green	White	Dark Grey	White	Dark Grey
	4.5	Green	Green	White	Green	White	Green	White	Green	White	Light Grey	White
	5	Green	White	Green	White	Green	White	Green	White	Green	White	Dark Grey
	5.5	Green	Green	White	Green	White	Green	White	Green	White	Green	White
	6	Green	White	Green	White	Green	White	Green	White	Green	White	Light Grey

Figure 5.4: Results of the extrudability test for hydrogel compositions of varying alginate concentration (% w/v) and calcium chloride concentration (mM). Green represents a composition that exhibited stable extrusion with a constant speed and no interruptions such as sputtering. Light grey represents a composition that produced unstable extrusion with observations such as varying flow rate, sputtering or temporary blockages. Dark grey represents a composition that was unable to achieve ongoing flow using extrusion pressures of 100 psi or less and became blocked for the remainder of the extrusion duration.

### 5.2.3. Extrusion Form

Figure 5.5 shows the results of the extrusion form section of the hydrogel composition optimisation experiment which contains alginate concentrations between 0.5 & 6.0 % w/v and CaCl<sub>2</sub> concentrations between 0 & 50 mM. Compositions that produced unstable flow



or non-flow in the previous extrudability test in Section 5.2.2 were not tested further and remained exempt. Samples were repeatedly extruded briefly over 20s, and the nozzle cleaned in between, using their previously determined pressure settings to observe whether samples produced liquid-like droplets or solid-like fibres post-extrusion.

All UC alginate samples produced a liquid-like droplet form despite increased alginate concentrations. PC compositions with alginate concentrations between 3 and 6 % w/v all displayed fibre forms post-extrusion. In contrast, PC compositions between 0.5 and 2.5 % w/v alginate concentrations with 5 mM CaCl<sub>2</sub> all displayed droplet forms. Additionally, 0.5 %/15 mM, 1.0 %/20 mM and 1.5 %/25 mM all displayed droplet material forms post-extrusion.

## Drop vs Fibre Formation

		Calcium Chloride Concentration (mM)										
		0	5	10	15	20	25	30	35	40	45	50
Alginate Concentration (% w/v)	0.5	Red	Red	White	Red	White	Dark Grey	White	Dark Grey	White	Dark Grey	White
	1	Red	White	Green	White	Red	White	Light Grey	White	Dark Grey	White	Dark Grey
	1.5	Red	Red	White	Green	White	Red	White	Dark Grey	White	Dark Grey	White
	2	Red	White	Green	White	Green	White	Green	White	Light Grey	White	Dark Grey
	2.5	Red	Red	White	Green	White	Green	White	Dark Grey	White	Dark Grey	White
	3	Red	White	Green	White	Green	White	Green	White	Light Grey	White	Dark Grey
	3.5	Red	Green	White	Green	White	Green	White	Light Grey	White	Light Grey	White
	4	Red	White	Green	White	Green	White	Green	White	Dark Grey	White	Dark Grey
	4.5	Red	Green	White	Green	White	Green	White	Green	White	Light Grey	White
	5	Red	White	Green	White	Green	White	Green	White	Green	White	Dark Grey
	5.5	Red	Green	White	Green	White	Green	White	Green	White	Green	White
	6	Red	White	Green	White	Green	White	Green	White	Green	White	Light Grey

Figure 5.5: Extrusion forms for hydrogel compositions of varying alginate concentration (% w/v) and calcium chloride concentration (mM). Green represents a solid-like extrusion form which presented material post-extrusion in the form of a fibre which would readily move away from the nozzle as further extruded material pushed it away. Red represents a liquid-like extrusion form that would pool at the tip and slowly build up as further material was extruded until a droplet detached and fell away. Compositions highlighted in white were not tested due to implementation of a fractional factorial experimental design. Compositions highlighted in light grey and dark grey were excluded as they produced unstable flow and non-flowing results respectively from the previously conducted extrusion test, hence were unsuitable.

### 5.2.4. Extrusion Pressure

The extrusion pressure results of the hydrogel composition optimisation can be seen in Figure 5.6 using alginate concentrations of 0.5 – 6.0 % w/v and CaCl<sub>2</sub> concentrations of 0 –

50 mM. Compositions that previously were not capable of producing stable flow as per the extrudability test in Section 5.2.2 were omitted. Printing occurred in lines of 0.5 mm width and 0.2 mm height with a nozzle speed of  $10 \text{ mms}^{-1}$ . The previously established estimate for extrusion pressure was finetuned through trial-and-error printing until a suitable pressure was found that provided the correct flow rate to accurately deposit material as desired.

There was a clear and distinct trend that as alginate concentration increased amongst both UC and PC compositions, extrusion pressure continually increased. The two exceptions were the 1.5 %/5 mM and 2.5% compositions which had marginally lower pressures than neighbouring compositions with lower alginate concentrations. Both the UC group and PC groups follow a loose exponential trend where rate of extrusion pressure increased with higher alginate concentrations. This effect was greatest for PC compositions, particularly ones with central calcium concentrations in the tested ranges e.g. 1.5 %/ 15 mM and 5.5 %/25 mM.

As alginate concentrations were combined with increasing calcium amounts, another clear trend was seen where extrusion pressures continually increase and then decrease. The point of maximum extrusion pressure was consistently located as a central calcium value in the differing ranges per alginate concentration such as 0.5 %/5 mM and 6 %/20 mM. 5.5 %/5 mM was an exception to this rule where a marginal extrusion pressure decrease was seen compared to the 5.5 % UC composition.

		Calcium Chloride Concentration (mM)										
		0	5	10	15	20	25	30	35	40	45	50
Alginate Concentration (% w/v)	0.5	0.6	2.5		0.6							
	1	0.8		4.0		0.6						
	1.5	1.4	2.4		4.0		1.7					
	2	2.5		9.2		6.3		4.6				
	2.5	1.7	5.4		11.1		7.4					
	3	5.3		17.5		13.4		10.4				
	3.5	8.7	9.8		20.5		18.0					
	4	10.0		23.5		24.2		20.8				
	4.5	15.2	16.9		30.5		31.1		30.0			
	5	19.5		31.3		34.9		30.2		28.3		
	5.5	21.2	21.0		39.2		39.2		36.4		33.4	
	6	22.9		43.1		53.4		40.5		36.9		

Figure 5.6: Extrusion pressure (psi) for various hydrogel compositions of varying alginate concentration (% w/v) and calcium chloride concentration (mM). This was the pressure required to extrude the correct volume of material for a line width 0.5 mm, height of 0.2 mm and nozzle speed of 10 mms<sup>-1</sup>. Compositions highlighted in white were not tested due to implementation of a fractional factorial experimental design. Compositions highlighted in light grey and dark grey were excluded as they produced unstable flow and non-flowing results respectively from the previously conducted extrusion test, hence were unsuitable. A linear 2-colour scale was then applied using 0 psi as the lower limit and the highest value of 53.4 psi as the upper limit, coloured with green and red respectively.

## 5.2.5. Layer Formation and Retention

Figure 5.7 shows the results of the layer formation and retention test section of the hydrogel composition optimisation where alginate concentrations of 0.5 – 6.0 % w/v and CaCl<sub>2</sub> concentrations of 0 – 50 mM were assessed. Compositions that were not capable of extruding with stable flow as per Section 5.2.2 were omitted. Each composition was used to 3D print a stress test lattice detailed in Section 4.4.5 comprised of multiple layers of individual lines. Experimental setup and print settings remained the same between compositions however extrusion pressure was changed to personalised results obtained in Section 5.2.4. Hydrogel compositions that were not able to form distinct layers were the poorest quality. Representative images of each layer formation and retention classification can be seen in Figure 5.8. The complete set of images can be found in the appendix (Figure 10.4 – Figure 10.14).

## Layer Formation & Retention

		Calcium Chloride Concentration (mM)										
		0	5	10	15	20	25	30	35	40	45	50
Alginate Concentration (% wt/v)	0.5											
	1											
	1.5											
	2											
	2.5											
	3											
	3.5											
	4											
	4.5											
	5											
	5.5											
	6											

Figure 5.7: Layer formation and retention of hydrogel compositions with alginate concentrations of 0.5 – 6 % (w/v) and calcium chloride concentrations of 0 – 50 mM. Light blue colouring represents a composition that was not seen to form fibres/layers and instead exhibited liquid-like pools. Red and amber colouring represent compositions that formed fibres however post-extrusion these were seen to collapse at < 2 s and between 2 – 10 s respectively. Green represents a composition that formed fibres and these fibres were not seen to collapse during the 10 s observation window. White indicates compositions that were not tested due to implementation of a fractional factorial experimental design. Compositions highlighted in light grey and dark grey were excluded as they produced unstable flow and non-flowing results respectively from the previously conducted extrusion test, hence were unsuitable.

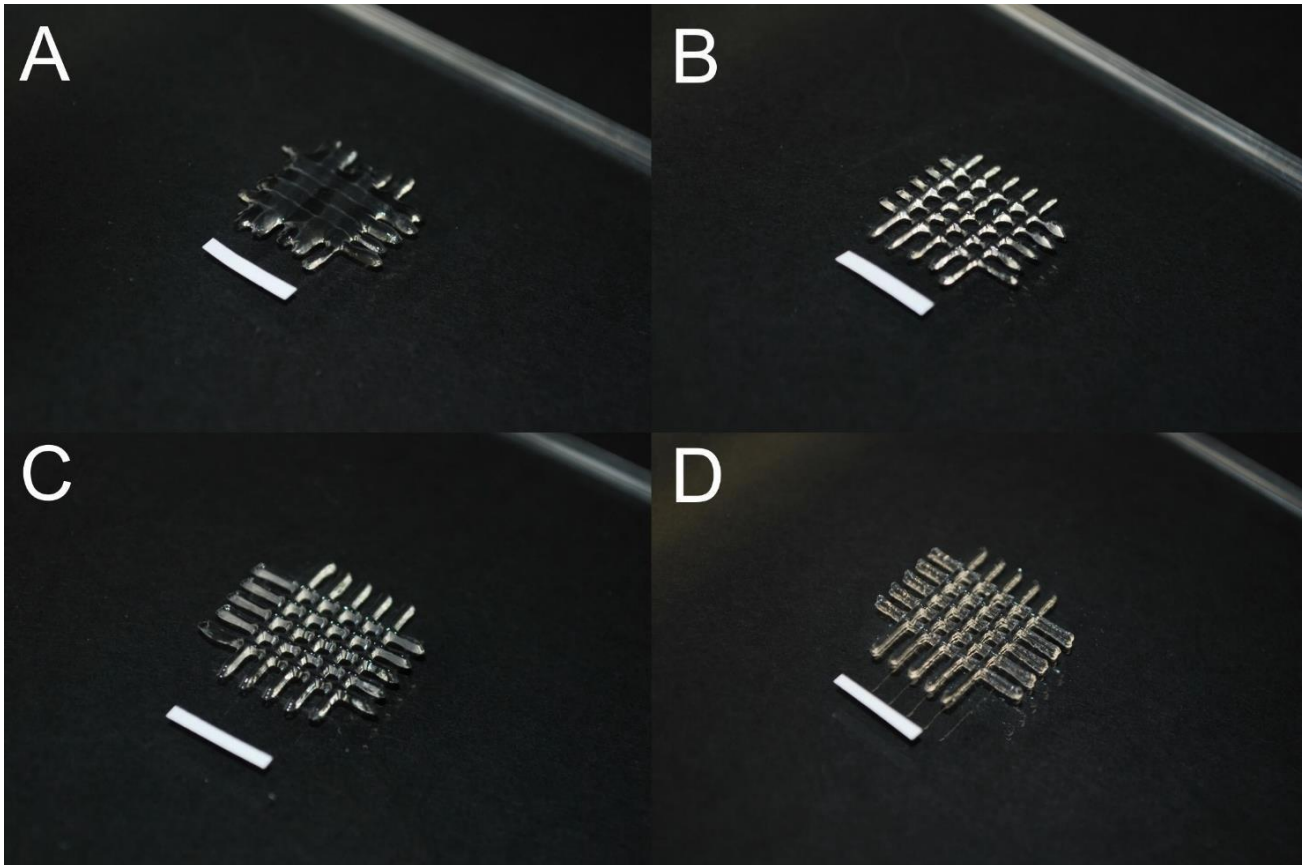


Figure 5.8: 3D printed lattice stress test models ( $20 \times 20 \times 1.2$  mm). Composition 1.5 %/25 mM did not form layers (A), 2.5 %/15 mM formed layers which collapsed after  $< 2$  s (B), 2 %/20 mM formed layers that collapsed after 2 – 10 s (C) and 4 %/25 mM formed layers that did not collapse over 10 s post-print (D). were captured using a digital camera with an attached polarising filter. Scale bar = 10 mm.

Generally, as both alginate and calcium concentrations increased above minimum values, hydrogel compositions exhibited improved layer formation and retention quality. This formed a loose cone-shaped trend where, at higher alginate concentrations, many compositions performed well, however, at lower concentrations, the range of compositions that performed well decreased. An increase of alginate concentration in the 0 mM UC group had no effect on layer quality with all compositions being unable to form distinct layers. This was the same for all PC hydrogels that contained 5 mM  $\text{CaCl}_2$ . Excluding these, all other results where distinct layers could not be formed were observed in samples with 1 – 1.5 % (w/v) alginate. Central calcium concentration values of these ranges performed better (10 – 15 mM), however, formed distinct layers that were still only retained for  $< 2$  s.

Excluding 5 mM calcium compositions, alginate concentrations of 2 – 6.0 % (w/v) had a clear trend of higher frequency of higher quality layer formation and retention as alginate

concentrations increased. Two exceptions to this were the 4 %/10 mM and 5 %/10 mM compositions which perform worse than their weaker alginate content counterpart, 3 %/10 mM. In higher alginate concentrations such as 5.5 – 6 % (w/v), increased CaCl<sub>2</sub> concentration above 5 mM have no further effect with all samples capable of forming and retaining distinct layers for > 10 s.

### 5.2.6. Viscosity

Results of the viscosity section of the hydrogel composition optimisation experiment can be seen in Figure 5.9 which include alginate concentrations between 0.5 – 6 % (w/v) and calcium concentrations between 0 – 50 mM. Hydrogel compositions that did not produce stable flow when previously tested for extrusion capabilities were omitted as per Section 5.2.2. Approximately 1 ml of sample was loaded onto the rheometer which used a 25 mm CP. Temperature was maintained at 20 °C and a shear rate of s<sup>-1</sup> was applied for 10 s after which sample viscosity was recorded to avoid sample inertial effects.

The general trend was that as alginate concentration increased, viscosity increased. This increase was less notable in UC samples compared to PC samples. UC samples followed an exponential trend except for the 1 % hydrogel which was marginally less viscous than 0.5 %. This exponential trend was broadly mimicked in PC samples at any CaCl<sub>2</sub> concentration except in the 35 mM and 40 mM where a trend cannot be seen due to omissions. 5 %/10 mM was an exception to this rule as it had a lower viscosity than the weaker alginate composition of 4 %/10 mM



### Viscosity, $\mu$ (Pa·s)

		Calcium Chloride Concentration (mM)										
		0	5	10	15	20	25	30	35	40	45	50
Alginate Concentration (% wt/v)	0.5	0.302	17.001		4.585							
	1	0.287		41.578		4.298						
	1.5	0.866	21.627		56.630		14.499					
	2	2.418		169.727		71.562		32.696				
	2.5	6.930	36.512		196.518		115.438					
	3	12.252		246.719		240.438		153.895				
	3.5	28.062	109.218		384.500		302.496					
	4	31.164		729.469		474.828		292.969				
	4.5	45.494	124.283		924.984		489.954		497.542			
	5	61.030		678.836		729.105		581.819		529.796		
	5.5	82.938	162.827		811.512		779.329		672.527		598.655	
	6	109.230		632.405		764.282		705.954		680.701		

Figure 5.9: Viscosity results for hydrogel compositions with alginate concentrations of 0.5 – 6 % (w/v) and calcium chloride concentrations of 0 – 50 mM. Samples were loaded onto a rheometer using a 25 mm plate-plate, temperature was maintained at 20 °C and a shear rate of  $1 \text{ s}^{-1}$  was applied. After 10 s, the value for viscosity (Pa·s) was recorded to avoid potential inertial effects. Compositions highlighted in white were not tested due to implementation of a fractional factorial experimental design. Compositions highlighted in light grey and dark grey were excluded as they produced unstable flow and non-flowing results respectively from the previously conducted extrusion test, hence were unsuitable. A linear 2-colour scale was then applied using 0 Pa·s as the lower limit and the highest value of 924.984 Pa·s as the upper limit, coloured with green and red respectively. Mean value plotted,  $n = 3$ .

As alginate concentrations were combined with increasing concentrations of calcium, viscosity increases and then later decreases with further increases. The greatest viscosity

at any given alginate concentration were consistently located in a central value of the calcium concentrations used for that alginate concentration such as 0.5 %/5 mM and 6 %/20 mM. Interestingly, the 4.5 %/15 mM composition had the greatest individual viscosity despite having neighbouring compositions with greater amounts of alginate, which typically increased viscosity.

## 5.3. Rheology

Of the 72 samples initially tested within the hydrogel composition optimisation, 7 of these were selected for rheological characterisation: UC 1, 3 & 5 % and PC 2 %/30 mM, 3 %/30 mM, 4 %/30 mM and 5 %/30 mM. These were selected to provide rheological data for a range of both UC and PC samples that displayed different material characteristics in Section 5.2.

### 5.3.1. Constant Shear

Figure 5.10 shows the results of the constant shear rheology experiment which was a uni-directional experiment used to measure viscosity of a sample. Samples were loaded into the rheometer using a 25 mm CP with a testing height of 0.104 mm and allowed to rest for 30 s. A shear rate of  $1 \text{ s}^{-1}$  was applied for 10 seconds at a temperature of 20 °C whilst measurements were collected every 0.5 s.

As seen in Figure 5.10 there were no substantial overall changes in viscosity for any samples during the test however some exhibited visible changes between 0.5 and 1s. All three UC samples and the 5 %/30 mM sample exhibited increases in viscosity whereas the remainder of PC samples did not. Note that the viscosity for the 1 % sample was recorded as negative (-0.076 Pa·s) at 0.5s hence omitted from the logarithmic axis. For both UC and PC groups, as alginate concentration increased, viscosity increased. Additionally, viscosities for PC 3 % and 5 % samples were larger than their UC counterparts with the same alginate

concentration.

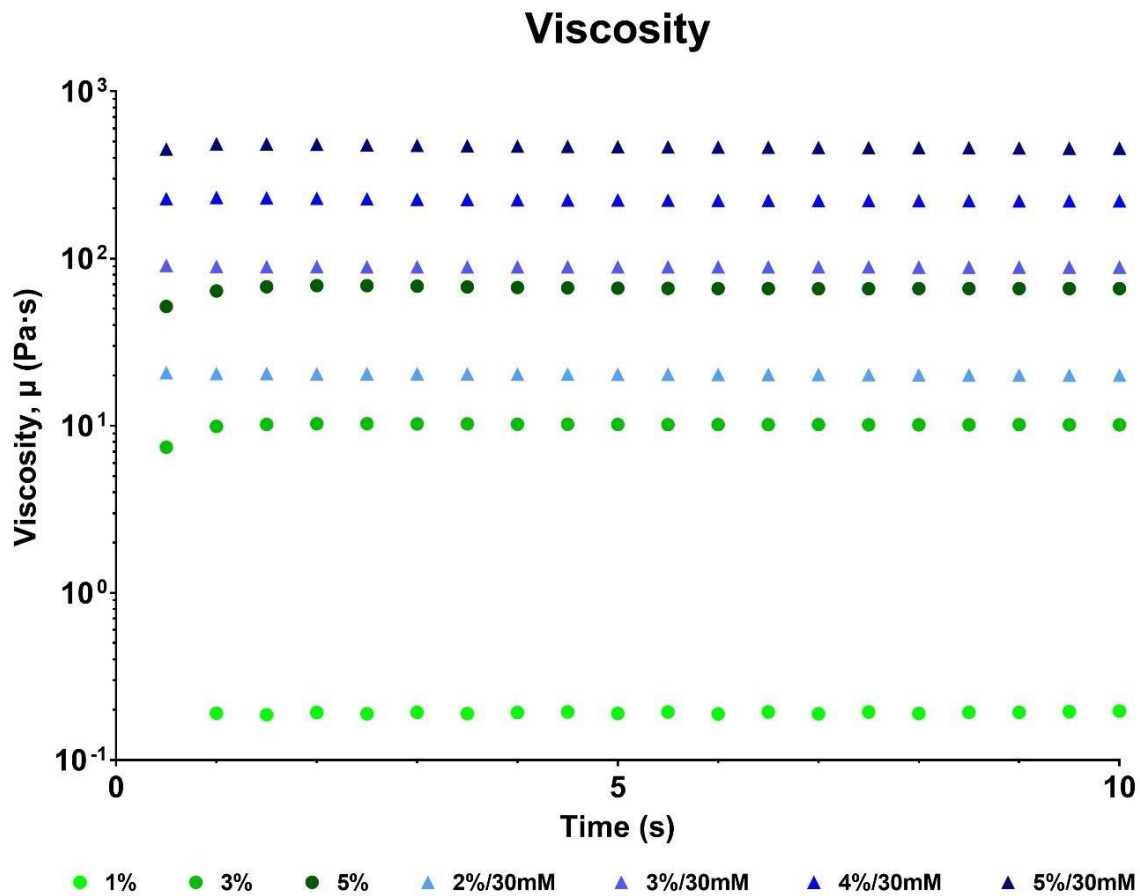


Figure 5.10: Viscosities of three UC alginate samples (1 %, 3 % & 5 % w/v) and four PC samples (2 %/30 mM, 3 %/30 mM, 4 %/30 mM & 5 %/30 mM w/v). A shear rate of  $1 \text{ s}^{-1}$  was applied and measurements recorded every 0.5 s over 10 s whilst temperature was maintained at 20 °C. Note: At 0.5 s the 1 % w/v sample was recorded as a negative value of -0.076 Pa·s. Mean value plotted,  $n = 3$ .

Initial and final viscosity values are displayed in Table 5.5 with the corresponding percentage changes and CoV values calculated from Section 4.5.3. Mean initial viscosity values and final viscosity values increased exponentially for both UC samples and crosslinked samples.

Table 5.5: Comparison of viscosity results from the initial and final measurement from the constant shear experiment.  $n = 3$ .

Sample	Initial Viscosity (Pa-s)		Final Viscosity (Pa-s)		Viscosity Change (%)	Initial % CoV	Final % CoV
	Mean	SD	Mean	SD			
1 %	-0.07	0.054	0.2	0.001	-385.71	-70.48	0.59
3 %	7.44	0.128	10.13	0.152	36.16	1.73	1.5
5 %	51.67	1.682	66.08	2.253	27.88	3.26	3.41
2 %/30 mM	20.75	2.82	22.03	1.588	6.16	13.59	7.93
3 %/30 mM	90.97	2.252	88.92	1.175	-2.25	2.48	1.32
4 %/30 mM	228.03	1.282	221.16	1.517	-3.01	0.56	0.69
5 %/30 mM	451.92	9.519	457.15	7.359	1.16	2.11	1.61

UC samples had considerably greater viscosity change over the 10 s test duration, particularly the 1 % sample, compared to their PC counterparts. The 1 % and 2 %/30 mM samples had unsatisfactory initial viscosity CoV values ( $> 10$  %) whereas other samples were acceptable. In contrast, all final viscosity CoV values were found to be satisfactory. The exponential trends for final viscosity measurements are plotted in Figure 5.11.

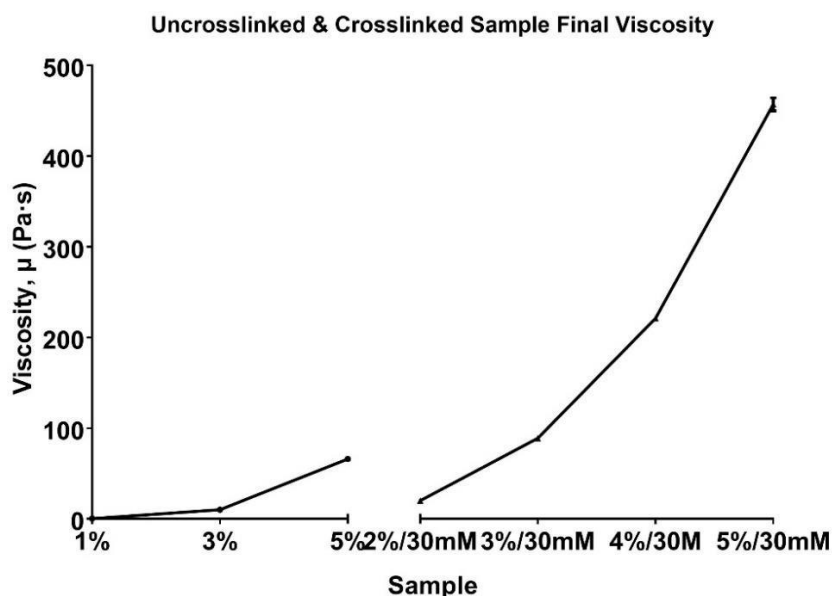


Figure 5.11: Comparison of final viscosity values after 10 s of an applied shear rate of  $1 \text{ s}^{-1}$  at  $20 \text{ }^\circ\text{C}$  including UC samples (1 %, 3 % & 5 % w/v) and PC samples (2 %/30 mM, 3 %/30 mM, 4 %/30 mM & 5 %/30 mM). Mean and SD are plotted samples besides 5 %/30 mM have an SD small enough that it lies behind plot symbols.

### 5.3.2. Amplitude Sweep

As discussed in Section 4.5.4, the amplitude sweep was the first oscillatory rheology experiment, the aim of which was to understand how samples behaved across a wide range of strains. Samples were loaded into the rheometer using a 25 mm CP with a testing height of 0.104 mm and allowed to rest for 30 s. A frequency of 1 Hz was used and temperature of 20 °C whilst strain was incrementally increased from 0.01 % to 1,000 % using a logarithmic ramp that provided 6 measuring points per decade.

Broadly speaking, Figure 5.12 shows that all  $G'$  and  $G''$  values decreased as strain increased. However, for the 1 % sample, this was marginal in comparison to others. All samples exhibited an area of little to no change in  $G'$  and  $G''$  values up until a specific strain value although this point varied drastically between samples. For example, this occurred at approximately 800 % strain for the 1 % sample, 80 % strain for the 5 % sample and 1 % strain for the 2 %/30 mM sample.

After this point, the 3 % and 5 % samples exhibited a temporary increased rate of reduction for  $G'$  and  $G''$ , seen as a curve, which then appeared to stabilise to another linear relationship. The same can be observed in the  $G'$  values for all PC samples however initially in each case there was a brief region between approximately 1 % and 30 % strain where  $G''$  increased, before decreasing afterwards. These eventually overlapped for all samples at strain values between approximately 9 % to 30 %. After this point, where  $G'$  and  $G''$  overlap, they continually diverged in all PC samples as  $G'$  was reduced by a greater amount than  $G''$ . This was also observed in the 3 % and 5 % UC samples after the end of the initial linear trend.

## Storage & Loss Moduli

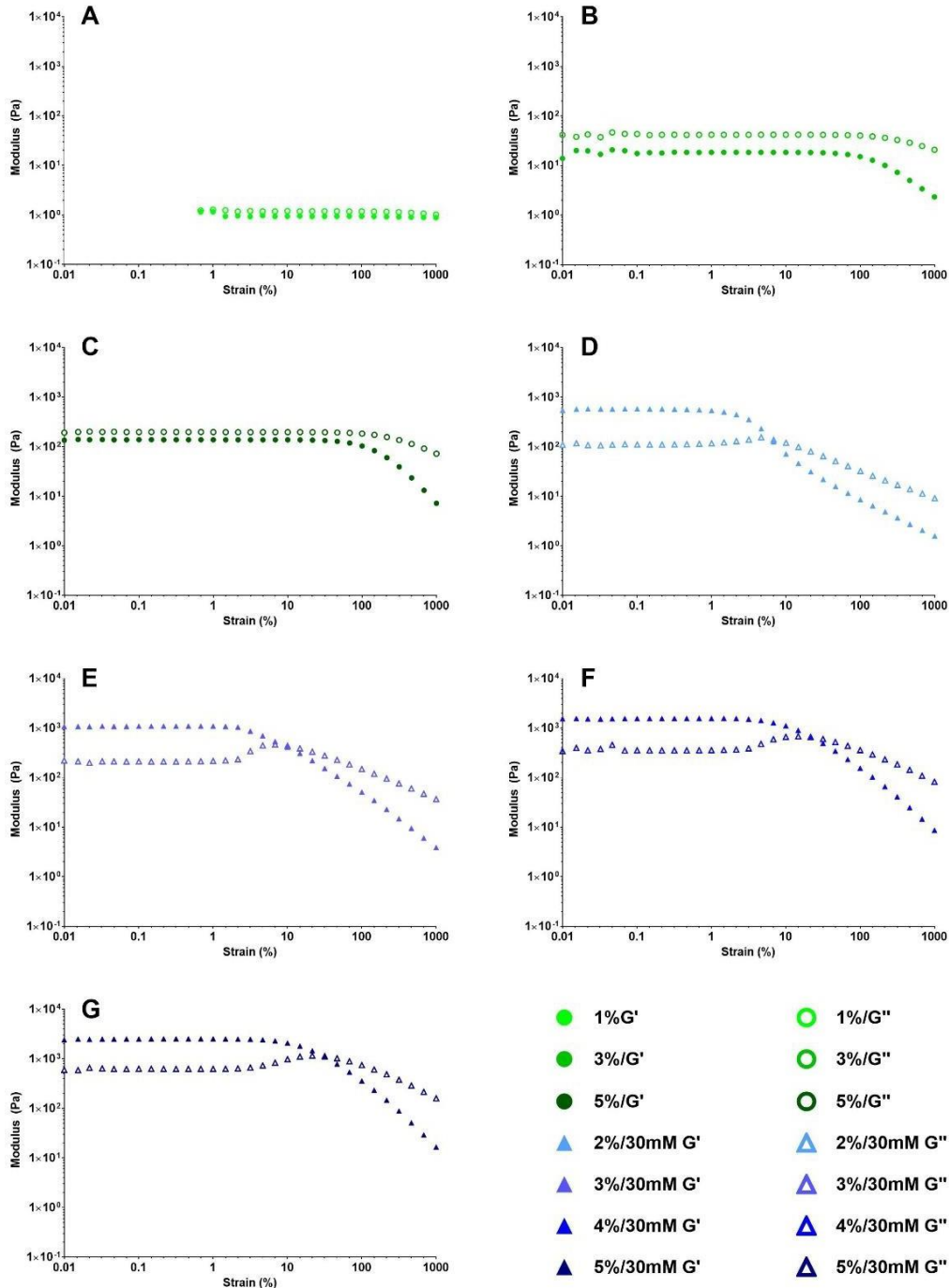


Figure 5.12: Storage ( $G'$ ) and loss ( $G''$ ) moduli outputs of the amplitude sweep conducted on UC samples 1 %, 3 % & 5 % (w/v) and PC samples 2 %/30 mM, 3 %/30 mM, 4 %/30 mM & 5 %/30 mM (w/v). Frequency was set to 1 Hz and temperature maintained at 20 °C whilst strain was continually increased from 0.01 % to 1,000 % through a logarithmic ramp that allowed for 6 measuring points per decade. The 1 % sample had points below 0.68 % strain omitted as these were observably inaccurate due to low SNR. Mean value plotted,  $n = 3$ .

At all strain values for all UC samples the modulus of  $G''$  was always greater than  $G'$  although this was marginal in low strain values for 1 %. In contrast, all PC samples had  $G'$  values that were greater than  $G''$  up until the point where the linear relationship began to change. These eventually overlapped for all samples at strain values between approximately 9 % to

30 %.

Below 0.68 % strain, the 1 % sample exhibited highly erratic data which due to a considerably low SNR at these points and were omitted, which is common practice in amplitude sweeps. Similar observations were seen below 0.1 % strain for the 3 % sample however this noise was within an acceptable range.

As previously explained in Section 4.5.4, Rheoplus was then used to analyse the LVER limit of samples using a  $G'$  tolerance of  $\pm 10\%$  and automatically apply the linear equation method to provide an improved  $\gamma_L$  and  $G'_L$  estimates. These results can be seen in Table 5.6 below.

*Table 5.6: Analysis was performed within RheoPlus (Anton Paar) using a tolerance of  $\pm 10\%$  of  $G'$  as per ASTM D7175 and DIN 51810 to determine the limit of the LVER for UC and PC samples. Mean and standard deviation are provided ( $n = 3$ ). 1 All results for the UC 1 % sample were invalid. 2 One of three technical repeats for the UC 3 % sample was invalid so the data was omitted.*

Tested hydrogel Sample	Calculated limit of LVER		Rheoplus analysis recommended $\gamma$ for testing within the LVER (%)
	$\gamma_L$ (%)	$G'_L$ (Pa)	
1 %	N/A <sup>1</sup>	N/A <sup>1</sup>	N/A <sup>1</sup>
3 %	N/A <sup>2</sup>	N/A <sup>2</sup>	N/A <sup>2</sup>
5 %	27.58 $\pm$ 13.31	131.80 $\pm$ 1.32	10
2 %/30 mM	0.86 $\pm$ 0.14	539.23 $\pm$ 17.16	0.5
3 %/30 mM	1.63 $\pm$ 0.11	1030.90 $\pm$ 40.23	1.0
4 %/30 mM	2.81 $\pm$ 0.72	1474.33 $\pm$ 12.42	1.0
5 %/30 mM	3.98 $\pm$ 1.07	2371.67 $\pm$ 70.88	1.0

Rheoplus recommended a LVER strain value slightly lower than the calculated  $\gamma_L$  estimate so that a reasonable margin of error could be tolerated. A lower LVER strain than recommended would have a negligible effect on samples that recommended higher values as it would remain within their LVER, just further from the limit. Different strain settings were not used as, while this would maximise individual SNR, it would introduce another variable. Therefore, a 0.5 % strain value was used in following rheological experiments as a suitable universal setting for all samples that could be used to perform non-destructive

testing. This had the potential to cause low SNR problems however was a calculated compromise.

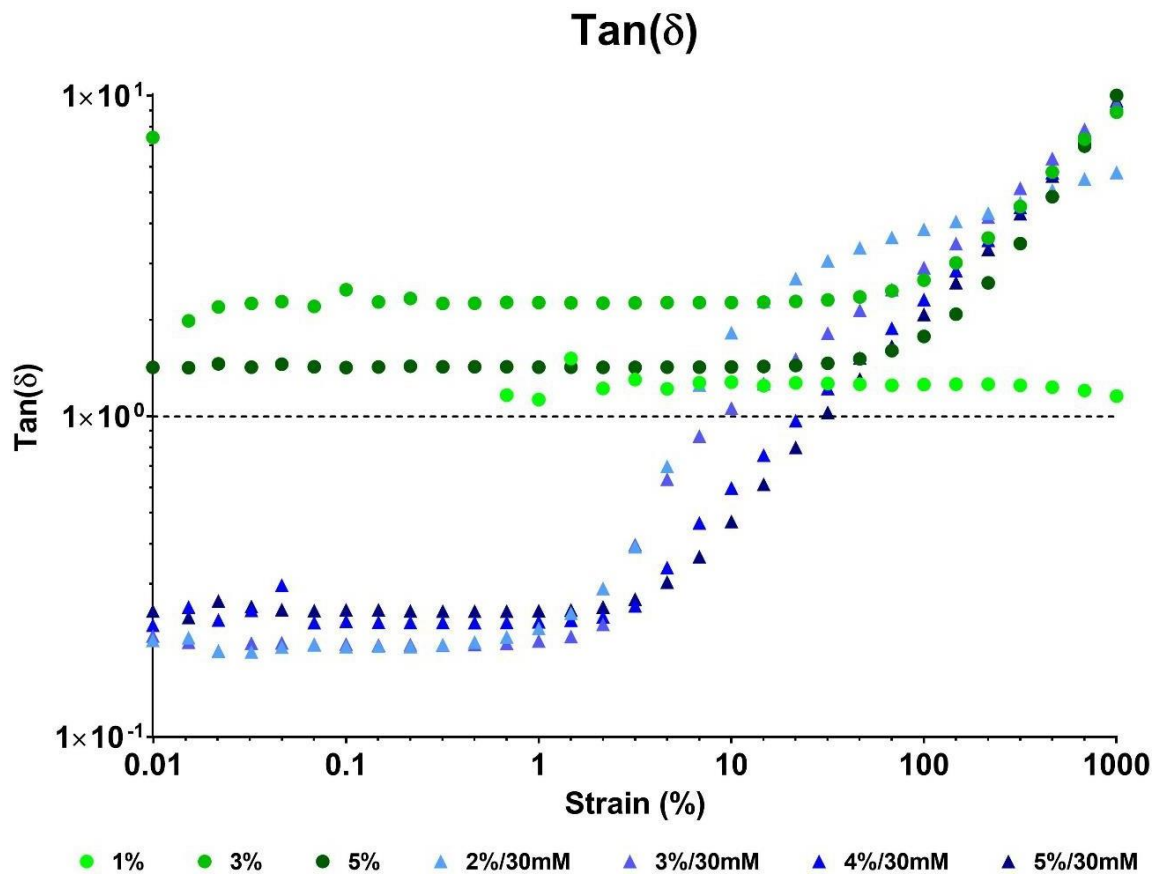


Figure 5.13:  $\text{Tan}(\delta)$  outputs for the amplitude sweep conducted on UC samples 1 %, 3 % & 5 % (w/v) and PC samples 2 %/30 mM, 3 %/30 mM & 5 %/30 mM (w/v). Frequency was set to 1 Hz and temperature maintained at 20 °C whilst strain was continually increased from 0.01 % to 1,000 % through a logarithmic ramp that allowed for 6 measuring points per decade. The 1 % sample had data points below 0.68 % strain omitted as these were observably inaccurate due to low SNR. Dashed line represents  $\text{tan}(\delta)$  of 1, values higher or lower than this are viscous-dominated and elastic-dominated respectively. Mean value plotted,  $n = 3$ .

As per Equation 1.4,  $\text{tan}(\delta)$  is a function of the relative  $G''$  and  $G'$  where the value was equal to 1 if they were the same size however increased towards infinity or decreased towards 0 as a material was increasingly viscous or elastic respectively. Below 0.68 % strain, the 1 % sample remained omitted due to previously mentioned erratic data due to suspected low SNR.

Figure 5.13 shows a clear distinction in  $\text{tan}(\delta)$  behaviour as strain was applied between the UC and PC groups. All UC samples remained at a  $\text{tan}(\delta)$  of  $> 1$  for the duration. PC samples had a  $\text{tan}(\delta)$  of  $< 1$  until approximately 5 % to 50 % strain where they increased to  $\text{tan}(\delta) >$



1 and continued to increase as strain was further increased.  $\tan(\delta)$  of PC samples began increasing between 0.5 % and 3 % strain which had previously not responded much to strain increase. Strain increase had no substantial effect on  $\tan(\delta)$  of the 3 % and 5 % UC samples until approximately 30 % strain where they both increased. In contrast, the 1 % UC sample  $\tan(\delta)$  was not affected by strain increased until approximately 500 % strain where it decreased.  $\tan(\delta)$  of the UC 3 % sample at 0.01 % strain was drastically different to the other presented patterns.

At low strain values of 0.7 % or less, PC samples presented a loose dose response of decreasing  $\tan(\delta)$  as alginate concentration decreased although 3 %/30 mM and 2 %/30 mM were too similar to differentiate meaningfully. Interestingly, UC samples did not present a similar dose response at low strain values. Instead, the UC 3 % alginate sample displayed the highest  $\tan(\delta)$  followed by 5 % and then 1 % except for at 1.46 % strain. Within the strain sections where  $\tan(\delta)$  was increasing for PC samples, different behaviours were also seen such as 2 %/30 mM and 3 %/30 mM forming curved, 'S-bend' trends whereas 4 %/30 mM and 5 %/30 mM had largely linear trends.

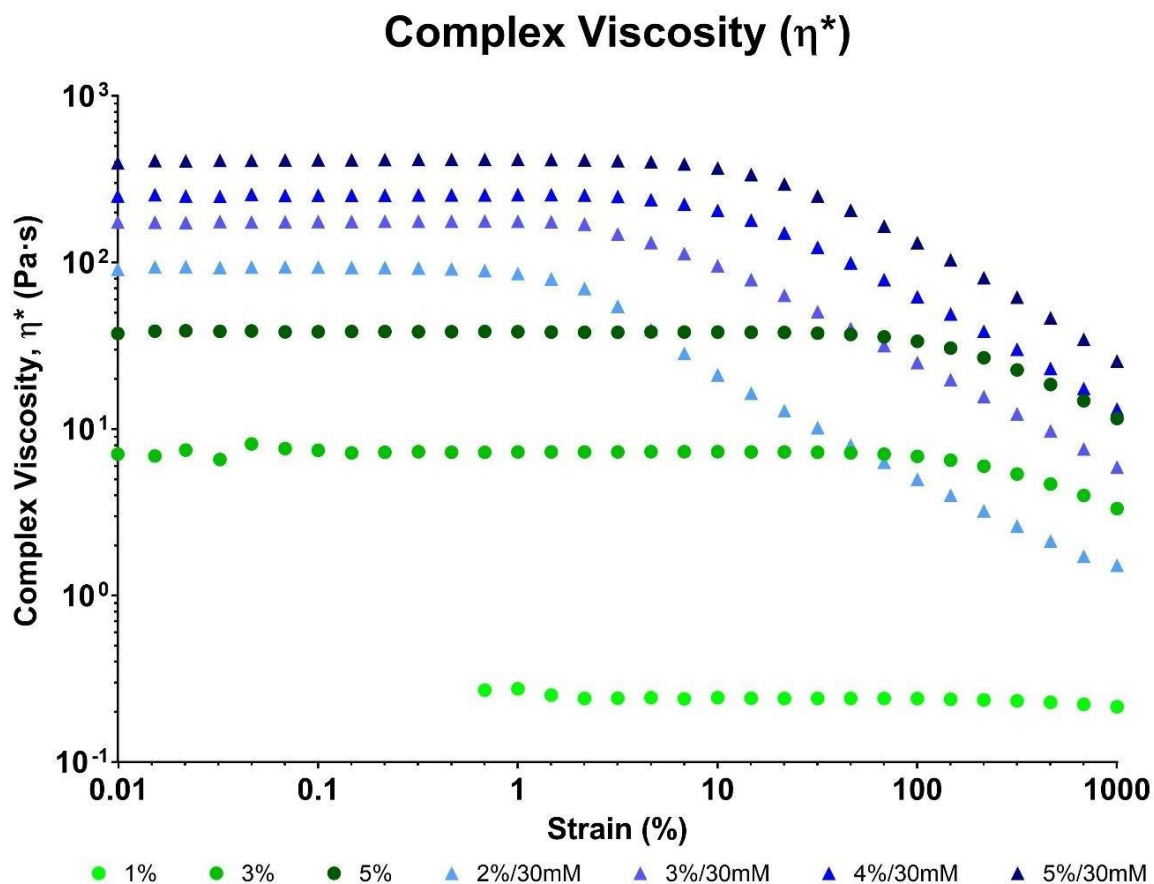


Figure 5.14: Complex viscosity ( $\eta^*$ ) outputs for the amplitude sweep conducted on UC samples 1 %, 3 % & 5 % (w/v) and PC samples 2 %/30 mM, 3 %/30 mM, 4 %/30 mM & 5 %/30 mM (w/v). Frequency was set to 1 Hz and temperature maintained at 20 °C whilst strain was continually increased from 0.01 % to 1,000 % through a logarithmic ramp that allowed for 6 measuring points per decade. The 1 % sample had data points below 0.68 % strain omitted as these were observably inaccurate due to low SNR. Mean value plotted,  $n = 3$ .

$\eta^*$  was calculated as per Equation 1.4 and was used in oscillation experiments like amplitude sweeps because it was far more suitable than rotational viscosity. While it was not the same calculation as conventional viscosity, it was comparable. As before, at strains below 0.68 %, the 1 % sample data was omitted due to previously mentioned erratic data due to suspected low SNR.

All samples had linear regions of  $\eta^*$  below strains of approximately 1 % where clear dose responses of increasing viscosity was seen where  $\eta^*$  increased as alginate concentration increased in both UC and PC samples. All PC had greater viscosities than any UC at strains of  $< 3\%$ .  $\eta^*$  of 2 %/30 mM fell below that of UC samples 3 and 5 % at approximately 3 % and 80 % strain respectively whereas 3 % / 30 mM also fell below 5 % at approximately 80 % strain. The UC 1 % sample had the least change across the range of strain values

however a marginal downward curve was observed past approximately 400 % strain.

Primary crosslinked samples exhibited roughly constant gradients of  $\eta^*$  reduction as strain increases above 1 % strain although slight curves were seen on the 2 %/30 mM sample as the trend gradient was reduced towards 1,000 %. Between 100 – 1,000 % strain,  $\eta^*$  reduction was lower in UC samples compared to crosslinked samples which was seen as relevant sample sets'  $\eta^*$  became closer as strain increased.

### 5.3.3. Frequency Sweep

A frequency sweep was performed following the amplitude sweep to understand how samples behaved across a wide range of frequencies using a set strain value that the amplitude sweep had found to be non-destructive. Samples were loaded into the rheometer using a 25 mm CP with a testing height of 0.104 mm and allowed to rest for 30 s. Using a strain of 0.5 % and temperature of 20 °C, oscillation frequency was then incrementally decreased from 100 to 0.01 Hz using a logarithmic ramp that provided 6 measuring points per decade. Figure 5.15 shows the  $G'$  and  $G''$  outputs of the test.

As frequency increased, all samples exhibited continuous increases in  $G'$  and  $G''$ . Crosslinked samples had considerably larger  $G'$  and  $G''$  values at low frequencies below approximately 1 Hz however, at frequencies above this, they had similar moduli. UC samples 3 % and 5 % had  $G' < G''$  at lower frequencies indicating viscous-dominated behaviour. However, as frequency increased, these intersected at 10 – 20 Hz after which  $G' > G''$  was clear for remaining, greater frequencies. 1 % was omitted below 1 Hz due to low SNR however, in remaining points,  $G' > G''$  was observed throughout, diverging more as frequency was increased.  $G''$  formed loose 'S-bend' trends in UC samples however  $G'$  was largely linear as frequency increased.

## Storage & Loss Moduli

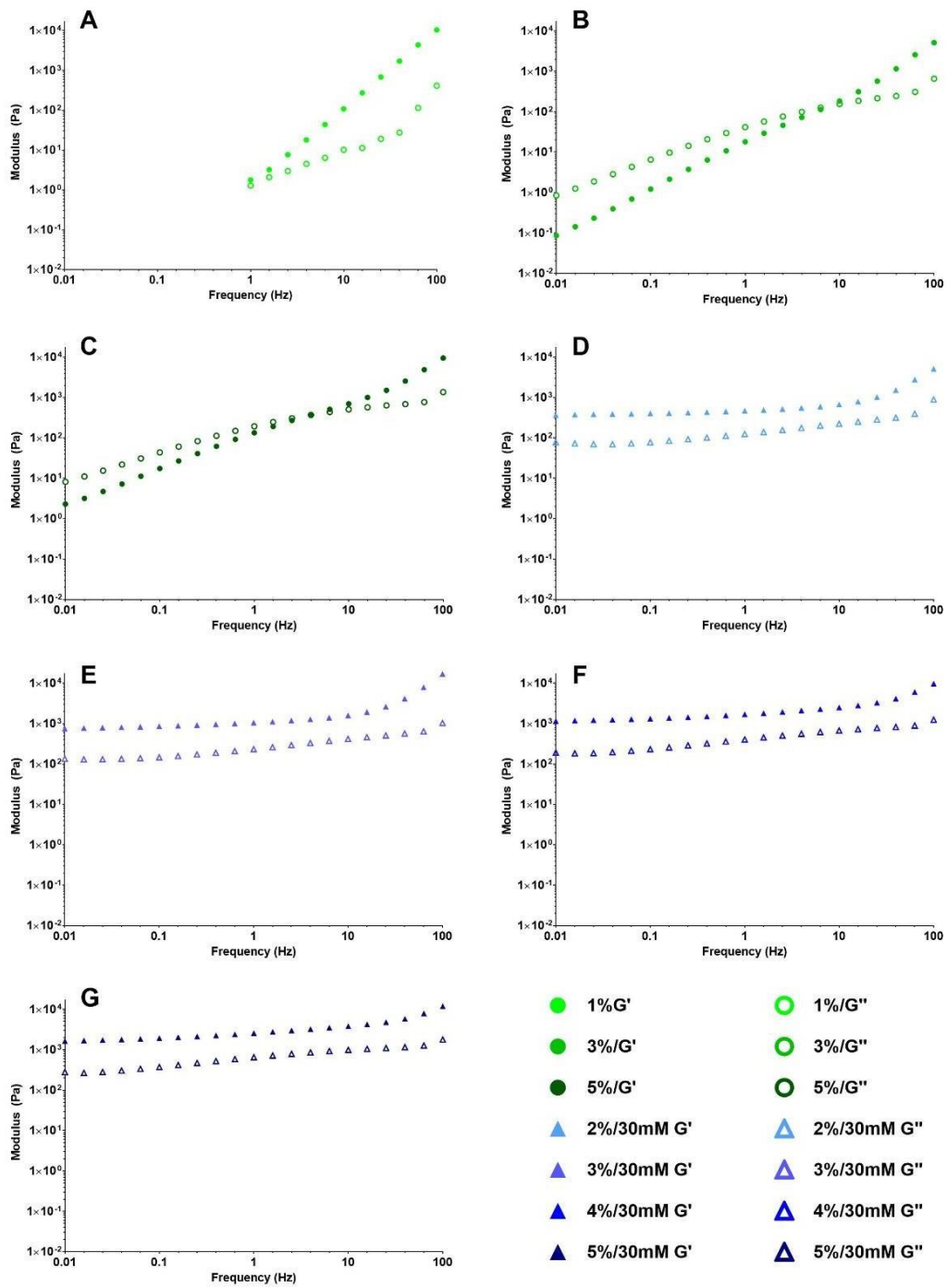


Figure 5.15: Storage ( $G'$ ) and loss ( $G''$ ) moduli outputs of the frequency sweep conducted on UC samples 1 % (A), 3 % (B) & 5 % (C) (w/v) and PC samples 2 %/30 mM (D), 3 %/30 mM (E), 4 %/30 mM (F) & 5 %/30 mM (G) (w/v). Strain was set to 0.5 % and temperature maintained at 20 °C whilst frequency was continually decreased from 100 to 0.01 Hz through a logarithmic ramp that allowed for 6 measuring points per decade. The 1 % sample had data points below 1 Hz omitted as these were observably inaccurate due to low SNR. Mean value plotted,  $n = 3$ .

In comparison, no PC samples displayed a crossover point for  $G'$  and  $G''$  at any of the tested frequencies and  $G' > G''$  was consistent throughout.  $G'$  and  $G''$  both steadily increased as frequency increased; however the gradient of this was much less compared to UC sample behaviour. Above approximately 30 Hz, the gradient for both  $G'$  and  $G''$  in all PC samples increased substantially. There were also minor convergences where the gap between  $G'$  and  $G''$  decreased during middle frequencies between approximately 1 and 10 Hz.

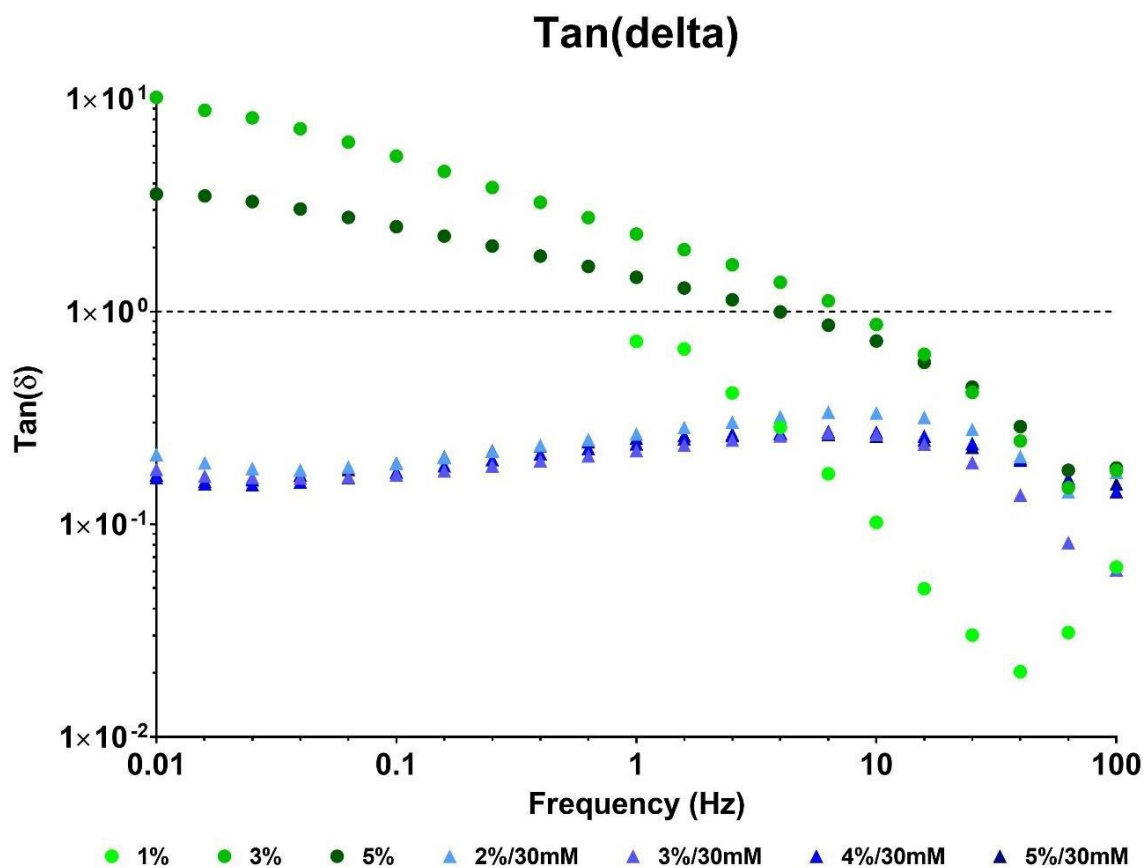


Figure 5.16:  $\text{Tan}(\delta)$  outputs for the frequency sweep conducted on UC samples 1 %, 3 % & 5 % (w/v) and PC samples 2 %/30 mM, 3 %/30 mM, 4 %/30 mM & 5 %/30 mM (w/v). Strain was set to 0.5 % and temperature maintained at 20 °C whilst frequency was continually decreased from 100 to 0.01 Hz through a logarithmic ramp that allowed for 6 measuring points per decade. The 1 % sample had data points below 1 Hz omitted as these were observably inaccurate due to low SNR. Dashed line represents  $\text{tan}(\delta)$  of 1, values higher or lower than this are viscous-dominated and elastic-dominated respectively. Mean value plotted,  $n = 3$ .

Figure 5.16 displays the  $\text{tan}(\delta)$  of alginate hydrogel samples. UC samples 3 % and 5 % were viscous-dominated (the former especially) but, as frequency increased, they presented steadily reduced values of  $\text{tan}(\delta)$  until a crossover point at approximately 10 and 4 Hz respectively. After this point, they continued to display reduced  $\text{tan}(\delta)$  as frequency

increased, at a slightly increased rate, until 40 Hz where they then slightly increased, breaking the trend. In comparison, the 1 % sample was solid-dominated for all valid data at frequencies  $\geq 1$  Hz.  $\tan(\delta)$  of 1 % reduced at a greater rate until 63 Hz thereafter it made a sharp upturn. At most frequencies there was no clear dose response between  $\tan(\delta)$  and alginate concentration however at 25 Hz and above, they were ordered so that as alginate concentration increased,  $\tan(\delta)$  also increased.

In contrast, PC samples behaved very differently. They were all relatively tightly grouped throughout the whole range of frequencies however at 40 Hz and higher, the 3 %/30 mM sample separated somewhat and  $\tan(\delta)$  was lower than the group. As frequency was increased from 0.01 to 0.025 Hz, all four PC samples appeared to display a flat-looking trend although 2 %/30 mM and 3 %/30 mM had marginal decreases in  $\tan(\delta)$ . As frequency increased from 0.025 Hz, all four PC samples steadily increased in  $\tan(\delta)$  until an apex between approximately 6.3 – 10 Hz;  $\tan(\delta)$  then decreased with additional frequency increase. Like UC 3 % and 5 %, PC samples exhibited an upturn at frequencies above 63 Hz except for 3 % / 30 mM which continued a downward trend in  $\tan(\delta)$ . There was no conclusive dose response amongst PC samples as alginate concentration increased, as there was not much difference between their values and the ordering changed erratically.

## Complex Viscosity

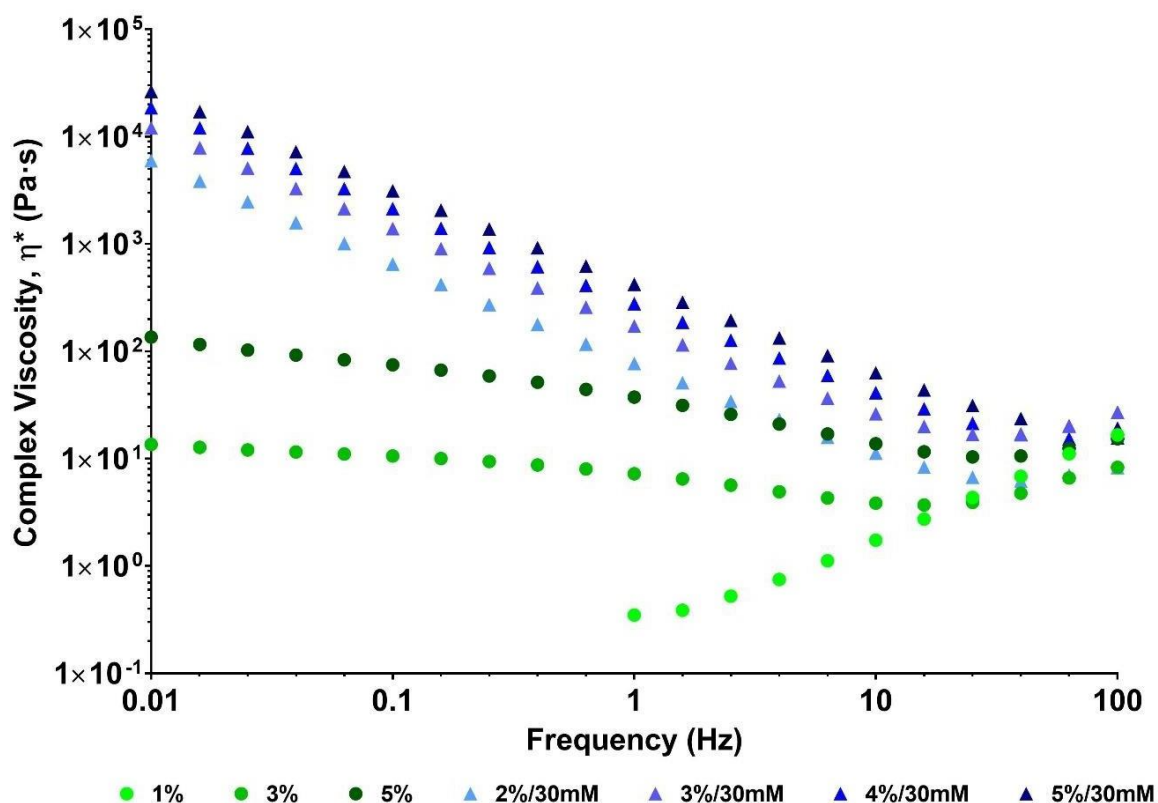


Figure 5.17: Complex viscosity ( $\eta^*$ ) outputs for the frequency sweep conducted on UC samples 1 %, 3 % & 5 % (w/v) and PC samples 2 %/30 mM, 3 %/30 mM, 4 %/30 mM & 5 %/30 mM (w/v). Strain was set to 0.5 % and temperature maintained at 20 °C whilst frequency was continually decreased from 100 to 0.01 Hz through a logarithmic ramp that allowed for 6 measuring points per decade. The 1 % sample had data points below 1 Hz omitted as these were observably inaccurate due to low SNR. Mean value plotted,  $n = 3$ .

Figure 5.17 shows the complex viscosity results for the frequency sweep. Up until 16 Hz, all samples followed the trend that as frequency was increased,  $\eta^*$  was reduced except for the UC 1 % sample which exhibited the opposite trend through its limited plotted range of 1 – 100 Hz. At frequencies of  $\geq 16$  and  $\geq 25$  Hz, UC 3 % and 5 % displayed reduced  $\eta^*$  respectively as frequency was further increased. The 2 %/30 mM and 3 %/30 mM PC samples mimicked this exception to the overall trend at frequencies of  $\geq 40$  Hz as did the 4 %/30 mM and 5 %/30 mM PC samples at frequencies of  $\geq 63$  Hz.

All UC samples displayed considerably lower  $\eta^*$  than PC samples at their lower ranges ( $< 10$  Hz for UC 1 % and  $< 1$  Hz for UC 3 % & 5 %) but this difference was reduced as frequency was increased. At frequencies of  $\leq 14$  Hz there was a clear dose response amongst UC samples that increased alginate concentration corresponds to greater  $\eta^*$ . Similarly, all PC

samples exhibited the same dose response but to a smaller degree at frequencies of  $\leq 40$  Hz. In comparison, PC samples had a greater reduction in  $\eta^*$  per frequency increase compared to their UC counterparts, as indicated by the lower gradient. There was also a much greater difference in  $\eta^*$  values, both between individual samples and separate sub-groups, however these converged as frequency was increased, particularly above 40 Hz.

#### 5.3.4. Temperature Sweep

A temperature sweep was the next stage in rheological characterisation of understanding how temperature affected material properties of alginate hydrogels. Samples were loaded into the rheometer using a 25 mm CP with a testing height of 0.104 mm and allowed to rest until the temperature had reached the starting value of  $5\text{ }^\circ\text{C} \pm 0.2$  before the test could begin. A strain of 0.5 % was then applied and frequency maintained at 1 Hz as the temperature was increased at a rate of  $0.2\text{ }^\circ\text{C s}^{-1}$  from 5 to  $70\text{ }^\circ\text{C}$  over 330 seconds. Figure 5.18 shows the  $G'$  and  $G''$  results of the temperature sweep.

Generally, as temperature increased throughout the experiment, UC samples mostly exhibited a reduction in  $G'$  and  $G''$  values whereas PC samples exhibited no change until higher temperatures above approximately  $50\text{ }^\circ\text{C}$ . The 1 % UC sample appeared to be influenced by noise due to the turbulence of the data however an overall trend was still extracted that  $G'' > G'$ , both of which reduced as temperature increased. The 3 % and 5 % also displayed  $G'' > G'$  and reductions in  $G'$  and  $G''$  however at approximately  $50\text{ }^\circ\text{C}$  the gradient of  $G''$  changed for both. For 3 % UC, this became positive and eventually crossed over with  $G'$  so that  $G' > G''$  whereas 5 % UC essentially flattened out so that no substantial changes to  $G''$  were observed with further temperature increase.



## Storage & Loss Moduli

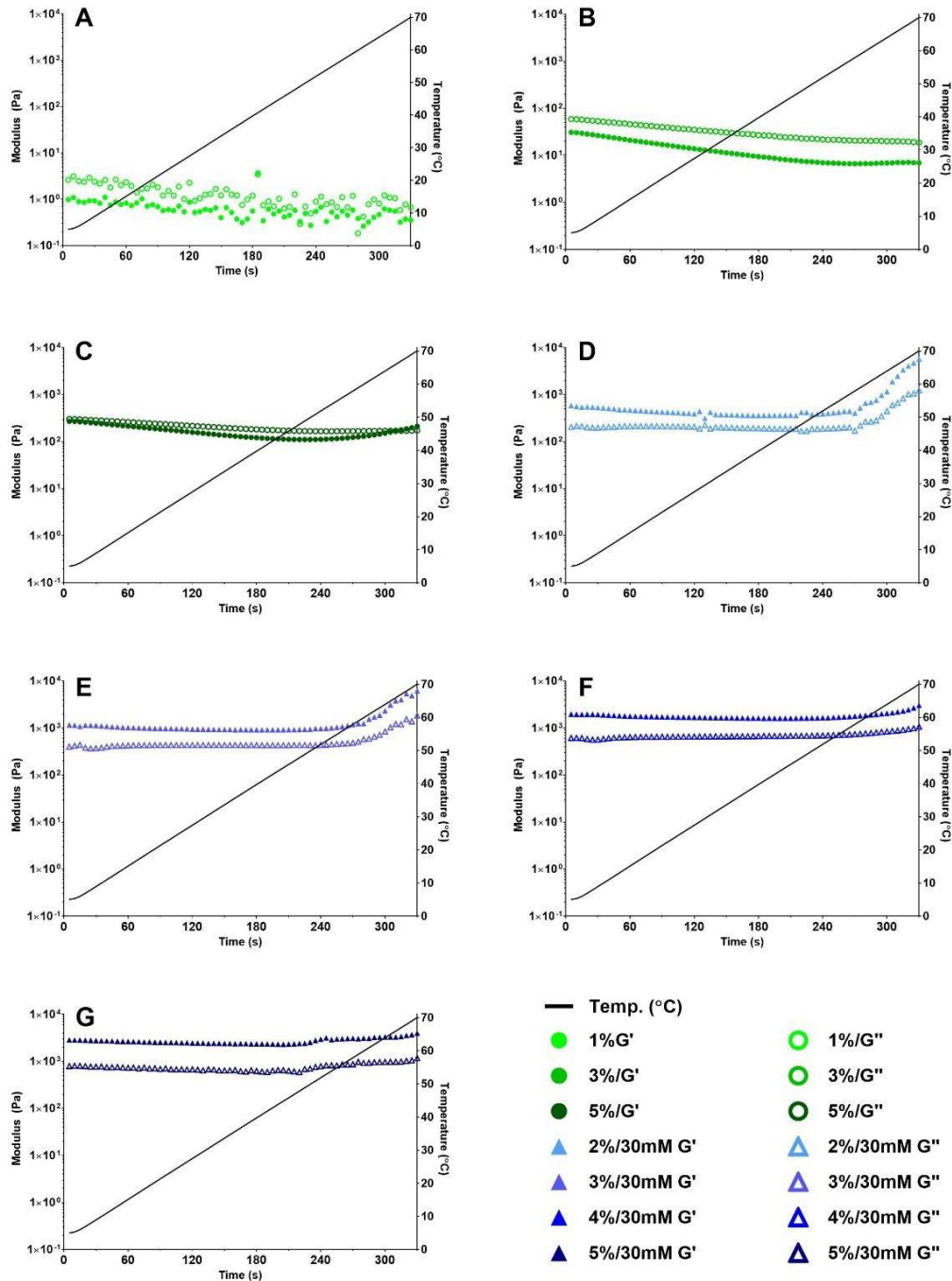


Figure 5.18: Storage ( $G'$ ) and loss ( $G''$ ) moduli outputs of the temperature sweep conducted on UC samples 1% (A), 3% (B) & 5% (C) (w/v) and PC samples 2%/30 mM (D), 3%/30 mM (E), 4%/30 mM (F) & 5%/30 mM (G) (w/v). Strain was set to 0.5% and frequency maintained at 1 Hz whilst measurements were recorded every 5 s. Initial temperature was set to 5  $^{\circ}\text{C}$  and was increased at a rate of 0.2  $^{\circ}\text{C s}^{-1}$  until a temperature of 70  $^{\circ}\text{C}$  was reached after 330 s. The solid black line indicates temperature at a given time, plotted on the right Y-axis. Mean value plotted,  $n = 3$ .

All PC samples maintain  $G' > G''$  at all temperatures. At lower temperatures below 40  $^{\circ}\text{C}$ , no substantial changes can be seen however there were some noticeable deviations at around 5  $^{\circ}\text{C}$  repeated in all PC samples except 5%/30 mM. Similarly, in all PC samples except 5%/30 mM, the gap between  $G'$  and  $G''$  was slightly decreased at temperatures below 40

°C. 5 %/30 mM displayed a minor reduction in  $G'$  and  $G''$  at these temperatures however the degree of separation was maintained. At approximately 55 °C, the 2 %/30 mM and 3 %/30 mM PC samples exhibited major increases to both  $G'$  and  $G''$  and results appeared more turbulent. This was mimicked in 4 %/30 mM and 5 %/30 mM PC samples to a lesser degree but at a greater temperature of approximately 65 °C. Across PC samples there appeared to be a loose pattern presented that, as alginate concentration increased, the relative increase of  $G'$  and  $G''$  at these higher temperatures was reduced.

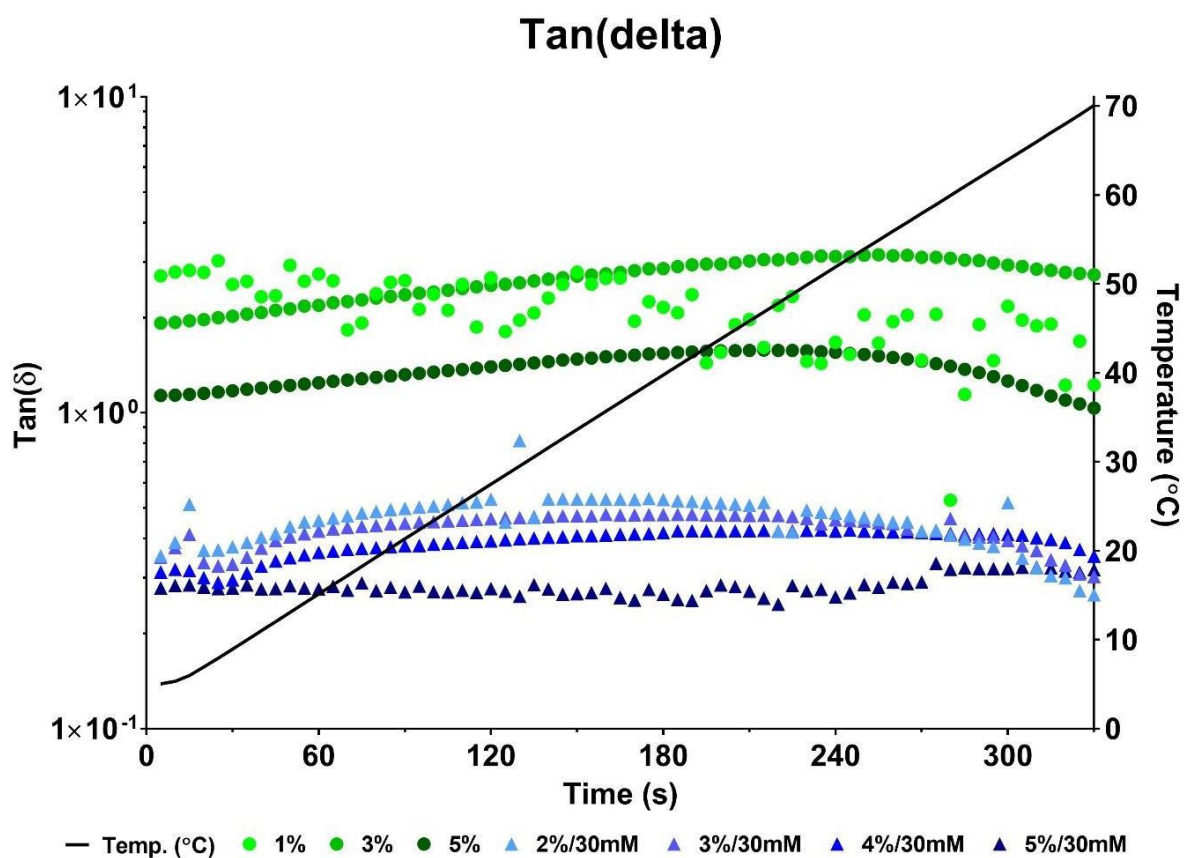


Figure 5.19:  $\text{Tan}(\delta)$  outputs of the temperature sweep conducted on UC samples 1 %, 3 % & 5 % (w/v) and PC samples 2 %/30 mM, 3 %/30 mM, 4 %/30 mM & 5 %/30 mM (w/v). Strain was set to 0.5 % and frequency maintained at 1 Hz whilst measurements were recorded every 5 s. Initial temperature was set to 5 °C and was increased at a rate of 0.2 °C s<sup>-1</sup> until a temperature of 70 °C was reached 330 seconds later. The solid black line indicates temperature at a given time, plotted on the right Y-axis. Mean value plotted,  $n = 3$ .

Figure 5.19 displays the  $\text{tan}(\delta)$  of the temperature sweep of tested alginate samples. There was a clear separation between the UC and PC groups where UC samples had a  $\text{tan}(\delta) > 1$  for the majority and PC samples had a  $\text{tan}(\delta) < 1$  throughout. The exceptions to the general UC sample rule were the 5 % UC results above 60 °C and a single 1 % UC outlying

data point at 60 °C where  $\tan(\delta)$  was much lower than all other 1 % UC data points. Separately, 2 %/30 mM present three potential anomalies at approximately 130, 220 and 300 where  $\tan(\delta)$  both deviates up or down, across multiple points, from an otherwise smooth trend.

As previously discussed, data for the 1 % UC appeared to contain considerable noise however a looser  $\tan(\delta)$  trend was still observed which decreased as temperature increased. 3 % and 5 % UC both presented increasing  $\tan(\delta)$  as temperature increased until a reversal around 50 °C. 3 % UC  $\tan(\delta)$  decreased to a final point which was greater than its beginning value whereas 5 % UC decreased at a greater rate to a crossover point at approximately 60 °C and continued to decrease past this.

Throughout increasing temperatures until approximately 55 °C there was a dose response across the PC samples that as alginate concentration increased,  $\tan(\delta)$  was reduced. Previously mentioned deviations were clearly seen at approximately 5 °C for the 2 %/30 mM and 3 %/30 mM PC samples where  $\tan(\delta)$  increased then decreased to form a slight 'S-bend' pattern. 4 %/30 mM PC appeared to exhibit this to a lesser degree without the large  $\tan(\delta)$  peak before the reduction. 5 %/30 mM PC may have presented a smaller peak as part of this pattern however this cannot be reliably distinguished from increased noise within the dataset compared to other PC samples.

Beyond this, for all PC samples except 5 %/30 mM,  $\tan(\delta)$  was shown to increase as temperature increased but then plateau and eventually reduce again after further temperature increase. The point in which the reduction in  $\tan(\delta)$  began differed between PC samples. This occurred at approximately 35 °C for 2 %/30 mM, 50 °C for 3 %/30 mM, 60 °C for 4 %/30 mM and 65 °C for 5 %/30 mM. This formed a secondary PC sample dose response that, as alginate concentration increased, the temperature that  $\tan(\delta)$  begins to reduce at was increased. At these higher temperatures above approximately 60-65 °C, the initial dose response no longer applied.

## Complex Viscosity

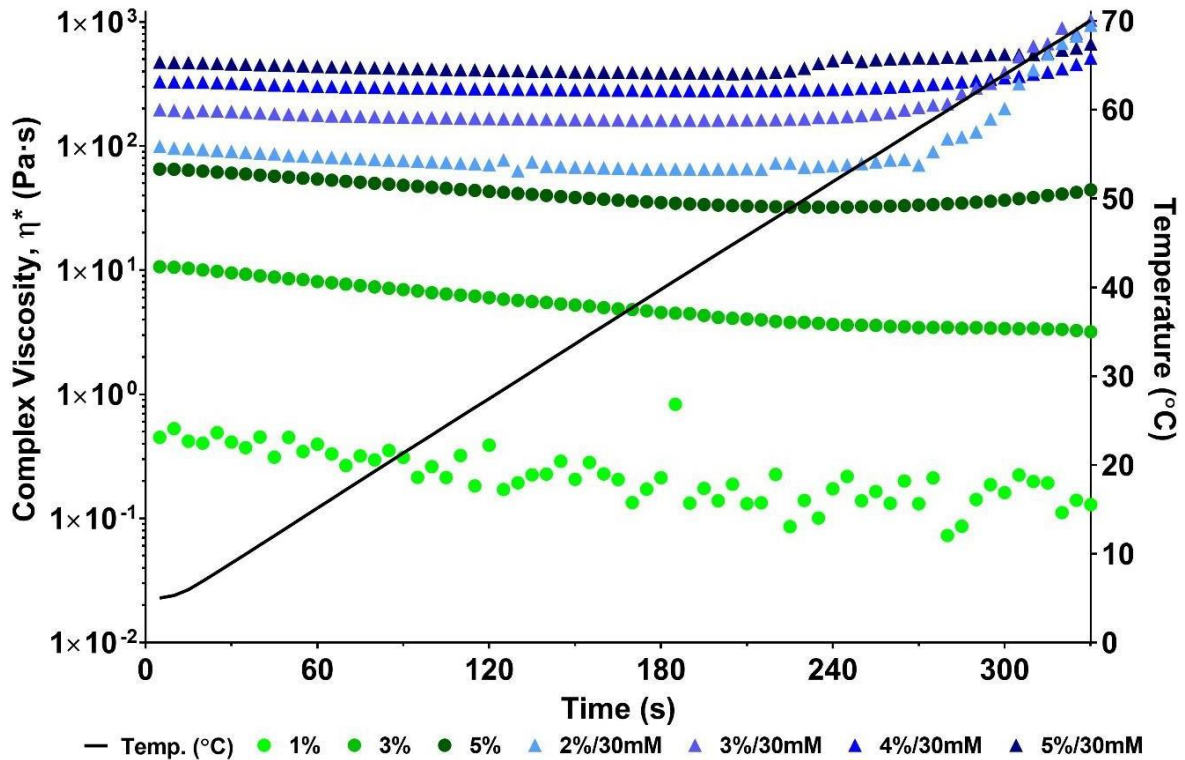


Figure 5.20: Complex viscosity ( $\eta^*$ ) outputs of the temperature sweep conducted on UC samples 1 %, 3 % & 5 % (w/v) and PC samples 2 %/30 mM, 3 %/30 mM, 4 %/30 mM & 5 %/30 mM (w/v). Strain was set to 0.5 % and frequency maintained at 1 Hz whilst measurements were recorded every 5 s. Initial temperature was set to 5 °C and was increased at a rate of 0.2 °C $s^{-1}$  until a temperature of 70 °C was reached 330 seconds later. The solid black line indicates temperature at a given time, plotted on the right Y-axis. Mean value plotted,  $n = 3$ .

Figure 5.20 shows the  $\eta^*$  results of the temperature sweep. Amongst UC samples there was a clear dose response that  $\eta^*$  increased as alginate concentration increased. As with the other temperature sweep results, the 1 % UC sample data set contained substantial noise. It also contained an individual outlier that was much greater in value than its neighbouring points, located at approximately 185 s. All UC samples exhibited reduced  $\eta^*$  as temperature increased, the rate of which decreased at temperatures above 40 °C. For 5 % UC specifically, this then increased above approximately 55 °C with further temperature increase.

PC samples exhibited greater  $\eta^*$  and were grouped closer together than their UC counterparts. PC samples also display the same dose response that  $\eta^*$  increased as alginate concentration increased however this did not apply above 60 °C. As temperature

was increased, all PC samples presented a slight decrease in  $\eta^*$  up to at least 20 °C although this was most visible for the 2 %/30 mM PC sample. As temperature was further increased, the other three PC samples then appeared to plateau and not respond to further temperature increase. For the 2 %/30 mM PC sample, however, a decrease in  $\eta^*$  was still observed with increasing temperatures until roughly 40 °C where it then also plateaued. The 2 %/30 mM PC dataset presented anomalies at 130 s and 220 s, like those seen in the associated  $\tan(\delta)$  results.

As temperature further increased, these plateau regions were interrupted. Firstly, a sudden increase in  $\eta^*$  for the 5 %/30 mM PC sample occurred at 50 °C which then plateaued again, something not mirrored in other samples. Similarly, to the  $\tan(\delta)$  results, each PC sample also has a point after which  $\eta^*$  increased as temperature was further increased. This occurred at approximately 50 °C for 2 %/30 mM & 3 %/30 mM, 55 °C for 4 %/30 mM and 65 °C for 5 %/30 mM. The precise location of these points appeared to differ slightly between the  $\tan(\delta)$  and  $\eta^*$  results however these were approximate locations.

### 5.3.5. 3-Interval Thixotropy Test

A 3ITT was ideal for better understanding the suitability of tested hydrogels for 3D printing as it simulated the high stresses that this would incur and determined what effect this had on material properties over time. Samples were loaded into the rheometer using a 25 mm CP with a testing height of 0.104 mm and allowed to rest for 30 s prior to the test starting. Throughout the test, frequency was maintained at 1 Hz and temperature at 20 °C whilst the strain was altered. The first and third intervals served as pre-excitation and post-excitation rest periods respectively that could be compared so used the non-destructive strain value of 0.5 %. The second interval was the excitation interval which increased from 1 % to 1,000 % using a logarithmic ramp to allow for 6 measuring points per decade. The first interval duration was from 0 – 120 s, second was 125 – 215 s and third 220 – 515 s. Figure 5.21 shows the  $G'$  and  $G''$  results for the 3ITT test.

As before, the 1 % UC sample had a high amount of noise compared to signal however overall trends were still observed. During the first interval,  $G'$  and  $G''$  appeared plateaued although relative moduli could not be distinguished reliably. During the second interval, SNR was higher and reliable, smooth trends began at approximately 3 % strain which displayed  $G'' > G'$  throughout. As strain increased above 100 %, both  $G'$  and  $G''$  slightly reduced. At the start of the third interval,  $G'$  and  $G''$  appeared to immediately mimic behaviour from the first interval and continued to do so for the remainder of the interval.

## Storage & Loss Moduli

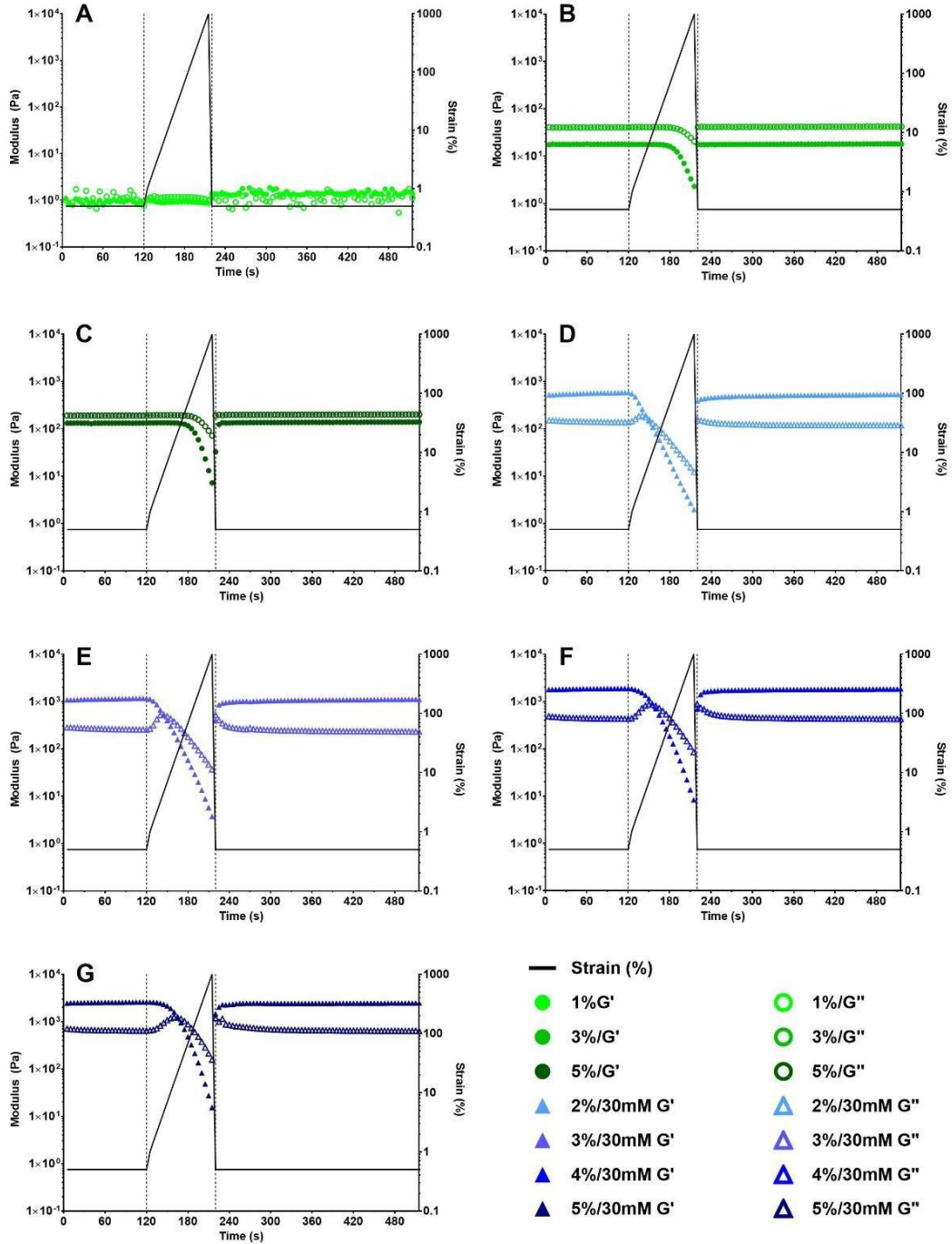


Figure 5.21: Storage ( $G'$ ) and loss ( $G''$ ) moduli outputs of the 3ITT conducted on UC samples 1 % (A), 3 % (B) & 5 % (C) (w/v) and PC samples 2 %/30 mM (D), 3 %/30 mM (E), 4 %/30 mM (F) & 5 %/30 mM (G) (w/v). A temperature of 20 °C and frequency of 1 Hz was maintained throughout the entire and measurements recorded every 5 seconds. During the first and third intervals, strain was set to a fixed value of 0.5 % however during the second interval strain was increased from 1 % to 1,000 % using a logarithmic ramp to allow for 6 measuring points per decade. The solid black line indicates strain at a given time, plotted on the right Y-axis whilst dashed vertical lines represent borders between intervals. Mean value plotted,  $n = 3$ .

The 3 % and 5 % UC samples' first intervals exhibited flat regions of  $G'$  and  $G''$  where moduli did not change. During the second interval no meaningful changes to this behaviour were seen until strain reached roughly 20-30 %. At this point both  $G'$  and  $G''$  started to



reduce exponentially as strain was further increased, although  $G'$  did this at a greater rate for both samples. During the third interval, the 3 % UC sample immediately returned to original resting values for  $G'$  and  $G''$  from the first interval and remained so for the remainder of the interval with no observable changes. The 5 % UC sample displayed evidence of time-dependence as, during the first 10 s of the third interval,  $G'$  was seen to be considerably reduced before returning to its original resting value from the first interval. Throughout all three intervals for the 3 % and 5 % UC samples  $G'' > G'$ .

All PC samples presented a first interval with  $G' > G''$ . Unlike 3 % and 5 % UC, shifts were seen in  $G'$  and  $G''$  through this stage with  $G'$  slightly increased and  $G''$  slightly decreased up until the start of the second interval. As alginate concentration increased amongst PC samples,  $G'$  and  $G''$  values increased. All four PC counterparts immediately responded to the increase of strain in the second interval compared to the delayed response in UC samples until much greater strains were used. All four PC samples presented a 'hump' at this stage where  $G''$  temporarily increases until it then reduced with further strain increases. Moduli increase for this 'hump' was greater with increasing alginate concentration. The peak was also located at greater strains as alginate concentration increased, at approximately 3 % for 2 %/30 mM & 3 %/30 mM, 6 % for 4 %/30 mM and 15 % for 5 %/30 mM.

The  $G'$  for PC samples 2 %/30 mM appeared as essentially a linear relationship during the second interval where  $G'$  reduced with increasing strain. The remaining PC samples also presented linear relationships in the second interval although began with a curved section where  $G'$  gradient increased exponentially. As alginate concentration increased, the strain range included within this exponential section increased. Within the linear regions of  $G'$  in latter sections of the second interval, the gradient of  $G'$  loss was markedly larger than  $G''$  loss in all PC samples. This produced a crossover point for each PC sample where  $G' < G''$  after a certain strain value which increased as alginate concentration increased. This was located at approximately 6 % for 2 %/30 mM & 3 %/30 mM, 15 % for 4 %/30 mM and



20 % for 5 %/30 mM.

As the third interval began, 2 %/30 mM & 5 %/30 mM PC immediately crossed over again such that  $G' > G''$  whereas 3 %/30 mM & 4 %/30 mM had a five second delay before which they continued to present  $G' < G''$  from the latter part of the second interval. Throughout the third interval,  $G'$  and  $G''$  of all four PC samples increased and decreased respectively. This initially occurred at a rapid rate, particularly during the first 30 s of the third interval, however rate of recovery (compared to final values at the end of the interval) lessened with increasing time, which formed a loose exponential decay form. Final third interval values of  $G'$  and  $G''$  were not drastically different to corresponding values from the end of the first interval for any PC sample.

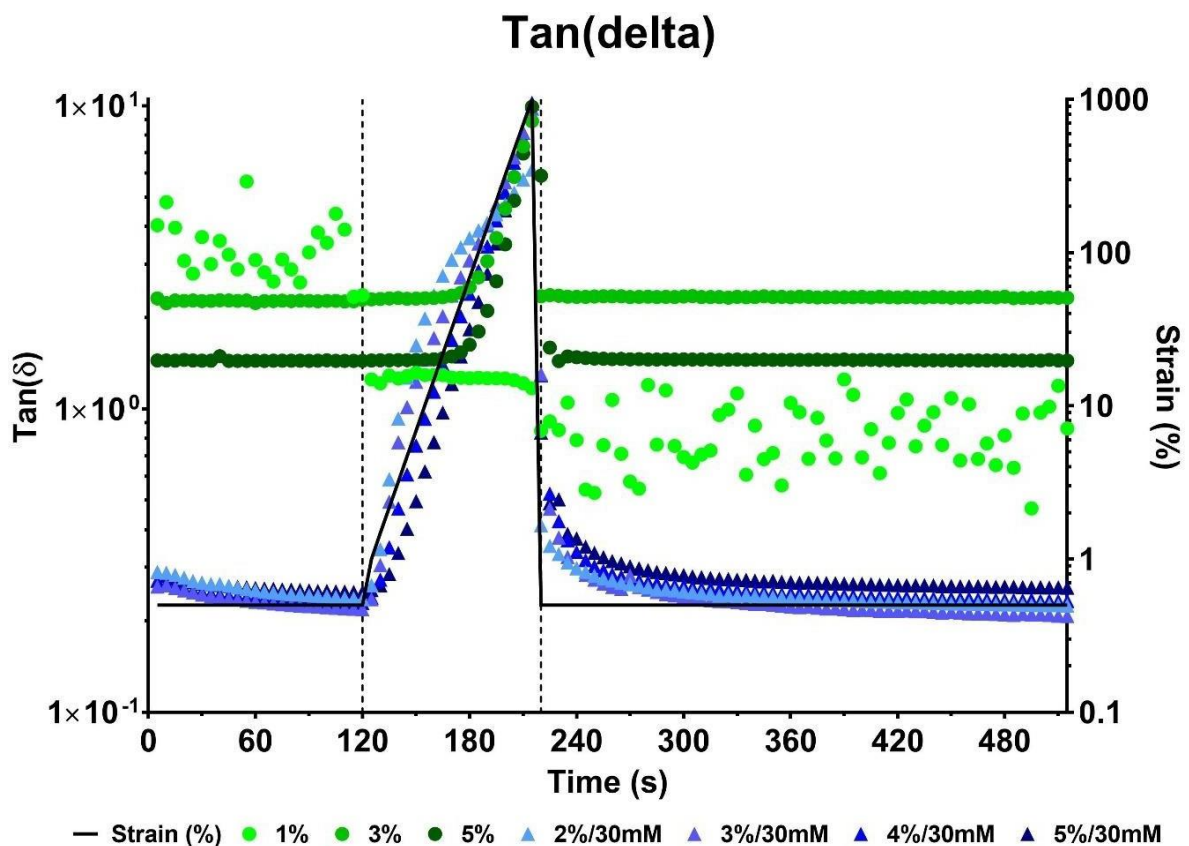


Figure 5.22:  $Tan(\delta)$  outputs of the 3ITT conducted on UC samples 1 %, 3 % & 5 % (w/v) and PC samples 2 %/30 mM, 3 %/30 mM, 4 %/30 mM & 5 %/30 mM (w/v). A temperature of 20 °C and frequency of 1 Hz was maintained throughout the entire and measurements recorded every 5 seconds. During the first and third intervals, strain was set to a fixed value of 0.5 % however during the second interval strain was increased from 1 % to 1,000 % using a logarithmic ramp to allow for 6 measuring points per decade. The solid black line indicates strain at a given time, plotted on the right Y-axis whilst dashed vertical lines represent borders between intervals. Mean value plotted,  $n = 3$ .

$Tan(\delta)$  results of the 3ITT are shown in Figure 5.22. UC and PC samples were seen to form distinct groups in the first and third interval. During the second interval, all samples except

1 % UC exhibited greatly increased  $\tan(\delta)$  with increasing strain. During the third interval, all samples except 1 % appeared to eventually return to their first interval values.

UC samples within the first interval presented lower  $\tan(\delta)$  with increasing alginate concentration. The 1 % UC sample, however, contained lots of noise within the first and third interval so only general trends could be estimated. 3 % and 5 % UC showed no time dependent change to  $\tan(\delta)$  during the first interval and no distinct trend was seen for 1 % UC either. Through interval 2,  $\tan(\delta)$  increased exponentially between approximately 10 to 100 % strain for 3 % and 5 % UC which then formed a loosely linear relationship with further strain increase. Within the latter section of the second interval, the rate of increase of  $\tan(\delta)$  was considerably greater for 5 % UC such that it was greater than the 3 % UC sample at 1,000 % strain.

The 1 % UC sample remained largely unchanged in the second interval until 200 % strain where it began to decrease at a lesser rate and with  $\tan(\delta) > 1$  being preserved. The 1 % UC sample changed behaviour in the third interval to predominantly display  $\tan(\delta) < 1$  with no clear time dependency. 3 % UC also showed no time dependency and immediately returned to a value equal to that from interval one for the interval entirety. 5 % UC initially had a much greater  $\tan(\delta)$  in the third interval, compared to its values from the first interval, and then displayed slight decreases in  $\tan(\delta)$  for approximately 30s seconds. It then reached a resting value for the remainder of the interval, equal to that of the first interval.

The four PC samples were more tightly grouped than their UC counterparts and were not seen to be ordered in interval 1. They all exhibited  $\tan(\delta) < 1$  and showed time dependency of reducing  $\tan(\delta)$  as time continued through the first interval in an exponential decay form.  $\tan(\delta)$  was still reducing at the end of the first interval, not at a resting state. In contrast to UC samples, an increase in strain in the second interval immediately showed substantial increases in  $\tan(\delta)$  in all four PC samples. Below 10 % strain, the gradient of this increase was greater as alginate concentration was reduced amongst PC samples. Above 10 %

strain, the gradient of 2 %/30 mM & 3 %/30 mM varied to form S-bend patterns of which the former does so to a greater degree. In contrast, 4 %/30 mM & 5 %/30 mM formed largely linear relationships during the second interval as their  $\tan(\delta)$  values increased at a steady rate with increased strain. Overall, the PC samples'  $\tan(\delta)$  increased considerably more than the UC samples during the second interval. All four PC samples crossed over from  $\tan(\delta) < 1$  to  $\tan(\delta) > 1$  during the second phase between 3 – 20 % strain.

During the third interval, 2 %/30 mM & 5 %/30 mM PC samples initially retained  $\tan(\delta) > 1$  whereas 3 %/30 mM & 4 %/30 mM immediately reverted to  $\tan(\delta) < 1$ . All four PC samples then exhibited rapid decrease in  $\tan(\delta)$ , particularly during the first 30 – 60 s of the third interval. Rate of decrease of  $\tan(\delta)$  was reduced as time continued, forming another exponential decay pattern. After 120 s of interval three,  $\tan(\delta)$  values were effectively equivalent to the final values of the first interval. That said, a continued marginal decrease in  $\tan(\delta)$  was seen for all PC samples for the remainder of the interval. There was no ordering of PC samples'  $\tan(\delta)$  during the third interval.

## Complex Viscosity

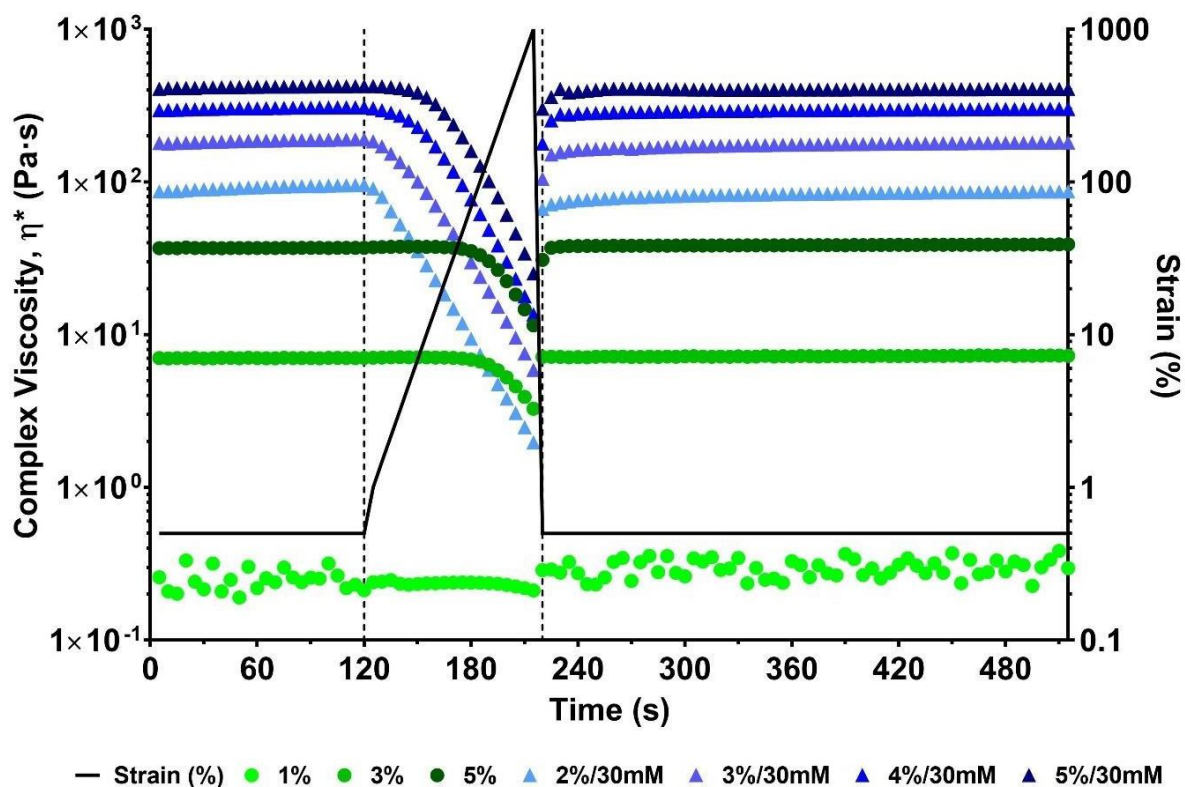


Figure 5.23: Complex viscosity ( $\eta^*$ ) outputs of the 3ITT conducted on UC samples 1 %, 3 % & 5 % (w/v) and PC samples 2 %/30 mM, 3 %/30 mM, 4 %/30 mM & 5 %/30 mM (w/v). A temperature of 20 °C and frequency of 1 Hz was maintained throughout the entire and measurements recorded every 5 seconds. During the first and third intervals, strain was set to a fixed value of 0.5 % however during the second interval strain was increased from 1 % to 1,000 % using a logarithmic ramp to allow for 6 measuring points per decade. The solid black line indicates strain at a given time, plotted on the right Y-axis whilst dashed vertical lines represent borders between intervals. Mean value plotted,  $n = 3$ .

Figure 5.23 shows the  $\eta^*$  results of the 3ITT experiment. During the first and third intervals, when a low strain of 0.5 % was applied,  $\eta^*$  of UC samples was lower than PC samples.  $\eta^*$  increased as alginate concentration increased in both UC and PC groups across all three intervals.

3 % and 5 % UC samples exhibited no changes to  $\eta^*$  throughout the first interval. The 1 % UC dataset contained noisy data but no overall changes were seen in interval 1. During the second interval, no major changes for 1 % or 3 % & 5 % UC were observed until roughly 100 % and 10 % strain respectively. After this point, the  $\eta^*$  of all UC samples was reduced with further strain increase. The greater the alginate concentration in UC samples, the greater the rate of decrease and corresponding overall  $\eta^*$  reduction during the second interval. At the beginning of the third interval, 1 % and 3 % immediately returned to their first

interval values with no further changes observed for the remainder of the interval. 5 % UC initially exhibited some retained  $\eta^*$  reduction for the first 20 s of the third interval before also returning to the original first interval value for the remainder of the interval.

Within interval one, all four PC samples displayed a consistent, slight increase in  $\eta^*$  as time progressed. These did not find a resting, steady state value by the end of the first interval. During the second interval, all four PC  $\eta^*$  were immediately and drastically reduced as strain values increased.  $\text{Tan}(\delta)$  of 2 %/30 mM & 3 %/30 mM exhibited linear relationships of this decrease and 4 %/30 mM & 5 %/30 mM formed brief curved regions at strains < 10 %, followed by linear regions thereafter. During the linear sections of  $\eta^*$  decrease during the second interval, all four PC samples appeared to maintain the same rate of  $\eta^*$  reduction. At the start of the third interval, all four PC samples immediately and radically regained  $\eta^*$  to similar values to the first interval. The rate of increase of  $\eta^*$  decreased as time continued where the majority of recovery occurred within 20 – 30 s. By 80 s into the third interval all four samples reached  $\eta^*$  values that were effectively the same as those from the first interval however  $\eta^*$  continued to marginally increase for the rest of the interval.

### 5.3.6. Post-mix Time Sweep

A post-mix time sweep was conducted to better understand the time-dependant material changes that occur to hydrogels after the primary-crosslinking process detailed in Section 4.2.2 which exerted considerable shear forces on materials. A 30-minute period had previously been allocated for materials to rest as an estimated duration but it was important to assess if this was sufficient or even necessary. Fresh PC hydrogels were produced immediately before testing but instead of the usual 30-minute resting period were used instantly. The UC samples were also mixed with the same method to eliminate unnecessary variables however no  $\text{CaCl}_2$  was present. Samples were then hastily loaded into the rheometer using a 25 mm CP with a testing height of 0.104 mm whilst ensuring fidelity. A

solvent trap with water was also used due to the extended duration of the experiment to mitigate evaporation within hydrogels. The experiment was then run using a frequency of 1 Hz, temperature of 20 °C and a non-destructive strain value of 0.5 %. The time at the start of the test was consistently 60 s post-crosslinking using this method.

Figure 5.24 shows the  $G'$  and  $G''$  results of the post-mix time sweep. Notably, omissions were made for  $G'/G''$ ,  $\tan(\delta)$  and  $\eta^*$  for the 1 % UC sample at 125 s, 910 s, 975 s and 1510 s for the third technical repeat, allowing for only two technical repeats at these times. These individual data points were deemed as erroneous outliers due to the vast difference between them and the rest of the dataset and the lack of corroborating neighbouring data. Appendix Figure 10.15 details a side-by-side comparison of original data versus the final data displayed here with omissions presents.

The 1 % UC sample was noisy and hard to distinguish separate  $G'$  and  $G''$  values however a roughly flat trend was seen for the duration of the test. The 3 % and 5 % UC samples showed no time dependency across the duration of the test and  $G'' > G'$  throughout. An increase in alginate concentration in UC samples corresponded to increased  $G''$  and  $G'$  resting values.

## Storage & Loss Moduli

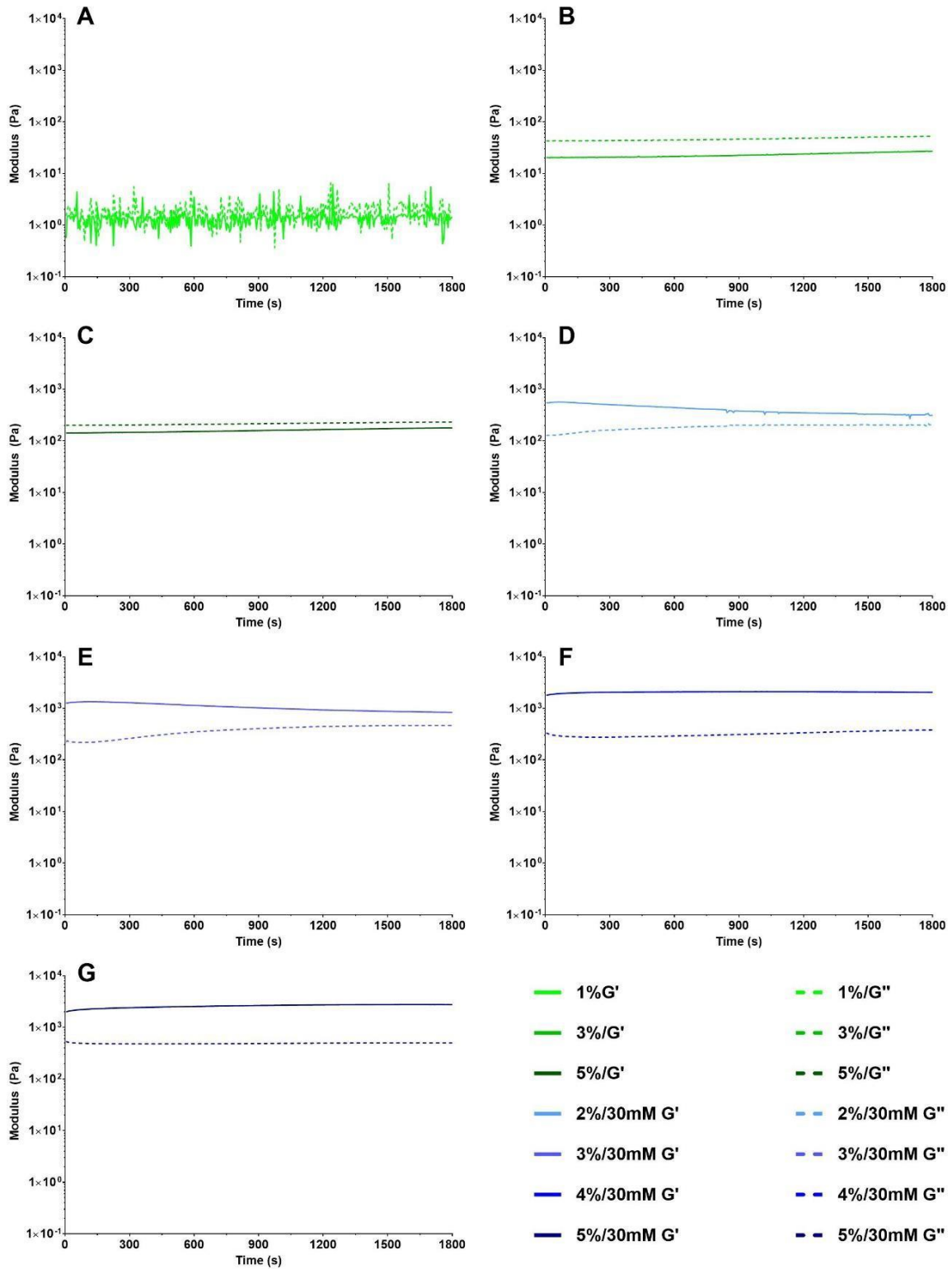


Figure 5.24: Storage ( $G'$ ) and loss ( $G''$ ) moduli outputs of the post-mix time sweep conducted on UC samples 1 % (A), 3 % (B) & 5 % (C) (w/v) and PC samples 2 %/30 mM (D), 3 %/30 mM (E), 4 %/30 mM (F) & 5 %/30 mM (G) (w/v). The test was initiated 60 s after primary-crosslinking completion to allow for rheometer setup. Strain was set to 0.5 %, frequency 1 Hz and temperature set to 20 °C. A measurement was recorded every 5 s for a total of 1,800 s. At 125 s, 910 s, 975 s and 1510 s the third technical repeat was omitted as erroneous. Mean value plotted,  $n = 3$ .

All four PC samples maintained  $G' > G''$  throughout the duration. 2 %/30 mM and 3 %/30 mM PC samples exhibited small increases in  $G'$  and decreases in  $G''$  during first 60 s.  $G'$  then decreased and  $G''$  increased at increasingly reduced rates as time goes on until, at approximately 1500 – 1650 s, they rested at stationary values for the remainder of the test.  $G'$  and  $G''$  of the 4 %/30 mM PC sample rose and lowered slightly until 240 s respectively. After this,  $G'$  plateaued and no further changes were seen whereas  $G''$  increased slightly at a steady rate for the remainder of the test. The 5 %/30 mM PC sample exhibited a  $G''$  that slightly lowered until it plateaued at around 120 s whereas  $G'$  slightly increased up until 600 s until the same effect.

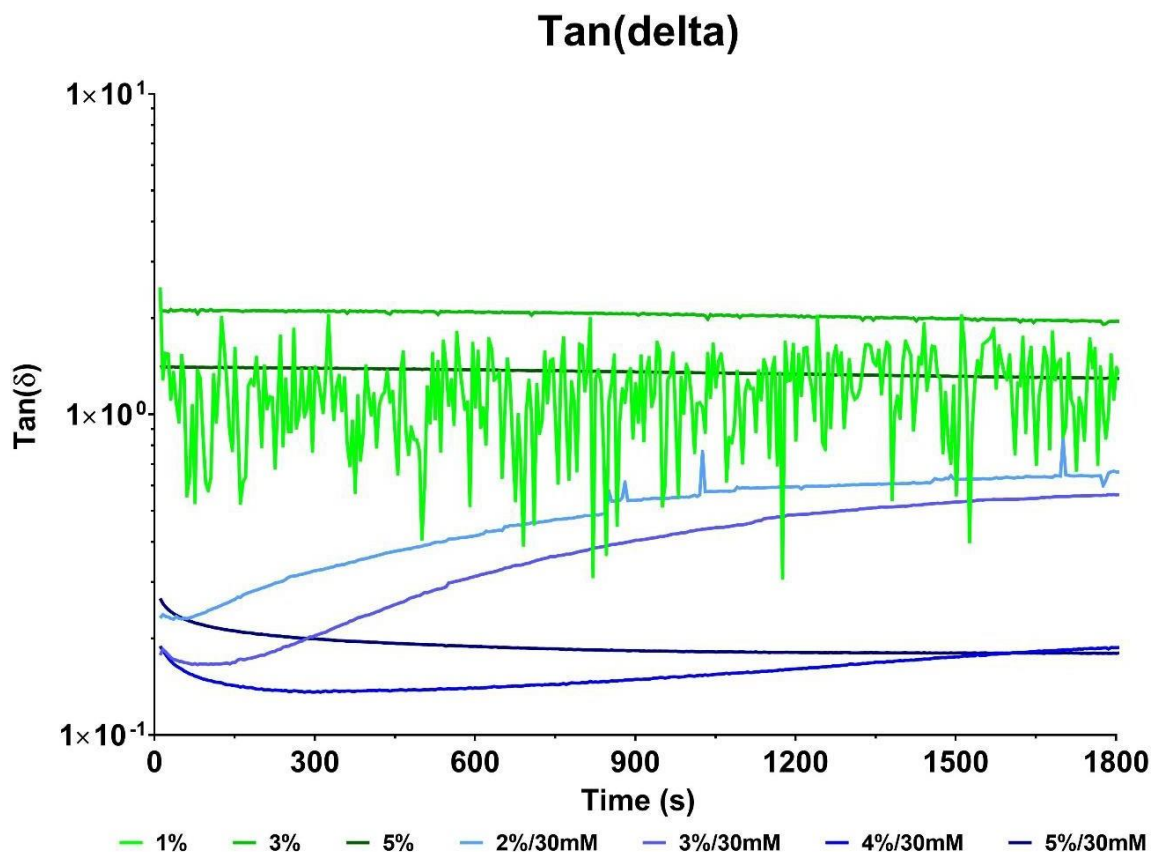


Figure 5.25:  $\tan(\delta)$  outputs of the post-mix time sweep conducted on UC samples 1 %, 3 % & 5 % (w/v) and PC samples 2 %/30 mM, 3 %/30 mM, 4 %/30 mM & 5 %/30 mM (w/v). The test was initiated 60 s after primary-crosslinking completion to allow for rheometer setup. Strain was set to 0.5 %, frequency 1 Hz and temperature set to 20 °C. A measurement was recorded every 5 s for a total of 1,800 s. At 125 s, 910 s, 975 s and 1510 s the third technical repeat was omitted as erroneous. Mean value plotted,  $n = 3$ .



Figure 5.25 shows  $\tan(\delta)$  results of the post-mix time sweep. The 1 % UC sample exhibited considerable noise although the general trend of the dataset did not drastically increase or decrease permanently at any point. The 3 % UC sample had a fixed  $\tan(\delta)$  of approximately 2.2 whilst the 5 % UC sample had a fixed  $\tan(\delta)$  of approximately 1.5 throughout the test.

The four PC samples exhibited variable  $\tan(\delta)$  values during the test which remained at  $< 1$  values. 2 %/30 mM and 3 %/30 mM PC samples behaved similarly, with initial  $\tan(\delta)$  values of 0.24 and 0.19 respectively which then decreased slightly until approximately 60 s. They then increased for the remainder of the test duration as time progressed although the gradient continually diminished. 2 %/30 mM also exhibited multiple, small anomalous spikes in  $\tan(\delta)$  at around 900s, 1050 s and 1700s. The 4 %/30 mM PC sample behaved similarly, starting with a  $\tan(\delta)$  of 0.19 which then decreased for around 300 s and increased thereafter. 5 %/30 mM PC behaved differently as it did not display any sections of the test where  $\tan(\delta)$  increased. It had a starting value of around 0.27 but decreased at a diminishing rate as time continued. The  $\tan(\delta)$  of PC samples were not ordered for most of the test but after 1650 s they presented a trend that  $\tan(\delta)$  decreased with increasing alginate concentration.

## Complex Viscosity

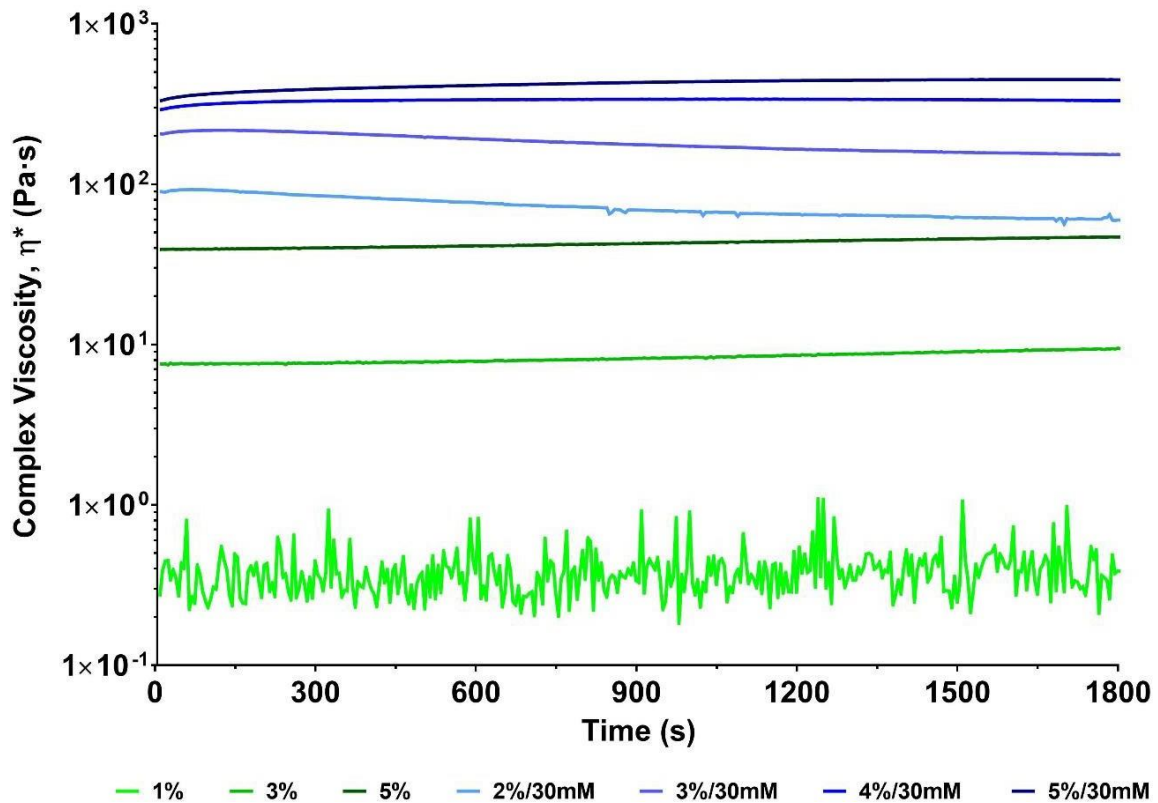


Figure 5.26: Complex viscosity ( $\eta^*$ ) outputs of the post-mix time sweep conducted on UC samples 1 %, 3 % & 5 % (w/v) and PC samples 2 %/30 mM, 3 %/30 mM, 4 %/30 mM & 5 %/30 mM (w/v). The test was initiated 60 s after primary-crosslinking completion to allow for rheometer setup. Strain was set to 0.5 %, frequency 1 Hz and temperature set to 20 °C. A measurement was recorded every 5 s for a total of 1,800 s. At 125 s, 910 s, 975 s and 1510 s the third technical repeat was omitted as erroneous. Mean value plotted,  $n = 3$ .

Figure 5.26 displays the  $\eta^*$  results of the post-mix time sweep. All samples were separate from each other whilst PC samples presented greater  $\eta^*$  than UC samples. Within each group, both presented an increase in  $\eta^*$  as alginate concentration increased however individual behaviours over time varied. 1 % UC presented considerable noise across the duration so whilst no overall changes in the  $\eta^*$  trend were observed, minor legitimate variations may have been obscured amongst noise. 3 % and 5 % UC initially had a  $\eta^*$  of around 7.5 Pa·s and 40 Pa·s respectively although these had a marginal, steady increase throughout the test.

The 2 %/30 mM and 3 %/30 mM PC samples started at a  $\eta^*$  of approximately 90 Pa·s and 200 Pa·s respectively and displayed a  $\eta^*$  increase for the first 60 s. This was followed by a

reduction in  $\eta^*$  for both samples for the remainder of the test in the form of exponential decay, with final values of roughly 60 Pa·s for 2 %/30 mM and 150 Pa·s for 3 %/30 mM. The 4 %/30 mM and 5 %/30 mM PC samples displayed initial  $\eta^*$  values of around 290 and 330 Pa·s however the pattern over time was different. They both display slight upward curves until they eventually plateaued out at approximately 600 s.

## 5.4. 3D Printing

### 5.4.1. Line Width

The Allevi 2 was used to 3D print individual line models (50 × 0.5 × 0.2 mm) using the three PC alginate hydrogels, 2 %/30 mM, 3 %/30 mM and 5 %/30 mM, that were previously highlighted as suitable printing materials. The extrusion pressure setting utilised previously calibrated individual values (for a 10 mm·s<sup>-1</sup> print speed) and values  $\pm 10\%$  and  $\pm 20\%$  of this. Additionally, print speeds of 6, 8, 12 and 14 mm·s<sup>-1</sup> were also investigated across this extrusion pressure range. Produced 3D printed lines were measured with a toolmaker's microscope as per Section 4.6.2 to see how they compared to the expected value of 0.5 mm selected during G-code generation.

Figure 5.27 shows the line width measurements that were collected using the 2 %/30 mM hydrogel with print speeds between 6 – 14 mm·s<sup>-1</sup> and extrusion pressures between 3.6 – 5.6 psi.

### 5.4.1.1. 2 %/30 mM Hydrogel

Pressure (psi)	Print Speed (mms-1)				
	6	8	10	12	14
3.6	0.67 ± 0.038	0.625 ± 0.017	0.569 ± 0.013	0.528 ± 0.07	0.407 ± 0.031
4.1	0.775 ± 0.038	0.799 ± 0.048	0.712 ± 0.023	0.555 ± 0.022	0.532 ± 0.03
4.6	0.902 ± 0.011	0.934 ± 0.019	0.766 ± 0.04	0.709 ± 0.027	0.601 ± 0.016
5.1	1.122 ± 0.051	1.033 ± 0.051	0.91 ± 0.006	0.774 ± 0.04	0.681 ± 0.028
5.6	1.184 ± 0.082	1.212 ± 0.044	1.044 ± 0.063	0.831 ± 0.05	0.733 ± 0.026

Figure 5.27: Mean and standard deviation ( $n = 3$ ) of width measurements of single-layer individual line models ( $50 \times 0.5 \times 0.2$  mm) that were 3D printed with 2 %/30 primary-crosslinked hydrogel. Print settings used extrusion pressures between 3.6 – 5.6 psi and print speeds of 6 – 14  $\text{mms}^{-1}$  while other print settings remained the same. A three-colour graded scale was applied using red for 0 mm, green for 0.5 mm and blue for 1.0 mm.

All line widths were greater than the target of 0.5 mm except for when using 3.6 psi and 14  $\text{mms}^{-1}$  print speed settings. The full range of line widths produced using the 2 %/30 mM hydrogel were 0.407 – 1.212 mm. Two clear relationships were seen which, together, formed a diagonal pattern in the colour-grading of the results.

The first was that, as pressure was increased or decreased, line width increased or decreased respectively, without any exceptions. The differences in line width ranged from as little as 0.027 mm to 0.219 mm when pressure was increased or decreased across the different print speeds. The average line width change was 0.11 mm per 0.5 psi adjustment however this was not uniform across different print speeds. The averages were: 0.129 mm for 6  $\text{mms}^{-1}$ , 0.147 mm for 8  $\text{mms}^{-1}$ : 0.119 mm for 10  $\text{mms}^{-1}$ , 0.076 mm for 12  $\text{mms}^{-1}$  and 0.082 mm for 14  $\text{mms}^{-1}$ . This demonstrated a loose derivative trend where, at greater print speeds, the differences measured in line width as pressure was adjusted were reduced.

The second main correlation was that as print speed was increased or decreased, line width decreased or increased respectively. The exceptions to this rule were the 4.1 – 4.6 psi/6  $\text{mms}^{-1}$  and 5.6 psi/6  $\text{mms}^{-1}$  results which exhibited marginally smaller line widths compared to their corresponding 8  $\text{mms}^{-1}$  values.

Figure 5.28 shows the line width measurements that were collected using the 3 %/30 mM hydrogel with print speeds between 6 – 14 mms<sup>-1</sup> and extrusion pressures between 8.4 – 12.4 psi.

### 5.4.1.2. 3 %/30 mM Hydrogel

Pressure (psi)	Print Speed (mms-1)				
	6	8	10	12	14
8.4	0.63 ± 0.045	0.669 ± 0.051	0.525 ± 0.029	0.47 ± 0.078	0.41 ± 0.048
9.4	0.879 ± 0.038	0.747 ± 0.04	0.622 ± 0.064	0.563 ± 0.057	0.576 ± 0.062
10.4	0.915 ± 0.059	0.91 ± 0.058	0.853 ± 0.025	0.65 ± 0.04	0.598 ± 0.056
11.4	1.13 ± 0.065	1.068 ± 0.07	0.996 ± 0.022	0.814 ± 0.034	0.791 ± 0.038
12.4	1.34 ± 0.02	1.239 ± 0.125	1.211 ± 0.064	1.1 ± 0.038	0.97 ± 0.033

Figure 5.28: Mean and standard deviation ( $n = 3$ ) of width measurements of single-layer individual line models ( $50 \times 0.5 \times 0.2$  mm) that were 3D printed with 3 %/30 primary-crosslinked hydrogel. Print settings used extrusion pressures between 8.4 – 10.4 psi and print speeds of 6 – 14 mms<sup>-1</sup> while other print settings remained the same. A three-colour graded scale was applied using red for 0 mm, green for 0.5 mm and blue for 1.0 mm.

Generally, the data was very similar to the 3 %/30 mM hydrogel results as indicated by the colour grading pattern and colour intensities. Similarly, only two results were measured that displayed line widths below the target of 0.5 mm, 8.4 psi/12 – 14 mms<sup>-1</sup>. The full range of line widths produced using the 3 %/30 mM hydrogel was 0.41 – 1.34 mm.

The same two principal relationships were seen here from the 2 %/30 mM hydrogel data. The first of these was as pressure was increased or decreased, line width increased or decreased respectively. As before, there were no exceptions to this first rule. Line width varied by 0.022 – 0.286 mm as extrusion pressure was increased. On average, this change in line width was equivalent to 0.158 mm per 1 psi adjustment. In contrast to the line width results for the 3 %/30 mM hydrogel, there was no discernible derivative trend observed where the magnitude of line width shift varied at different print speeds. These averages were: 0.178 mm for 6 mms<sup>-1</sup>, 0.143 mm for 8 mms<sup>-1</sup>: 0.172 mm for 10 mms<sup>-1</sup>, 0.158 mm for 12 mms<sup>-1</sup> and 0.14 mm for 14 mms<sup>-1</sup>.

Secondly, as print speed was increased or decreased, line width decreased or increased respectively. The two exceptions to this rule here were the 8.4 psi/8 mms<sup>-1</sup> and 9.4 psi/10 mms<sup>-1</sup> results when compared to neighbouring values.

Figure 5.29 displays the results of line width measurements using the 5 %/30 mM hydrogel with print speeds between 6 – 14 mms<sup>-1</sup> and extrusion pressures between 24.4 – 36.4 psi.

#### 5.4.1.3. 5 %/30 mM Hydrogel

Pressure (psi)	Print Speed (mms-1)				
	6	8	10	12	14
24.4	0.413 ± 0.024	0.376 ± 0.015	0.284 ± 0.072	0.295 ± 0.033	0.307 ± 0.037
27.4	0.451 ± 0.068	0.379 ± 0.016	0.344 ± 0.111	0.355 ± 0.034	0.342 ± 0.056
30.4	0.839 ± 0.043	0.772 ± 0.037	0.517 ± 0.018	0.483 ± 0.026	0.441 ± 0.07
33.4	0.931 ± 0.02	0.885 ± 0.026	0.735 ± 0.055	0.585 ± 0.119	0.497 ± 0.012
36.4	1.027 ± 0.06	0.865 ± 0.064	0.916 ± 0.105	0.645 ± 0.062	0.576 ± 0.037

Figure 5.29: Mean and standard deviation ( $n = 3$ ) of width measurements of single-layer individual line models ( $50 \times 0.5 \times 0.2$  mm) that were 3D printed with 5 %/30 primary-crosslinked hydrogel. Print settings used extrusion pressures between 24.4 – 36.4 psi and print speeds of 6 – 14 mms<sup>-1</sup> while other print settings remained the same. A three-colour graded scale was applied using red for 0 mm, green for 0.5 mm and blue for 1.0 mm.

The data was noticeably different to the other two hydrogels as fewer > 0.5 mm and more < 0.5 mm line width results were recorded. This resulted in decreased lower and upper limit values of measured line widths in comparison, measuring 0.284 – 1.027 mm.

The trend that as extrusion pressure was increased, line width increased was once again repeated across all print speeds for the 5 %/30 mM hydrogel. One exception to this was the 36.4 psi/6 mms<sup>-1</sup> result which had a smaller line width compared to 33.4 psi/6 mms<sup>-1</sup>. Interestingly, the derivative trend where magnitude of line width change varied at different print speeds, which was seen in 2 %/30 mM but not 3 %/30 mM, was observed here. The average line width change was: 0.154 mm for 6 mms<sup>-1</sup>, 0.122 mm for 8 mms<sup>-1</sup>: 0.158 mm for 10 mms<sup>-1</sup>, 0.088 mm for 12 mms<sup>-1</sup> and 0.067 mm for 14 mms<sup>-1</sup>, representing a loose-

fitting correlation.

The relationship where line width increases as print speed decreased (and *vice versa*) was still present for pressures 30.4 psi, 33.4 psi and 36.4 psi, although 36.4 psi/10 mms<sup>-1</sup> was an exception which broke the trend. For pressures 27.4 and 24.4 psi, this trend was only observed between print speeds of 6 – 10 mms<sup>-1</sup>. However, between 10 – 14 mms<sup>-1</sup>, no meaningful decrease in line width was seen as print speed was increased further.

### 5.4.2. Single Layer Infill

The Allevi 2 was used to 3D print single layer infill models (30 × 30 × 0.2 mm) using three PC alginate hydrogels, 2 %/30 mM, 3 %/30 mM and 5 %/30 mM. The extrusion pressure setting utilised previously calibrated individual values (for a 10 mms<sup>-1</sup> print speed) and values ±10 % and ±20 % of this. Additionally, print speeds of 6, 8, 12 and 14 mms<sup>-1</sup> were also investigated across this extrusion pressure range. Single layer infill models were 3D printed and visually assessed for layer quality with a categorisation as previously detailed in Section 4.6.3. Figure 5.30 shows the results of the single layer infill experiment for the 2 %/30 mM hydrogel.



### 5.4.2.1. 2 %/30 mM Hydrogel

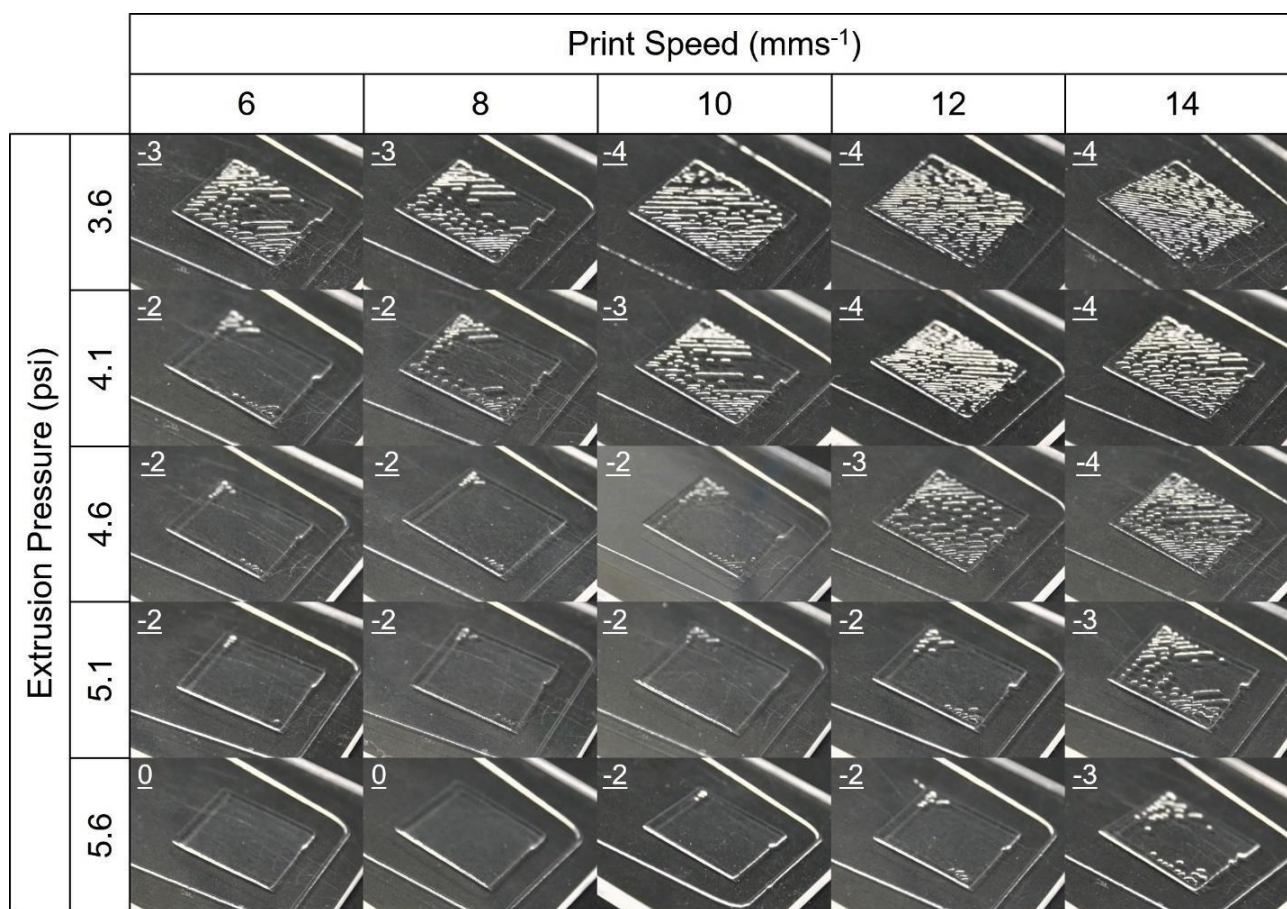


Figure 5.30: Single layer infill experiment results which used a 2 %/30 mM primary-crosslinked hydrogel to 3D print a 30 × 30 × 0.2 mm model. The detached skirt of the 3D print is also seen around the exterior of the model. Extrusion pressures were assessed between 3.6 – 5.6 psi as well as printing speeds of 6 – 14 mms<sup>-1</sup>. Images were captured using a digital camera with an attached polarising filter. Scores were awarded for presence of no exposed area (0), minor dot- like flaws (-1), peripheral line-shaped flaws (-2), central line-shaped flaws (-3), severe flaws with no discernible continuous area (-4).

Many of these 3D prints showed inadequate layer formation with only 2 samples displaying completely formed layers (0) which were 5.6 psi/6 mms<sup>-1</sup> and 5.6 psi/8 mms<sup>-1</sup>. Several of the settings produced 3D prints that contained line-shaped flaws in peripheral sections (-2): 4.1 – 5.1 psi/6 mms<sup>-1</sup>, 4.6 – 5.1 psi/8 mms<sup>-1</sup>, 5.1 psi/10 mms<sup>-1</sup> and 5.1 – 5.6 psi /12 mms<sup>-1</sup>. Of these, flaws were only present in upper corner of 5.1 – 5.6 psi/10 mms<sup>-1</sup> compared to both upper and lower corners in remaining images. Several other 3D prints contained line-shaped defects in central regions of the print area (-3): 3.6 – 4.1 psi/6 mms<sup>-1</sup>, 3.6 – 4.1 psi/8 mms<sup>-1</sup>, 4.1 psi/10 mms<sup>-1</sup>, 4.6 psi/12 mms<sup>-1</sup> and 5.1 – 5.6 psi/14 mms<sup>-1</sup> samples. Finally, many of the 3D prints contained severe flaws where no continuous area of fused material can be seen: 3.6 psi/10 mms<sup>-1</sup>, 3.6 – 4.1 psi/12 mms<sup>-1</sup> and 3.6 – 4.6/14 mms<sup>-1</sup>.



Two individual relationships were identified from these results. The first was that, as extrusion pressure was increased, the severity of the defects present in 3D prints was reduced. This was supported by the associated defect scores remaining the same or lowering as extrusion pressure increased, with no exceptions present. The second relationship was that as print speed decreased, the same effect can be seen where defect severity decreased. Again, this was supported through the scoring system which remained the same or reduced in severity as print speed was reduced, without exception. In Figure 5.30, these two individual trends combined to display a loose diagonal pattern where severity generally increased more to the top right and less to the bottom left.

Another feature identifiable within images was the presence of either individual or several 'notches', located in the upper section of the right-side perimeter. The severity of these notches varied in size between samples. A weak trend was seen where, as either print speed increased or extrusion pressure decreased (or *vice versa*), the notches expanded in size. Additionally, fragmented material was seen on the right-hand side of several images where the lines that comprise the perimeter of the print had not fused correctly. This was seen as separate to presence of notches as the effect was more widespread. The results that contained improperly formed perimeters were 3.6 – 4.2 psi/10 mms<sup>-1</sup>, 3.6 – 4.6 psi/12 mms<sup>-1</sup> and 3.6 – 5.1/14 mms<sup>-1</sup>.

Figure 5.31 displays results of the single layer infill experiment for the 3%/30 mM hydrogel.

### 5.4.2.2. 3 %/30 mM Hydrogel

		Print Speed (mms <sup>-1</sup> )				
		6	8	10	12	14
Extrusion Pressure (psi)	8.4	-2	-2	-3	-4	-4
	9.4	-2	-1	-2	-3	-3
	10.4	0	-1	-1	-2	-2
	11.4	0	0	0	-1	-2
	12.4	0	0	0	-1	0

Figure 5.31: Single layer infill experiment results which used a 3 %/30 mM primary-crosslinked hydrogel to 3D print a 30 × 30 × 0.2 mm model. The detached skirt of the 3D print is also seen around the exterior of the model. Extrusion pressures were assessed between 8.4 – 12.4 psi as well as printing speeds of 6 – 14 mms<sup>-1</sup>. Images were captured using a digital camera with an attached polarising filter. Scores were awarded for presence of no exposed area (0), minor dot-like flaws (-1), peripheral line-shaped flaws (-2), central line-shaped flaws (-3), severe flaws with no discernible continuous area (-4).

Several more 3D prints displayed a complete layer without any gaps (0) compared to the 2 %/30 mM hydrogel results which were: 10.4 – 12.4 psi/6 mms<sup>-1</sup>, 11.4 – 12.4 psi/8 mms<sup>-1</sup> and 11.4 – 12.4 psi/10 mms<sup>-1</sup>. Other 3D prints displayed a complete layer except for the presence of some minor dot-like flaws (-1) which was a previously unseen category in the 2 %/30 mM results. These were the 9.4 – 10.4 psi/8 mms<sup>-1</sup>, 10.4 psi/10 mms<sup>-1</sup> and 11.4 – 12.4 psi/12 mms<sup>-1</sup> samples. Several 3D prints contained line-shaped flaws (-2): 8.4 – 9.4 psi/6 mms<sup>-1</sup>, 8.4 psi/8 mms<sup>-1</sup>, 9.4 psi/10 mms<sup>-1</sup>, 10.4 psi/12 mms<sup>-1</sup> and 10.4 – 11.4psi/14 mms<sup>-1</sup>. In contrast to the 2 %/30 mM results there were only three samples that produced a 3D print with centrally-located line-shaped defects (-3) which were 8.4 psi/10 mms<sup>-1</sup>, 9.4 psi/12 mms<sup>-1</sup> and 9.4 psi/14 mms<sup>-1</sup>. Similarly, there were only two results with severe flaws and no

continuous area of fused material (-4), 8.4 psi/12 mms<sup>-1</sup> and 8.4 psi/14 mms<sup>-1</sup>. In contrast to Figure 5.30 where scores of -3 and -4 were found across all tested extrusion pressures, here they were only found in the two lower settings.

Compared to the results obtained from 3D printing using the 2%/30 mM hydrogel, the overall results showed an improvement in production of single layers without flaws. Increase of extrusion pressure produced the same trend and reduced severity of flaws as indicated by assigned scores increasing or remaining the same. Generally, the trend that as print speed decreased, the defect severity reduced was also preserved as per the scoring system however there were two exceptions. The 12.4 psi/12 mms<sup>-1</sup> sample had a lower score than the 12.4 psi/10 mms<sup>-1</sup> sample whilst the 9.4 psi/6 mms<sup>-1</sup> sample had a higher score than the 9.4 psi/8 mms<sup>-1</sup> one. Overall, this formed a loose diagonal pattern where defect severity increased towards the upper right corner of Figure 5.31 and *vice versa*, like in Figure 5.30.

Interestingly, the presence of notches in the upper section of the right-side perimeter was greatly diminished overall but minor notches were still be seen in results across extrusion pressures of 8.4 psi and 9.4 psi. The incidence of improperly formed perimeters was also seen in 8.4 – 9.4 psi/12 mms<sup>-1</sup> and 8.4 – 9.4 psi/14 mms<sup>-1</sup> results. Additionally, the surface texture of some of the 3D prints was visibly rough in all the 3D prints that used 12.4 psi extrusion pressure and 11.4 psi/14 mms<sup>-1</sup>.

Figure 5.32 shows the final set of results for the single layer infill test which used the 5%/30 mM hydrogel.

### 5.4.2.3. 5 %/30 mM Hydrogel

		Print Speed (mms <sup>-1</sup> )				
		6	8	10	12	14
Extrusion Pressure (psi)	24.4	-3	-4	-4	-4	-4
	27.4	-2	-2	-3	-4	-4
	30.4	-1	-1	0	-1	-2
	33.4	0	0	0	0	-2
	36.4	-1	-1	0	-1	0

Figure 5.32: Single layer infill experiment results which used a 5 %/30 mM primary-crosslinked hydrogel to 3D print a 30 × 30 × 0.2 mm model. The detached skirt of the 3D print is also seen around the exterior of the model. Extrusion pressures were assessed between 24.4 – 36.4 psi as well as printing speeds of 6 – 14 mms<sup>-1</sup>. Images were captured using a digital camera with an attached polarising filter. Scores were awarded for presence of no exposed area (0), minor dot-like flaws (-1), peripheral line-shaped flaws (-2), central line-shaped flaws (-3), severe flaws with no discernible continuous area (-4).

Similar amounts of 3D prints displayed a complete layer without any gaps (0) compared to the 2 %/30 mM hydrogel. These results were: 33.4 psi/6 mms<sup>-1</sup>, 33.4 psi/8 mms<sup>-1</sup>, 30.4 – 36.4 psi/10 mms<sup>-1</sup>, 33.4 psi/12 mms<sup>-1</sup> and 36.4 psi/14 mms<sup>-1</sup>. These were found only when printing with the central and two increased extrusion pressures, the same as in Figure 5.31. Multiple 3D prints were produced containing only dot-like flaws (-1) however these were more dispersed compared to those tightly grouped in Figure 5.31 and were also interweaved amongst 0 scores. -1 scores were given to 3D prints that used settings of 30.4 & 36.4 psi /6 mms<sup>-1</sup>, 30.4 & 36.4 psi/8 mms<sup>-1</sup> and 30.4 & 36.4 psi/12 mms<sup>-1</sup>.

Fewer 3D prints containing line-like defects (-2) were produced than those seen compared to 3D printing with the 2 %/30 mM and 3 %/30 mM hydrogels. These were the 27.4 psi/6 mms<sup>-1</sup>, 27.4 psi/8 mms<sup>-1</sup> and 30.4 – 33.4 psi/14 mms<sup>-1</sup> settings results.

However, these had notably less overall exposed area compared to the other -2 scores awarded in Figure 5.30 and Figure 5.31. Only two results contained central line-like flaws whilst retaining a continuous fused area which were 24.4 psi/6 mms<sup>-1</sup> and 27.4 psi/10 mms<sup>-1</sup>. The incidence of -3 scores was similar to results obtained using the 3 %/30 mM hydrogel and far less than those produced using the 2 %/30 mM, however they appear in visibly different forms. Previously, localised fused sections of hydrogel could be seen in the centre of the printed area whereas in Figure 5.32, lesser flaws were seen equally spread across the whole print area (whilst still retaining a large section of fused material).

Several 3D prints were also produced where there was no considerable continuous area of fused material (-4): 24.4 psi/8 mms<sup>-1</sup>, 24.4 psi/10 mms<sup>-1</sup>, 24.4 – 27.4 psi/12 mms<sup>-1</sup> and 24.4 – 27.4 psi/14 mms<sup>-1</sup>. These represented increased numbers of -4 scores awarded compared to results gathered using the 3 %/30 mM hydrogel and the same number as using the 2 %/30 mM hydrogel. -3 and -4 scores were also only awarded to 3D prints produced using the lower two extrusion pressure settings.

The same two fundamental trends were observed in Figure 5.32 that were found in Figure 5.30 and Figure 5.31. The first was that as pressure was increased, the severity of flaws that caused exposed print area was reduced. There were three exceptions to this rule, in contrast to no exceptions in previous results, which were 36.4 psi/6 mms<sup>-1</sup>, 36.4 psi/8 mms<sup>-1</sup> and 36.4 psi/12 mms<sup>-1</sup>, which produced more exposed area than their 33.4 psi counterparts. For the former two, this exposed print area was localised to one section printed area peripheral, which can be seen in the upper right of images, something which was not previously been seen. Whereas for 36.4 psi/12 mms<sup>-1</sup>, this was due to the presence of several scattered dot-like defects. Similarly, 27.4 psi/8 mms<sup>-1</sup> and 27.4 psi/14 mms<sup>-1</sup> also presented unique forms

of exposed area in the lower right section of images where multiple individual defects were arranged in a line, slightly away from a corner. However, this did not form an exception to the trend.

The second trend where print speed reduction resulted in reduced defect severity was not as absolute. It was observed in extrusion pressures of 24.4 psi, 27.4 psi and 33.4 psi where, as print speed decreased, flaw severity scores remained the same or were reduced. Whereas, for extrusion pressures of 30.4 psi and 36.4 psi, no clear trend was seen and there were multiple instances of severity (and associated scores) increasing as print speed decreased. Due to this, the previously highlighted loose diagonal pattern that formed in Figure 5.30 and Figure 5.31 cannot be seen.

Interestingly, previously observed notches from Figure 5.30 and Figure 5.31 cannot be seen for 3D prints that used any print settings. However, more improperly formed perimeters were observed compared to Figure 5.30 and Figure 5.31: 24.4 psi/8 mms<sup>-1</sup>, 24.4 psi/10 mms<sup>-1</sup>, 24.4 – 27.4 psi/12 mms<sup>-1</sup> and 24.4 – 27.4 psi/14 mms<sup>-1</sup>.

Previously unseen straight lines were seen in the surface texture of several 3D prints which reproducibly stretched from the bottom corner of the printed area to the approximate centre of the left side. The affected samples were 33.4 – 36.4 psi/6 mms<sup>-1</sup>, 33.4 – 36.4 psi/8 mms<sup>-1</sup>, 33.4 – 36.4 psi/10 mms<sup>-1</sup>, 33.4 – 36.4 psi/12 mms<sup>-1</sup> and 36.4 psi/14 mms<sup>-1</sup>.

3D prints produced at higher extrusion pressures in Figure 5.32 were also visibly less 'bulbous' in appearance compared to Figure 5.30 and Figure 5.31. This was seen along the edges of printed areas, particularly amongst results in the highest-pressure settings where print speeds of 6 – 8 mms<sup>-1</sup> were used. However, determination of precisely which samples were included as bulbous was limited from visual inspection.



### 5.4.3. Multi-Layer Geometries

The Allevi 2 was used to 3D print several models using three PC alginate hydrogels, 2 %/30 mM, 3 %/30 mM and 5 %/30 mM to assess print fidelity in multi-layered prints. The models were a cube ( $10 \times 10 \times 5$  mm), a wall model ( $10 \times 10 \times 5$  mm, wall thickness 1 mm), 22.5 ° overhang model (base area  $10 \times 10$  mm, 5 mm height) and a 45 ° overhang model (base area  $10 \times 10$  mm, 5 mm height). G-code was generated using a  $10\text{mms}^{-1}$  print speed and originally calibrated extrusion pressures of 4.6 psi, 10.4 psi and 30.4 psi were used respectively. Once printing was complete, images were captured as per section 4.6.4 for visual assessment of the results.

#### 5.4.3.1. Cube

##### 5.4.3.1.1. 2 %/30 mM Hydrogel

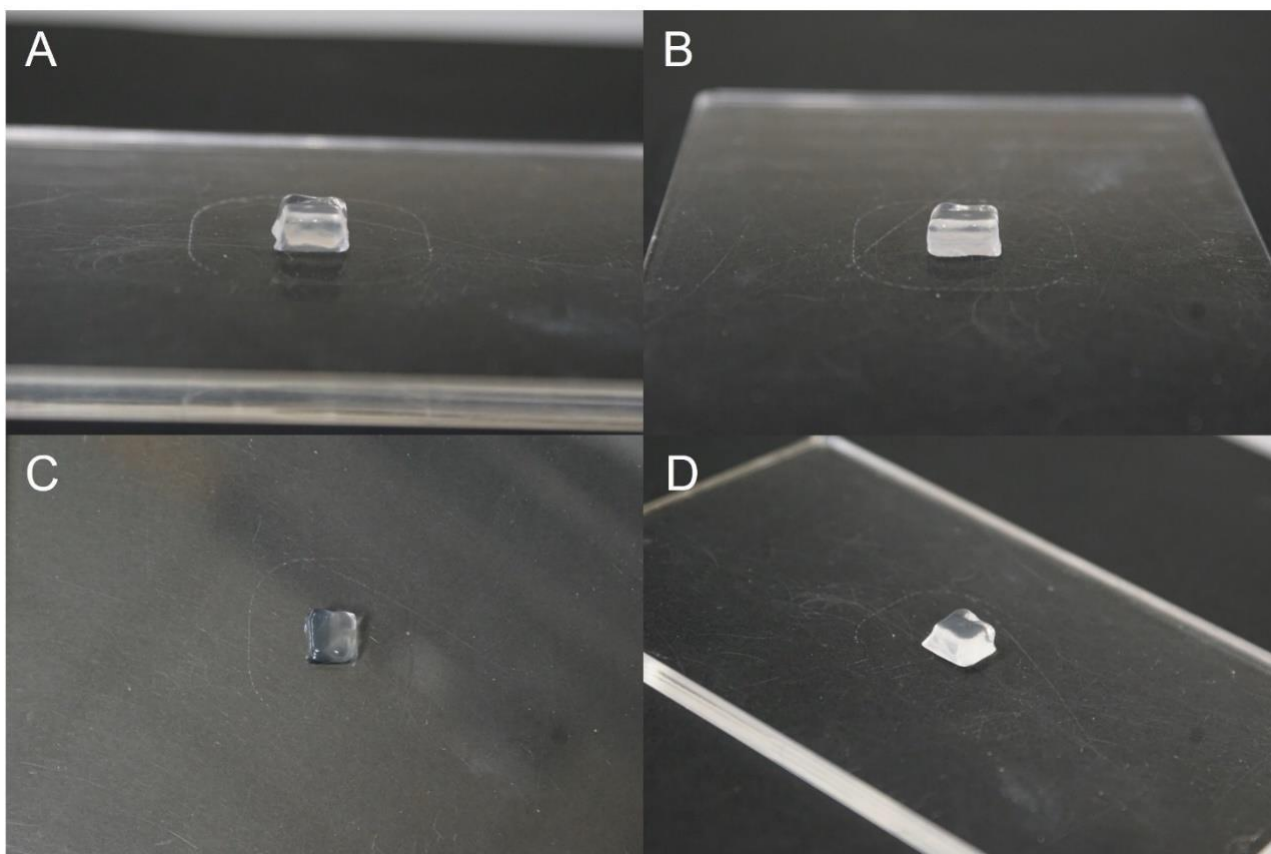


Figure 5.33: 3D printed cube model ( $10 \times 10 \times 5$  mm) produced using a 2 %/30 mM primary-crosslinked hydrogel at a print speed of  $10\text{mms}^{-1}$  and an extrusion pressure of 4.6 psi. (A) front, (B) side, (C) top and (D) orthographic views were captured using a digital camera with an attached polarising filter. The detached skirt of the 3D print can also be seen.

As seen in Figure 5.33, 3D printing of the cube model with the 2 %/30 mM hydrogel had poor fidelity compared to the desired  $10 \times 10 \times 5$  mm model. Horizontal edges were not uniform but were generally wider towards corners and thinner in central wall sections. The X- and Y-axis also had poor symmetry which can be seen when comparing Figure 5.33A and B. These images also showed that the walls were not aligned perfectly vertical either, but instead, collapsed inwards towards the centre of the object. This formed a large ‘elephant’s’ foot where the lower layers were larger than upper layers, shown clearly in Figure 5.33D. Here, the upper surface was also shown as irregular and had one corner which was substantially lower than others.

#### 5.4.3.1.2. 3 %/30 mM Hydrogel

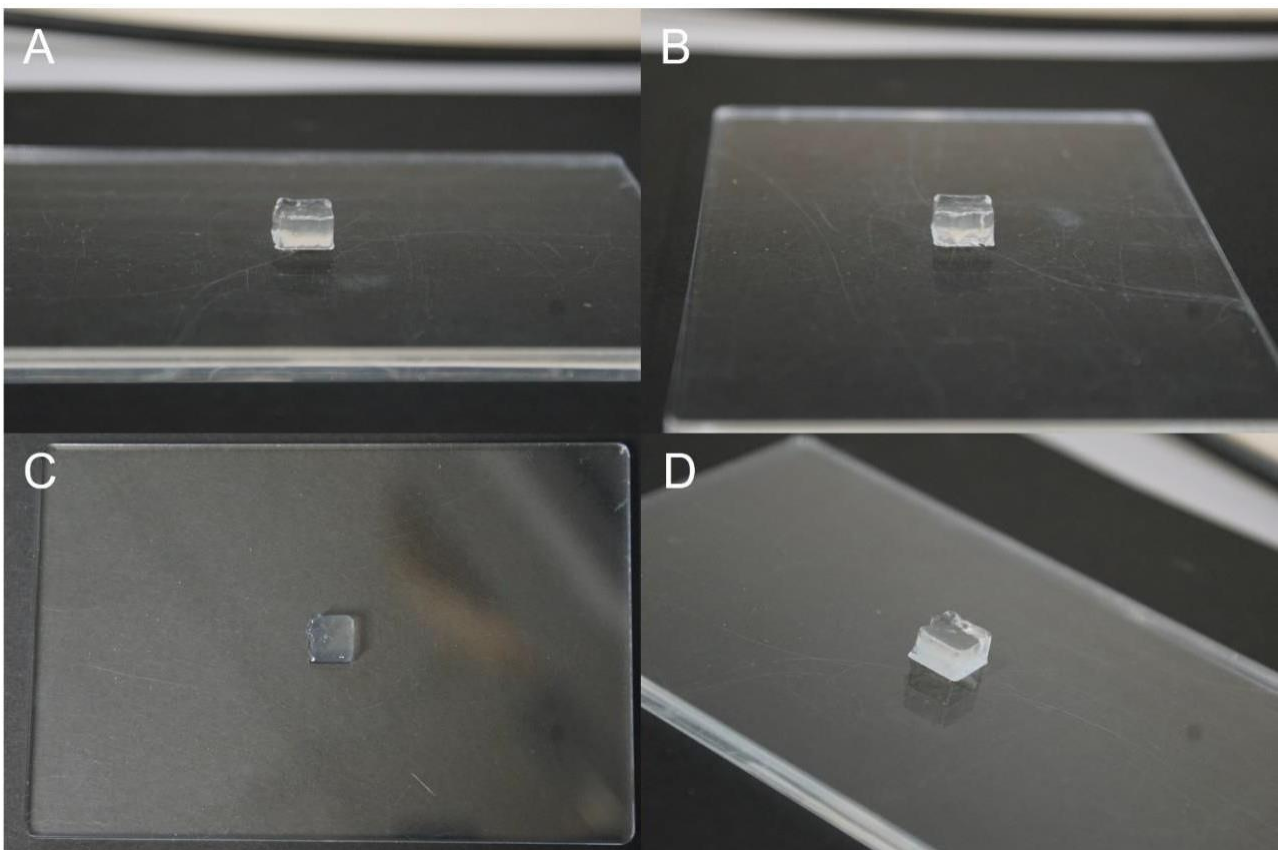


Figure 5.34: 3D printed cube model ( $10 \times 10 \times 5$  mm) produced using a 3 %/30 mM primary-crosslinked hydrogel at a print speed of  $10\text{mm}\cdot\text{s}^{-1}$  and an extrusion pressure of 10.4 psi. (A) front, (B) side, (C) top and (D) orthographic views were captured using a digital camera with an attached polarising filter. The detached skirt of the 3D print can also be seen.



Figure 5.34 shows the results of the 2 %/30 mM hydrogel 3D printed cube which had an improved printing fidelity but still presented many inaccuracies. Horizontal edges of the cube were mostly uniform but still presented flaws. Figure 5.34B shows a small missing section of the perimeter at the base whilst the upper right corner in Figure 5.34C shows that the walls were not perpendicular. The X- and Y-axis had better symmetry when comparing Figure 5.34A and B however the left wall of the former was formed poorly and not uniform. Other walls were formed correctly vertical although a sizable elephant's foot could still be seen in one corner, demonstrated in Figure 5.33D. The top layer surface was more uniform compared to the 2 %/30 mM results however was still uneven, shown best in Figure 5.34D.

#### 5.4.3.1.3. 5 %/30 mM Hydrogel

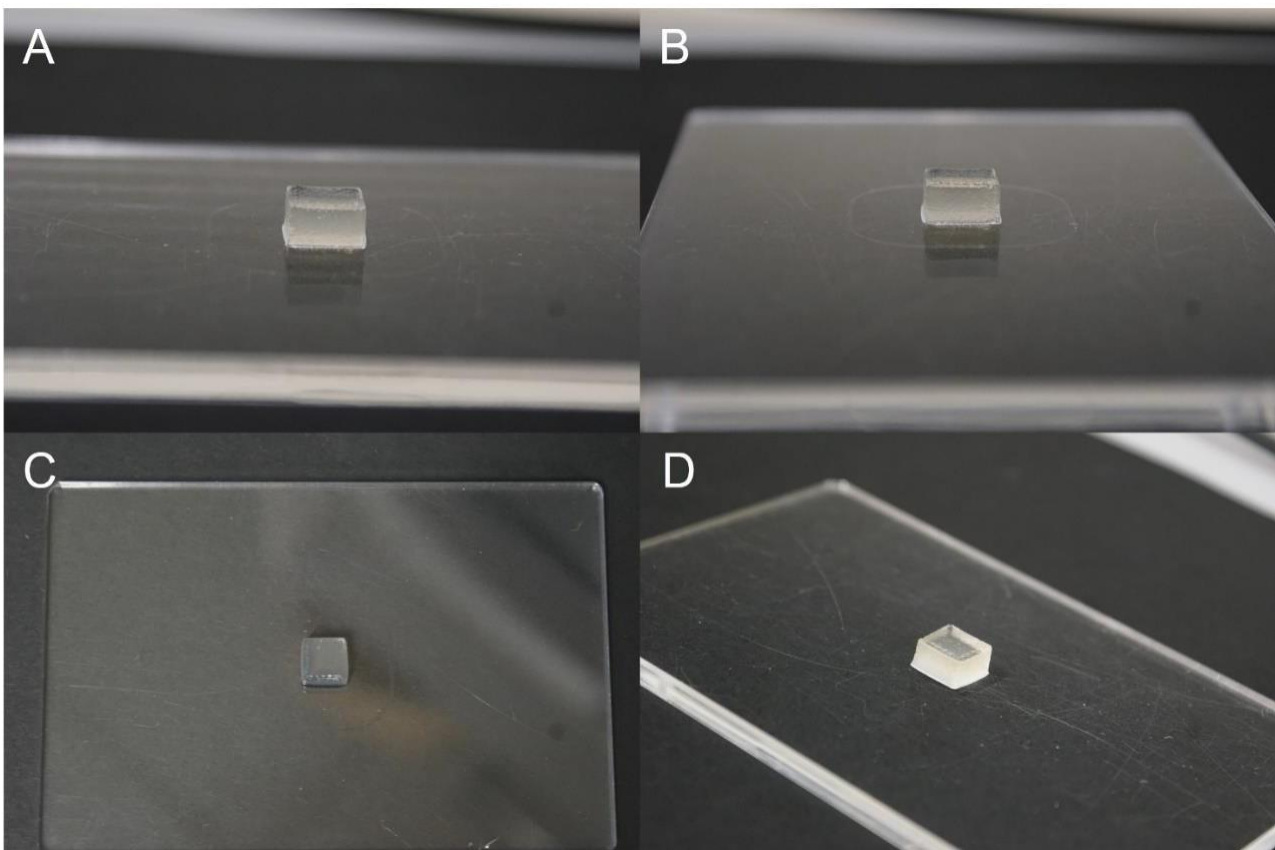


Figure 5.35: 3D printed cube model ( $10 \times 10 \times 5$  mm) produced using a 5 %/30 mM primary-crosslinked hydrogel at a print speed of  $10\text{mm}\cdot\text{s}^{-1}$  and an extrusion pressure of 30.4 psi. (A) front, (B) side, (C) top and (D) orthographic views were captured using a digital camera with an attached polarising filter. The detached skirt of the 3D print can also be seen.

The results for the 3D printing cube with the 5 %/30 mM hydrogel can be seen in Figure 5.35 which presented a marked overall improvement in print fidelity. Horizontal edges were vertical and uniform, however a minute elephant's foot was still seen at the base of the print, although this was uniform across different sides. When comparing Figure 5.35A and B, no substantial differences were seen between X- and Y-axis symmetry. The same symmetry was seen from the top view in Figure 5.35C. The top layer surface formation specifically, was greatly improved compared to the results of the 2 %/30 mM and 3 %/30 mM 3D printed cubes. However, as seen in Figure 5.35A, corners appeared slightly raised compared to central sections. Small ridges were also seen in Figure 5.35D in peripheral sections of the top layer.

### 5.4.3.2. Wall

#### 5.4.3.2.1. 2 %/30 mM Hydrogel

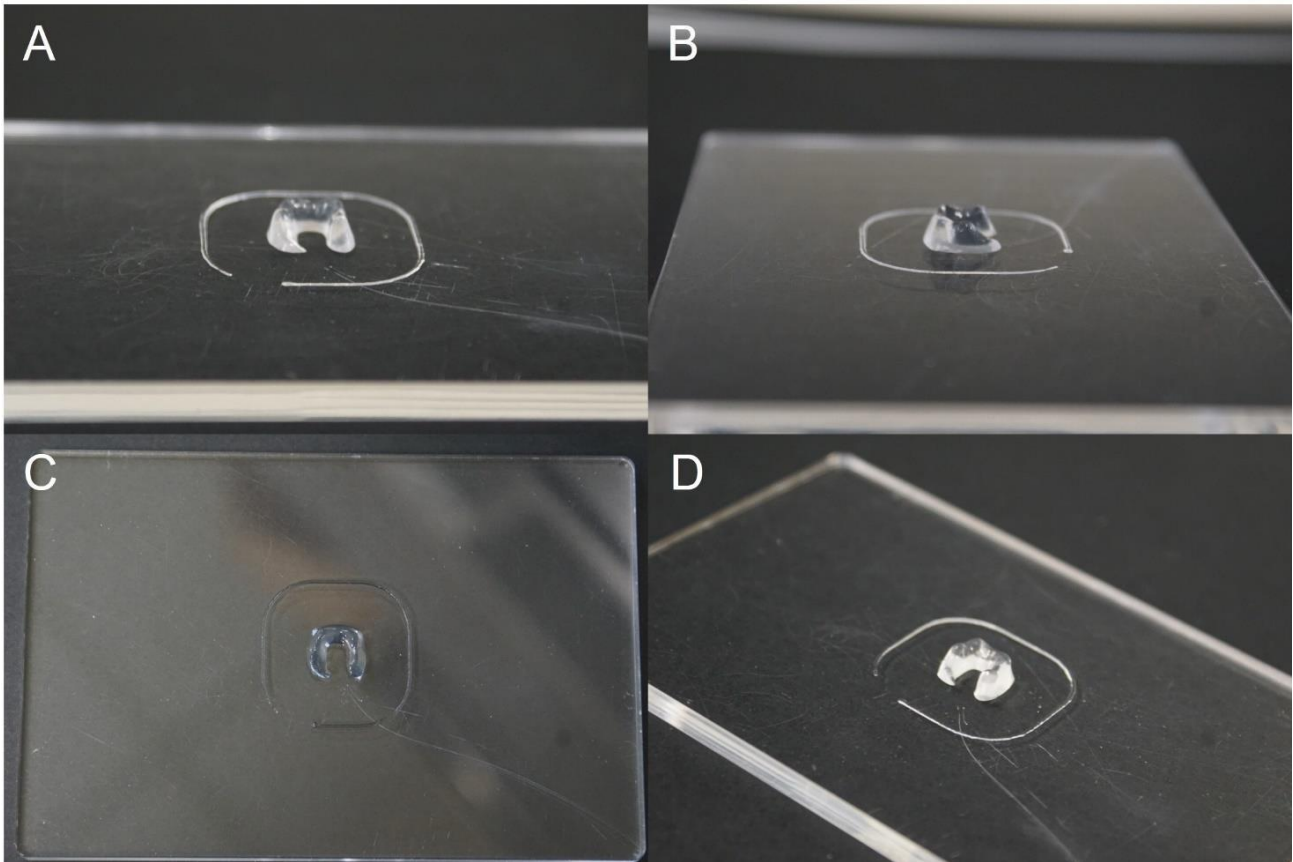


Figure 5.36: 3D printed wall model ( $10 \times 10 \times 5$  mm, wall thickness 1 mm) produced using a 2 %/30 mM primary- crosslinked hydrogel at a print speed of  $10\text{mms}^{-1}$  and an extrusion pressure of 4.6 psi. (A) front, (B) side, (C) top and (D) orthographic views were captured using a digital camera with an attached polarising filter. The detached skirt of the 3D print can also be seen.

Figure 5.36 shows the result of the 3D printed wall model ( $10 \times 10 \times 5$  mm, wall thickness 1 mm) using the 2 %/30 mM hydrogel where the overall print fidelity was evidently poor. Specifically, X- and Y- axis did not have good symmetry as one side of the print was nearly entirely absent except for a ramp-like feature on the far left where the wall began to form. The walls were not vertical as seen in Figure 5.36A and B where they were angled inwards, whilst their overall thickness was much larger than intended. The walls were thicker at the base than at the top as seen in Figure 5.36A however this was simply the shape of the wall in this instance, not a distinct elephant's foot feature. The top layer was also taller in the corners compared to midsections of the wall, demonstrated in Figure 5.36B and D.

#### 5.4.3.2.2. 3 %/30 mM Hydrogel

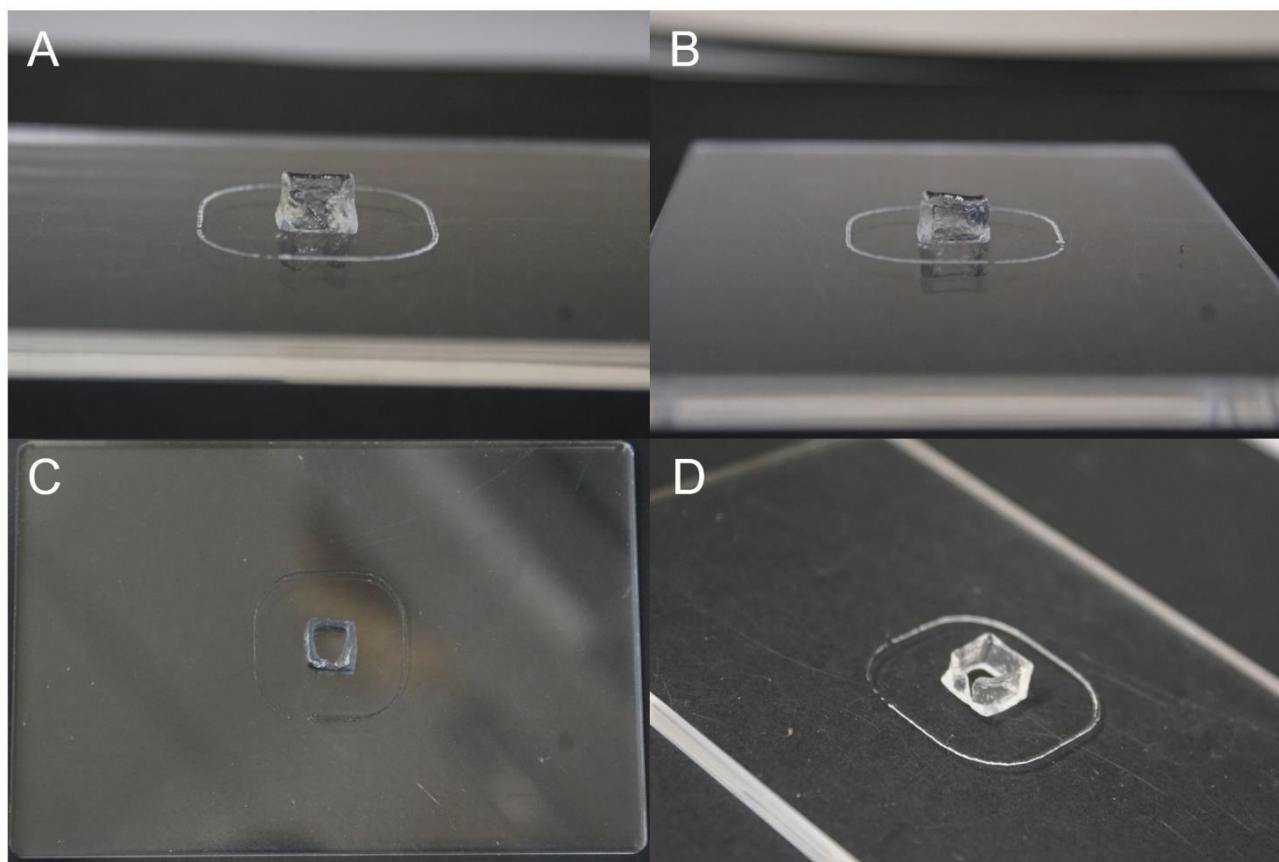


Figure 5.37: 3D printed wall model ( $10 \times 10 \times 5$  mm, wall thickness 1 mm) produced using a 3 %/30 mM primary- crosslinked hydrogel at a print speed of  $10\text{mm s}^{-1}$  and an extrusion pressure of 10.4 psi. (A) front, (B) side, (C) top and (D) orthographic views were captured using a digital camera with an attached polarising filter. The detached skirt of the 3D print can also be seen.

The results for the 3D printed wall model with the 3 %/30 mM hydrogel can be seen in Figure 5.37. There was an improvement in fidelity compared to the wall model that was 3D printed using 2 %/30 mM however several flaws were still identified. Primarily, a missing section of the front wall was present, however it was drastically thinner and was connected at the base. The upper sections of the complete walls were correctly vertical as seen in Figure 5.37A and D. The lower sections of walls, however, were seen to direct inwards, albeit to a lesser degree than that of the 3 %/30 mM 3D printed wall model. There was also a substantial reduction in wall thickness that appeared generally accurate to the model design. An uneven top layer was seen, shown in Figure 5.37A and B, that was also seen to lower with increasing proximity to the incomplete wall section. Figure 5.37C also revealed rounding of corners to

the left and right of the incomplete wall section.

#### 5.4.3.2.3. 5 %/30 mM Hydrogel

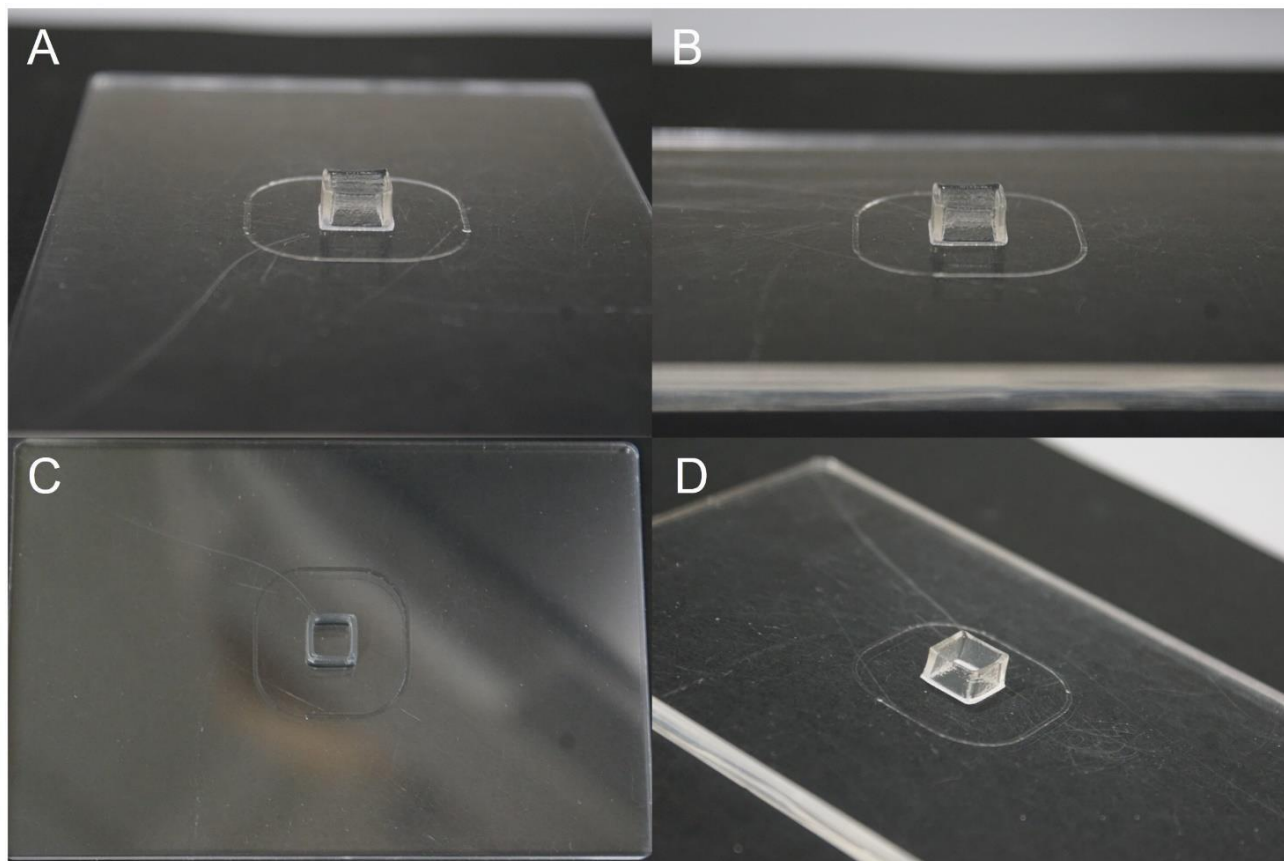


Figure 5.38: 3D printed wall model ( $10 \times 10 \times 5$  mm, wall thickness 1 mm) produced using a 5 %/30 mM primary- crosslinked hydrogel at a print speed of  $10\text{mms}^{-1}$  and an extrusion pressure of 30.4 psi. (A) front, (B) side, (C) top and (D) orthographic views were captured using a digital camera with an attached polarising filter. The detached skirt of the 3D print can also be seen.

Figure 5.38 shows the results of the 3D printed wall model using the 5 %/30 mM hydrogel. There was a sizeable improvement in the quality of this model and overall fidelity with regards to the model design, compared to those seen in Figure 5.36 and Figure 5.37. Firstly, there was no missing section of the front wall or any indication of lack of material there. The upper sections of the wall were also vertical however the lower parts still curved inwards slightly, albeit it to a lesser extent than in both other hydrogel results. Separately, a small elephant's foot was seen at the base of the wall in Figure 5.38A, B and C. Wall thickness appeared to be uniform and true to the dimensions of the model. There was also clear X- and Y-axis symmetry that was, seen by comparing Figure 5.38A and B. These also show



that there was a minor difference in height within the top layer where corners were slightly taller than mid-wall sections. Figure 5.38C also revealed far less serious rounding of corners compared to that seen in previous results for the other two hydrogels.

### 5.4.3.3. 22.5 Degree Overhang

#### 5.4.3.3.1. 2 %/30 mM Hydrogel

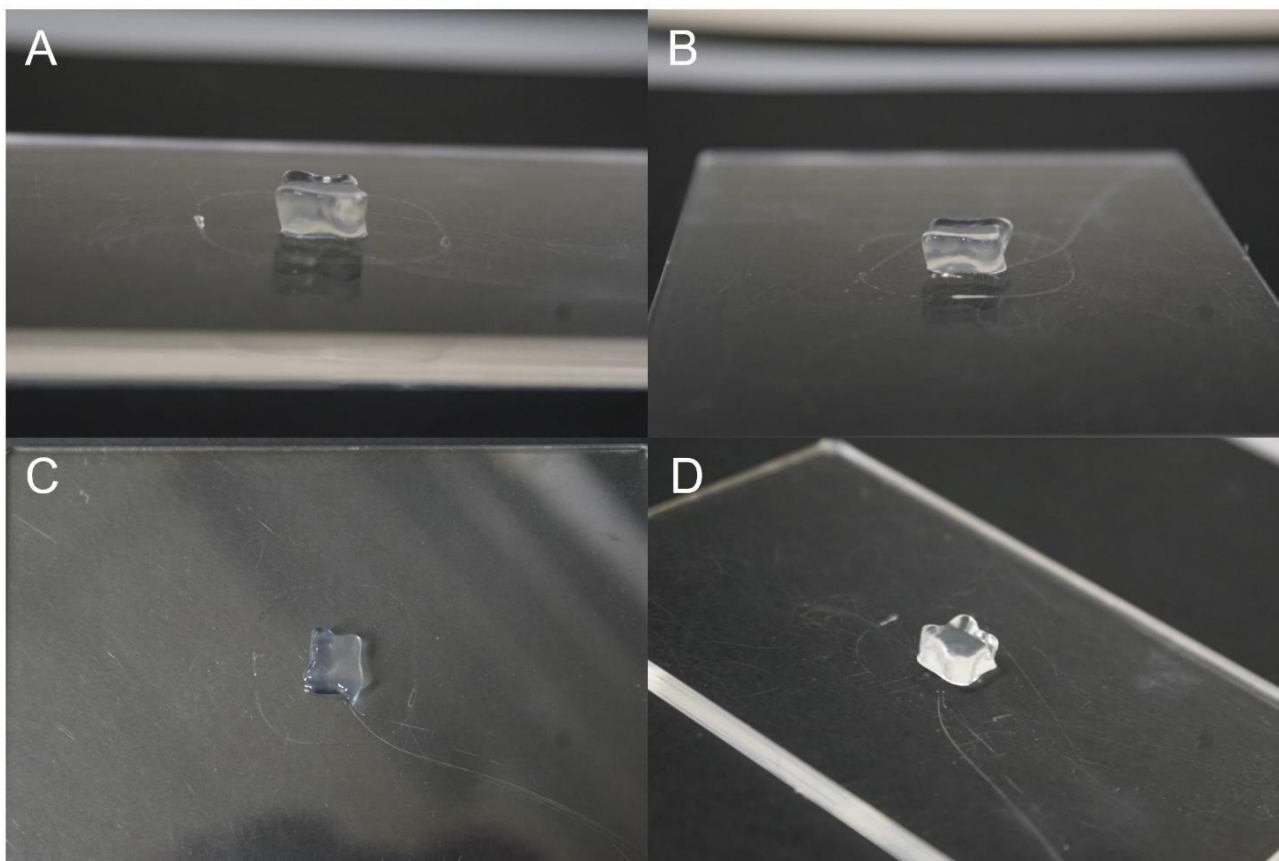


Figure 5.39: 3D printed 22.5 ° overhang model (base area 10 × 10 mm, 5 mm height) produced using a 2 %/30 mM primary-crosslinked hydrogel at a print speed of 10mms<sup>-1</sup> and an extrusion pressure of 4.6 psi. (A) front, (B) side, (C) top and (D) orthographic views were captured using a digital camera with an attached polarising filter. The detached skirt of the 3D print can also be seen.

The results of the 22.5 ° overhang model (base area 10 × 10 mm and 5 mm height) that was 3D printed using the 2 %/30 mM hydrogel can be seen in Figure 5.39. The general fidelity of the print did not accurately resemble that of the model design where an inverted, truncated square-based pyramid should have been seen. Instead, a loose rotational symmetry was formed where walls of the material curve to form extensions in each corner. Of these extensions, the rear-right corner was substantially smaller than the others. The overall overhang angle at the extension appeared to be representative of the model in Figure 5.39A, B and C. However, Figure 5.39C clearly shows that middle sections of the wall did not overhang at the correct angle and were more vertical. Figure 5.39A and B also show that the top layer of the 3D print was uneven, being noticeably taller in the corner extensions.

#### 5.4.3.3.2. 3 %/30 mM Hydrogel

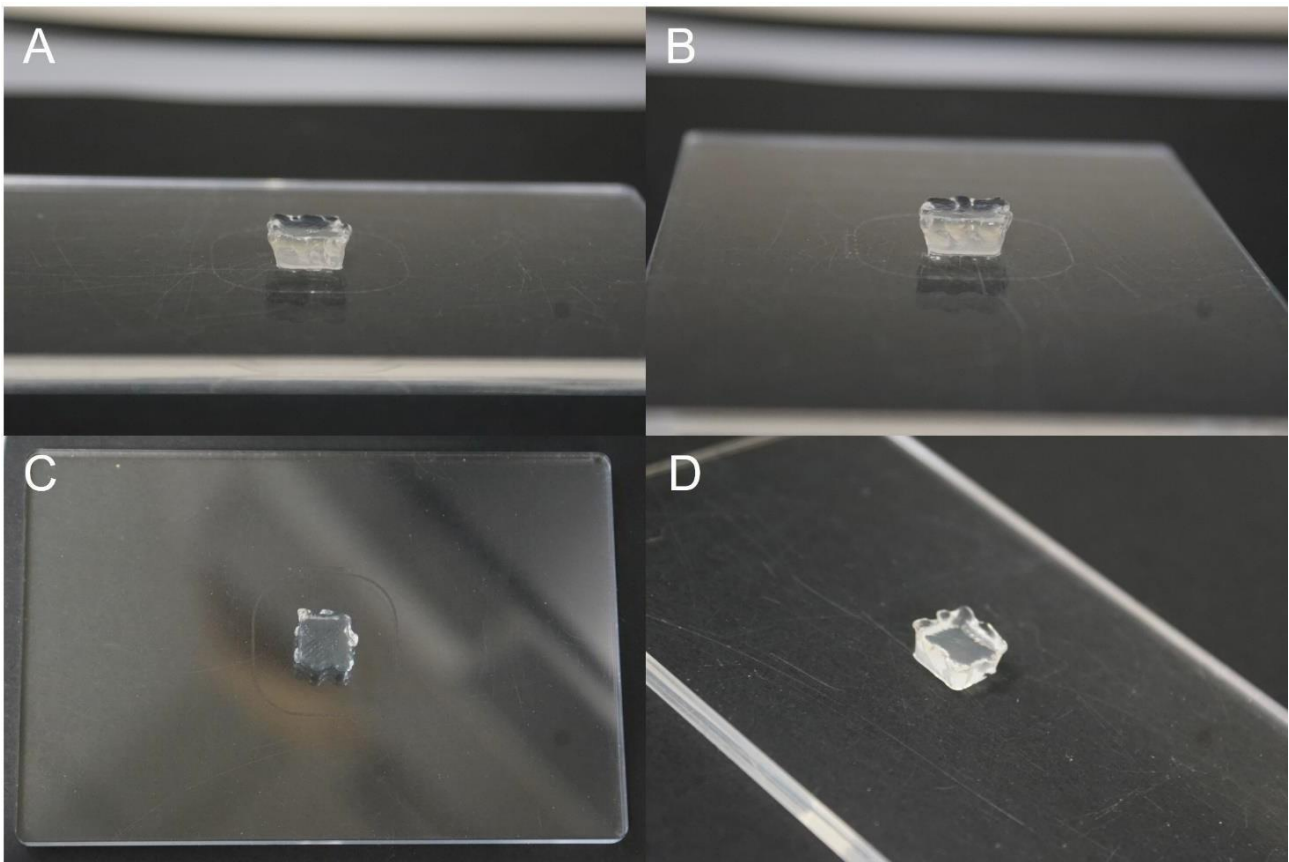


Figure 5.40: 3D printed 22.5 ° overhang model (base area 10 × 10 mm, 5 mm height) produced using a 3 %/30 mM primary-crosslinked hydrogel at a print speed of 10mms<sup>-1</sup> and an extrusion pressure of 10.4 psi. (A) front, (B) side, (C) top and (D) orthographic views were captured using a digital camera with an attached polarising filter. The detached skirt of the 3D print can also be seen.

Figure 5.40 shows the results of 3D printing the 22.5 ° overhang model using the 3 %/30 mM hydrogel. The overall fidelity better resembled the model design than Figure 5.39 however there were still major flaws present. The extensions in the upper section of the model were still present however instead of large, individual extensions on corners there were now several, smaller extensions on both corners and in mid-sections of walls. Bar these, the cross section far better resembled the desired square-shape as seen in Figure 5.40C. Figure 5.40A and B show that the walls did not appear straight in lower sections but as height increased, the overhang angle increased. But, as seen in Figure 5.40C, similar to the 2 %/30 mM results, middle sections of the wall were seen to have low overhang angles and were too vertical. The surface was also considerably flatter which can be seen in Figure 5.40A and B however this was still not accurate to the model design.



#### 5.4.3.3.3. 5 %/30 mM Hydrogel

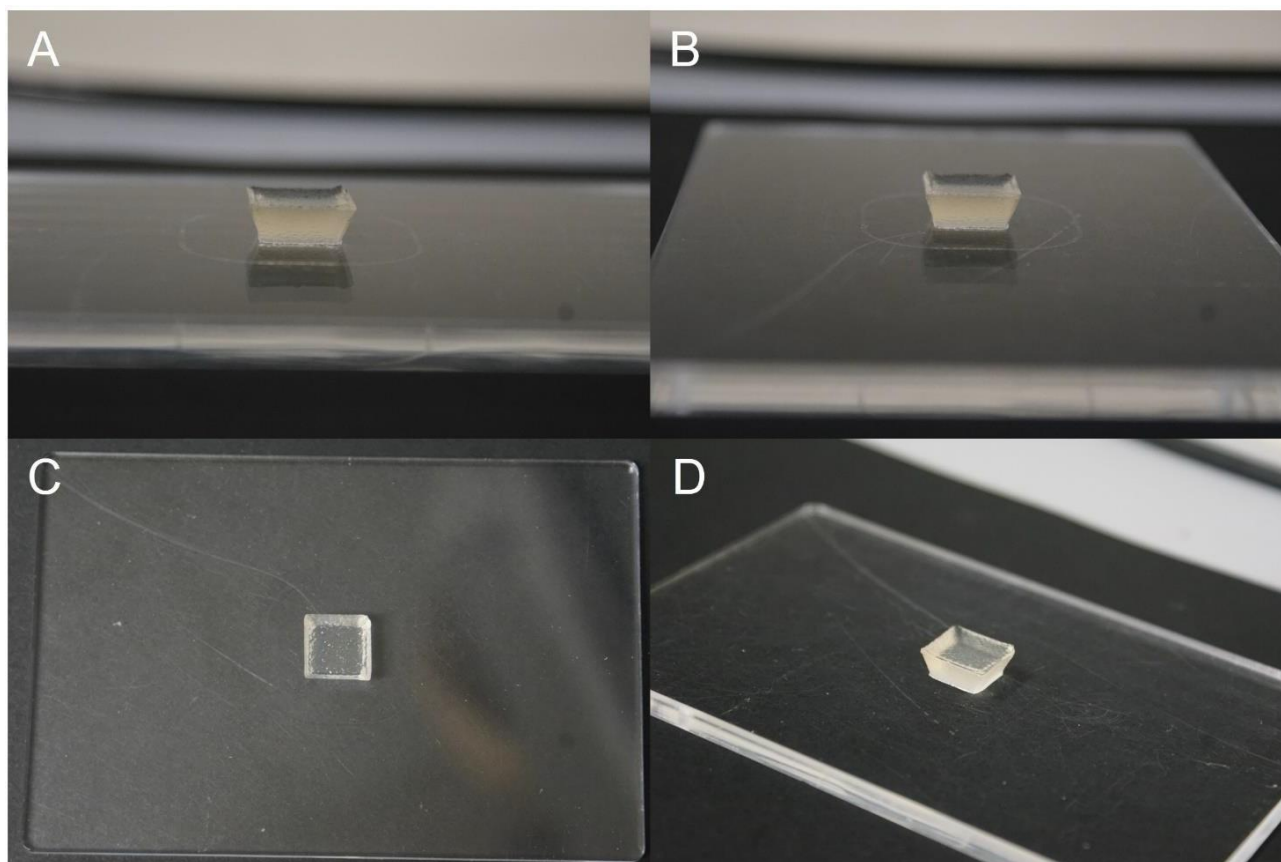


Figure 5.41: 3D printed 22.5 ° overhang model (base area 10 × 10 mm, 5 mm height) produced using a 5 %/30 mM primary-crosslinked hydrogel at a print speed of 10mm<sup>s</sup><sup>-1</sup> and an extrusion pressure of 30.4 psi. (A) front, (B) side, (C) top and (D) orthographic views were captured using a digital camera with an attached polarising filter. The detached skirt of the 3D print can also be seen.

Results of 3D printing the 22.5 ° overhang model using the 5 %/30 mM hydrogel are seen in Figure 5.41. There was a strong improvement in fidelity which clearly resembled the design model far better than results seen in Figure 5.39 and Figure 5.40. No extensions were present and edges of the 3D print, both at the top and bottom, were straight. All of the walls also maintained the same overhang angle throughout their length which resembled that of the design model. The cross section was also square-shaped as intended, with uniform X- and Y-axis as seen in Figure 5.41C. The top of the 3D print was largely flat, which was a substantial fidelity improvement compared to results using the other hydrogel compositions however some of the corner extremities still displayed a minor increase in height in Figure 5.41A and B.

#### 5.4.3.4. 45 Degree Overhang

##### 5.4.3.4.1. 2 %/30 mM Hydrogel

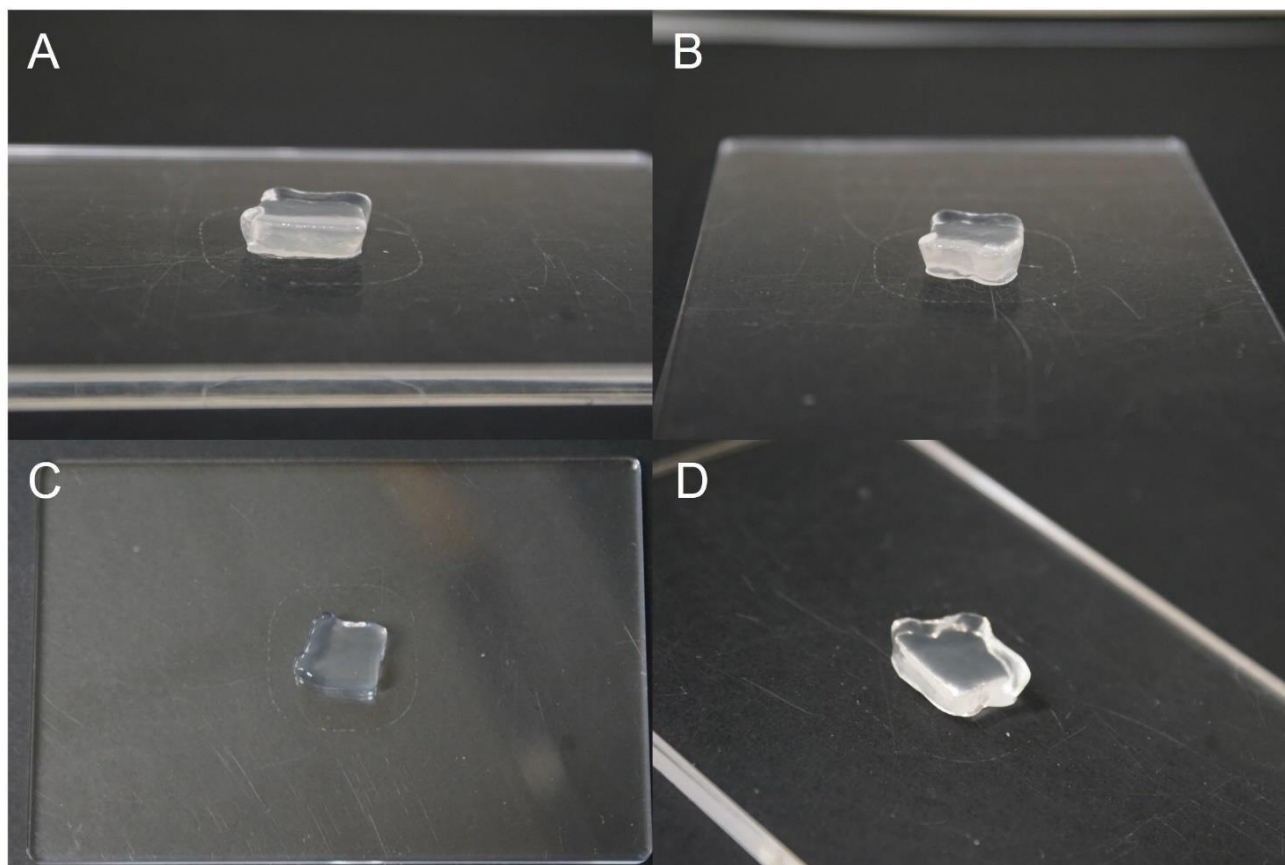


Figure 5.42: 3D printed 45 ° overhang model (base area 10 × 10 mm, 5 mm height) produced using a 2 %/30 mM primary-crosslinked hydrogel at a print speed of 10mm<sup>s</sup><sup>-1</sup> and an extrusion pressure of 4.6 psi. (A) front, (B) side, (C) top and (D) orthographic views were captured using a digital camera with an attached polarising filter. The detached skirt of the 3D print can also be seen.

Figure 5.42 shows the results of 3D printing the 45 ° overhang model (base area 10 × 10 mm and 5 mm height) using the 2 %/30 mM hydrogel. The overall fidelity of the print was poor, with no straight edges being present at either the base section or the top section. Additionally, the walls did not exhibit the target overhang angle of 45 ° and presented an elephant's foot which are both seen Figure 5.42A and B. The overall cross section that was seen in Figure 5.42C presented extensions in each corner which matched that seen when printing with the same hydrogel to produce the 22.5 °, seen in Figure 5.39. Again, this formed a loose rotational symmetry however sizes of the corner extension varied. The top layer was also seen to be non-flat in Figure 5.42A and B where corners were taller than mid-

sections of walls.

#### 5.4.3.4.2. 3 %/30 mM Hydrogel

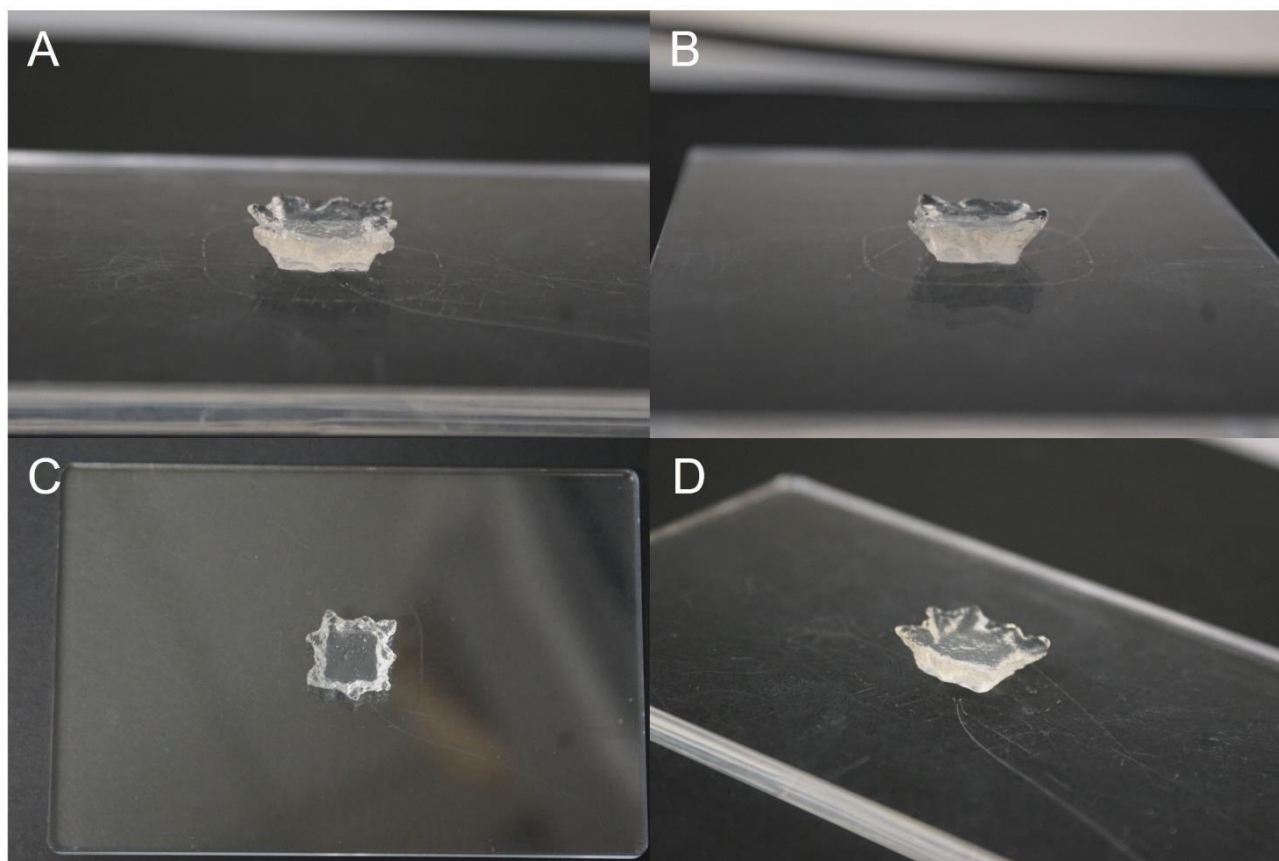


Figure 5.43: 3D printed 45 ° overhang model (base area 10 × 10 mm, 5 mm height) produced using a 3 %/30 mM primary-crosslinked hydrogel at a print speed of 10mms<sup>-1</sup> and an extrusion pressure of 10.4 psi. (A) front, (B) side, (C) top and (D) orthographic views were captured using a digital camera with an attached polarising filter. The detached skirt of the 3D print can also be seen.

The results of 3D printing the 45 ° overhang model using the 3 %/ 30 mM hydrogel can be seen in Figure 5.43. Again, there was low fidelity of the print compared to the model design although there were minor features that represented an improvement versus the 2 %/30 mM hydrogel results. The base of the print adhered well to the square shape it should have been, however, this was imperfect as demonstrated by the distorted front wall section in Figure 5.43A and D. In contrast, multiple curved extensions were seen on the top of the print that extended from the centre, seen in Figure 5.43C, which did not accurately represent the intended square shape cross section. This was similar to results obtained from the 22.5 ° overhang model using the same hydrogel as seen in Figure 5.40. In addition, the wall

overhang angle was mostly accurate to the design model, however, Figure 5.43B and D clearly show the overhang angle increased with increased print height which was undesired. Figure 5.43A and B also clearly display an irregular surface which was seen to be particularly tall at the front-left and rear-right corners.

#### 5.4.3.4.3. 5 %/30 mM Hydrogel

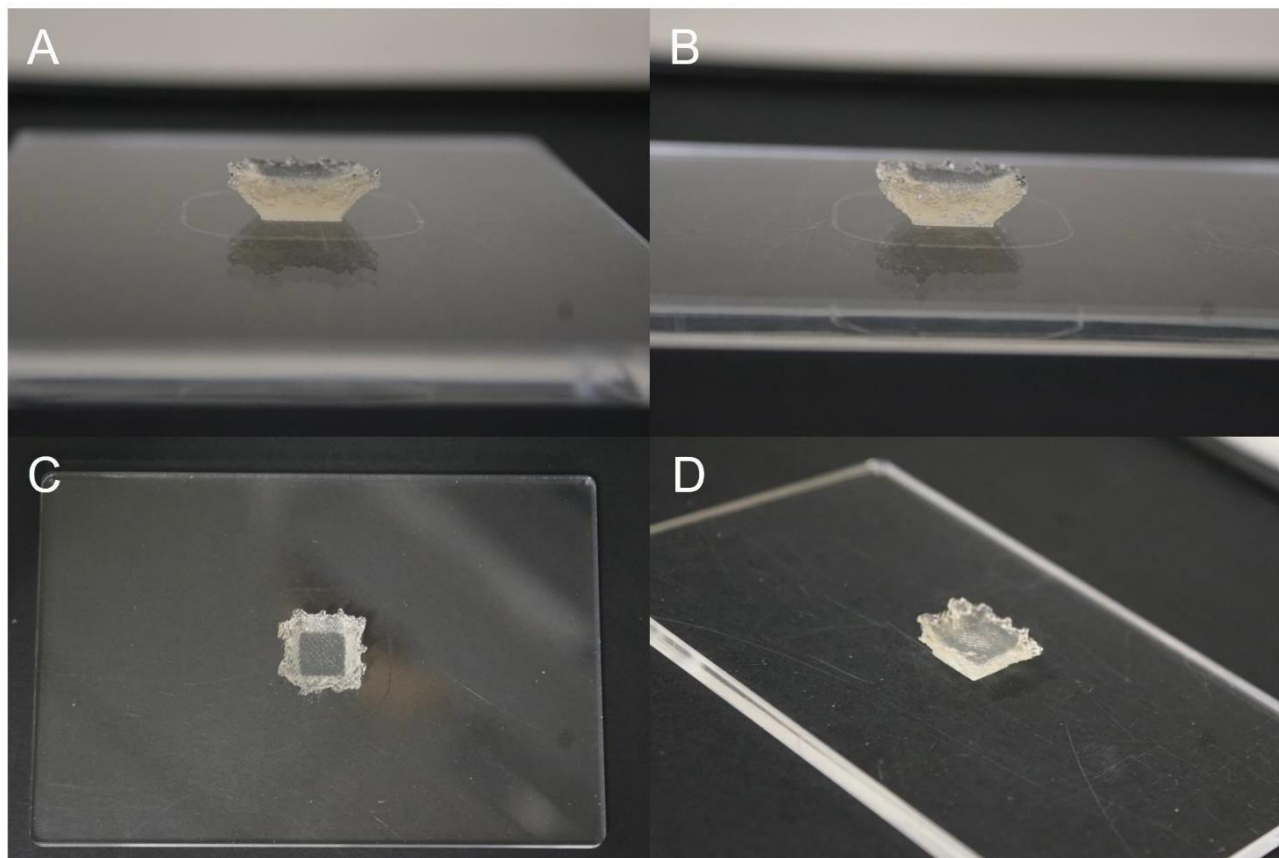


Figure 5.44: 3D printed 45 ° overhang model (base area 10 × 10 mm, 5 mm height) produced using a 5 %/30 mM primary-crosslinked hydrogel at a print speed of 10mm<sup>s</sup><sup>-1</sup> and an extrusion pressure of 30.4 psi. (A) front, (B) side, (C) top and (D) orthographic views were captured using a digital camera with an attached polarising filter. The detached skirt of the 3D print can also be seen.

Figure 5.44 displays the results of the 45 ° overhang model using the 5 %/30 mM hydrogel. The fidelity was still imperfect compared to the design model however distinct features could be identified that demonstrated an improvement compared to results from the 2 %/30 mM and 3 %/30 mM hydrogels. The base of the print was seen to be square as intended and possessed good X- and Y-axis symmetry as seen in Figure 5.44A and Figure 5.44B although a very slight elephant's foot was still seen. The overall overhang angle was also accurate to the design model and was seen to be straight at all layer heights. The upper surface did not

present a uniform square shape and exhibited extensions similar to Figure 5.42 and Figure 5.43. However, as seen when comparing the top views (C) of results, it was clear that the surface of the 5 %/30 mM print incorporated a substantially larger area which better resembled the design model. The surface of the top layer was also notably flatter as intended, compared to the other two hydrogel results.

## **5.5. Mechanical Testing of 3D Printed Hydrogels**

Evaluation of 3D printing multi-layer geometries showed that the PC sample 5 %/30 mM performed well and exhibited high fidelity in experiments so was selected as the final composition, to be used in mechanical testing. Compression specimens (diameter 15 mm, length 5 mm) were 3D printed using the Allevi 2 using a 5 %/30 mM hydrogel composition, extrusion pressure of 30.4 psi and print speed of 10 mms<sup>-1</sup>. Post-print, specimens were secondary-crosslinked by being submerged in CaCl solutions of 50 – 300 mM for 15 – 240 mins. Compression experiments were performed on the specimens and resultant data analysed in Excel and GraphPad to calculate elastic modulus and toughness.

### **5.5.1. Elastic modulus**

Figure 5.45 displays the elastic moduli of secondary-crosslinked hydrogel specimens. There was a clear overall trend at 50, 100 and 200 mM secondary crosslinker concentrations that as crosslinking time increased, elastic moduli also increased, with few exceptions. Within the 50 mM group, the only samples with elastic modulus values that were not significantly different to each other were the 120 and 240 mins crosslinking durations. Within the 100 mM group, elastic moduli of the 30 – 240 mins crosslinking durations all showed significant elastic modulus increases compared to the 15 mins value, as did the 240 mins duration to the 30, 60 and 120 mins results. However, between the 30, 60 and 120 mins values, no



significant differences were seen.

## Secondary-Crosslinked Hydrogel Elastic Modulus

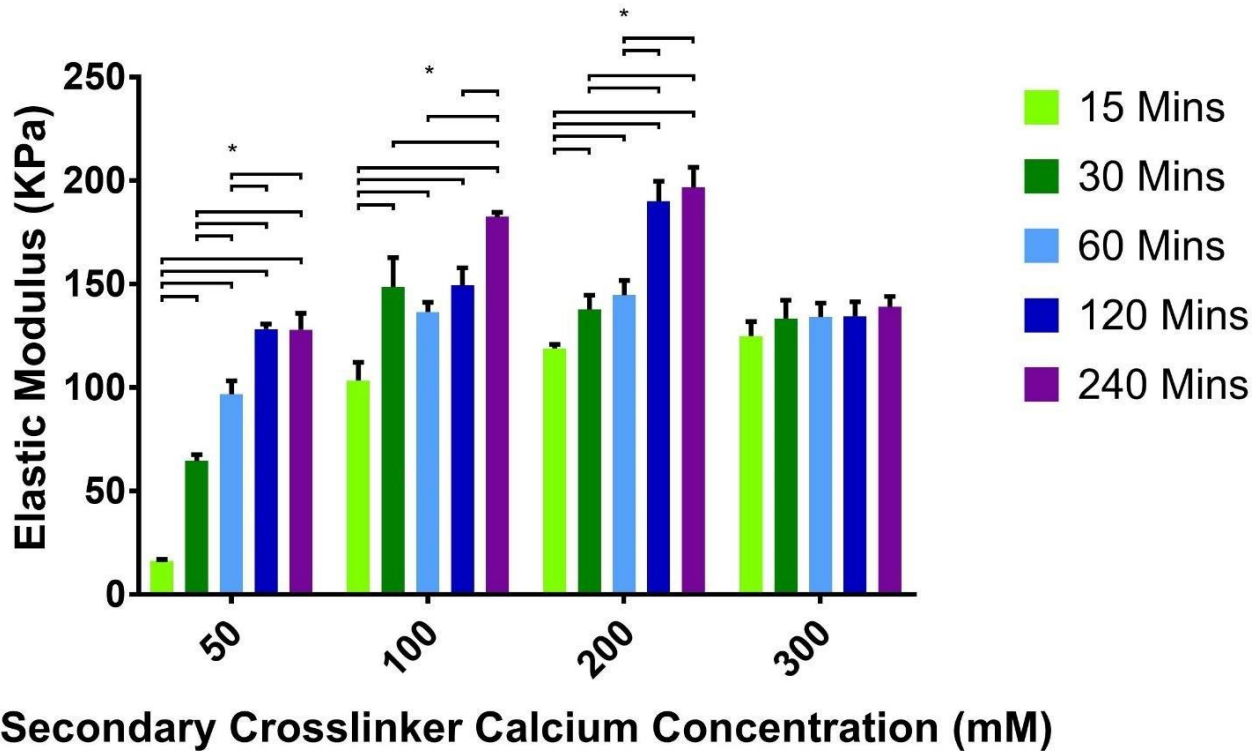


Figure 5.45: Elastic modulus of hydrogel specimens (diameter 15 mm, length 5 mm) that were 3D printed using the 5 %/30 mM hydrogel and secondary-crosslinked with CaCl solutions of 50 – 300 mM for 15 – 240 minutes. Mean and standard deviation plotted,  $n = 3$ . A two way ANOVA statistical significance test was performed. A  $p$  value of  $\leq 0.5$  was considered statistically significant (\*).

Within the 200 mM group, the elastic moduli of specimens that were crosslinked for 30 – 240 mins were significantly greater than the 15 mins one. Those crosslinked for 120 mins and 240 mins also exhibited significantly greater elastic moduli than the 30 and 60 mins specimens. Individually, the 60 mins sample elastic modulus was not significantly different to the 30 mins one nor the 120 mins sample to the 240 mins sample. The results within the 300 mM group did not present any significant differences between any crosslinking durations.

### 5.5.2. 60 % Strain Toughness

60 % strain toughness results of secondary-crosslinked hydrogel specimens can be seen in

Figure 5.46. For all secondary crosslinker concentrations there was a relationship that toughness increased with longer crosslinking durations. Within the 50, 100 and 200 mM secondary crosslinker concentration groups this formed a direct response with few exceptions. However, for the 300 mM group, a significant increase in elastic moduli was only seen when comparing a 15 mins crosslinking duration to 30 – 240 mins. This was in contrast to the observed non-significance between the same specimens when comparing elastic moduli in Figure 5.45. The 50, 100 and 200 mM groups, however, presented identical intra-group significance.

Each subsequent increase in crosslinking duration within the 50 mM secondary crosslinking concentration group provided a sequential increase in toughness that was significant except for between the 120 and 240 mins results. Within the 100 mM group, increasing the crosslinking duration from 15 mins to 30 – 240 mins caused a significant increase in toughness. Further increasing the duration from 30 – 120 mins to 240 mins also caused a significant increase however this was not seen when increasing from 30 to 60 mins or 60 to 120 mins.

## Secondary-Crosslinked Hydrogel Toughness

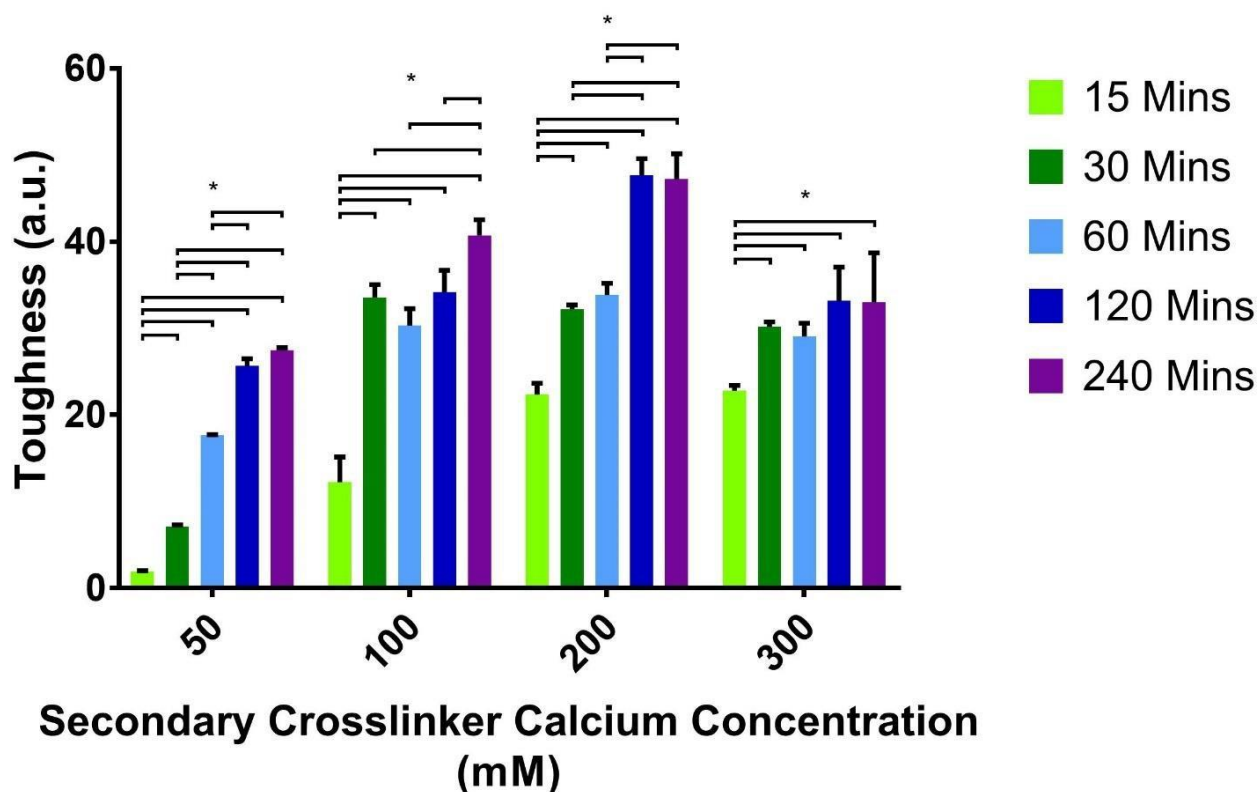


Figure 5.46: 60 % strain toughness of hydrogel specimens (diameter 15 mm, length 5 mm) that were 3D printed using the 5 %/30 mM hydrogel and secondary-crosslinked with CaCl solutions of 50 – 300 mM for 15 – 240 minutes. Calculated toughness is a dimensionless quantity so arbitrary unit (a.u.) was used as the axis unit. Mean and standard deviation plotted,  $n = 3$ . A two way ANOVA statistical significance test was performed. A  $p$  value of  $\leq 0.5$  was considered statistically significant (\*).

The elastic moduli of specimens within the 200 mM group that were crosslinked for 30 – 240 mins were significantly greater than the sample that was secondary-crosslinked for 15 mins. Samples that were secondary-crosslinked for 120 mins and 240 mins also possessed greater elastic moduli than the 30 and 60 mins samples. However, increases from 30 to 60 mins crosslinking duration and 120 to 240 mins did not show significant changes in the elastic moduli of samples.



## 6. Discussion

This section will discuss the results obtained within the project with respect to the literature and original aims of the project. To recap, the original aim of this project was to employ recent advancements in 3D printing technology to produce biocompatible and biodegradable devices that could be used as palatal obturators as an alternative to traditional flap surgery materials.

### 6.1. Proton Nuclear Magnetic Resonance Spectroscopy

The six major  $^1\text{H}$  NMR spectra peaks detailed within the ASTM F2259-10 image (Figure 4.4) were displayed in all three tested alginate strains (Figure 5.1). Overall, each strain's spectra profile accurately reflected the template by producing six prominent peaks (4.45, 4.66, 4.69, 4.71, 4.75 and 5.05 ppm); however, some minor differences in relative intensity were seen. Figure 4.4 clearly shows a B3 peak larger than B2, however, in strains 1 and 2 the results gathered in this project displayed the opposite. Additionally, the template demonstrated a C peak larger than the A peak although the opposite was found in strains 2 and 3, however the intensities of these peaks were very similar.

ASTM F2259-10 did not refer to whether the image provided was simply arbitrary or whether it represented a rigid model with respect to relative peak intensity. However, as this was not explicitly stated within official standardisation documentation, the former can be assumed with high confidence and the peak intensities were deemed accurate. This was supported by other  $^1\text{H}$  NMR alginate studies where similar variation was reported (Grasdalen, 1983; Belattmania *et al.*, 2020).

The selection of peaks within the method was potentially open to some selection bias as many minor peaks were initially labelled within MestReNova during the automatic labelling process, which needed to be removed manually. In those results, however, there was a clear distinction between the large intensity of the six expected peaks and the considerably smaller intensities of automatically labelled additional peaks. One possible exception to this statement was the unlabelled peak located at 4.3 ppm where, in strain 3 specifically, it appeared prominent. However, this peak was present in the ASTM example image (Figure 4.4) and not labelled there; hence the same distinction was applied to this project's  $^1\text{H}$  NMR results.

The standard did not explicitly state the location of expectant peaks however, Figure 4.4 exhibited peaks at approximately 4.45 (C), 4.66 (B4), 4.7 (B3), 4.72 (B2), 4.75 (B1) and 5.05 ppm (A). These peaks closely resembled those found within this project which were located at 4.45, 4.66, 4.69, 4.71, 4.75 and 5.05 ppm, as seen in Figure 5.1. This level of variation was in-line with what was reported in surrounding literature (Grasdalen, 1983; Belattmania *et al.*, 2020).

However, as these peaks were measured through analysing identical chemical bonds signatures, there should theoretically be no variation between peak locations. Possible sources of this variation were differences between the NMR system used in the project versus the one used in ASTM F2259-10. Whilst core specifications ensured important settings remained the same, machine calibration could have also been a factor. This peak location variance could have also been caused by the processing of the spectra within MestReNova. This, however, was unlikely as functions within MestReNova focused on smoothing and baseline correction as opposed to effects along the X-axis. All things considered, variation between peak locations of the three tested alginate strains and ASTM F2259-10 was only  $\pm 0.01\text{ppm}$ , which was negligible. Thus, in summary, the collected spectra and corresponding peak locations were deemed valid and within reasonable

tolerance limits of the standard.

Overall, the final quantifiable outputs in Table 5.3 and Table 5.4 detailed the amount of G and M and two-length blocks (MM GM/MG and GG). This successfully achieved one of the objectives of the project which was to investigate the chemical structure of commercial alginate strains. One of the limitations of this method was that not all three-length blocks were quantified and varying amounts of the total three-length sequences remained uncharacterised (66.40 % for strain 1, 70.60 % for strain 2 and 77.11% for strain 3). These missing sections were, however, likely an unnecessary level of precision as knowledge of triple block sequences has limited practical applications. In contrast, double block sequences such as GG were far more relevant as these form binding sites for ionic crosslinking (Ertesvåg and Skjåk-Bræk, 1999). Therefore, additional GG sequences would allow a greater degree of crosslinking within hydrogels before saturation was reached.

Other studies have utilised  $^1\text{H}$  NMR for analysing alginate chemical composition but also used size exclusion chromatography to calculate molecular weight (Kong *et al.*, 2004). The molecular weight of sodium alginate is known to have a heavy impact on viscosity and the inter-connectivity of crosslinked alginate chains, so this would be an ideal addition to this body of work. The purity of alginate could also be investigated as the description of alginate strains was beige and faint yellow, whereas pure sodium alginate is known to be white. Studies have shown that alginate purity significantly affects the biocompatibility of alginate-based scaffolds and medical devices (Zhang *et al.*, 2001; Wang *et al.*, 2003). High purity is therefore essential for producing alginate devices that may hold the potential to develop medical devices. One suitable method for determining alginate purity is determining the uronic acid content through sulfuric acid hydrolysis which reacts with 3-phenylphenol to form pink colouration, the intensity of which is measured by spectrophotometry (Vauchel *et al.*, 2008).

## 6.2. Hydrogel Composition Optimisation

### 6.2.1. Visual Assessment

The results of the visual assessment in Section 4.4.2 showed that, as alginate concentration increased, the depth of the olive colour within hydrogels increased, which was seen in other studies (Tabriz *et al.*, 2015). This was due to the off-white, beige colour of sodium alginate powder used in the project which transferred to the hydrogel once dissolved. There was also increase in opacity when higher concentrations of  $\text{CaCl}_2$  were present within hydrogels.

Alginate hydrogels are known to turn opaque during secondary crosslinking as they are subjected to large concentration of divalent ions and transition from a gel to a solid. This was a clear indicator that the degree of crosslinking within the opaque syringes was likely too great for 3D printing as material properties would be less gel-like. The diminished presence of opaque hydrogel samples as alginate concentration increased were evidence that the degree of crosslinking that occurred, reduced as ratios of alginate to  $\text{CaCl}_2$  increased, which is a known factor in gelation rate (Catherine K Kuo and Ma, 2001). This was supported by the phase separation seen in samples that had the lowest alginate to  $\text{CaCl}_2$  concentration amongst the produced range. The solid particulate was fibrous in nature which would suggest that this was individual alginate strands that hold undergone sol-gel transition which also their density.

### 6.2.2. Extrudability

Section 5.2.2 detailed results of the extrudability experiment which demonstrated that there was a clear limit to what was reliably extrudable within the selection of hydrogel compositions. An upper limit was identified at each alginate concentration where any further  $\text{CaCl}_2$  would cause an irregular flow rate or prevent flow altogether.

Many of the opaque samples that were previously highlighted produced unstable flow or failed to extrude material altogether which supported the belief that these samples had been over-crosslinked. For permanent blockages to occur, solid-like regions larger than the 0.41 mm dispensing tip diameter had to be present. Likewise, for unstable flow to occur, both varied strengths of hydrogel must have been present to resist the steady-state extrusion pressure by differing amounts. Neither of these qualities were suitable for FFF printing which required a steady flow of homogenous material.

One method of overcoming this would be to increase the dispensing tip size as some others have done (Menshutina *et al.*, 2021). This, however, would have detrimental effects on the 3D printing resolution that could be achieved. This is because individual filament width and height, would both increase to correspond with the new dispensing tip size. For this reason, the 0.41 mm dispensing tip was still considered appropriate.

### 6.2.3. Extrusion Form

Samples that were reliably extruded were then examined in Section 5.2.3 to analyse their extrusion form. This revealed that all UC samples produced liquid-like extrusion as well as some of the samples that contained lower concentrations of alginate whilst the majority produced fibre-form extrusion. This demonstrated that there was a minimum amount of alginate and  $\text{CaCl}_2$  that was required to produce fibre-like extrusion and the relative amounts of each were important. Specifically, increasing alginate concentration in the 1 and 1.5 % alginate concentrations generated an unexpected result where extrusion form reverted back to liquid-like.

This demonstrated that there was not a linear relationship between crosslinker concentration and extrusion form. This presented a curious instance where the average crosslinked degree was known to have increased but the overall material appeared less crosslinked. The logical

reason for this was that gelation rate within these samples was also too high which led to a minority of the alginate chains receiving a disproportionate amount of crosslinking. Unlike samples that produced unreliable flow in the extrudability test, the size of more solid-like alginate portions within these samples must have been low enough to still exhibit stable flow.

#### 6.2.4. Extrusion Pressure

Section 5.2.4 detailed the results of the extrusion pressure test which indicated that pressures between 0.6 – 53.4 psi could be used to extrude the tested hydrogels. This was in-line with other pressures that had been reported to work well with printing alginates with the Allevi 2 (Lewicki *et al.*, 2019; Serafin *et al.*, 2021). Each column that related to a specific CaCl<sub>2</sub> concentration presented an increase in the extrusion pressure that was required to correctly print a 0.5 × 0.2 mm filament at a speed of 10mms<sup>-1</sup>. In contrast, when observing rows that corresponded to a specific alginate concentration, pressure values increased then decreased over the range of samples that were reliably extrudable.

This was further evidence that a linear relationship did not exist between increasing crosslinker concentration and associated effects such as extrusion form, or in this instance, extrusion pressure. Amongst PC samples, extrusion pressure was greater in samples that previously produced fibre-form extrusion however, as demonstrated with the high extrusion pressure UC samples that exhibited liquid-like extrusion, this was not a universal rule.

Interestingly, despite using a broad range of hydrogel samples, the required extrusion pressure capped at 53.4 psi whilst the Allevi 2 could operate to 100 psi. This demonstrated that, using this project's hardware setup, constraints were imposed primarily due to material attributes such as alginate solubility and dual-syringe mixing method efficacy. However, the Allevi 2 did underperform in some situations such as when low extrusion pressures of <5 psi were required. Within that range, limited extrusion pressure precision could be obtained through the 'higher' and 'lower' functions within Bioprint. This was because the same amount

of motor movement was applied regardless of pressure, which caused relatively larger changes at lower extrusion pressures.

Low viscosity hydrogels are desirable in applications where cell-laden hydrogels are used. This is because less shear force is induced amongst cells which corresponds to less cell damage and a greater viability post-extrusion (Blaeser *et al.*, 2016). This was not the focus of this project, however, if future studies want to explore low-viscosity hydrogels in more detail, other forms of 3D printing such as droplet-based techniques are more suited to this (Burdis and Kelly, 2019). A workaround using this project's setup would be to utilise a larger gauge dispensing tip however, as previously discussed, this would incur losses in printing precision.

### 6.2.5. Layer Formation and Retention

Section 5.2.5 shows the results of the layer formation and retention part of the hydrogel composition optimisation experiment where all of the UC samples and samples that contained either lower concentrations of alginate or  $\text{CaCl}_2$  did not form distinct layers. Interestingly, the three highest alginate concentration samples that contained 5 mM  $\text{CaCl}_2$  previously exhibited fibre-form extrusion but could not form distinct layers. This was evidence that a fibre-form extrusion was not a guarantee of a material being suitable for FFF 3D printing.

The layer formation and retention test demonstrated that there is a distinct region where specific values of alginate and  $\text{CaCl}_2$  concentration combine to provide optimal characteristics for 3D printing. Previous studies have explored 3D printing at lower alginate concentrations however this test suggests that they are not suitable, or at the least, not optimal for 3D printing (Song *et al.*, 2011).

One limitation of this test was that some hydrogels demonstrated poor fidelity but were still

awarded the best score for layer formation and retention. That said, this was a stress test and was expected to produce poor fidelity as it was designed to push the limits of material printability, something actively avoided in routine 3D printing. Additionally, the layer formation and retention test were not designed to evaluate 3D printing fidelity and was instead limited in scope to layer characteristics. Further 3D printing evaluation that focused on fidelity was performed later in the project.

### 6.2.6. Viscosity

The viscosity results can be seen in Section 5.2.6 where a similar trend was seen compared to the extrusion pressure results in Section 5.2.4 where central  $\text{CaCl}_2$  concentrations possessed higher viscosities. However, amongst the hydrogels that contained 10 and 15 mM  $\text{CaCl}_2$ , a maximum viscosity was observed after which further increases in alginate concentration lowered the viscosity. This was evidence that excess alginate concentrations can also be the reason for limiting the strength of hydrogels, not just the previously discussed  $\text{CaCl}_2$  concentration.

The heat maps demonstrated that peak extrusion pressure did not directly correlate with peak viscosity, demonstrating the shear thinning properties of alginate that had been previously reported (Rezende *et al.*, 2009; Eskens, Villani and Amin, 2021; Feng *et al.*, 2021). This was because viscosity could be used as a rough indicator of hydrogel strength whereas extrusion pressure was how much shear force was required to cause flow. Shear thinning is a principle that was beneficial when 3D printing alginate as it allowed ease of printing whilst retaining a high hydrogel strength, one of the main cited drawbacks to their use (Drury and Mooney, 2003; Augst, Kong and Mooney, 2006).

Specifically, the UC samples clearly demonstrated that increased viscosity was not an indication of a material's suitability in 3D printing as this had not previously enabled better results in the layer formation and retention experiment. Many 3D printing-focused studies



only provided viscosity values as rheological characterisation of bioinks however the results of the hydrogel composition optimisation clearly demonstrate this is an unsuitable metric for describing viscoelastic behaviour (Freeman and Kelly, 2017; Mallakpour, Azadi and Hussain, 2021). This was the reason a full rheological characterisation was performed.

## 6.3. Rheology

### 6.3.1. Constant Shear

Section 5.3.1 shows the results of the constant shear rheology experiment where, within both the UC and PC groups, viscosity increased as alginate concentration increased. PC samples had greater viscosities than UC samples except for 2 %/30 mM which had a lower viscosity than 5 %. There was some variance between 0.5 and 1 s, particularly within the UC samples, but this was not seen for the remainder of the test. Specifically, the rheometer recorded a negative value for viscosity for the 1 % UC sample which was impossible as that would mean the hydrogel propelled flow instead of resisted it. This was likely due to a phenomenon known as sample inertia and that can produce erroneous results (Hudson *et al.*, 2017). It could also simply be limitations of the rheometer itself where a relatively short sampling time was used with a low shear rate. Combined, these two factors cause a SNR that approaches the limit of what the MCR 301 rheometer can resolve.

Ultimately, a compromise must be made when collecting rheological data in this way to maximise result precision through small sampling times whilst not sacrificing a suitable SNR (Ghiringhelli *et al.*, 2012). The initial inertia was, however, overcome within < 1 s on a minimal shear rate. This validated that later rheological experiments, which used sampling times of 5 s, would contain negligible data that had been affected by inertia.

The first data point was compared to the last to demonstrate how sample inertia affected variance and how using a 10 s test duration reduced this. The effects were seen most in the

1 % UC sample which was to be expected as this presented the lowest viscosity and thus, lowest SNR amongst the data set. Interestingly, PC samples displayed less change to the CoV values which indicated that the PC samples were less susceptible to error generated through initial sample inertia.

Exponential trends for viscosity values after 10 s indicated an exponential trend for both UC and PC samples as alginate concentration increases. This mirrored previous exponential trends that were seen in the extrusion pressure results of the hydrogel composition optimisation experiments. These exponential trends mirrored those previously reported, however more detailed comparisons cannot be drawn as test settings are often not provided in studies (Tabriz *et al.*, 2015). Viscosity, by definition, is the resistance to flow which is directly influenced by variables such as shear rate and temperature. Without providing these, viscosity results (and any other rheological data) are ultimately futile.

### 6.3.2. Amplitude sweep

The amplitude sweep storage and loss moduli results in Section 5.3.2 showed that all UC and PC samples exhibited linear regions. This was to be expected as, regardless of crosslinking status, all hydrogels formed a network of alginate chains that possessed a degree of organisation, which would resist flow. The 1 % UC sample had results below 0.68 % strain removed which was evidence that the rheometer was setup to a good compromise of maximising data collection precision whilst retaining a good SNR. This is because 0.5 – 1 % strain is typically used as a low, near-zero strain rate and, whilst values below that adds overall knowledge, they were not as important (Ozbekova and Kulmyrzaev, 2017; Labaky *et al.*, 2020).

When testing samples at low strain values, omission of results that displayed noise due to low SNR was standard (Wang *et al.*, 2021). Noisy data was easily distinguishable from otherwise smooth data so any omissions were conducted with high confidence that they

were appropriate. As strain increases, the forces exerted on the sample increased and subsequently resistance forces increased too, which was why low SNR not an issue at higher strain rates.

Complex viscosity results showed that all UC and PC samples exhibit shear thinning however in PC samples this was more noticeable and happens at lower strains. As previously discussed, this could be beneficial in future studies that use cell-laden hydrogels.  $\text{Tan}(\delta)$  results further evidenced this where a clear distinction was seen between the changes in gradients, which signalled the start of a shear thinning region at lower strains.

### 6.3.3. Frequency Sweep

Section 5.3.3 contains results for the frequency sweep that were performed to further investigate the linear viscoelastic regions of materials where all the UC samples exhibited crossover points whereafter  $G' > G''$ . This was previously unseen in amplitude sweeps results in Section 5.3.2 as this used a fixed frequency of 1Hz and the crossover points occur at approximately 6 – 8 Hz for both 3 % and 5 %. The lowest concentration UC sample, 1 %, did not exhibit a crossover point and all data showed  $G' > G''$ . However, the trends of  $G'$  and  $G''$  of 1 % suggested that the crossover point lay in the region that was omitted for low SNR. This was an interesting and unforeseen phenomenon where uncrosslinked hydrogels, which were visibly viscous-dominated during loading, were reported as being elastic-dominated at higher frequencies. There was limited information on this available within literature, however, one theory was that the time between oscillations became small enough that network relaxation did not occur which enabled resistive stresses that mimicked crosslinked networks.

PC samples did not present any crossover points which was to be expected as this is one of the fundamental principles of testing within the LVER, that any frequency remains non-destroyed (Leick *et al.*, 2010). Interestingly, it appeared there was very little deviation

between the  $\tan(\delta)$  of the four PC results. This was also unexpected as previously, in the amplitude sweep, there was a loose trend that  $\tan(\delta)$  was lower in samples with lower alginate concentrations (above 1 % strain).

#### 6.3.4. Temperature Sweep

Results of the temperature sweep can be found in Section 5.3.4 where the UC samples exhibited decreasing  $G'$  and  $G''$  from 5 °C through to approximately 50 °C, after which  $G''$  gradient increased. For PC samples,  $G'$  steadily decreased as temperature increased whilst  $G''$  gradually increased for all samples except 5 %/30 mM. 2 %/30 mM and 3 %/30 mM exhibited large increases in  $G'$  and  $G''$  at temperatures above 60 °C whereas 4 %/30 mM and 5 %/30 mM had only minor increases. The UC samples behaved as a group with minor differences in rate of change of  $G''$  but the PC samples were more varied. The reduction in UC storage and loss moduli as temperature increased was in accordance with previously reported studies that found the same in temperature ranges up to 45 °C (Ghanbari, Salavati-Niasari and Mohandes, 2021). This was likely due to the viscous- dominated nature of these samples and that temperature would have more impact on thermokinetics of uncrosslinked alginate chains. In comparison, the PC sample alginate chains were not able to move freely within the hydrogel so an increase in kinetic energy would have less effect.

The decrease in all  $\tan(\delta)$  for all samples after between 30 – 50 °C was likely due to dehydration of the sample, where results after this were invalid as the loaded sample no longer accurately represents its initial form. As water evaporates, the hydrogel artificially becomes more concentrated which was why increases in  $G'$  and  $G''$  can be seen. This was supported by previous studies limiting temperature ranges to 45 – 50 °C, likely to exclude results affected by evaporation (Eskens, Villani and Amin, 2021; Ghanbari, Salavati-Niasari and Mohandes, 2021).

One of the limitations of the oscillatory experiments that used fixed sampling durations was

the sampling efficiency of the MCR 301. Using sampling times  $< 5$  s at a frequency of 1 Hz did not generate enough data to provide a measurement within Rheoplus. A compromise was therefore used to minimise sampling time to provide the best precision possible, without causing data to be omitted. Other devices could be considered in future studies that are able to resolve data more effectively over short measuring times to provide better precision.

### 6.3.5. 3-Interval Thixotropy Test

Section 5.3.5 details the results of the 3ITT. UC samples exhibited drastically decreased  $G'$  and  $G''$  moduli during interval 2 which immediately return to original values, from interval 1, in interval 3. PC samples exhibit the same reduction in  $G'$  and  $G''$  during interval 2 but all contained a crossover after which  $G'' > G'$ . Samples 2 %/30 mM, 3 %/30 mM and 4 %/30 mM all immediately returned to an elastic dominated state in interval 3 (where  $G'' < G'$ ) whereas 5 %/30 mM takes 5 s to do so. Over the next 30 s, substantial changes were observed in PC sample  $G'$  and  $G''$  values, seen in Figure 5.22, where they approach resting values from interval 1.

As previously discussed, the shear thinning of alginate exhibited in interval 2 was beneficial to enable ease of printing however can cause problems within 3D printing if not reversed quickly. An immediate return to a mechanically strong, elastic-dominated state was essential in a 3D printing material to prevent oozing. Oozing is where deposited material would incorrectly spread to surrounding areas whilst in a viscous-dominated state, substantially reducing X- and Y-axis precision. Additionally, if material was not solid- dominated by the time another layer of the print began, additional material would be deposited on top of that which would lead to partial or total collapse of the structure.

Previous studies only included viscosity measurements when conducting 3ITT experiments which does not provide enough information about the overall viscoelastic state (Rial, Liu and Ruso, 2020). This can present misleading results because viscosity returns to resting

states much faster than  $G'$  and  $G''$ , seen when comparing Figure 5.22 and Figure 5.23. In comparison to other alginate 3ITT studies, the results included in this experiment displayed improved rates of recovery (Toker *et al.*, 2015). Overall, the 3ITT test indicated that all four of the PC samples would be good candidate materials for 3D printing due to their rapid return to elastic-dominated states.

### 6.3.6. Post-mix Time Sweep

Post-mix time sweep results are found in Section 5.3.6 where UC samples showed no variation except for the noise within the 1 % sample whilst PC samples showed that  $G'$  and  $G''$  gradually settled to resting values over varied times. Interestingly, 2 %/30 mM and 3 %/30 mM exhibited considerable changes to relative  $G'$  and  $G''$  values during this, as seen in Figure 5.25. These were difficult to clarify as the amplitude results in Section 5.3.2 measured the same 0.5 % strain values but PC sample results were closely grouped and ordered in terms of increasing alginate concentration. Dehydration of the sample was one potential reason however a solvent trap was used to prevent this and any effects would have been seen across all PC samples. Whilst this was seemingly anomalous, it had no bearing on any other rheological results so had negligible impact on overall characterisation.

The rate of recovery within the post-mix time sweep also presented differing results to the 3ITT experiment which previously showed rapid return to relaxation over only 300 s. Although, there were differences in experimental setup of these two experiments. The post-mix time sweep involved larger amounts of material being exposed to larger shear forces over longer times so it stands to reason that recovery time would be increased. Additionally, the fundamental difference in setup was that a 30 minute rest after crosslinking was not utilised, so the relaxation could also be caused by long-term elongated crosslinking effects. This was unlikely however as the crosslinking time for  $\text{CaCl}_2$  was well documented and known to take a matter of seconds without long-term effects (Pan *et al.*, 2015; Naghieh *et*

*al.*, 2018).

One of the limitations of the study was the 150 s required to crosslink and load the sample correctly before the experiment began which meant that early rheological data was missed. Other experimental setups were considered to overcome this, such as adding crosslinking solution to loaded uncrosslinked alginate during rheometer operation which would document all of the crosslinking. The benefits of this would be limited, however, as the degree of crosslinking would be difficult to control and central areas of the sample remain uncrosslinked due to their distance from the crosslinker solution. Ultimately, the aim of this experiment was not to capture early rheological data but to validate when hydrogels reached resting states after production, so the setup was deemed suitable.

## **6.4. 3D Printing**

### **6.4.1. Line width**

Results of the line width experiment can be seen in Section 5.4.1 which showed that for the three PC hydrogels that were tested in this section, as extrusion pressure was increased or print speed was reduced, larger line widths were exhibited (or *vice versa*). It was important to ensure accurate filament line widths were produced as this was the most fundamental level of FFF. Any minor under-extrusion or over-extrusion of material here would cumulate as a 3D print progressed and caused major problems. The G-code used a 0.5 mm line width setting that corresponded with the 0.41 mm internal diameter of the dispensing tip.

When conducting FFF, it is good practice to use a line width slightly larger than your nozzle (or dispensing tip). This is because extruded filaments are produced with a circular cross section that matches tip aperture, but during slicing, rectangular sections are allocated for filaments to fill. This means it is difficult to extrude material to the outer corners of the print area for filament, a known limitation of FFF, which may then lack material (Garzon-

Hernandez *et al.*, 2020). Slicer settings that produced a rectangular cross section were selected to mitigate this error and improve coalescence between filaments.

Extrusion pressures had been previously calibrated in Section 4.4.5.4 to correspond to a print speed of  $10 \text{ mms}^{-1}$  which correlated to a volumetric flow rate of  $1 \text{ mm}^3\text{s}^{-1}$ . Therefore, it was unexpected to see such a large degree of variation from the target line width of 0.5 mm in the two weaker hydrogels when using the default settings of 4.6/10.4 psi and  $10 \text{ mms}^{-1}$ . As the overall volume was known to be correct, a line width greater than 0.5 mm meant that a layer height lower than the 0.2 mm was also produced, thus inaccuracies in all three axis. This increased line width was due to oozing of the 2 %/30 mM and 3 %/30 mM materials. This is where the materials were too weak to stand upright against gravity as a rectangular filament and instead collapsed to some degree. This indicated that, whilst these were elastic-dominated materials, they were still unsuitable for high fidelity 3D printing.

By increasing the print speed and reducing extrusion pressures of the two weaker hydrogels, line widths closer to 0.5 mm were produced successfully. However, the decreased relative extrusion rate used at these settings would undoubtedly correspond to a lower layer height and considerable problems as printing scale was increased after this experiment. Interestingly, when compared to other hydrogel 3D printing studies, the change in line width exhibited in this project was greater (He *et al.*, 2016). Although, this can be explained by the greater range of material properties that were selected for 3D printing testing.

An increase in hydrogel strength from the 2 %/30 mM sample to the 3 %/30 mM sample also should have reduced this degree of oozing. This is because as the relative amount of viscous energy, which was responsible for oozing, had decreased, as documented in the rheology results of the project. Thus, a general reduction in line widths to better reflect 0.5 mm should have been seen but was not. This indicates that simply having an elastic-dominated material with a  $\tan(\delta) < 1$  is not sufficient for hydrogel 3D printing and other factors such as increased viscosity may also determine the oozing of materials. Or maybe there is a specific value for



$\tan(\delta)$  that must be achieved and values closer to 1 are not suitable. The 5 %/30 mM hydrogel produced accurate line widths using the calibrated settings of 30.4 psi/10 mms<sup>-1</sup> and correctly produced reduced line widths in area with a reduction in relative volumetric extrusion rate and *vice versa*. Whilst this sample performed as expected, large increases in line width are still seen for relatively small increases of extrusion pressure (10 and 20 %). This is evidence that selection of an extrusion pressure to a high precision is important and appropriate consideration should be given to this.

The line widths produced using both increased print speed and reduced pressures with the 5 %/30 mM hydrogel are skewed because there was a lower limit to what could be assessed with this method. Specifically, instead of a continuous, even filament being produced using these settings, a broken filament was produced that contained sections without printed material. This presented a dilemma whereby measuring a broken section would have recorded a line width of 0 mm whilst actively selecting correctly printed sections would introduce selection bias. Ultimately, it was deemed better to consciously select a printed area that best resembled the average width of printed sections as this produced results that better reflected the true line width of these samples.

#### 6.4.2. Single layer infill

The results of the single layer infill test are seen in Section 5.4.2. The 2 %/30 mM sample in particular unexpected results when printing with pressure settings of 4.6 – 5.6 psi that previously produced exaggerated line widths. All of these were at least 20 % larger than the desired line width of 0.5 mm which, when considered en masse, should have readily covered the 30 × 30 mm print area in the single layer infill test. Instead, flaws were present where material was not present across this area, predominantly in the upper and lower corners. The 5.1 psi/6 mms<sup>-1</sup> and 5.1 psi/8 mms<sup>-1</sup> print settings in particular, possessed both a slower print speed and greater extrusion pressure than calibrated values which ensured over-

extrusion, yet these also possessed flaws. This was further evidence that the 2 %/30 mM was not well suited to hydrogel 3D printing as, not only were lines not deposited accurately, but material did form fused areas as intended. One explanation for this phenomenon was water cohesion and surface tension, which could explain why, despite extrusion over specific areas, material preferred to pool in areas that already possessed printed material. This would make sense as the hydrogels were predominantly water although was unexpected with the previously established elastic-dominated nature of the 2 %/30 mM hydrogel from rheology results of the project. Multiple experiments exist which assess the cohesive and surface tension effects of hydrogels and could be performed in future studies using PC hydrogels to further understanding (Chakrabarti and Chaudhury, 2013).

In comparison, the 3 %/30 mM and 5 %/30 mM hydrogels performed much closer to what was expected from the experiment where large, exposed areas are only seen when using settings that provided a lower relative extrusion volume. Despite this, many scores of -1 were still given when settings were used that had a higher relative extrusion volume which was a limitation of the scoring system used in this experiment. A score of -1 was given for printed images that contained "dot-like flaws" which were very minor and, in practice, are not normally considered a problem in routine 3D printing.

This is because as 3D printing progresses into additional layers, these very minor flaws would blend in with additional extruded material. An example of dot-like flaws, being unavoidable is when using the popular rectilinear infill pattern (orientated at 45 °) that was used in this project. A geometric restraint exists where, within corners, areas will be present that are too small to incorporate another filament and remain bare. Slic3r settings could be further refined to allow for increased overlap of perimeters and infill sections to combat this, however this can cause problems with over-extrusion in these areas. This inaccuracy due to geometric restraints demonstrates an advantage in micro-scale accuracy that other 3D printing methods possess compared to compared to FFF such as SLS or SLA (Burdis

and Kelly, 2019).

Additionally, a score of 0 could also be considered misleading as the best score was awarded to samples despite them exhibiting clear over-extrusion. While true, this was a lot harder to quantify and was less definitive in exactly where over-extrusion began and where normal-extrusion occurred. Scoring them based on over-extrusion would have therefore been vulnerable to bias so was not included in the experiment.

Another limitation of the scoring system was that the same scores between different hydrogels are not representative of the overall quality. For example, many more scores of -4 were awarded to the 5 %/30 mM hydrogel results when using reduced extrusion rates however this under-extrusion was equally dispersed. This is actually an improvement on other, uneven results because is still being accurately and reliably deposited across the print area during under-extrusion. Whilst the scoring system was beneficial in identifying legitimate distinctions in the 2 %/30 mM and 3 %/30 mM results, a dilemma is presented for the 5 %/30 mM sample where a worse score was awarded for a better technical result.

The presence of notches in the 2 %/30 mM and, to a lesser degree, 3 %/30 mM was evidence of viscous material properties in the materials. Notches were found exclusively on the perimeter at the location where extrusion began during 3D printing. This was a small section of the perimeter where material was not extruded correctly due to latency arising from the pneumatic extrusion system. This lack of start/stop ability of these materials was a critical factor for their suitability within 3D printing as, during 3D printing, the extruder turns off and on multiple times so a quick response is essential to avoid multiple non-extruded errors throughout printing. A skirt was used to prime dispensing tips before each print, so it can be definitively stated that this was not a priming issue.

One key difference between the different hydrogels was how settings that caused over-extrusion appeared in the results. 2 %/30 mM produced a convex, bulging print whereas 3

%/30 mM exhibited the same with a rough-looking surface. 5 %/30 mM in comparison produced much flatter samples that were not distinguishable in height compared to settings that extruded the correct amount of material such as 30.4 psi/10 mms<sup>-1</sup>. This demonstrates that the 5 %/30 mM exhibited a better tolerance for imperfect pressure settings than the other two samples. Or, alternatively, that the extrusion rate was not directly proportional to extrusion pressure which has been found in other studies although these hydrogels used different materials such as gelatin methacrylate so could behave differently (Koti *et al.*, 2019; Udofia, Udofia and Zhou, 2019).

Evidence of top surface scarring (or ploughing) was observed only when using the 5 %/30 mM hydrogel at settings that caused over-extrusion which is seen clearly in the 36.4 psi/6 mms<sup>-1</sup> and 36.4 psi/6 mms<sup>-1</sup> results. This is where the dispensing tip travels across the surface of the material at the first layer height of 0.2 mm and inadvertently disturbs material that are present at heights above that. It was interesting therefore that in the 2 %/30 mM and 3 %/30 mM samples, where over-extrusion and exaggerated layer heights were clearly identified, that this scarring was not seen. This means that the material absorbed the deformation and returned to the area once the nozzle had passed, which is characteristic of viscous-behaviour. This should not have been possible due to rheological characterisation of the 2 %/30 mM and 3 %/30 mM hydrogels as elastic-dominated, the same as the 5 %/30 mM hydrogel.

The final limitation of the single layer infill test was how samples were imaged. Minor differences between angles caused substantial changes in the appearance of printed areas which would provide unrepresentative images. This was most evident in the 5 %/30 mM results where print fidelity was greatly improved where micro-ridges present on the upper surface of the print could portray evidence of severe flaws, depending on the light refraction.

### 6.4.3. Multi-Layer Geometries

The multi-layer geometries 3D printing results can be seen in Section 5.4.3 where clear distinctions in printing fidelity were made between each of the three hydrogel compositions: 2 %/30 mM, 3 %/30 mM and 5 %/30 mM. Original print pressures and print speeds were used despite investigation into potential alternatives in the line width and single-layer infill test. This was because no noticeable benefits were seen through experimenting with these settings and it would introduce more variables.

Across all of the multi-layered tests, the 2 %/30 mM exhibited considerable amounts of viscous behaviour. This is most evident when analysing the corners of the 3D printed models which should have exhibited sharp, 90 ° corners and edges but are instead rounded. Despite this, it is still clearly elastic-dominated as demonstrated by the models' ability to stay relatively organised when elevated by 5 mm. This is further evidence to support the theory that, whilst elastic-dominated behaviour is beneficial, there are other factors at work in determining high print fidelity. Previous studies concur that  $G' > G''$  is a crucial factor but little discussion is given to the precise ratios that are preferably or whether there is a minimum value to aim for (Schwab *et al.*, 2020).

The elephant's foot phenomenon was visible across multiple print models but also even amongst the weaker hydrogels that performed poorly, it was never critical which was a positive. This indicated that the calibration of the Allevi 2 was largely correct, although some improvement may have been beneficial. This did not come as much of a surprise as the Allevi 2 had quite rudimentary calibration for the Z-axis. The smallest movement that Bioprint allowed for, without manually writing custom G-code, was increments of 0.1 mm.

When considering this as  $\pm 50$  % of the 0.2 mm layer height, it is easy to see how minor errors in Z-calibration can occur; despite manufacturer precision claiming a Z-axis precision of 1  $\mu\text{m}$  (Allevi, 2022). Instead of relying on a visual inspection and manual calibration, a

laser or induction sensor could be used to provide more reliable and precise calibration.

The wall model presented increased wall width at the base of walls however this was distinct to an elephant's foot and actually represented wall collapse. One obvious cause for this was a lack of rigidity in lower layers to support upper layers, but if this were the cause, the effects would have been exacerbated in the 22.5 ° and 45 ° overhang models. Instead, the probable source was the drag forces exhibited by the dispensing tip onto the hydrogel structure as it deposited material. As previously mentioned, the dispensing tip diameter was 0.41 mm but the line thickness was 0.5 mm, so material was smeared between the tip and previous printed layers. This would typically not cause problems but, due to the wall model being hollow, forces that acted along the X- and Y-axis were resisted by less material and thus allowed some movement. As printing progressed and drag forces were induced across multiple layers, minor wall collapse occurred. Furthermore, if the wall collapse was due to gravity, it would be equally dispersed on both sides of the walls, whereas in Section 5.4.3 the collapse was consistently inwards.

The gaps presented in the wall models for the 2 %/30 mM and 3 %/30 mM were further evidence for the lack of an adequate start-and-stop behaviour for those hydrogel samples, as the extruder turned on and off. Here, minor errors aggregated in the same X/Y position during printing across multiple layers. It was noticeably less severe in the 3 %/30 mM compared to the 2 %/30 mM, which indicated that the more elastic-dominated a material was, the less it was affected by start-and-stop errors during 3D printing. This was supported by the lack of any wall gaps in the 5 %/30 mM which presented the greatest ratio of elastic to viscous behaviour. These aggregated errors could be mitigated by selection of a random seam position alignment as minor errors would merge across larger sections of the printed object.

The extensions that were seen across many of the printed objects in the 22.5 ° and 45 ° overhang experiments were an indication of how close to the required standard of elasticity

materials were. These extensions were caused by insufficient support material which prevented adherence of additional extruded material. Material then briefly aggregated at the dispensing tip until it was large enough to bridge the gap and reach the support material at a later point. However, the adjoining section would then possess excess material which had 'skipped' the previous section. As printing progressed, this caused a positive feedback loop where the sections that received material would be closer to the dispensing tip in the next layer, forming these extensions. Multiple, short extensions indicated that skipping occurred over less distance and extruded less material at the incorrect position. Whereas a rotational symmetry of one large extension on each corner indicated skipping may have occurred across the entire wall length and only adhered to the object as the dispensing tip changed directions.

The general rule when printing thermoplastics such as PLA or ABS, the quality of which is considered a gold standard in FFF, is that an overhang angle should not exceed  $45^\circ$  or it will fail (Jiang *et al.*, 2018). In this project, a  $45^\circ$  degree overhang was evaluated which was ambitious for PC hydrogels. The outcome of the 5 %/30 mM hydrogel, in particular, served as testament to the quality that can be achieved. Whilst the fidelity of the printed object was evidently not perfect, the overhang angle was produced effectively which is evidence of good filament elasticity that many bioinks do not possess. Additionally, the extensions were small, indicating a lesser degree of incorrectly extruded material than printing with other hydrogels.

Overall, the 3D printing section successfully achieved one of the objectives of the project which was to evaluate the 3D printed fidelity of PC hydrogels. Specifically, the fidelity of the 5 %/30 mM hydrogel stood out as excellent and outperformed the accuracy that was demonstrated in other published studies that used FFF to 3D print alginate (Leppiniemi *et al.*, 2017; Shang *et al.*, 2017; Amr *et al.*, 2021).

## 6.5. Mechanical testing

Section 5.5 contained the mechanical testing results for crosslinked specimens that were 3D printed using the 5 %/30 mM hydrogel that performed best during previous 3D printing fidelity evaluation. Both the elastic modulus and 60 % strain toughness increased considerably as crosslinker concentration and/or crosslinker duration increased except for when using 300 mM crosslinking concentration. This was expected as both of these factors are well known influences on the degree of crosslinking that occur between individual alginate chains which corresponds with improved mechanical strength (Naghieh *et al.*, 2018).

Both the elastic modulus and 60 % strain toughness of specimens that were crosslinked with 300 mM was drastically lower than their 200 mM counterparts which was not expected given the trend observed across all other concentrations. Whilst concentrations of 300 mM had been used to crosslink alginate in other studies, it was less notably less common than lower concentrations (Tabriz *et al.*, 2015). Whilst not explicitly stated, this is likely because the rate of crosslinking was too high when using 300 mM which led to reduced permeability of alginate. This meant that dissolved divalent cations such as  $\text{Ca}^{2+}$  were unable to travel as readily across the hydrogel and the amount of crosslinking that occurred would be reduced as a result, particularly at the specimen centre which was furthest away from the solution.



This is supported by the differences between elastic modulus result and the 60 % strain toughness results of specimens that used the 300 mM concentration. Elastic modulus was limited in scope to observing elastic stress and strain regions whereas the 60 % strain toughness reflected on the overall degree of crosslinking. The differences between the two were a clear indication of varied degrees of crosslinking across the specimens in this group. A compromise therefore exists where, to obtain the highest elastic modulus and 60 % strain toughness, the highest concentration of crosslinking solution should be used until crosslinking becomes restricted. This will be specimen-size dependant, however, as with increase specimen size the distance cationic divalent ions are required to travel to crosslink central regions of a specimens increases.

One of the noted limitations of compression testing using alginate was the removal of data that presented a normal force of  $< 0.05$  N, detailed in Section 4.7. Whilst using a pre-loading region was standard methodology, some relevant parts of the stress strain curve may have been removed because of this. However, 0.05 N represented a minute portion of the total 40 N force that the rheometer could exert this would have limited impact. Additionally, when inspecting stress strain curves to identify linear regions, all of the regions detailed in ISO 604:2003 were present without exception. Tensile testing may have provided an alternative to this to avoid this problem. Regardless, tensile testing would provide additional insight into mechanical properties of specimens and provide a definitive point of failure.

Overall, elastic moduli of between 20 to 200 kPa were reliably produced which could enable the production of tailor-made hydrogels with specific mechanical properties for different applications. Within the context of replacing soft tissues in the body, these recorded elastic moduli exhibit similar stiffnesses to soft tissues which vary from 0.1 kPa to 1 MPa (Liu *et al.*, 2015). Specifically, tissues around the mouth such as the cheek and lower lip were measured as 31 and 33.7 kPa respectively (Luboz, Promayon and Payan, 2014). As such, the 3D printable materials developed in this thesis are ideal candidates for future oral

therapeutic applications.

## 7. Conclusions

The conclusion of the thesis following the work carried out are as follows:

- $^1\text{H}$  NMR was used to analyse the chemical structure of three commercially available alginate strains to assess which one was best suited to 3D printing. Relative amounts of overall G and M were successfully quantified through analysis of  $^1\text{H}$  NMR spectra. Two-length sequences GG, GM/MG and MM were also quantified which was important as GG is known for providing binding sites for divalent cations such as  $\text{Ca}^{2+}$  (Paques *et al.*, 2014). Several triple-length sequences could not be resolved through this method however this has limited impact.
- A high M content alginate strain was selected for use in further experiments in the thesis due to its improved biocompatibility which could be beneficial as part of a regenerative medicine approach to treating CP. This displayed good crosslinking capabilities despite a lack of GG sequences, demonstrating the flexibility of alginate as a potential 3D printing material. High M-content alginates are generally considered inferior to high G alginates in 3D printing although this thesis suggests that they may be suitable. It should be noted that this crosslinking is only ionic however, and additional components are required in the bioink to form a comprehensively sound structure.
- The hydrogel composition optimisation experiment successfully evaluated a broad range of alginate and  $\text{CaCl}_2$  concentrations to see how these constituent parts interacted. Hydrogel compositions were evaluated with respect to several fundamental factors that are associated with successful 3D printing of viscoelastic hydrogels which included extrusion form and layer formation & retention. This successfully expanded on published studies which often use arbitrary hydrogel compositions or limited ranges of compositions (Liu *et al.*, 2018; Amr *et al.*, 2021;

Feng *et al.*, 2021). By providing a more detailed understanding of the relationship between alginate and  $\text{CaCl}_2$  concentration, bioinks can be further improved.

- The feasible limits of hydrogel compositions due to constraints such as over-crosslinking and alginate dissolution limits were evaluated. The full range of materials that could be 3D printed successfully using an Allevi 2 with a 0.41 mm dispensing tip was established.
- The rheological characterisation of alginate successfully evaluated viscoelastic properties of hydrogels and their potential suitability as candidate materials for 3D printing. Rotational and oscillatory techniques were used alongside non-destructive testing which. Materials were observed under a range of conditions including varied shear rates, frequencies, temperatures and a 3ITT study which formed a more complete understanding of their viscoelastic behaviours. This demonstrated that UC alginate hydrogels were fundamentally unsuitable in a FFF 3D printing modality due to their viscous-dominated behaviour. In comparison, PC hydrogels were deemed good candidate printing materials due to their elastic-dominated behaviour and rapidly return this following shear forces in the 3ITT experiment.
- This rheological characterisation was compared against the simple viscosity measurements often provided by 3D printing studies that used hydrogels (Freeman and Kelly, 2017; Mallakpour, Azadi and Hussain, 2021). The thesis demonstrated that viscosity alone has little relevance when considering important characteristics of a material such as relative elastic and viscous behaviours. A full rheological characterisation should therefore be provided when discussing behaviours that are relevant to 3D printing. Specifically, details of the conditions that experiments were performed under such as shear rate and temperature must be included, as these directly affect viscoelastic properties. Without them, measurements cannot be compared reliably.
- The use of a hydrogel composition optimisation experiment and rheological

characterisation of hydrogels established a rigorous methodological platform for screening and optimising candidate hydrogel materials for 3D printing applications. It should be noted that however that this requires further research to consolidate these claims.

- The line width, single layer infill and multi-layer geometry 3D printing experiments evaluated the fidelity of 3D printed hydrogel objects. The 2 %/30 mM and 3 %/30 mM hydrogels contained fidelity issues such as poor adherence to line width. Additionally, despite exaggerated line widths, the layer infill tests exhibited areas of prints that did not contain extruded material which was evidence of water cohesion effects. The 5 %/30 mM performed superiorly compared to the two weaker hydrogels and exhibited reliable and accurate line widths and infill fidelity.
- Multi-layer geometries were printed which demonstrated how problems with the 2 %/30 mM and 3 %/30 mM hydrogels at the fundamental levels of forming accurate filaments and fused areas cumulated as 3D printing was scaled up. The 5 %/30 mM hydrogel demonstrated a high fidelity which appears competitive when compared with other 3D printing hydrogel studies however further work is required to confirm this (Leppiniemi *et al.*, 2017; Shang *et al.*, 2017; Amr *et al.*, 2021).
- As all three of the PC hydrogels that were used within the 3D printing section had been previously characterised as elastic-dominated, the thesis demonstrated that more information is relevant when considering 3D printing material candidacy. Specifically, the ratio of elastic-dominated to viscous-dominated portions of viscoelastic behaviour.
- Secondary crosslinking of the 5 %/30 mM hydrogel produced materials that possessed relevant mechanical properties which were closely resemble that of soft tissue in the body (Liu *et al.*, 2015). Specifically, hydrogels were produced that mimicked soft tissue around the mouth (Luboz, Promayon and Payan, 2014). Use of different secondary crosslinking durations and concentrations demonstrated that

hydrogels could be tailor-made to possess specific mechanical properties for individual therapeutic applications.

- Further modification of alginates will be required in order to achieve the requirements for a successful biomaterials approach, previously summarised in Section 2.5. Several key criteria remain uninvestigated including the degradation rate and assessing the fixation mechanism. This thesis demonstrates that 3D printing alginate could be considered a platform for treating cleft palate but without significant further work, no concrete conclusions can be made. Specifically, alginate will require modification to enable its survival in physiological environments which other studies have shown is not sufficient in its naturally-occurring form with  $\text{CaCl}_2$  crosslinking (Rosiak et al., 2021).

## 8. Future Work

The results of the experimental work and subsequent discussions that led to significant areas of work that are still required in order to fully investigate the suitability of alginate as a 3D printing biomaterial to treat CP. The following future work aims to solidify what is currently a basic understanding of this.

The quality of alginate that was used could be improved upon. Within this thesis, three commercially available alginate strains were selected and characterised using  $^1\text{H}$  NMR in order to make up for limited information from suppliers. Molecular weight heavily influences viscosity whilst uronic acid content is known to affect biocompatibility and crosslinking. Additionally, purity is also known to increase biocompatibility. Utilising a supplier that provides this information will allow better insight into the full capabilities of alginate as a bioink material. However, the greatly increased price of these better characterised, high purity alginates is greatly increased which may limit widespread uptake.

Further analysis could be done at a filament level to quantify the water cohesion effects of alginate. Contact angle analysis and evaluation of surface energy effects would be ideal for exploring this in further detail and producing standards that should be adhered to for ideal bioinks.

Hydrogels are known to shrink as crosslinking occurs which is important to quantify if work within this thesis was to advance towards presenting a clinical alternative. If CP imaging data was used and a 3D obturator produced from this, design changes would need to be implemented so that printed objects retained their fidelity after crosslinking. A dual crosslinking methodology, with appropriate material additions, could be used so that secondary ionic crosslinking was less dominant and these geometry changes were mitigated.

Degradation studies are another essential component to this body of work as ionically crosslinked alginate have been shown to be unstable in physiological conditions. Critically, work needs to be undertaken into modifications of alginate to make it more suitable to survive in these conditions where it would ultimately be used in practice. Previous works have identified that the structural strength of unedited sodium alginate hydrogels that have been crosslinked with  $\text{CaCl}_2$  degrade rapidly over the course of days. A biomaterials solution would require a scaffold to survive in physiological conditions over the course of multiple months. Methods of chemical modification include reaction of hydroxyl groups, oxidation of alginates and utilisation of carbonyl groups, modification of carboxyl groups, etc. Specifically, the addition of bioactive peptides such as arginyglycylaspartic acid is of particular importance to improve the biocompatibility of scaffolds.

The biocompatibility of 3D printed alginate models needs to be evaluated. Whilst high biocompatibility of alginate is generally well known in the literature, it needs to be established using the particular materials and methods featured in this study. Any previously mentioned chemical modifications then need to be assessed using unedited sodium alginate as a baseline. Additional test such as invasion assays and proliferation assessment are also needed to show that the scaffold is behaving as ultimately required for a potential CP treatment method.



## 9. References

- 3dprinterprices.com (2017) *3D Printer Resolution*. Available at: <http://www.3dprinterprices.net/the-importance-of-3d-printer-resolutions/>.
- Abdel-Aziz, M. and Ghandour, H. (2011) "Comparative study between V-Y pushback technique and Furlow technique in cleft soft palate repair," *European Journal of Plastic Surgery*, 34(1), pp. 27–32. Available at: <https://doi.org/10.1007/s00238-010-0443-3>.
- A.D.A.M. (2015) "Eustachian Tube Anatomy," *A.D.A.M. Medical Encyclopedia* [Preprint]. Available at: <https://medlineplus.gov/ency/imagepages/19596.htm>.
- Agarwal, A., Rana, V. and Shafi, S. (2010) "A feeding appliance for a newborn baby with cleft lip and palate.," *National journal of maxillofacial surgery*, 1(1), pp. 91–3. Available at: <https://doi.org/10.4103/0975-5950.69149>.
- Agrawal, K. (2009) "Cleft palate repair and variations," *Indian Journal of Plastic Surgery : Official Publication of the Association of Plastic Surgeons of India*, 42(Suppl), p. S102. Available at: <https://doi.org/10.4103/0970-0358.57197>.
- Agulhon, P. *et al.* (2012) "Structure of alginate gels: Interaction of diuronate units with divalent cations from density functional calculations," *Biomacromolecules*, 13(6), pp. 1899–1907. Available at: <https://doi.org/10.1021/bm300420z>.
- Albanna, M.Z. *et al.* (2016) *Skin Tissue Engineering and Regenerative Medicine, Skin Tissue Engineering and Regenerative Medicine*. Available at: <https://doi.org/10.1016/B978-0-12-801654-1.00013-9>.
- Aldekhayel, S.A., Sinno, H. and Gilardino, M.S. (2012) "Acellular Dermal Matrix in Cleft Palate Repair," *Plastic and Reconstructive Surgery*, 130(1), pp. 177–182. Available at: <https://doi.org/10.1097/PRS.0b013e318254b2dc>.
- Allevi (2022). Available at: <https://www.allevi3d.com/allevi-2/> (Accessed: July 11, 2022).
- Amr, M. *et al.* (2021) "3D printed, mechanically tunable, composite sodium alginate, gelatin and Gum Arabic (SA-GEL-GA) scaffolds," *Bioprinting*, 22. Available at: <https://doi.org/10.1016/j.bprint.2021.e00133>.
- Anton Paar (2015) *Rheometry: Selecting the Right Measuring System - Anton Paar Blog*. Available at: <https://blog.anton-paar.com/rheometry-selecting-the-right-measuring-system/> (Accessed: May 1, 2019).
- ASTM F2259-10 (2012) "Standard Test Method for Determining the Chemical Composition and Sequence in Alginate by Proton Nuclear Magnetic Resonance ( <sup>1</sup> H NMR) Spectroscopy 1." Available at: <https://doi.org/10.1520/F2259-10R12E01>.
- Atzeni, E. and Salmi, A. (2012) "Economics of additive manufacturing for end-useable metal parts," *International Journal of Advanced Manufacturing Technology*, 62(9–12), pp. 1147–1155. Available at: <https://doi.org/10.1007/s00170-011-3878-1>.

- Augst, A.D., Kong, H.J. and Mooney, D.J. (2006) "Alginate Hydrogels as Biomaterials," pp. 623–633. Available at: <https://doi.org/10.1002/mabi.200600069>.
- Bao Ha, T. le *et al.* (2013) "Naturally Derived Biomaterials: Preparation and Application," in *Regenerative Medicine and Tissue Engineering*. InTech. Available at: <https://doi.org/10.5772/55668>.
- Bardach, J. (1995) "Two-Flap palatoplasty: Bardach's technique," *Operative Techniques in Plastic and Reconstructive Surgery*, 2(4), pp. 211–214. Available at: [https://doi.org/10.1016/S1071-0949\(06\)80034-X](https://doi.org/10.1016/S1071-0949(06)80034-X).
- Barrera, J.E. *et al.* (2017) "Anatomic measures of upper airway structures in obstructive sleep apnea," *World Journal of Otorhinolaryngology - Head and Neck Surgery*, 3(2), pp. 85–91. Available at: <https://doi.org/10.1016/j.wjorl.2017.05.002>.
- Basuki, I. (2013) *Von Langenbeck Palatoplasty*, *Slideshare.net*.
- Baumers, M. *et al.* (2011) "Energy inputs to additive manufacturing: Does capacity utilization matter?," *Solid Freeform Fabrication Symposium*, (January), pp. 30–40. Available at: <https://doi.org/10.1017/CBO9781107415324.004>.
- Baxter, D.J.G. and Shroff, M.M. (2011) "Developmental Maxillofacial Anomalies," *Seminars in Ultrasound, CT and MRI*, 32(6), pp. 555–568. Available at: <https://doi.org/10.1053/j.sult.2011.06.004>.
- Belattmania, Z. *et al.* (2020) "Isolation and FTIR-ATR and <sup>1</sup>H NMR characterization of alginates from the main alginophyte species of the atlantic coast of Morocco," *Molecules*, 25(18). Available at: <https://doi.org/10.3390/molecules25184335>.
- Bhattacharya, S., Khanna, V. and Kohli, R. (2009) "Cleft lip: The historical perspective.," *Indian journal of plastic surgery : official publication of the Association of Plastic Surgeons of India*, 42 Suppl(Suppl), pp. S4-8. Available at: <https://doi.org/10.4103/0970-0358.57180>.
- Billiet, T. *et al.* (2012) "A review of trends and limitations in hydrogel-rapid prototyping for tissue engineering," *Biomaterials*, pp. 6020–6041. Available at: <https://doi.org/10.1016/j.biomaterials.2012.04.050>.
- Biomaterials (2017) *Biomaterial Definition*, *Biomaterials*. Available at: <https://www.journals.elsevier.com/biomaterials>.
- Blaeser, A. *et al.* (2016) "Controlling Shear Stress in 3D Bioprinting is a Key Factor to Balance Printing Resolution and Stem Cell Integrity," *Advanced healthcare materials*, 5(3), pp. 326–333. Available at: <https://doi.org/10.1002/ADHM.201500677>.
- Blausen.com staff (2014) *Upper Respiratory System*, *Wikiversity Journal of Medicine*. Available at: [https://en.wikipedia.org/wiki/Respiratory\\_tract#/media/File:Blausen\\_0872\\_UpperRespiratorySystem.png](https://en.wikipedia.org/wiki/Respiratory_tract#/media/File:Blausen_0872_UpperRespiratorySystem.png).
- Boneva, R.S., Folks, T.M. and Louisa, E. (2001) "Infectious Disease Issues in Xenotransplantation Infectious Disease Issues in Xenotransplantation," 14(1), pp. 1–14. Available at: <https://doi.org/10.1128/CMR.14.1.1>.

- Borzabadi-Farahani, A. *et al.* (2012) "The Nance Obturator, a New Fixed Obturator for Patients with Cleft Palate and Fistula," *Journal of Prosthodontics*, 21(5), pp. 400–403. Available at: <https://doi.org/10.1111/j.1532-849X.2012.00853.x>.
- Bouhadir, K.H. *et al.* (2001) "Degradation of partially oxidized alginate and its potential application for tissue engineering," *Biotechnology Progress*, 17(5), pp. 945–950. Available at: <https://doi.org/10.1021/bp010070p>.
- Boulet, S.L. *et al.* (2009) "Children with Orofacial Clefts: Health-Care Use and Costs Among a Privately Insured Population," *Public health reports*, 124(June), pp. 447–453.
- Bratthall, G. *et al.* (2001) "Comparison of ready-to-use EMDOGAIN a -gel and EMDOGAIN a in patients with chronic adult periodontitis A multicenter clinical study," (1997), pp. 923–929.
- Burdis, R. and Kelly, D.J. (2019) "3D Bioprinting Hardware," *Polymer-Based Additive Manufacturing*, pp. 161–186. Available at: [https://doi.org/10.1007/978-3-030-24532-0\\_8](https://doi.org/10.1007/978-3-030-24532-0_8).
- Burg, M.L. *et al.* (2016) "Epidemiology, etiology, and treatment of isolated cleft palate," *Frontiers in Physiology*, 7(MAR), pp. 1–16. Available at: <https://doi.org/10.3389/fphys.2016.00067>.
- Bye, F.J. *et al.* (2013) "Development of bilayer and trilayer nanofibrous/microfibrous scaffolds for regenerative medicine," *Biomaterials Science*, 1(9), p. 942. Available at: <https://doi.org/10.1039/c3bm60074b>.
- Campbell, T. *et al.* (2012) "Could 3D Printing Change the World?," *Strategic Foresight Report*, pp. 3–7.
- Carlson, L., Hatcher, K.W. and Burg, R. vander (2013) "Elevated infant mortality rates among oral cleft and isolated oral cleft cases: A meta-analysis of studies from 1943 to 2010," *Cleft Palate-Craniofacial Journal*, 50(1), pp. 2–12. Available at: <https://doi.org/10.1597/11-087>.
- Carmichael, S.L. (2014) "Birth defects epidemiology," *European Journal of Medical Genetics*, 57(8), pp. 355–358. Available at: <https://doi.org/10.1016/j.ejmg.2014.03.002>.
- Chakrabarti, A. and Chaudhury, M.K. (2013) "Direct measurement of the surface tension of a soft elastic hydrogel: Exploration of elastocapillary instability in adhesion," *Langmuir*, 29(23), pp. 6926–6935. Available at: <https://doi.org/10.1021/la401115j>.
- Chandna, P., Adlakha, V.K. and Singh, N. (2011) "Feeding obturator appliance for an infant with cleft lip and palate.," *Journal of the Indian Society of Pedodontics and Preventive Dentistry*, 29(1), pp. 71–3. Available at: <https://doi.org/10.4103/0970-4388.79950>.
- Chen, Q. and Thouas, G.A. (2015) "Metallic implant biomaterials," *Materials Science and Engineering R: Reports*, 87, pp. 1–57. Available at: <https://doi.org/10.1016/j.msar.2014.10.001>.
- Chetan, K. (2015) *Palate Anatomy*, *Slideshare.net*. Available at: <https://www.slideshare.net/mystyleid/palate-anatomy>.

- Christensen, K. *et al.* (2004) “Long term follow up of survival associated with cleft lip and palate birth Long term follow up study of survival associated with cleft lip and palate at birth,” (January 2017), pp. 0–4. Available at: <https://doi.org/10.1136/bmj.38106.559120.7C>.
- Christianson, A., Howson, C.P. and Modell, B. (2006) “Global Report on Birth Defects,” *March of Dimes Birth Defects Foundation* [Preprint]. Available at: <http://www.marchofdimes.org/materials/global-report-on-birth-defects-the-hidden-toll-of-dying-and-disabled-children-executive-summary.pdf>.
- Chu, K.M.Y. and McPherson, B. (2005) “Audiological status of Chinese patients with cleft lip/palate,” *Cleft Palate-Craniofacial Journal*, 42(3), pp. 280–285. Available at: <https://doi.org/10.1597/03-143.1>.
- Cohen, A. *et al.* (2009) “Mandibular reconstruction using stereolithographic 3-dimensional printing modeling technology,” *Oral Surgery, Oral Medicine, Oral Pathology, Oral Radiology and Endodontology*, 108(5), pp. 661–666. Available at: <https://doi.org/10.1016/j.tripleo.2009.05.023>.
- Cohen, S.R. *et al.* (1991) “Cleft palate fistulas: A multivariate statistical analysis of prevalence, etiology, and surgical management,” *Plastic and Reconstructive Surgery*, 87(6), pp. 1041–1047. Available at: <https://doi.org/10.1097/00006534-199106000-00005>.
- Collins, P.C. *et al.* (2016) “Microstructural Control of Additively Manufactured Metallic Materials,” *Annual Review of Materials Research*, 46(1), pp. 63–91. Available at: <https://doi.org/10.1146/annurev-matsci-070115-031816>.
- Conway, J.C. *et al.* (2015) “Ten-year experience of more than 35,000 orofacial clefts in Africa,” *BMC Psychiatry*, 15(1), pp. 1–9. Available at: <https://doi.org/10.1186/s12887-015-0328-5>.
- Costa, S.S. da, Rosito, L.P.S. and Dornelles, C. (2009) “Sensorineural hearing loss in patients with chronic otitis media,” *European Archives of Oto-Rhino-Laryngology*, 266(2), pp. 221–224. Available at: <https://doi.org/10.1007/s00405-008-0739-0>.
- Croisier, F. and Jérôme, C. (2013) “Chitosan-based biomaterials for tissue engineering,” *European Polymer Journal*, 49(4), pp. 780–792. Available at: <https://doi.org/10.1016/j.eurpolymj.2012.12.009>.
- Czeizel, A.E. (2004) “The primary prevention of birth defects: Multivitamins or folic acid?,” *International journal of medical sciences*, 1(1), pp. 50–61. Available at: <https://doi.org/10.7150/ijms.1.50>.
- Dávila, J.L. and d’Ávila, M.A. (2017) “Laponite as a rheology modifier of alginate solutions: Physical gelation and aging evolution,” *Carbohydrate Polymers*, 157, pp. 1–8. Available at: <https://doi.org/10.1016/j.carbpol.2016.09.057>.
- Dixon, M. *et al.* (2011) “Cleft lip and palate: understanding genetic and environmental influences,” 12(3), pp. 167–178. Available at: <https://doi.org/10.1038/nrg2933.Cleft>.
- Drury, J.L. and Mooney, D.J. (2003) “Hydrogels for tissue engineering: Scaffold design variables and applications,” *Biomaterials*, 24(24), pp. 4337–4351. Available at: [https://doi.org/10.1016/S0142-9612\(03\)00340-5](https://doi.org/10.1016/S0142-9612(03)00340-5).

- Duncan, M.D. and Wilkes, D.S. (2005) "Transplant-related Immunosuppression: A Review of Immunosuppression and Pulmonary Infections," *Proceedings of the American Thoracic Society*, 2(5), pp. 449–455. Available at: <https://doi.org/10.1513/pats.200507-073JS>.
- Ernst & Young (2016) "EY's Global 3D printing Report 2016," *Ey*, pp. 1–26.
- Ertesvåg, H. and Skjåk-Bræk, G. (1999) "Modification of Alginate Using Mannuronan C-5-Epimerases," pp. 71–78. Available at: [https://doi.org/10.1007/978-1-59259-261-6\\_6](https://doi.org/10.1007/978-1-59259-261-6_6).
- Esch, E.W., Bahinski, A. and Huh, D. (2015) "Organs-on-chips at the frontiers of drug discovery," *Nature Reviews Drug Discovery*, 14(4), pp. 248–260. Available at: <https://doi.org/10.1038/nrd4539>.
- Eskens, O., Villani, G. and Amin, S. (2021) "Rheological investigation of thermoresponsive alginate-methylcellulose gels for epidermal growth factor formulation," *Cosmetics*, 8(1), pp. 1–11. Available at: <https://doi.org/10.3390/COSMETICS8010003>.
- Fayyaz, G. Q., Gill, N. A., Alam, I., Chaudary, A., Aslam, M., Ishaq, I., Hameed, A., Ganatra, A., Sheikh, T., & Bilal, M. (2018). Continuous versus interrupted sutures for primary cleft palate repair. *Plastic and Reconstructive Surgery - Global Open*, 6(11). <https://doi.org/10.1097/GOX.0000000000002001>
- Feldman, D. S., & Osborne, S. (2018). Fibrin as a tissue adhesive and scaffold with an angiogenic agent (FGF-1) to enhance burn graft healing in vivo and clinically. *Journal of Functional Biomaterials*, 9(4). <https://doi.org/10.3390/jfb9040068>
- Feng, C. *et al.* (2021) "Improvement of 3D printing properties of rose-sodium alginate heterogeneous gel by adjusting rose material," *Journal of Food Process Engineering*, 44(1). Available at: <https://doi.org/10.1111/jfpe.13583>.
- FMC Corporation (2003) "Alginates," *FMC Corporation* [Preprint]. Available at: <http://www.fmcbiopolymer.com/portals/pharm/content/docs/alginate.pdf>.
- Freeman, F.E. and Kelly, D.J. (2017) "Tuning alginate bioink stiffness and composition for controlled growth factor delivery and to spatially direct MSC Fate within bioprinted tissues," *Scientific Reports*, 7(1). Available at: <https://doi.org/10.1038/s41598-017-17286-1>.
- Furlow, L.T. (1986) "Cleft palate repair by double opposing Z-plasty.," *Plastic and reconstructive surgery*, 78(6), pp. 724–38. Available at: <http://www.ncbi.nlm.nih.gov/pubmed/3786527> (Accessed: September 6, 2017).
- Gajjar, C.R. and King, M.W. (2014) "Resorbable Fiber-Forming Polymers for Biotextile Applications," pp. 7–11. Available at: <https://doi.org/10.1007/978-3-319-08305-6>.
- Garrett, A. (2012) *Cleft Palate Feeding*, *blogger.co.uk*. Available at: <http://thegarrettsaregrowing.blogspot.co.uk/2012/04/cleft-palate-feeding.html>.
- Garzon-Hernandez, S. *et al.* (2020) "Design of FDM 3D printed polymers: An experimental-modelling methodology for the prediction of mechanical properties," *Materials and Design*, 188. Available at: <https://doi.org/10.1016/j.matdes.2019.108414>.
- Ghanbari, A. *et al.* (2020) "Experimental methods in chemical engineering: Rheometry," *The Canadian Journal of Chemical Engineering*, 98(7), pp. 1456–1470. Available at: <https://doi.org/10.1002/CJCE.23749>.

- Ghanbari, M., Salavati-Niasari, M. and Mohandes, F. (2021) "Thermosensitive alginate-gelatin-nitrogen-doped carbon dots scaffolds as potential injectable hydrogels for cartilage tissue engineering applications," *RSC Advances*, 11(30), pp. 18423–18431. Available at: <https://doi.org/10.1039/d1ra01496j>.
- Ghiringhelli, E. *et al.* (2012) "Optimal fourier rheometry," *Rheologica Acta* 2012 51:5, 51(5), pp. 413–420. Available at: <https://doi.org/10.1007/S00397-012-0616-Z>.
- Goh, C.H., Heng, P.W.S. and Chan, L.W. (2012) "Alginates as a useful natural polymer for microencapsulation and therapeutic applications," *Carbohydrate Polymers*, 88(1), pp. 1–12. Available at: <https://doi.org/10.1016/j.carbpol.2011.11.012>.
- Goodacre, T. and Swan, M.C. (2008) "Cleft lip and palate: current management," *Paediatrics and Child Health*, 18(6), pp. 283–292. Available at: <https://doi.org/10.1016/j.paed.2008.03.008>.
- Grasdalen, H. (1983) *Note High-field, <sup>1</sup>H-n.m.r. spectroscopy of alginate: sequential structure and linkage conformations, Carbohydrate Research.*
- Grasdalen, H., Larsen, B. and Smisrod, O. (1981) "<sup>13</sup>C-n.m.r. studies of monomeric composition and sequence in alginate," *Carbohydrate Research*, 89(2), pp. 179–191. Available at: [https://doi.org/10.1016/S0008-6215\(00\)85243-X](https://doi.org/10.1016/S0008-6215(00)85243-X).
- Gunst, R.F. and Mason, R.L. (2009) "Fractional factorial design," *Wiley Interdisciplinary Reviews: Computational Statistics*, 1(2), pp. 234–244. Available at: <https://doi.org/10.1002/WICS.27>.
- Hagberg, C., Larson, O. and Milerad, J. (1998) "Incidence of cleft lip and palate and risks of additional malformations," *Cleft Palate-Craniofacial Journal*, 35(1), pp. 40–45. Available at: [https://doi.org/10.1597/1545-1569\(1998\)035<0040:IOCLAP>2.3.CO;2](https://doi.org/10.1597/1545-1569(1998)035<0040:IOCLAP>2.3.CO;2).
- Hak, D.J. *et al.* (2014) "Use of Carbon-Fiber-Reinforced Composite Implants in Orthopedic Surgery," *Orthopedics*, 37(12), pp. 825–830. Available at: <https://doi.org/10.3928/01477447-20141124-05>.
- Hannink, G. and Arts, J.J.C. (2011) "Bioresorbability, porosity and mechanical strength of bone substitutes: What is optimal for bone regeneration?," *Injury*, 42(SUPPL. 2), pp. S22–S25. Available at: <https://doi.org/10.1016/j.injury.2011.06.008>.
- Hassan, M.E. and Askar, S. (2007) "Does palatal muscle reconstruction affect the functional outcome of cleft palate surgery?," *Plastic and reconstructive surgery*, 119(6), pp. 1859–65. Available at: <https://doi.org/10.1097/01.prs.0000259185.29517.79>.
- He, Y. *et al.* (2016) "Research on the printability of hydrogels in 3D bioprinting.," *Scientific reports*, 6, p. 29977. Available at: <https://doi.org/10.1038/srep29977>.
- Hench, L.L. and Polak, J.M. (2002) "Third-generation biomedical materials.," *Science (New York, N.Y.)*, 295(5557), pp. 1014–1017. Available at: <https://doi.org/10.1126/science.1067404>.
- Hickey, A.J. and Salter, M. (2006) "Prosthetic and psychological factors in treating patients with congenital and craniofacial defects," *Journal of Prosthetic Dentistry*, 95(5), pp. 392–396. Available at: <https://doi.org/10.1016/j.prosdent.2006.03.002>.
- Hopkinson, N. and Dickens, P. (2003) "Analysis of rapid manufacturing — using layer

- manufacturing processes for production,” *Science*, 217, pp. 31–39. Available at: <https://doi.org/10.1243/095440603762554596>.
- Hormdee, D., Yamsuk, T. and Sutthiprapaporn, P. (2020) “Palatal Soft Tissue Thickness on Maxillary Posterior Teeth and Its Relation to Palatal Vault Angle Measured by Cone- Beam Computed Tomography,” *International Journal of Dentistry*, 2020. Available at: <https://doi.org/10.1155/2020/8844236>.
- Hosein, M. and Motamedi, K. (2013) *A textbook of Advanced Oral and Maxillofacial Surgery*. Available at: <https://www.intechopen.com/books/a-textbook-of-advanced-oral-and-maxillofacial-surgery/cleft-lip-and-palate-surgery>.
- Hudson, R.E. *et al.* (2017) “An enhanced rheometer inertia correction procedure (ERIC) for the study of gelling systems using combined motor-transducer rheometers,” *Physics of Fluids*, 29(12), p. 121602. Available at: <https://doi.org/10.1063/1.4993308>.
- Hunt, O. *et al.* (2005) “The psychosocial effects of cleft lip and palate: A systematic review,” *European Journal of Orthodontics*, 27(3), pp. 274–285. Available at: <https://doi.org/10.1093/ejo/cji004>.
- Hybrid Manufacturing Technologies (2012) *7 Families of Additive Manufacturing*, [hybridmanutech.com](http://www.hybridmanutech.com). Available at: <http://www.hybridmanutech.com/resources.html>.
- Imanishi, J. and Choong, P.F.M. (2015) “Three-dimensional printed calcaneal prosthesis following total calcanectomy,” *International Journal of Surgery Case Reports*, 10, pp. 83–87. Available at: <https://doi.org/10.1016/j.ijscr.2015.02.037>.
- Jiang, B. *et al.* (2016) “Targeting Heparin to Collagen within Extracellular Matrix Significantly Reduces Thrombogenicity and Improves Endothelialization of Decellularized Tissues,” *Biomacromolecules*, 17(12), pp. 3940–3948. Available at: <https://doi.org/10.1021/acs.biomac.6b01330>.
- Jiang, J. *et al.* (2018) “International Journal of Computer Integrated Manufacturing Investigation of printable threshold overhang angle in extrusion-based additive manufacturing for reducing support waste Investigation of printable threshold overhang angle in extrusion-based additive manufacturing for reducing support waste.” Available at: <https://doi.org/10.1080/0951192X.2018.1466398>.
- Johnson, C.Y. and Little, J. (2008) “Folate intake, markers of folate status and oral clefts: Is the evidence converging?,” *International Journal of Epidemiology*, 37(5), pp. 1041–1058. Available at: <https://doi.org/10.1093/ije/dyn098>.
- Karl (2016) *Veau-Wadrill-Kilner Palatoplasty*, [pocketdentistry.com](http://pocketdentistry.com). Available at: <https://pocketdentistry.com/cleft-palate-repair-concepts-and-controversies/>.
- Katzel, E.B. *et al.* (2009) “Current surgical practices in cleft care: cleft palate repair techniques and postoperative care.,” *Plastic and reconstructive surgery*, 124(3), pp. 899–906. Available at: <https://doi.org/10.1097/PRS.0b013e3181b03824>.
- Kernahan, D. and Stark, R. (1971) “The Striped Y-A Symbolic Classification for Cleft Lip and Palate,” *Plastic and reconstructive surgery*, 47(5), pp. 469–470.
- Khan, R. and Khan, M.H. (2013) “Use of collagen as a biomaterial: An update.,” *Journal of Indian Society of Periodontology*, 17(4), pp. 539–42. Available at: <https://doi.org/10.4103/0972-124X.118333>.

- Khosla, R.K., Mabry, K. and Castiglione, C.L. (2008) "Clinical outcomes of the Furlow Z-plasty for primary cleft palate repair," *Cleft Palate-Craniofacial Journal*, 45(5), pp. 501–510. Available at: <https://doi.org/10.1597/07-063.1>.
- Kimotho, S.G. and Macharia, F.N. (2020) "Social stigma and cultural beliefs associated with cleft lip and/or palate: parental perceptions of their experience in Kenya," *Humanities and Social Sciences Communications*, 7(1). Available at: <https://doi.org/10.1057/s41599-020-00677-7>.
- Kong, H.J. *et al.* (2004) "Controlling rigidity and degradation of alginate hydrogels via molecular weight distribution," *Biomacromolecules*, 5(5), pp. 1720–1727. Available at: <https://doi.org/10.1021/bm049879r>.
- Koti, P. *et al.* (2019) "Use of GelMA for 3D printing of cardiac myocytes and fibroblasts," *Journal of 3D Printing in Medicine*, 3(1), pp. 11–22. Available at: <https://doi.org/10.2217/3dp-2018-0017>.
- Kumbhar, N.N. and Mulay, A. v. (2016) "Post Processing Methods used to Improve Surface Finish of Products which are Manufactured by Additive Manufacturing Technologies: A Review," *Journal of The Institution of Engineers (India): Series C* [Preprint]. Available at: <https://doi.org/10.1007/s40032-016-0340-z>.
- Kummer, A.W. (2011) "Disorders of resonance and airflow secondary to cleft palate and/or velopharyngeal dysfunction," *Seminars in Speech and Language*, 32(2), pp. 141–149. Available at: <https://doi.org/10.1055/s-0031-1277716>.
- Kuo, Catherine K. and Ma, P.X. (2001) "Ionically crosslinked alginate hydrogels as scaffolds for tissue engineering: Part 1. Structure, gelation rate and mechanical properties," *Biomaterials*, 22(6), pp. 511–521. Available at: [https://doi.org/10.1016/S0142-9612\(00\)00201-5](https://doi.org/10.1016/S0142-9612(00)00201-5).
- Kuo, Catherine K and Ma, P.X. (2001) *Ionically crosslinked alginate hydrogels as scaffolds for tissue engineering: Part 1. Structure, gelation rate and mechanical properties, Biomaterials*.
- Labaky, P. *et al.* (2020) "Innovative non-destructive sorting technique for juicy stone fruits: textural properties of fresh mangos and purees," *Food and Bioprocess Processing*, 123, pp. 188–198. Available at: <https://doi.org/10.1016/J.FBP.2020.06.013>.
- Landheer, J.A., Breugem, C.C. and van Mink Der Molen, A.B. (2010) "Fistula incidence and predictors of fistula occurrence after cleft palate repair: Two-stage closure versus one-stage closure," *Cleft Palate-Craniofacial Journal*, 47(6), pp. 623–630. Available at: <https://doi.org/10.1597/09-069>.
- Langdon, J.D. (2011) *Operative oral and maxillofacial surgery*. Hodder Arnold. Available at: [https://books.google.co.uk/books?id=UrvMBQAAQBAJ&pg=PA615&lpg=PA615&dq=secondary+revision+failure+rate+palate&source=bl&ots=kehY2Ey8Ea&sig=NJ9abYeU2yM6SUiNUV4xYmt9I9M&hl=en&sa=X&ved=0ahUKEwjYi4ij9ZPWAhWCAxoKHTItBD0Q6AEITTAH#v=onepage&q=secondary revision](https://books.google.co.uk/books?id=UrvMBQAAQBAJ&pg=PA615&lpg=PA615&dq=secondary+revision+failure+rate+palate&source=bl&ots=kehY2Ey8Ea&sig=NJ9abYeU2yM6SUiNUV4xYmt9I9M&hl=en&sa=X&ved=0ahUKEwjYi4ij9ZPWAhWCAxoKHTItBD0Q6AEITTAH#v=onepage&q=secondary%20revision) (Accessed: September 7, 2017).
- Lee and Mooney (2011) "Alginate: properties and biomedical applications," 37(1), pp. 106–126. Available at: <https://doi.org/10.1016/j.progpolymsci.2011.06.003>.Alginate.
- Leick, S. *et al.* (2010) "Deformation of liquid-filled calcium alginate capsules in a spinning



- drop apparatus," *Physical Chemistry Chemical Physics*, 12(12), pp. 2950–2958. Available at: <https://doi.org/10.1039/b921116k>.
- Lendlein, A. (2010) "Polymers in biomedicine," *Macromolecular Bioscience*, 10(9), pp. 998–1007. Available at: <https://doi.org/10.1002/mabi.201000071>.
- Leppiniemi, J. *et al.* (2017) "3D-Printable Bioactivated Nanocellulose-Alginate Hydrogels," *ACS Applied Materials and Interfaces*, 9(26), pp. 21959–21970. Available at: <https://doi.org/10.1021/acsami.7b02756>.
- Leukers, B. *et al.* (2005) "Hydroxyapatite scaffolds for bone tissue engineering made by 3D printing," *Journal of Materials Science: Materials in Medicine*, 16(12), pp. 1121–1124. Available at: <https://doi.org/10.1007/s10856-005-4716-5>.
- Levi, B. *et al.* (2011) "Palatogenesis: engineering, pathways and pathologies.," *Organogenesis*, 7(4), pp. 242–54. Available at: <https://doi.org/10.4161/org.7.4.17926>.
- Lewicki, J. *et al.* (2019) "Optimization of 3D bioprinting of human neuroblastoma cells using sodium alginate hydrogel," *Bioprinting*, 16. Available at: <https://doi.org/10.1016/j.bprint.2019.e00053>.
- Liberski, A.R. (2016) "Three-dimensional printing of alginate: From seaweeds to heart valve scaffolds," *QScience Connect*, 2016(2), p. 3. Available at: <https://doi.org/10.5339/connect.2016.3>.
- Liu, J. *et al.* (2015) "Hydrogels for engineering of perfusable vascular networks," *International Journal of Molecular Sciences*. MDPI AG, pp. 15997–16016. Available at: <https://doi.org/10.3390/ijms160715997>.
- Liu, Q. *et al.* (2018) "Preparation and properties of 3D printed alginate-chitosan polyion complex hydrogels for tissue engineering," *Polymers*, 10(6). Available at: <https://doi.org/10.3390/polym10060664>.
- Liu, Y., Zheng, Y. and Hayes, B. (2017) "Degradable, absorbable or resorbable—what is the best grammatical modifier for an implant that is eventually absorbed by the body?," *Science China Materials*, 60(5), pp. 377–391. Available at: <https://doi.org/10.1007/s40843-017-9023-9>.
- Losken, H.W. *et al.* (2011) "Achieving low cleft palate fistula rates: Surgical results and techniques," *Cleft Palate-Craniofacial Journal*, 48(3), pp. 312–320. Available at: <https://doi.org/10.1597/08-288>.
- Luboz, V., Promayon, E. and Payan, Y. (2014) "Linear Elastic Properties of the Facial Soft Tissues Using an Aspiration Device: Towards Patient Specific Characterization," *Annals of Biomedical Engineering*, 42(11), pp. 2369–2378. Available at: <https://doi.org/10.1007/s10439-014-1098-1>.
- Mahyudin, F., Widhiyanto, L. and Hermawan, H. (2016) "Biomaterials in orthopaedics," *Advanced Structured Materials*, 58(July), pp. 161–181. Available at: [https://doi.org/10.1007/978-3-319-14845-8\\_7](https://doi.org/10.1007/978-3-319-14845-8_7).
- Maitz, M.F. (2015) "Applications of synthetic polymers in clinical medicine," *Biosurface and Biotribology*, 1(3), pp. 161–176. Available at: <https://doi.org/10.1016/j.bsbt.2015.08.002>.
- Malda, J. *et al.* (2013) "25th anniversary article: Engineering hydrogels for biofabrication,"

- Advanced Materials*, 25(36), pp. 5011–5028. Available at: <https://doi.org/10.1002/adma.201302042>.
- Mallakpour, S., Azadi, E. and Hussain, C.M. (2021) “State-of-the-art of 3D printing technology of alginate-based hydrogels—An emerging technique for industrial applications,” *Advances in Colloid and Interface Science*. Elsevier B.V. Available at: <https://doi.org/10.1016/j.cis.2021.102436>.
- Maroni, S.N. (2016) *Fused filament fabrication anisotropy*, *linkedin.com*. Available at: <https://www.linkedin.com/pulse/prototyping-apple-pencil-case-betabox-sean-newman-maroni>.
- Marro, A., Bandukwala, T. and Mak, W. (2016) “Three-Dimensional Printing and Medical Imaging: A Review of the Methods and Applications,” *Current Problems in Diagnostic Radiology*, 45(1), pp. 2–9. Available at: <https://doi.org/10.1067/j.cpradiol.2015.07.009>.
- Martin, J. (2017) *Rotational Rheometry*. Available at: [https://commons.wikimedia.org/wiki/File:Rotational\\_geometries.png](https://commons.wikimedia.org/wiki/File:Rotational_geometries.png).
- Mathews, T.J. and MacDorman, M.F. (2013) “Infant mortality statistics from the 2009 period linked birth/infant death data set.,” *National vital statistics reports : from the Centers for Disease Control and Prevention, National Center for Health Statistics, National Vital Statistics System*, 61(8), pp. 1–27. Available at: <http://www.ncbi.nlm.nih.gov/pubmed/24979974>.
- Maxson, E. L., Young, M. D., Noble, C., Go, J. L., Heidari, B., Khorramirouz, R., Morse, D. W., & Lerman, A. (2019). In vivo remodeling of a 3D-Bioprinted tissue engineered heart valve scaffold. *Bioprinting*, 16. <https://doi.org/10.1016/j.bprint.2019.e00059>
- McKay, D.B., Park, K. and Perkins, D. (2010) “What Is Transplant Immunology and Why Are Allografts Rejected?,” in *Kidney Transplantation: A Guide to the Care of Kidney Transplant Recipients*. Boston, MA: Springer US, pp. 25–39. Available at: [https://doi.org/10.1007/978-1-4419-1690-7\\_3](https://doi.org/10.1007/978-1-4419-1690-7_3).
- Menea, F., Menea, A. and Menea, B. (2013) “Hyaluronic Acid and Derivatives for Tissue Engineering.,” *Journal of Biotechnology & Biomaterials*, s3, pp. 1–7. Available at: <https://doi.org/10.4172/2155-952X.S3-001>.
- Menshutina, N. *et al.* (2021) “Extrusion-based 3D printing for highly porous alginate materials production,” *Gels*, 7(3). Available at: <https://doi.org/10.3390/gels7030092>.
- Meyer, S.R. *et al.* (2005) “Decellularization reduces the immune response to aortic valve allografts in the rat,” *Journal of Thoracic and Cardiovascular Surgery*, 130(2), pp. 469–476. Available at: <https://doi.org/10.1016/j.jtcvs.2005.03.021>.
- Micheli, B., Wannomae, K. and Muratoglu, O. (2017) *Orthopaedic proceedings., Bone Joint J. British Editorial Society of Bone and Joint Surgery*. Available at: [http://bjjprocs.boneandjoint.org.uk/content/99-B/SUPP\\_5/10](http://bjjprocs.boneandjoint.org.uk/content/99-B/SUPP_5/10) (Accessed: September 30, 2017).
- Mironov, V. *et al.* (2003) “Organ printing: Computer-aided jet-based 3D tissue engineering,” *Trends in Biotechnology*, 21(4), pp. 157–161. Available at: [https://doi.org/10.1016/S0167-7799\(03\)00033-7](https://doi.org/10.1016/S0167-7799(03)00033-7).
- Mitchell, J.C. and Wood, R.J. (2000) “Management of cleft lip and palate in primary care,”

*Journal of Pediatric Health Care*, 14(February), pp. 13–19. Available at: [https://doi.org/10.1016/S0891-5245\(00\)70039-3](https://doi.org/10.1016/S0891-5245(00)70039-3).

Modulevsky, D. J., Lefebvre, C., Haase, K., Al-Rekabi, Z., & Pelling, A. E. (2014). Apple derived cellulose scaffolds for 3D mammalian cell culture. *PLoS ONE*, 9(5). <https://doi.org/10.1371/journal.pone.0097835>

Mondal, D., Griffith, M. and Venkatraman, S.S. (2016) “Polycaprolactone-based biomaterials for tissue engineering and drug delivery: Current scenario and challenges,” *International Journal of Polymeric Materials and Polymeric Biomaterials*, 65(5), pp. 255–265. Available at: <https://doi.org/10.1080/00914037.2015.1103241>.

Mossey, P.A. *et al.* (2009) “Cleft lip and palate,” *The Lancet*, 374(9703), pp. 1773–1785. Available at: [https://doi.org/10.1016/S0140-6736\(09\)60695-4](https://doi.org/10.1016/S0140-6736(09)60695-4).

Mossey, P.A. and Modell, B. (2012) “Epidemiology of oral clefts 2012: An international perspective,” *Frontiers of Oral Biology*, 16(December), pp. 1–18. Available at: <https://doi.org/10.1159/000337464>.

Murphy, S. v and Atala, A. (2014) “3D bioprinting of tissues and organs,” *Nature Biotechnology*, 32(8), pp. 773–785. Available at: <https://doi.org/10.1038/nbt.2958>.

Murray, J.C. (2002) “Gene/environment causes of cleft lip and/or palate.,” *Clinical genetics*, 61(4), pp. 248–256. Available at: <https://doi.org/10.1034/j.1399-0004.2002.610402.x>.

Murthy, J. (2009) “Management of cleft lip and palate in adults.,” *Indian journal of plastic surgery : official publication of the Association of Plastic Surgeons of India*, 42 Suppl(Suppl), pp. S116-22. Available at: <https://doi.org/10.4103/0970-0358.57202>.

Nagarajan, R., Savitha, V.H. and Subramaniyan, B. (2009) “Communication disorders in individuals with cleft lip and palate: An overview.,” *Indian journal of plastic surgery : official publication of the Association of Plastic Surgeons of India*, 42 Suppl(Suppl), pp. S137-43. Available at: <https://doi.org/10.4103/0970-0358.57199>.

Naghieh, S. *et al.* (2018) “Influence of crosslinking on the mechanical behavior of 3D printed alginate scaffolds: Experimental and numerical approaches,” *Journal of the Mechanical Behavior of Biomedical Materials*, 80, pp. 111–118. Available at: <https://doi.org/10.1016/j.jmbbm.2018.01.034>.

Nair, L.S. and Laurencin, C.T. (2007) “Biodegradable polymers as biomaterials,” *Progress in Polymer Science (Oxford)*, 32(8–9), pp. 762–798. Available at: <https://doi.org/10.1016/j.progpolymsci.2007.05.017>.

Navarro-Gasparetto, C.E. (2007) “Technique of Closing Cleft Palates Without the Relaxing Incisions,” *Www.Smiletrain.Org* [Preprint]. Available at: <https://www.smiletrain.org/sites/default/files/medical/medical-research-library/search/pdfs/technique-of-closing-cleft.pdf>.

Ngai, C. *et al.* (2005) “Are isolated facial cleft lip and palate associated with increased perinatal mortality? A cohort study from the West Midlands Region, 1995–1997,” *The Journal of Maternal-Fetal & Neonatal Medicine*, 17(3), pp. 203–206. Available at: <https://www.ncbi.nlm.nih.gov/pubmed/16147824>.

O’Brien, F. (2011). Biomaterials & scaffolds for tissue engineering. *Materials Today*, 14(3), 87–95.

Oostra, R.-Jan., Steding, Gerd. and Virágh, Szabolcs. (2007) *Steding's and Virágh's scanning electron microscopy atlas of the developing human heart*. Springer. Available at: <https://clinicalgate.com/head-and-neck-6/> (Accessed: September 7, 2017).

OPTN (2016) *Number of donors and transplantations in the US from 1991 to 2015*. Available at: <https://optn.transplant.hrsa.gov/>.

Orive, G. *et al.* (2002) "Biocompatibility of microcapsules for cell immobilization elaborated with different type of alginates," *Biomaterials*, 23(18), pp. 3825–3831. Available at: [https://doi.org/10.1016/S0142-9612\(02\)00118-7](https://doi.org/10.1016/S0142-9612(02)00118-7).

Otterlei, M. *et al.* (1991) "Induction of cytokine production from human monocytes stimulated with alginate.," *Journal of immunotherapy : official journal of the Society for Biological Therapy*, 10(4), pp. 286–91. Available at: <http://www.ncbi.nlm.nih.gov/pubmed/1931864> (Accessed: October 3, 2017).

Ozbekova, Z. and Kulmyrzaev, A. (2017) "Fluorescence spectroscopy as a non destructive method to predict rheological characteristics of Tilsit cheese," *Journal of Food Engineering*, 210, pp. 42–49. Available at: <https://doi.org/10.1016/J.JFOODENG.2017.04.023>.

Ozbolat, I.T., Peng, W. and Ozbolat, V. (2016) "Application areas of 3D bioprinting," *Drug Discovery Today*, 21(8), pp. 1257–1271. Available at: <https://doi.org/10.1016/j.drudis.2016.04.006>.

Paar, A. (2017) *Basics of Rheology*. Available at: <https://wiki.anton-paar.com/en/basics-of-rheology/> (Accessed: May 3, 2019).

Pan, T. *et al.* (2015) "3D Bioplotting of Gelatin/Alginate Scaffolds for Tissue Engineering: Influence of Crosslinking Degree and Pore Architecture on Physicochemical Properties," *Journal of Materials Science and Technology*, 32(9), pp. 889–900. Available at: <https://doi.org/10.1016/j.jmst.2016.01.007>.

Panda, A., Kumar, S., Kumar, A., Bansal, R., & Bhartiya, S. (2009). Current Ophthalmology Fibrin glue in ophthalmology.

Pansky, B. (1982) *Review of Medical Embryology*. Macmillan USA. Available at: <https://discovery.lifemapsc.com/library/review-of-medical-embryology/chapter-55-development-of-the-palate>.

Paques, J.P. *et al.* (2014) "Preparation methods of alginate nanoparticles," *Advances in Colloid and Interface Science*, 209(March), pp. 163–171. Available at: <https://doi.org/10.1016/j.cis.2014.03.009>.

Parwaz, M.A. *et al.* (2009) "Width of cleft palate and postoperative palatal fistula - do they correlate?," *Journal of Plastic, Reconstructive and Aesthetic Surgery*, 62(12), pp. 1559–1563. Available at: <https://doi.org/10.1016/j.bjps.2008.05.048>.

Patel, P.K. (2016) *Double-opposing Z-plasties*, *medscape.com*. Available at: <http://emedicine.medscape.com/article/1279283-treatment#d10>.

Pawar, S.N. and Edgar, K.J. (2012) "Alginate derivatization: A review of chemistry, properties and applications," *Biomaterials*, 33(11), pp. 3279–3305. Available at: <https://doi.org/10.1016/j.biomaterials.2012.01.007>.

Perko, M. (1986) "The history of treatment of cleft lip and palate.," *Progress in pediatric surgery*, 20(1844), pp. 238–51. Available at: <http://www.ncbi.nlm.nih.gov/pubmed/3095876>.

Phua, Y.S. and de Chalain, T. (2008) "Incidence of oronasal fistulae and velopharyngeal insufficiency after cleft palate repair: An audit of 211 children born between 1990 and 2004," *Cleft Palate-Craniofacial Journal*, 45(2), pp. 172–178. Available at: <https://doi.org/10.1597/06-205.1>.

Puwanun, S. *et al.* (2016) "Production and characterization of a novel, electrospun, tri-layer polycaprolactone membrane for the segregated co-culture of bone and soft tissue," *Polymers*, 8(6), pp. 1–10. Available at: <https://doi.org/10.3390/polym8060221>.

Ramakrishna, S. *et al.* (2001) "Biomedical applications of polymer-composite materials : a review," 61. Available at: [https://doi.org/10.1016/S0266-3538\(00\)00241-4](https://doi.org/10.1016/S0266-3538(00)00241-4).

Raman, S.P., Gurikov, P. and Smirnova, I. (2015) "Hybrid alginate based aerogels by carbon dioxide induced gelation: Novel technique for multiple applications," *Journal of Supercritical Fluids*, 106, pp. 23–33. Available at: <https://doi.org/10.1016/j.supflu.2015.05.003>.

Ravi, P., Shiakolas, P.S. and Welch, T.R. (2017) "Poly-L-lactic acid: Pellets to fiber to fused filament fabricated scaffolds, and scaffold weight loss study," *Additive Manufacturing*, 16, pp. 167–176. Available at: <https://doi.org/10.1016/j.addma.2017.06.002>.

Ravishanker, R. (2006) "Furlow's palatoplasty for cleft palate repair," *Medical Journal Armed Forces India*, 62(3), pp. 239–242. Available at: [https://doi.org/10.1016/S0377-1237\(06\)80010-9](https://doi.org/10.1016/S0377-1237(06)80010-9).

Reprap (2014) *Fused filament fabrication*, [wikipedia.org](http://reprap.org/wiki/Fused_filament_fabrication). Available at: [http://reprap.org/wiki/Fused\\_filament\\_fabrication](http://reprap.org/wiki/Fused_filament_fabrication).

Reprap (2017) *Fused Filament Fabrication*. Available at: [http://reprap.org/wiki/Fused\\_filament\\_fabrication](http://reprap.org/wiki/Fused_filament_fabrication).

Rezaie, H.R., Bakhtiari, L. and Öchsner, A. (2015) "Biomaterials and their applications in medicine," *Regulatory Affairs for Biomaterials and Medical Devices*, pp. 1–10. Available at: <https://doi.org/10.1533/9780857099204.1>.

Rezende, R.A. *et al.* (2009) "Rheological Behavior of Alginate Solutions for Biomanufacturing," *J Appl Polym Sci*, 113, pp. 3866–3871. Available at: <https://doi.org/10.1002/app.30170>.

Rial, R., Liu, Z. and Ruso, J.M. (2020) "Soft actuated hybrid hydrogel with bioinspired complexity to control mechanical flexure behavior for tissue engineering," *Nanomaterials*, 10(7), pp. 1–20. Available at: <https://doi.org/10.3390/nano10071302>.

Richardson, S. and Agni, N.A. (2014) "Palatal fistulae: a comprehensive classification and difficulty index.," *Journal of maxillofacial and oral surgery*, 13(3), pp. 305–309. Available at: <https://doi.org/10.1007/s12663-013-0535-2>.

Rogers, B.O. (1976) "Treatment of cleft lip and palate during the Revolutionary war: bicentennial reflections.," *The Cleft palate journal*, pp. 371–390.

- Rosiak, P., Latanska, I., Paul, P., Sujka, W., & Kolesinska, B. (2021). Modification of alginates to modulate their physico-chemical properties and obtain biomaterials with different functional properties. In *Molecules* (Vol. 26, Issue 23). MDPI. <https://doi.org/10.3390/molecules26237264>
- Rotaru, H. *et al.* (2012) "Cranioplasty with custom-made implants: Analyzing the cases of 10 patients," *Journal of Oral and Maxillofacial Surgery*, 70(2), pp. e169–e176. Available at: <https://doi.org/10.1016/j.joms.2011.09.036>.
- Sadhu, P. (2009) "Oronasal fistula in cleft palate surgery.," *Indian journal of plastic surgery : official publication of the Association of Plastic Surgeons of India*, 42 Suppl(Suppl), pp. S123-8. Available at: <https://doi.org/10.4103/0970-0358.57203>.
- Sadler, T. (2014) "Head and Neck," in *Medical Embryology*. Thirteenth, pp. 295–297.
- Saini, M. (2015) "Implant biomaterials: A comprehensive review," *World Journal of Clinical Cases*, 3(1), p. 52. Available at: <https://doi.org/10.12998/wjcc.v3.i1.52>.
- Schubert, C., van Langeveld, M.C. and Donoso, L.A. (2014) "Innovations in 3D printing: a 3D overview from optics to organs," *British Journal of Ophthalmology*, 98(2), pp. 159–161. Available at: <https://doi.org/10.1136/bjophthalmol-2013-304446>.
- Schwab, A. *et al.* (2020) "Printability and Shape Fidelity of Bioinks in 3D Bioprinting," *Chemical Reviews*. American Chemical Society, pp. 11028–11055. Available at: <https://doi.org/10.1021/acs.chemrev.0c00084>.
- Sculpteo (2017) *Comparison between 3D printing and traditional manufacturing processes for plastics*. Available at: <https://www.sculpteo.com/en/3d-printing/3d-printing-and-traditional-manufacturing-processes/>.
- Sekhon, P.S. *et al.* (2011) "Congenital anomalies associated with cleft lip and palate - An analysis of 1623 consecutive patients," *Cleft Palate-Craniofacial Journal*, 48(4), pp. 371–378. Available at: <https://doi.org/10.1597/09-264>.
- Serafin, A. *et al.* (2021) "Printable alginate/gelatin hydrogel reinforced with carbon nanofibers as electrically conductive scaffolds for tissue engineering," *Materials Science and Engineering C*, 122. Available at: <https://doi.org/10.1016/j.msec.2021.111927>.
- Shang, W. *et al.* (2017) "Hybrid 3D printing and electrodeposition approach for controllable 3D alginate hydrogel formation," *Biofabrication*, 9(2). Available at: <https://doi.org/10.1088/1758-5090/aa6ed8>.
- Sharma, R.K. and Nanda, V. (2009) "Problems of middle ear and hearing in cleft children.," *Indian journal of plastic surgery : official publication of the Association of Plastic Surgeons of India*, 42 Suppl(Suppl), pp. S144–S148. Available at: <https://doi.org/10.4103/0970-0358.57198>.
- Shaw (1995) "1995 Shaw et al - vitamins and folic.pdf."
- Sheahan, P. *et al.* (2003) "Incidence and outcome of middle ear disease in cleft lip and/or cleft palate," *International Journal of Pediatric Otorhinolaryngology*, 67(7), pp. 785–793. Available at: [https://doi.org/10.1016/S0165-5876\(03\)00098-3](https://doi.org/10.1016/S0165-5876(03)00098-3).
- Shi, B. and Losee, J. (2010) "The impact of cleft lip and palate on the parent-child relationships," *Archives of pediatrics*, 17(9), pp. 1380–1385. Available at:

<https://doi.org/10.1016/j.arcped.2010.06.026>.

Singare, S. *et al.* (2004) "Design and fabrication of custom mandible titanium tray based on rapid prototyping," *Medical Engineering and Physics*, 26(8), pp. 671–676. Available at: <https://doi.org/10.1016/j.medengphy.2004.06.001>.

Singh, G. (2015) "Prenatal Growth of Cranium, Facial and Oral Structures," in *Textbook of Orthodontics*. Third, p. 26.

Sitzman, T.J. *et al.* (2017) "Variation among cleft centres in the use of secondary surgery for children with cleft palate: a retrospective cohort study," *BMJ Paediatrics Open*, 1(1), p. e000063. Available at: <https://doi.org/10.1136/bmjpo-2017-000063>.

Slifer, K. *et al.* (2003) "Self-concept and satisfaction with physical appearance in youth with and without oral clefts," *Children's Health Care*, 32(2), pp. 81–101. Available at: <https://jhu.pure.elsevier.com/en/publications/self-concept-and-satisfaction-with-physical-appearance-in-youth-w-4> (Accessed: March 30, 2017).

Song, S.J. *et al.* (2011) "Sodium Alginate Hydrogel-Based Bioprinting Using a Novel Multinozzle Bioprinting System," *Artificial Organs*, 35(11), pp. 1132–1136. Available at: <https://doi.org/10.1111/j.1525-1594.2011.01377.x>.

Stanier, P. and Moore, G.E. (2004) "Genetics of cleft lip and palate : syndromic genes contribute to the incidence of non-syndromic clefts," 13(1), pp. 73–81. Available at: <https://doi.org/10.1093/hmg/ddh052>.

Subramaniam, V. *et al.* (2015) "Otological and audiological manifestations in cleft lip and cleft palate children: a clinical study," *International Journal of Otorhinolaryngology and Head and Neck Surgery*, 1(1), p. 7. Available at: <https://doi.org/10.18203/issn.2454-5929.ijohns20150579>.

Sun, J. and Tan, H. (2013) "Alginate-based biomaterials for regenerative medicine applications," *Materials*, 6(4), pp. 1285–1309. Available at: <https://doi.org/10.3390/ma6041285>.

Tabriz, A.G. *et al.* (2015) "Three-dimensional bioprinting of complex cell laden alginate hydrogel structures.," *Biofabrication*, 7(4), p. 045012. Available at: <https://doi.org/10.1088/1758-5090/7/4/045012>.

Tam, M.D. *et al.* (2012) "3-D printout of a DICOM file to aid surgical planning in a 6 year old patient with a large scapular osteochondroma complicating congenital diaphyseal aclasia," *Journal of Radiology Case Reports*, 6(1), pp. 31–37. Available at: <https://doi.org/10.3941/jrcr.v6i1.889>.

Tamay, D.G. *et al.* (2019) "3D and 4D printing of polymers for tissue engineering applications," *Frontiers in Bioengineering and Biotechnology*. Frontiers Media S.A. Available at: <https://doi.org/10.3389/fbioe.2019.00164>.

Thomas, D. and Gilbert, S. (2014) "Costs and Cost Effectiveness of Additive Manufacturing - A Literature Review and Discussion," *NIST Special Publication*, 1176, pp. 1–77. Available at: <https://doi.org/10.6028/NIST.SP.1176>.

Tibesar, R.J., Black, A. and Sidman, J.D. (2009) "Surgical repair of cleft lip and cleft palate," *Operative Techniques in Otolaryngology-Head and Neck Surgery*, 20(4), pp. 245–255. Available at: <https://doi.org/10.1016/j.otot.2009.10.010>.

- Toker, O.S. *et al.* (2015) "Three interval thixotropy test (3ITT) in food applications: A novel technique to determine structural regeneration of mayonnaise under different shear conditions," *Food Research International*, 70, pp. 125–133. Available at: <https://doi.org/10.1016/j.foodres.2015.02.002>.
- Tommila, M. *et al.* (2013) "Cellulose - A Biomaterial with Cell-Guiding Property," in *Cellulose - Medical, Pharmaceutical and Electronic Applications*. InTech. Available at: <https://doi.org/10.5772/54436>.
- Torrado, A.R. and Roberson, D.A. (2016) "Failure Analysis and Anisotropy Evaluation of 3D-Printed Tensile Test Specimens of Different Geometries and Print Raster Patterns," *Journal of Failure Analysis and Prevention*, 16(1), pp. 154–164. Available at: <https://doi.org/10.1007/s11668-016-0067-4>.
- Udofia, E., Udofia, E.N. and Zhou, W. (2019) *Microextrusion Based 3D Printing-A Review Cooperative 3D Printing View project Production of 3-D Geometric Models with Aluminium Scraps Using CAD/CAM Systems View project Microextrusion Based 3D Printing-A Review*. Available at: <https://www.researchgate.net/publication/335430080>.
- Ulery, B.D., Nair, L.S. and Laurencin, C.T. (2011) "Biomedical Applications of Biodegradable Polymers," *Journal of Environmental Polymer Degradation*, 1(1), pp. 65–80. Available at: <https://doi.org/10.1002/polb.22259>.Biomedical.
- Varoni, E. *et al.* (2012) "Agarose Gel as Biomaterial or Scaffold for Implantation Surgery: Characterization, Histological and Histomorphometric Study on Soft Tissue Response," *Connective Tissue Research*, 53(6), pp. 548–554. Available at: <https://doi.org/10.3109/03008207.2012.712583>.
- Vauchel, P. *et al.* (2008) "A new process for extracting alginates from *Laminaria digitata*: Reactive extrusion," *Food and Bioprocess Technology*, 1(3), pp. 297–300. Available at: <https://doi.org/10.1007/s11947-008-0082-x>.
- Ventola, C.L. (2014) "Medical Applications for 3D Printing: Current and Projected Uses.," *P & T: a peer-reviewed journal for formulary management*, 39(10), pp. 704–711. Available at: <https://doi.org/10.1016/j.infsoph.2008.09.005>.
- Wang, J. *et al.* (2021) "3D printed agar/ calcium alginate hydrogels with high shape fidelity and tailorable mechanical properties," *Polymer*, 214. Available at: <https://doi.org/10.1016/j.polymer.2020.123238>.
- Wang, L. *et al.* (2003) "Evaluation of sodium alginate for bone marrow cell tissue engineering," *Biomaterials*, 24(20), pp. 3475–3481. Available at: [https://doi.org/10.1016/S0142-9612\(03\)00167-4](https://doi.org/10.1016/S0142-9612(03)00167-4).
- Wehby, G. and Murray, J.C. (2011) "Folic Acid and Orofacial Clefts: A Review of the Evidence," *Oral Diseases*, 16(1), pp. 11–19. Available at: <https://doi.org/10.1111/j.1601-0825.2009.01587.x>.Folic.
- Williams, D.F. (2008) "On the mechanisms of biocompatibility," *Biomaterials*, 29(20), pp. 2941–2953. Available at: <https://doi.org/10.1016/j.biomaterials.2008.04.023>.
- Williams, L.J. *et al.* (2002) "Prevalence of spina bifida and anencephaly during the transition to mandatory folic acid fortification in the United States," *Teratology*, 66(1), pp. 33–39. Available at: <https://doi.org/10.1002/tera.10060>.



- Wong, K. v. and Hernandez, A. (2012) "A Review of Additive Manufacturing," *ISRN Mechanical Engineering*, 2012, pp. 1–10. Available at: <https://doi.org/10.5402/2012/208760>.
- Yan, J. *et al.* (2016) "Injectable alginate/hydroxyapatite gel scaffold combined with gelatin microspheres for drug delivery and bone tissue engineering," *Materials Science and Engineering C*, 63, pp. 274–284. Available at: <https://doi.org/10.1016/j.msec.2016.02.071>.
- Yoon, H.S. *et al.* (2014) "A comparison of energy consumption in bulk forming, subtractive, and additive processes: Review and case study," *International Journal of Precision Engineering and Manufacturing - Green Technology*, 1(3), pp. 261–279. Available at: <https://doi.org/10.1007/s40684-014-0033-0>.
- Yu, W. *et al.* (2009) "Cleft lip and palate genetics and application in early embryological development," (March 2014). Available at: <https://doi.org/10.4103/0970-0358.57185>.
- Yuan (2010) "Osteoinductive ceramics as a synthetic alternative to autologous bone grafting." Available at: <http://www.pnas.org/content/107/31/13614.full>.
- Zangana, A. (2011) *Veau Classification System*, *Slideshare.net*. Available at: <https://www.slideshare.net/dsmr/surgery-5th-year-3rd-lecturepart-one-dr-ari-raheem-qader>.
- Zhang, W.J. *et al.* (2001) *Purity of Alginate Affects the Viability and Fibrotic Overgrowth of Encapsulated Porcine Islet Xenografts*.
- Zhang, Z. *et al.* (2017) "Post-operative outcomes after cleft palate repair in syndromic and non-syndromic children: A systematic review protocol," *Systematic Reviews*, 6(1), pp. 1–7. Available at: <https://doi.org/10.1186/s13643-017-0438-2>.
- Zheng, W. *et al.* (2008) "The Natural History of Audiologic and Tympanometric Findings in Patients With an Unrepaired Cleft Palate." Available at: <https://doi.org/10.1597/07-152.1>.
- Zhu, J. and Marchant, R.E. (2011) "Design properties of hydrogel tissue-engineering scaffolds," *Expert Review of Medical Devices*, 8(5), pp. 607–626. Available at: <https://doi.org/10.1586/erd.11.27>.
- Zreaqat, M.H., Hassan, R. and Hanoun, A. (2017) "Cleft Lip and Palate Management from Birth to Adulthood: An Overview," *Insights into Various Aspects of Oral Health* [Preprint], (December). Available at: <https://doi.org/10.5772/intechopen.68448>.

# 10. Appendix

Table 10.1: Acquisition parameters for  $^1\text{H}$  NMR analysis of alginate strains.

Parameter	Code	Value
Pulse program	PULPROG	ZG30
Time domain	TD	65546
Number of scans	NS	128
Number of dummy scans	DS	2
Spectral width in Hz	SWH	10000 Hz
Free induction decay resolution	FIDRES	0.305176 Hz
Acquisition time	AQ	3.2767999 sec
Receiver gain	RG	189.1
Dwell time	DW	50.000 $\mu\text{sec}$
Delay length (channel 1)	D1	2.00000000 sec
Irradiation frequency (channel 1)	SFO1	500.1330883 MHz
Nucleus observed (channel 1)	NUC1	$^1\text{H}$
Pulse length (channel 0)	P0	3.33 $\mu\text{sec}$
Pulse length (channel 1)	P1	10.00 $\mu\text{sec}$
Power level (channel 1)	PLW1	22.00000000 W

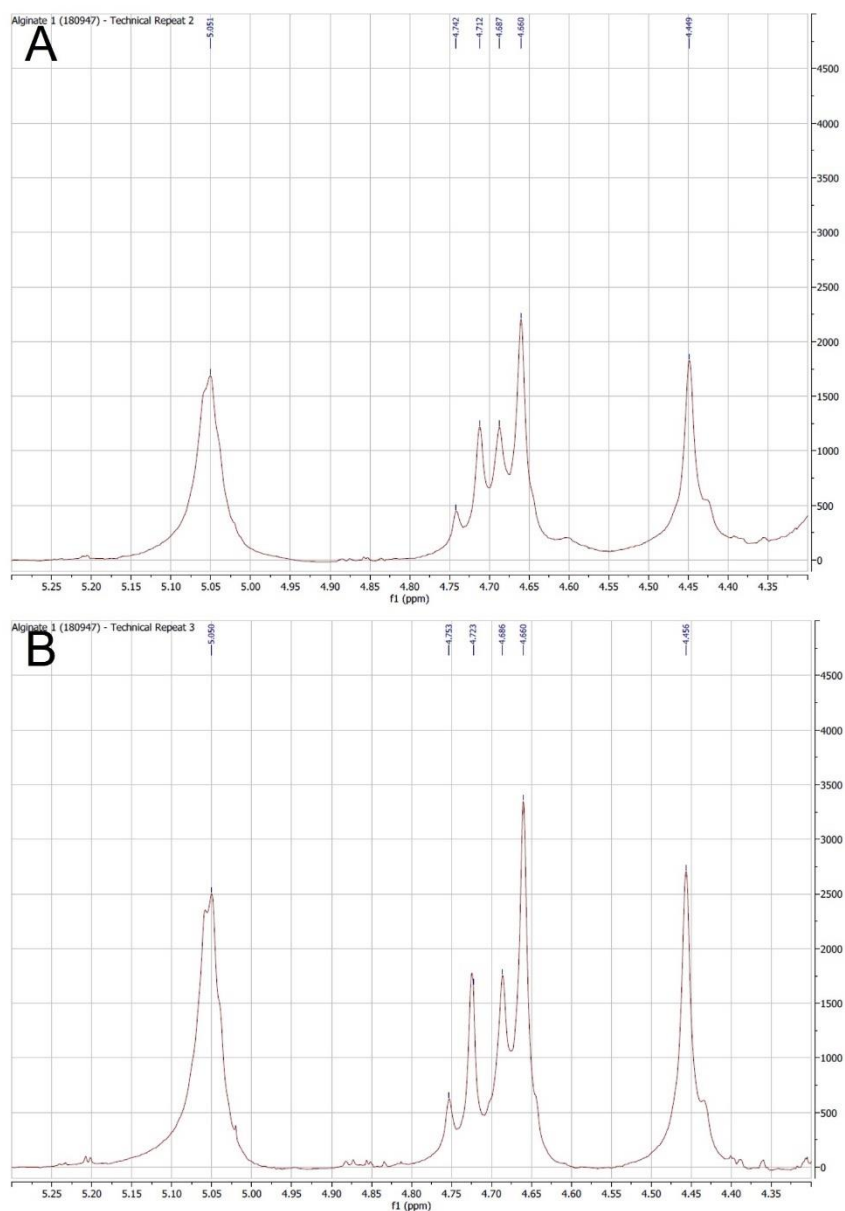


Figure 10.1: Additional  $^1\text{H}$  NMR spectra technical repeats of alginate 1 (180947) characterisation. MestReNova was used to apply Fourier transform, phase correction, baseline correction and peak labelling.

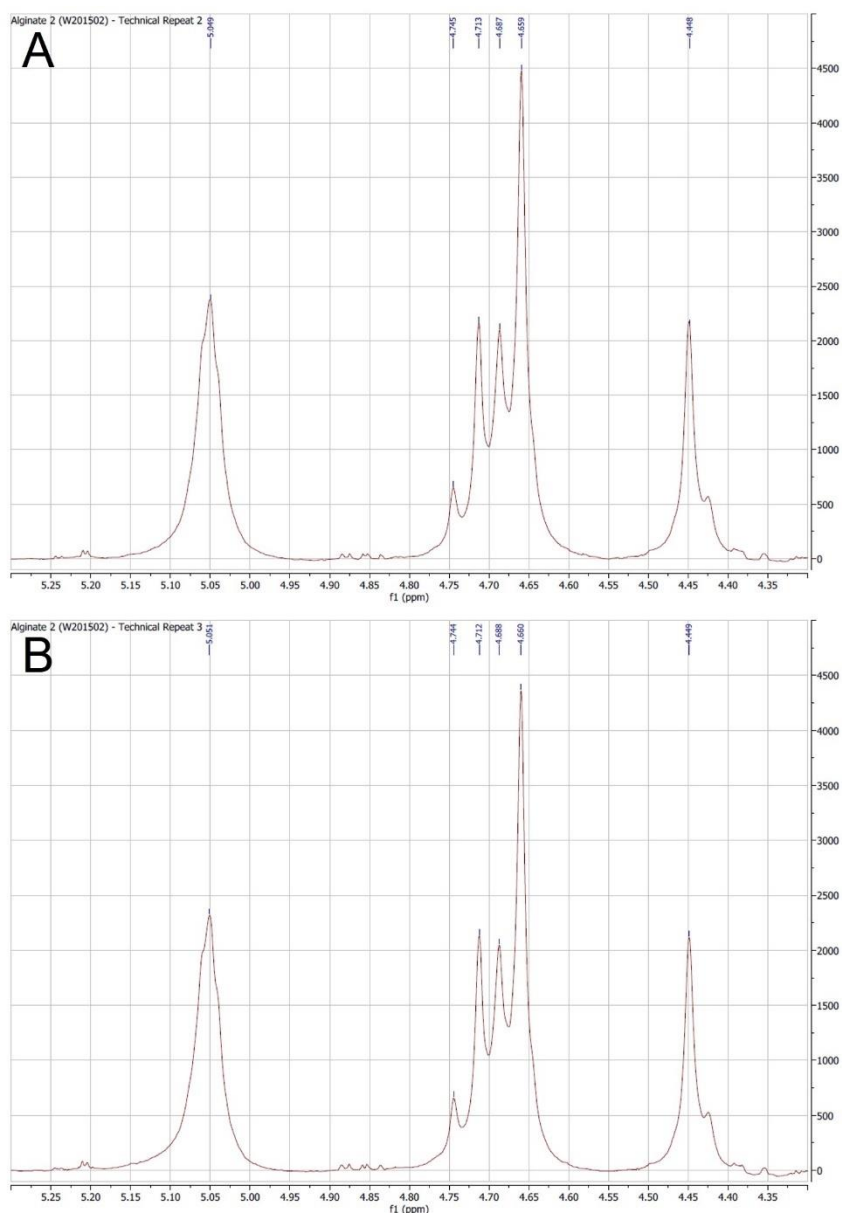


Figure 10.2: Additional  $^1\text{H}$  NMR spectra technical repeats of alginate 2 (W201502) characterisation. MestReNova was used to apply Fourier transform, phase correction, baseline correction and peak labelling.

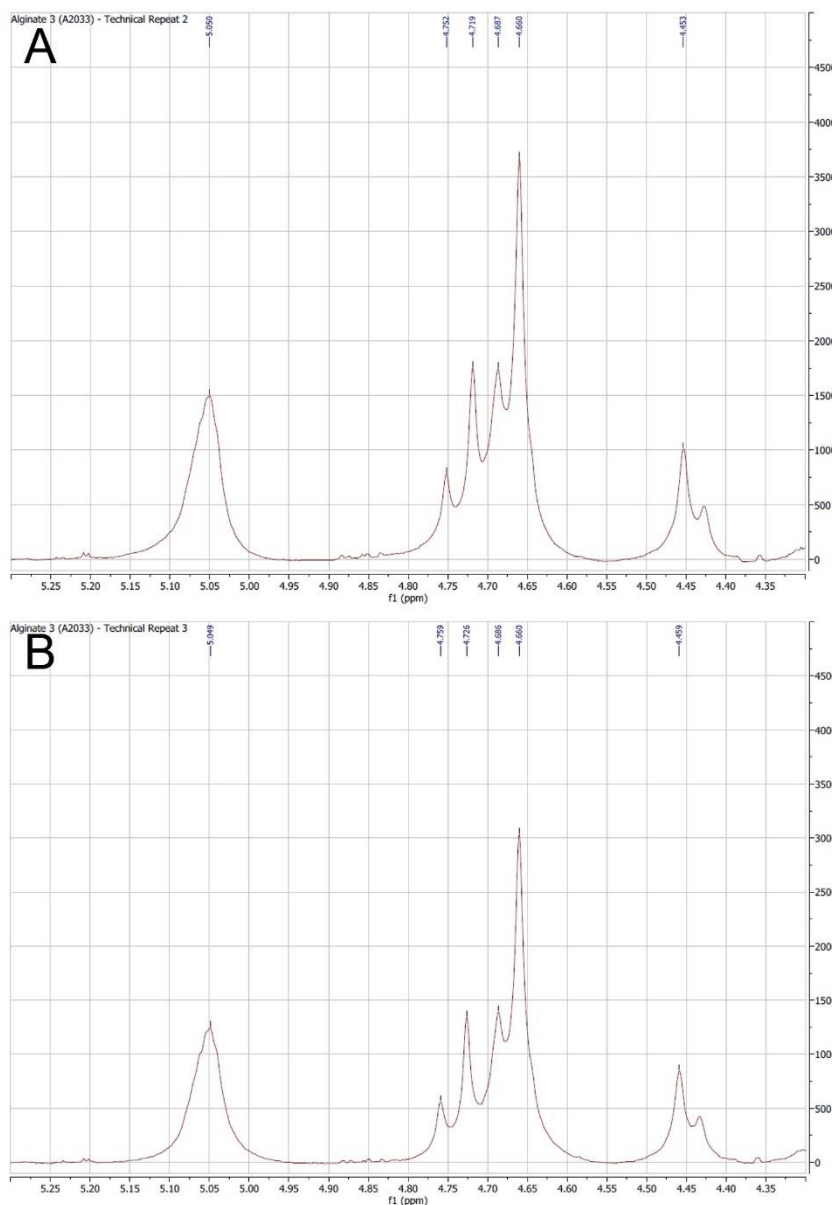


Figure 10.3: Additional  $^1\text{H}$  NMR spectra technical repeats of alginate 3 (A2033) characterisation. MestReNova was used to apply Fourier transform, phase correction, baseline correction and peak labelling.

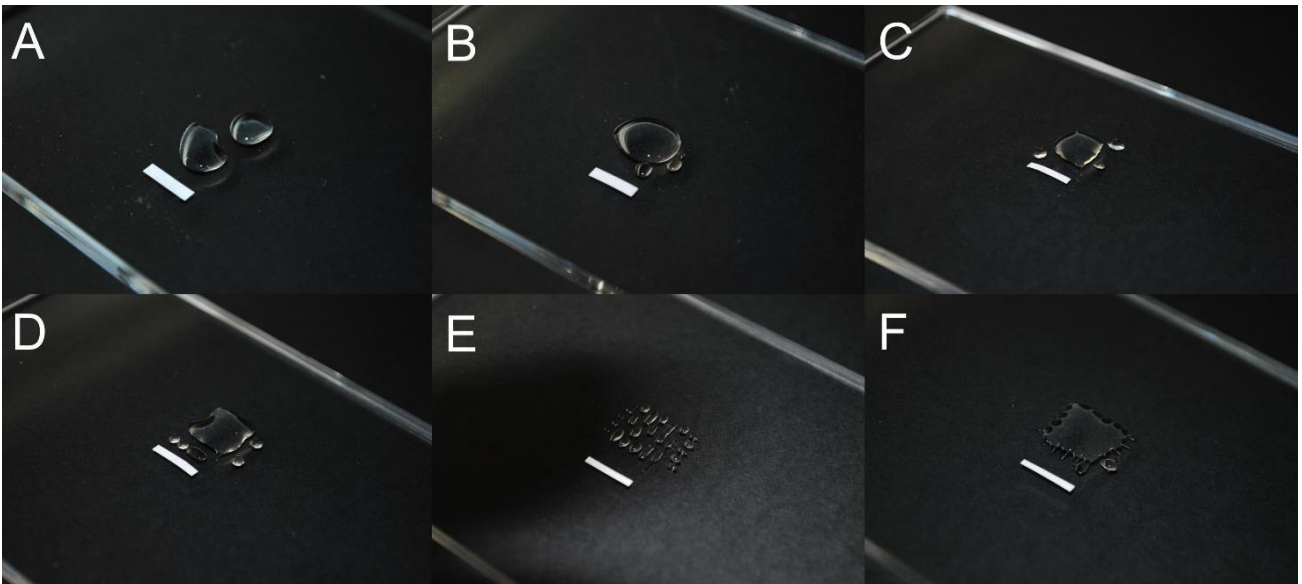


Figure 10.4: 3D printed lattice stress test models ( $20 \times 20 \times 1.2$  mm) of UC samples 0.5 % (A), 1.0 % (B), 1.5 % (C), 2.0 % (D), 2.5 % (E) and 3.0 % (F). Captured using a digital camera with an attached polarising filter. Scale bar = 10 mm.

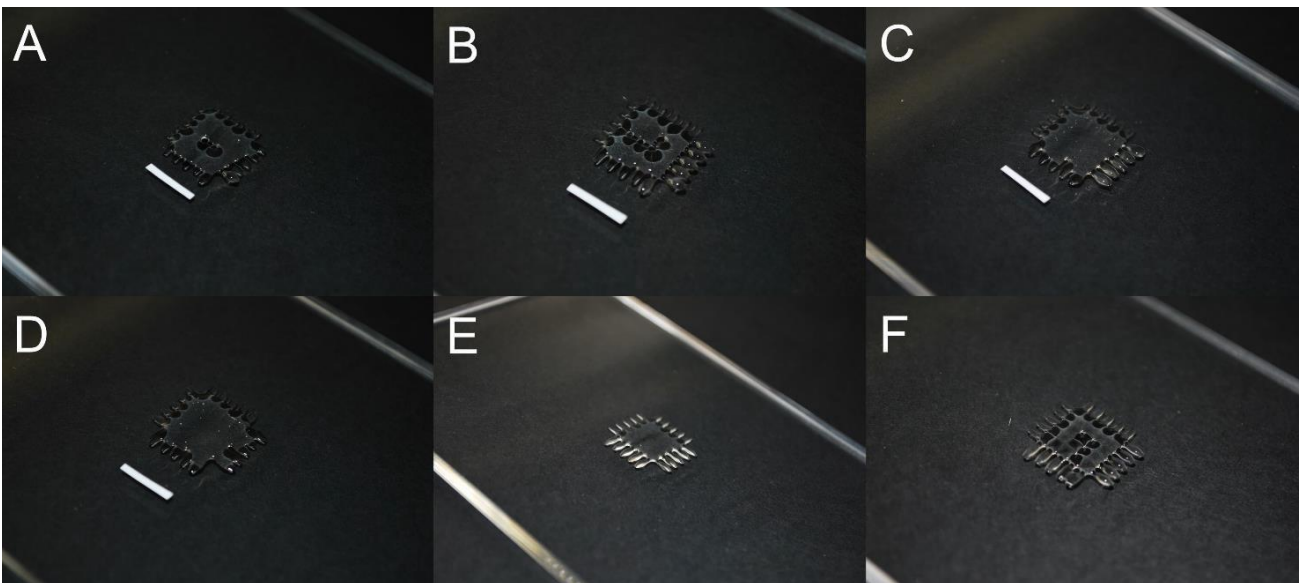


Figure 10.5: 3D printed lattice stress test models ( $20 \times 20 \times 1.2$  mm) of UC samples 3.5 % (A), 4.0 % (B), 4.5 % (C), 5.0 % (D), 5.5 % (E) and 6.0 % (F). Captured using a digital camera with an attached polarising filter. Scale bar = 10 mm.

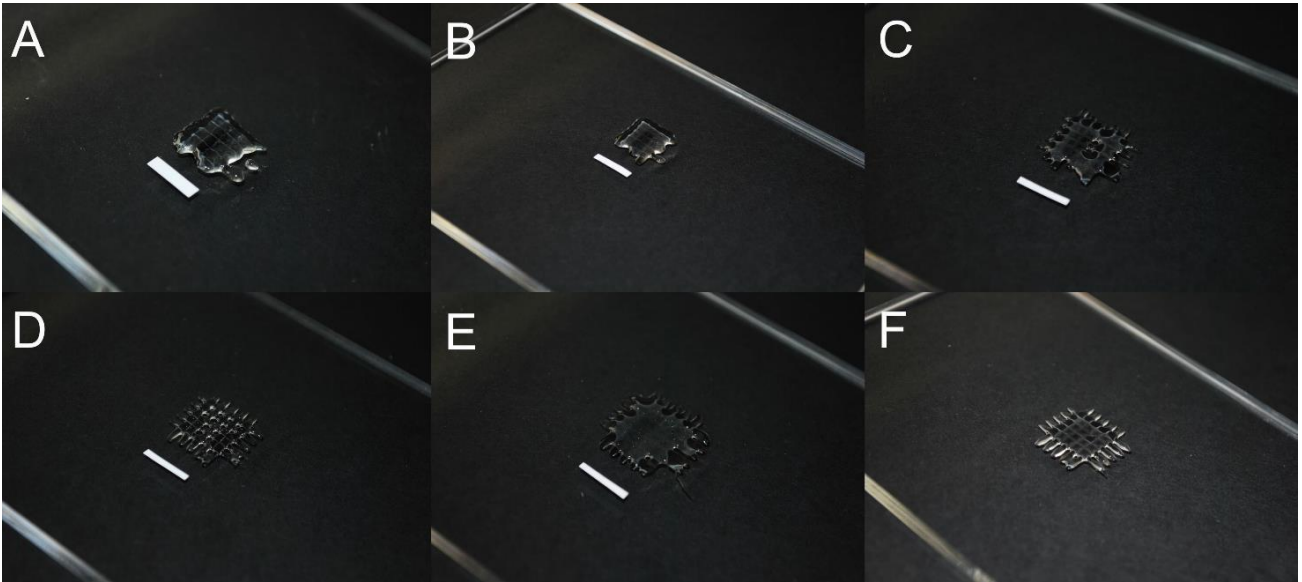


Figure 10.6: 3D printed lattice stress test models ( $20 \times 20 \times 1.2$  mm) of PC samples 0.5 %/5 mM (A), 1.5 %/5 mM (B), 2.5 %/5 mM (C), 3.5 %/5 mM (D), 4.5 %/5 mM (E) and 5.5 %/5 mM (F). Captured using a digital camera with an attached polarising filter. Scale bar = 10 mm.

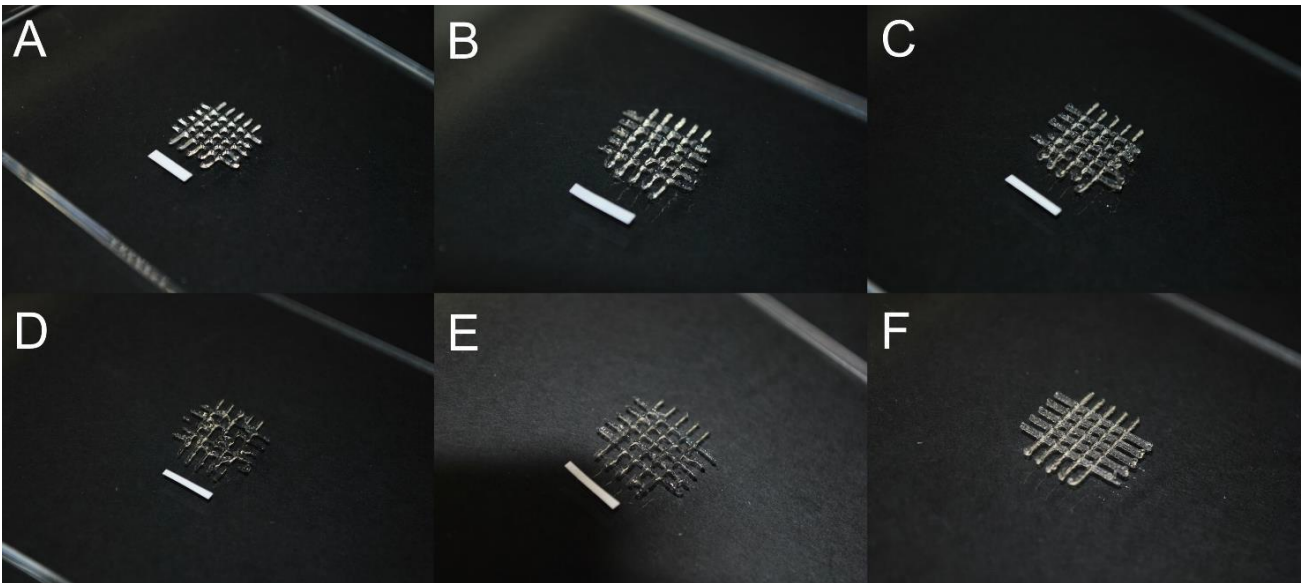


Figure 10.7: 3D printed lattice stress test models ( $20 \times 20 \times 1.2$  mm) of PC samples 1 %/10 mM (A), 2 %/10 mM (B), 3 %/10 mM (C), 4 %/10 mM (D), 5 %/10 mM (E) and 6 %/10 mM (F). Captured using a digital camera with an attached polarising filter. Scale bar = 10 mm.



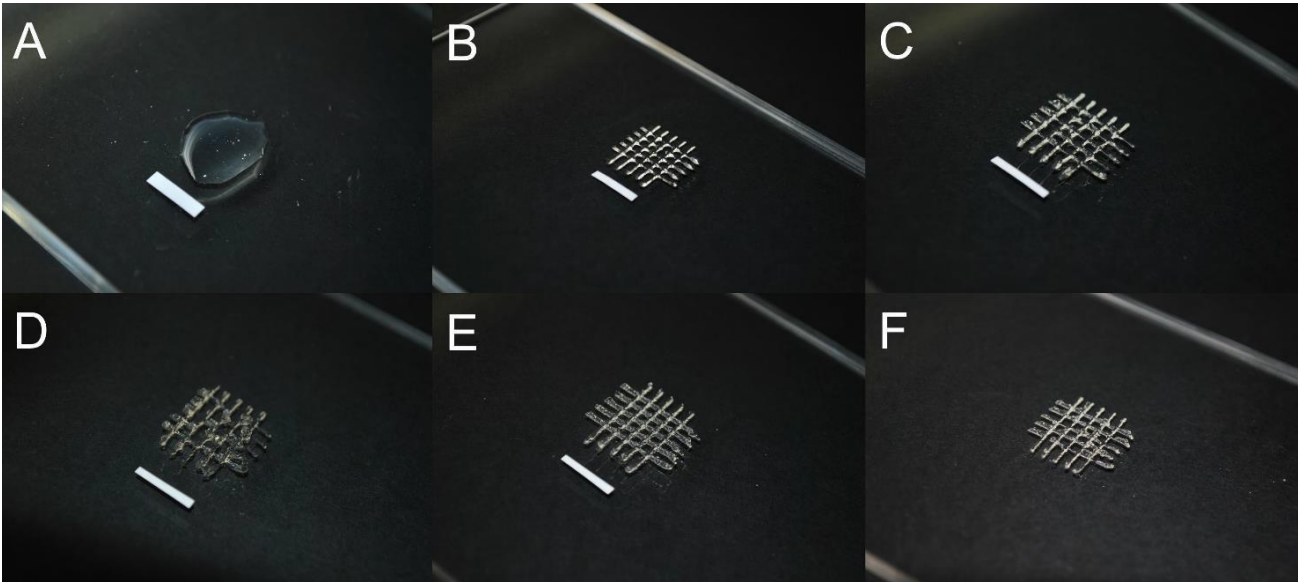


Figure 10.8: 3D printed lattice stress test models ( $20 \times 20 \times 1.2$  mm) of PC samples 0.5 %/15 mM (A), 1.5 %/15 mM (B), 2.5 %/15 mM (C), 3.5 %/15 mM (D), 4.5 %/15 mM (E) and 5.5 %/15 mM (F). Captured using a digital camera with an attached polarising filter. Scale bar = 10 mm.

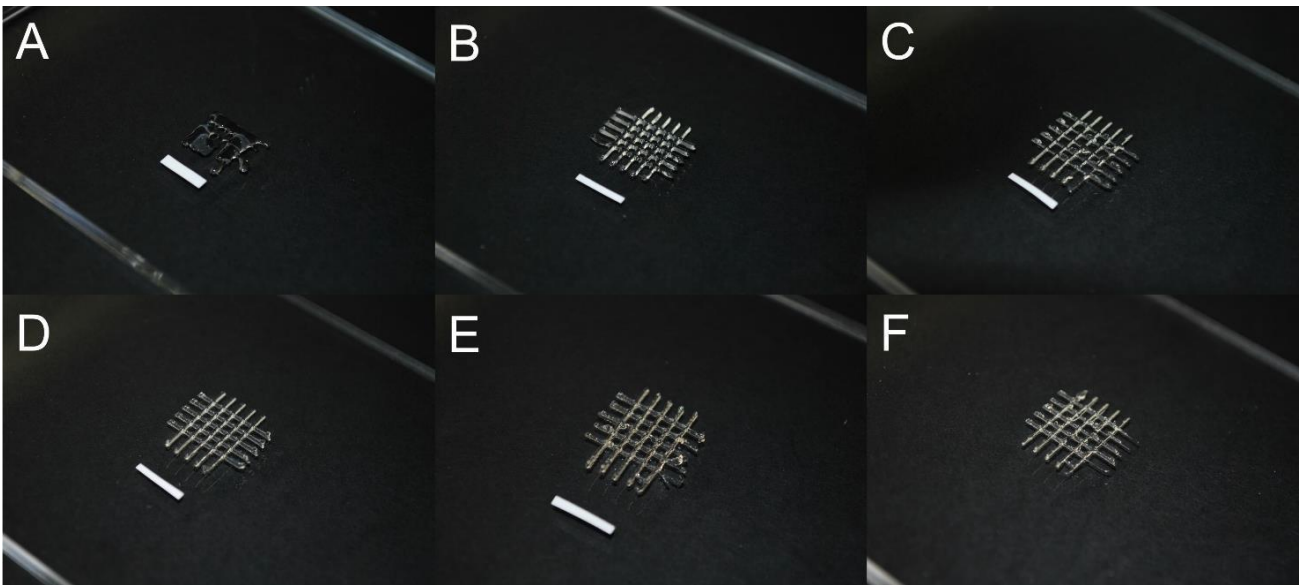


Figure 10.9: 3D printed lattice stress test models ( $20 \times 20 \times 1.2$  mm) of PC samples 1 %/20 mM (A), 2 %/20 mM (B), 3 %/20 mM (C), 4 %/20 mM (D), 5 %/20 mM (E) and 6 %/10 mM (F). Captured using a digital camera with an attached polarising filter. Scale bar = 10 mm.



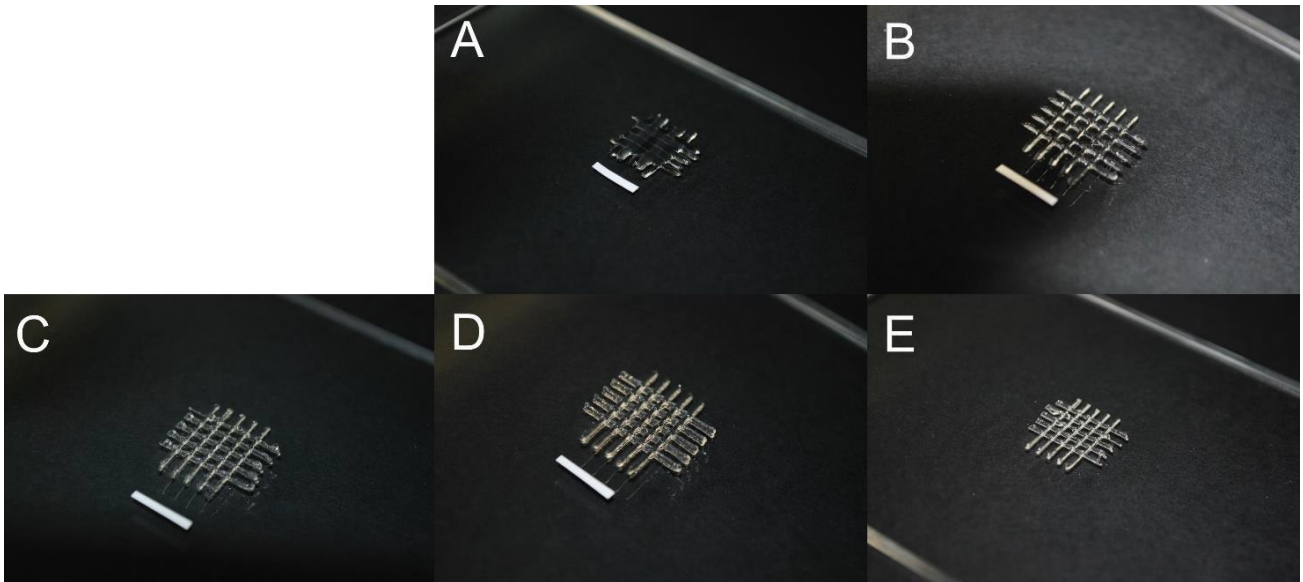


Figure 10.10: 3D printed lattice stress test models ( $20 \times 20 \times 1.2$  mm) of PC samples, 1.5 %/25 mM (A), 2.5 %/25 mM (B), 3.5 %/25 mM (C), 4.5 %/25 mM (D) and 5.5 %/25 mM (E). Captured using a digital camera with an attached polarising filter. Scale bar = 10 mm.

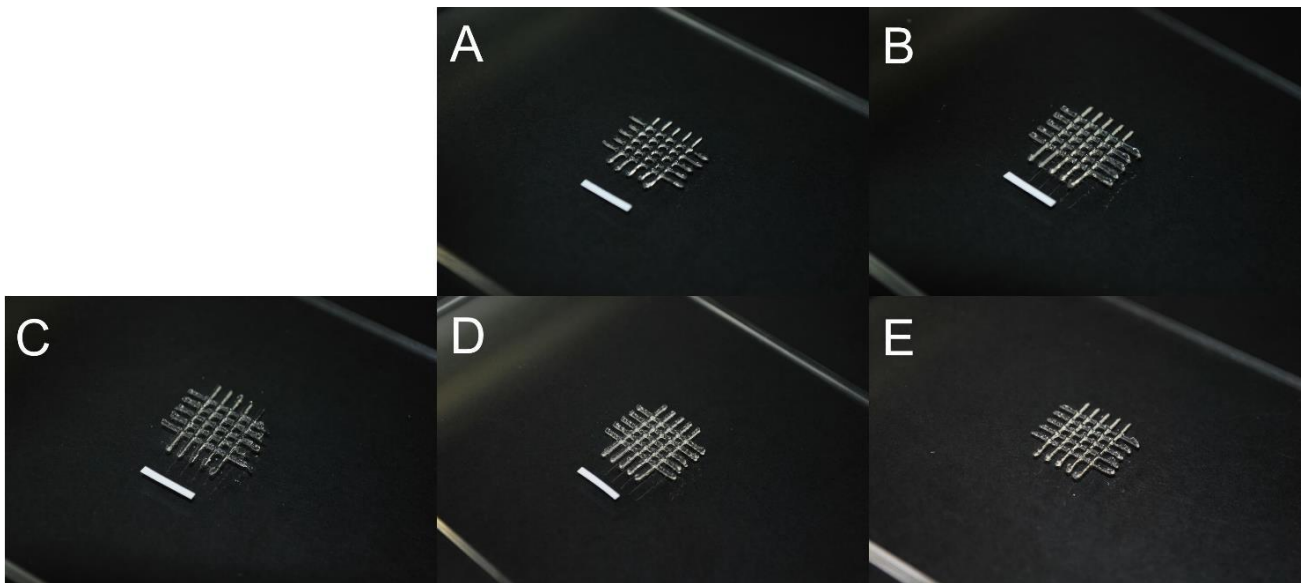


Figure 10.11: 3D printed lattice stress test models ( $20 \times 20 \times 1.2$  mm) of PC samples, 2 %/20 mM (A), 3 %/20 mM (B), 4 %/20 mM (C), 5 %/20 mM (D) and 6 %/20 mM (E). Captured using a digital camera with an attached polarising filter. Scale bar = 10 mm.

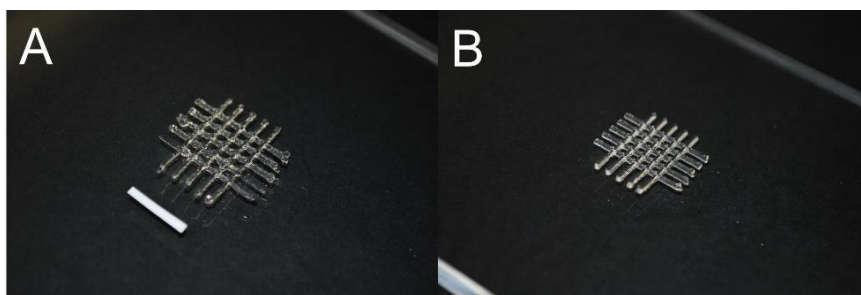


Figure 10.12: 3D printed lattice stress test models ( $20 \times 20 \times 1.2$  mm) of PC samples, 4.5 %/35 mM (A) and 5.5 %/35 mM (B). Captured using a digital camera with an attached polarising filter. Scale bar = 10 mm.

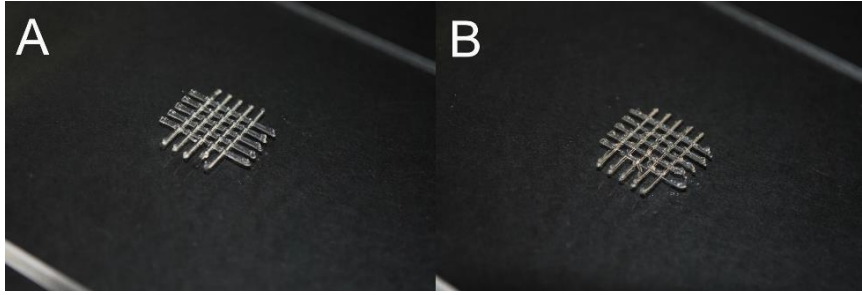


Figure 10.13: 3D printed lattice stress test models ( $20 \times 20 \times 1.2$  mm) of PC samples, 5%/40 mM (A) and 5%/50 mM (B). Captured using a digital camera with an attached polarising filter. Scale bar = 10 mm.

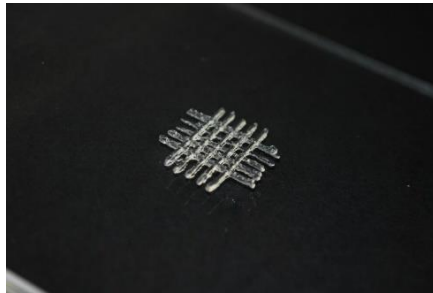


Figure 10.14: 3D printed lattice stress test models ( $20 \times 20 \times 1.2$  mm) of PC samples 5.5%/45 mM. Captured using a digital camera with an attached polarising filter. Scale bar = 10 mm.

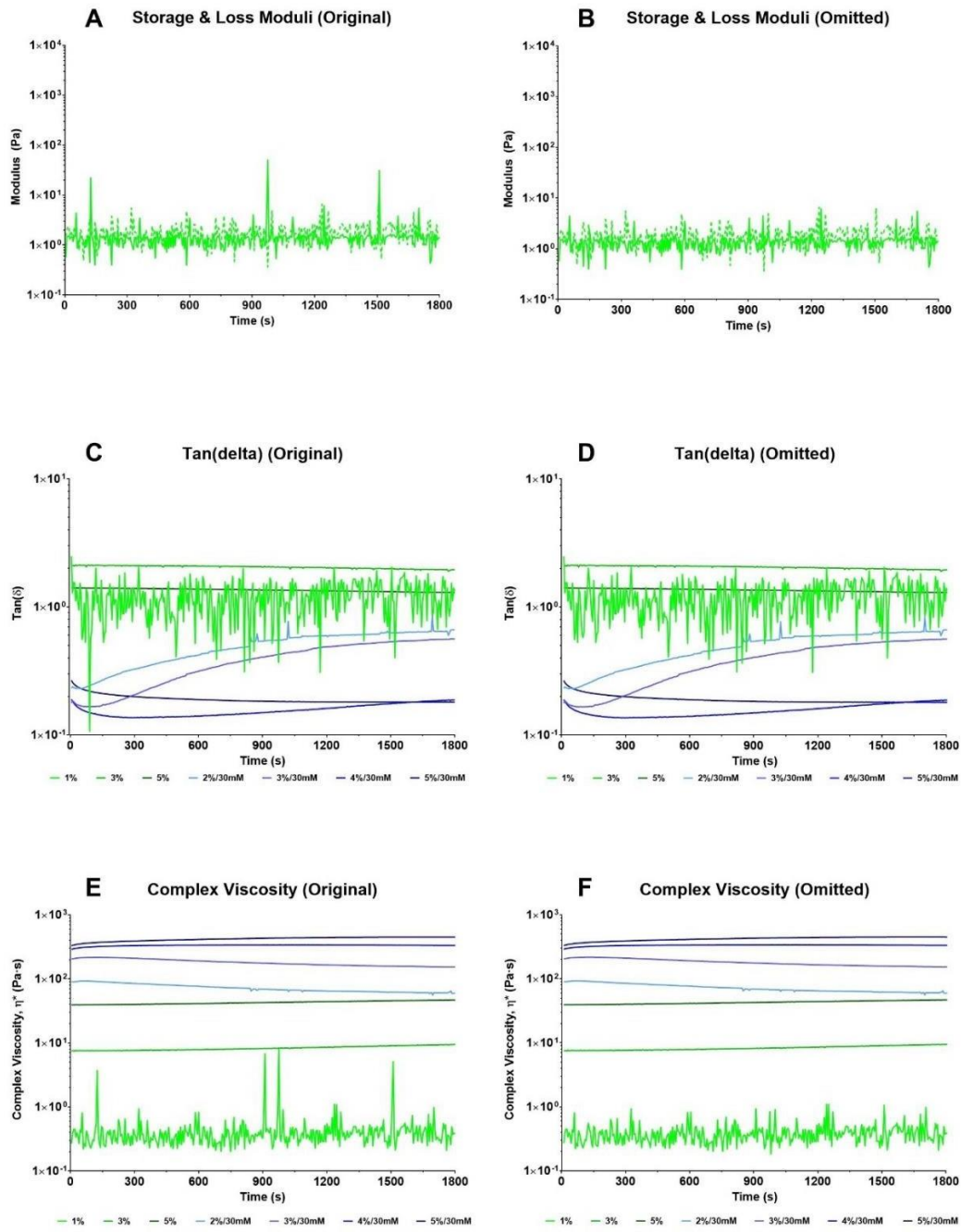


Figure 10.15: Comparison of all three results graphs of the post-mix time sweep with original results (left) and results that contained an omission (right) at 125 s, 910 s, 975 s and 1510 s for the third technical repeat of the 1 % UC data series.